A Theoretical Investigation of the Microsolvation of Multivalent Ions in Clusters

Sean Hughes

A Thesis
In
The Department
of
Chemistry and Biochemistry

Presented in Partial Fulfilment of the Requirements
for the Degree of Doctor of Philosophy at
Concordia University
Montreal, Quebec, Canada

August 2006

Your file Votre référence
ISBN: 978-0-494-23831-8
Our file Notre référence
ISBN: 978-0-494-23831-8

A Theoretical Investigation of the Microsolvation of Multivalent Ions in Clusters

Sean Hughes, Ph.D.
Concordia University, 2006

Trivalent lanthanide metals (Ln^{3+}) are among the most spectroscopically active ions in the periodic table and are characterized by their exceptional ability to absorb and emit light in the ultraviolet, visible and near infra-red regions of the electromagnetic spectrum. These ions are sensitive to the nature of their ligands, as has been evidenced from their spectral properties in different environments. In an effort to predict the behaviour of lanthanide ions in different environments, solvated Ln^{3+} ions in clusters, $Ln^{3+}(solvent)_n$, were investigated as a model system. Cluster studies provide an ideal means of monitoring progressive changes in the properties of the lanthanide ions with cluster size increases. The electronic, energetic and thermodynamic properties of $Ln^{3+}(H_2O)_n$ and $Ln^{3+}(CH_3CN)_n$ clusters were simulated using a combination of quantum chemistry calculations, model potential development and Monte Carlo simulations, paying close attention to possible cluster-to-bulk transitions.

The properties of small $Ln^{3+}(H_2O)_n$ clusters obtained from quantum chemistry calculations indicate, much akin to other multi-valent $M^{q+}(H_2O)_n$ clusters, that the metal ion-water interactions are predominantly electrostatic. Mutual polarization of both the ion and the water molecules accounts for the large $Ln^{3+}(H_2O)_n$ cluster binding energies and the resulting structural properties of the clusters. The quantum chemistry results were the basis for designing and parameterising polarizable model potentials for use in Monte Carlo simulations. The simulations revealed that bulk-like properties of $Ln^{3+}(H_2O)_n$ clusters, namely first-shell coordination numbers and bulk thermodynamic

properties, are obtained at very large cluster sizes ($n \geq 64$), thus showing that cluster studies are a good model for studying bulk solvation.

The $Ln^{3+}(H_2O)_n$ cluster binding enthalpies were found to be quite large, even at small cluster size, implying that these species should be stable under experimental conditions. However, small clusters have rarely been observed experimentally when they contain protic solvents and charge-reduced clusters, where the metal loses its 3+ charge, are observed instead. Thus, $Eu^{3+}(H_2O)_n$ cluster deprotonation was investigated as a possible explanation for the lack of experimental observation of small $Ln^{3+}(H_2O)_n$ clusters. The small clusters were found to favour loss of (solvated) hydronium ions from the cluster, explaining the experimentally-observed, charge-reduced clusters. Only recently (June 2006) was the experimental observation of large $Ln^{3+}(H_2O)_n$ clusters ($n > 15$) reported. This is consistent with our prediction that deprotonation becomes less favourable with cluster size.

Finally, investigation of $Ln^{3+}(CH_3CN)_n$ clusters, using a similar methodology, reveals that formation of these clusters is also energetically favourable and that convergence to bulk, structural and thermodynamic properties are obtained at smaller cluster sizes than those observed in water clusters. Given that the thermodynamic properties of $Ln^{3+}(CH_3CN)_n$ and large $Ln^{3+}(H_2O)_n$ clusters have yet to be determined, the results herein may serve as benchmarks for future experimentation.

ACKNOWLEDGMENTS

First and foremost, I would like to acknowledge the hard work and dedication of both my supervisors, Dr. John A. Capobianco and Dr. Gilles H. Peslherbe. Without their valuable insight and input, this work would not have been possible. To Dr. Peslherbe, I would like to thank you for introducing me to the field of computational chemistry, which I firmly believe taught me more about chemistry, physics and math than I would have imagined possible. To Dr. Capobianco, I would like to thank you for all the support and guidance you have given me over the years. Be they from an academic, administrative or personal standpoint, the (hard) lessons I learned under your wing will forever be ingrained in me. I would also like to say express my sincere thanks to my committee members. Thank you to Dr. Cameron Skinner who was instrumental in setting up this meeting under incredible time constraints. To Dr. Peter Bird, I have enjoyed our many discussions over the years, be they of a pedagogical or for all his valuable insight over the years and to both external examiners, Dr. Alexandre Shvartsburg and Dr. Reginald Storms for useful discussions and for their contributions to this work.

I cannot fail to mention the support of my friends and colleagues at Concordia University. Thank you to Lillian Jackson and Dr. Geza Szamosi for affording me the opportunity to come to Concordia University as a Science College member. To Denise, Qadir, Yin, Lei, Rob, Sacha, Sichaun, Etienne, Grygoriy, Svetlana, Tania, Elizabeth, Pierre, Andrea, Fabiano and last but not least Nabil, thank you for all the good times and helpful advice, and I wish you all the best of luck in the future. A special thank you to all the secretaries (Donna, Carole, Kathy and Lisa 1 and 2) and the technical staff for their

help over the years. I would like to acknowledge all of the Graduate Conference Organising Committee members with whom I had the privilege of working with throughout the years. Thank you to Dr. Christine DeWolf for organizing all those great soccer games and giving me an excuse to get some air. I would also like to say a special thank you to Dr. Louis Cuccia whose love for science is truly inspiring.

To Celine, Pascal, Jeff, David and Paul, I wish to thank you for all the great discussions we used to have every afternoon and for all the time well spent. I will cherish that time forever. I would like to acknowledge Tao-Nhan for having introduced me to many of the techniques used over the course of this study and for being a good friend and confidante.

Finally, to Chris, Fiore and Rafik, I want to say that I have never had anything but the utmost respect for you guys. We have been together since the very beginning and I couldn't ask for a better crew to work with. All the early mornings and late nights studying for exams, writing assignments, running scans (when I was allowed to) and practising speeches were made all the more bearable by having you guys around. Oddly enough, I wish it didn't have to change. I sincerely hope we can stay in touch in the years to come... maybe we can even collaborate and finally find out what makes Rafik so 'elusive'.

I would like to acknowledge the FCAR grant agency for funding. Last, but certainly not least, I want to say a big thank you to my close friends (the Posse and my chemistry crew), my family, especially my parents Sally and Lloyd, my brother Scott, and Tina for all their love, patience, understanding and support. I hope I have made you all proud.

This thesis is dedicated to my grandparents, Basseran and Sultan Mohammed and

to Ekaterini and Antonios Kolokythas

"If we knew what it was we were doing, it would not be called research, would it?"

- Albert Einstein

TABLE OF CONTENTS

LIST OF FIGURES ..... **xii**

LIST OF TABLES ..... **xv**

CONTRIBUTIONS OF AUTHORS ..... **xvii**

CHAPTER 1 ..... **1**

1.1. INTRODUCTION TO CLUSTERS 1
1.2. EXPERIMENTAL METHODS FOR CLUSTER GENERATION 4
1.3. LANTHANIDE SOLVENT CLUSTERS 5
1.3.1. An Introduction to the Lanthanides *5*
1.3.2. The Properties of Lanthanide Ions in Clusters *10*
1.4. COMPUTATIONAL CHEMISTRY 11
1.5. STATEMENT OF THE PROBLEM 14
1.6. FORMAT OF THE THESIS 15

CHAPTER 2 ..... **17**

On the Nature of Bonding Interactions in Small Metal Ion-Water Clusters **17**

ABSTRACT 17
2.1. INTRODUCTION 19
2.2. COMPUTATIONAL PROCEDURES 22
2.3. RESULTS AND DISCUSSION 25
2.3.1. Structures *25*
2.3.2. Energetics *31*
2.3.3. Charge Analysis *34*
2.3.4. Natural Bond Orbital (NBO) *36*
2.3.5. Electron localisation function (ELF) *39*
2.3.6. Atoms in Molecules (AIM) *46*
2.4. CONCLUSIONS 52
AUTHOR'S NOTES AND SIGNIFICANCE OF PAPER TO THESIS 54

CHAPTER 3 ..... **55**

A Theoretical Study of Trivalent Lanthanide Ion Microsolvation in Water Clusters from First Principles **55**

ABSTRACT 55
3.1. INTRODUCTION 56
3.2. QUANTUM CHEMISTRY CALCULATIONS FOR SMALL $Ln^{3+}(H_2O)_N$ CLUSTERS 59
3.2.1. Computational Details *59*
3.2.2. $Ln^{3+}(H_2O)$ - Structural and Energetic Properties *60*
3.2.3. $Ln^{3+}(H_2O)$ - Electronic Properties *61*
3.2.4. Larger $Ln^{3+}(H_2O)_n$ Clusters (n =6,8,9) *62*
3.3. MODEL POTENTIAL AND SIMULATIONS/PROCEDURE 66

3.3.1. Functional form of the Model Potentials *66*
3.3.2. Parameterization of the Model Potentials *67*
3.3.3. Monte Carlo Simulations *71*
3.4. RESULTS AND DISCUSSION 72
3.4.1. Structural Data *72*
3.4.2. Thermodynamic Data *77*
3.5. CONCLUSIONS 80
3.7. AUTHOR'S NOTES AND SIGNIFICANCE OF PAPER TO THESIS 82

CHAPTER 4 ..... **83**

A Theoretical Study of the Hydration of Trivalent Lanthanide Ions Across the Series **83**

ABSTRACT 83
4.1. INTRODUCTION 84
4.2. COMPUTATIONAL PROCEDURE 87
4.2.1. Model Potentials *87*
4.2.2. Quantum Chemistry Calculations of Ln^{3+}-complexes *88*
4.2.3. Parameterization of the Model Potentials *91*
4.2.4. Monte Carlo Simulations *93*
4.3. RESULTS AND DISCUSSION 95
4.3.1. Structural Data *95*
4.3.2. Thermodynamic Data *100*
4.4. CONCLUSIONS 103
AUTHOR'S NOTES AND SIGNIFICANCE OF PAPER TO THESIS 105

CHAPTER 5 ..... **107**

Are Trivalent Europium-Water Clusters Stable Species? A Theoretical Study of the Deprotonation of $Eu^{3+}(H_2O)_n$ Clusters **107**

ABSTRACT 107
5.1. INTRODUCTION 109
5.2. METHODS 111
5.3. RESULTS AND DISCUSSION 112
5.3.1. Structures *112*
5.3.2. Energetics *118*
5.3.3. Reaction Mechanism for Pathway (4) *123*
5.3.4. Charge Analysis *132*
5.4. CONCLUSIONS 133
AUTHOR'S NOTES AND SIGNIFICANCE OF PAPER TO THESIS 135

CHAPTER 6 ..... **136**

Structural and Thermodynamic Properties of Lanthanide-Acetonitrile Clusters . **136**

ABSTRACT 136
6.1. INTRODUCTION 138
6.2. METHODS 141

6.2.1. Computational Details *141*
6.2.2. $Ln^{3+}(CH_3CN)_{1,2}$ - Structural and Energetic Properties *142*
6.3. MODEL POTENTIALS AND SIMULATIONS/PROCEDURE 146
6.3.1. Functional Form of the Model Potentials *146*
6.3.2. Parameterization of the Model Potentials *148*
6.3.3. Monte Carlo Simulations *150*
6.4. RESULTS AND DISCUSSION 151
6.4.1. Structural Data *151*
6.4.2. Thermodynamic Data *157*
6.5. CONCLUSIONS 161
AUTHOR'S NOTE AND SIGNIFICANCE OF PAPER TO THESIS 164

CHAPTER 7 ..... **165**

7.1. CONCLUSIONS 165
7.2 FUTURE WORK 166

REFERENCES **171**

LIST OF FIGURES

Figure 1.3.1.1. Average coordination numbers in aqueous solution for each of the trivalent lanthanide ions, taken from Ref. [58-62]..... **9**

Figure 2.1.1. Typical C_2 and D_{2d} $M^{q+}(H_2O)_2$ structures..... **20**

Figure 2.3.5.1. ELF isosurfaces and contour diagrams for $Be^{2+}(H_2O)$, $Al^{3+}(H_2O)$, $Sc^{3+}(H_2O)$ and $Na^{+}(H_2O)$ clusters. Each contour plot is the plane containing the V(M,O), C(M) and C(O) basins. The ELF values for each plot are $\eta(r)$ = 0.89, 0.85, 0.86 and 0.85 respectively. The ELF was determined using B3LYP wavefunctions. **40**

Figure 2.3.5.2. ELF isosurfaces and contour diagrams for $Al^{3+}(H_2O)_2$ and $Sc^{3+}(H_2O)_2$. Each contour plot is a slice through the plane defined by the O-M-O bond angle. The ELF values for each plot are $\eta(r)$ = 0.86 and 0.83, respectively, and were determined using B3LYP wavefunctions. **44**

Figure 2.3.6.1. AIM contour plots of the Laplacian for $Be^{2+}(H_2O)$, $Al^{3+}(H_2O)$, and $Na^{+}(H_2O)$. All plots are based on MP2 wavefunctions..... **48**

Figure 2.3.6.2. AIM contour plots of the Laplacian for $Al^{3+}(H_2O)_2$ and $Sc^{3+}(H_2O)_2$. All plots are based on MP2 wavefunctions..... **51**

Figure 3.2.4.1. Minimum energy $Er^{3+}(H_2O)_n$ cluster structures for a) n = 6, b) n = 8 and c) n = 9 obtained from quantum chemistry calculations with the HF/SDD/6-31+G(2d,p) model chemistry. Distances are in Å. **64**

Figure 3.4.1.1. Representative structures obtained for $Eu^{3+}(H_2O)_n$ clusters from Monte Carlo simulations with model potentials..... **73**

Figure 3.4.1.2. Radial probability distribution functions and cumulative radial probability distribution functions vs. Ln^{3+}-O distance for $Ln^{3+}(H_2O)_{12}$ and $Ln^{3+}(H_2O)_{64}$ (Ln^{3+} = Nd^{3+}, Eu^{3+}, Er^{3+} and Yb^{3+}). First-shell coordination numbers derived from the cumulative functions are listed in Table 3.4.1.1. and average ion-oxygen distances in Table 3.4.1.2.**74**

Figure 3.4.2.1. a) Stepwise binding enthalpy vs. cluster size for $Ln^{3+}(H_2O)_n$ clusters (n = 1-9); b) reduced cluster enthalpy vs. cluster size for Ln^{3+} $(H_2O)_n$ clusters (n = 1-128). The experimental heat of vaporization of bulk water, shown as a dashed line, has a value of -9.7 kcal/mol; c) total cluster enthalpy vs. cluster size for $Ln^{3+}(H_2O)_n$ clusters (n = 1-128). All enthalpies are in kcal/mol..... **79**

Figure 4.3.1.1. Representative $La^{3+}(H_2O)_n$ cluster structures obtained from room temperature Monte Carlo simulations using model potentials. **96**

Figure 4.3.1.2. Radial probability distributions (–) of Ln^{3+}-O distances for select $Ln^{3+}(H_2O)_{64}$ clusters (Ln^{3+} = La^{3+}, Gd^{3+}, Lu^{3+}). Also shown is the distance-dependent coordination (- - -) obtained by integration of the radial probability distribution. The

first-shell Ln^{3+}-O distances and coordination numbers are listed in Tables 4.3.1.1. and 4.3.1.2., respectively. 97

Figure 4.3.1.3. Average first-shell coordination numbers obtained from Monte Carlo simulations of $Ln^{3+}(H_2O)_{128}$ (▲) and those obtained from bulk solution data (●)..... **101**

Figure 4.3.2.1. a) Cluster enthalpy and b) the reduced cluster enthalpy vs. cluster size for $Ln^{3+}(H_2O)_n$. The heat of vaporization of water (-9.7 kcal/mol) is indicated on the plot with a dashed line. All enthalpies are in kcal/mol. **102**

Figure 5.3.1.1. Minimum energy structures associated with the parent clusters (PC), $Eu^{3+}(H_2O)_n$. **114**

Figure 5.3.1.2. Minimum energy structures associated with the dissociated clusters (DC), $Eu^{2+}OH(H_2O)_{n-1}$. **117**

Figure 5.3.2.1. a) Parent cluster (PC) stepwise binding energies, b) PC cluster binding energies. All energies are in kcal/mol. **119**

Figure 5.3.2.2. Parent cluster (PC) dissociation energies as a function of cluster size for pathways 3 (solid line with ●), 4 (solid line), 5 (long-dashed line with ◆) and 6 (short-dashed line with ×). All energies are in kcal/mol..... **121**

Figure 5.3.2.3. Dissociated cluster (DC, ●) and H_3O^+ (■) stepwise solvation energies as a function of cluster size. All energies are in kcal/mol. **122**

Figure 5.3.3.1. Minimum energy structures associated with the TS1 transition state clusters, $Eu^{3+}(H_2O)_n$. Arrows represent the mode associated with the imaginary frequency of the transition state. **124**

Figure 5.3.3.2. Minimum energy structures associated with the MIN2 intermediate clusters, $Eu^{3+}(H_2O)_{n-1}H_2O$..... **125**

Figure 5.3.3.3. Minimum energy structures associated with the TS2 transition state clusters, $Eu^{2+}OH(H_2O)_{n-2}H_3O^+$. **127**

Figure 5.3.3.4. A comparison of the energetics associated with parent cluster (PC) dissociation via pathway (4) and with single ligand loss (SLL) for cluster sizes n = 2-9. TS1 and TS2 structures represent transition states along the reaction path, MIN2 structures are reaction intermediates associated with the displacement of one solvent molecule from the first to the second coordination shell and DC is the deprotonated cluster of the form $Eu^{2+}OH(H_2O)_{n-2}$. All energies are in kcal/mol. **129**

Figure 6.4.1.1. Representative structures of $Lu^{3+}(CH_3CN)_n$ clusters obtained from room temperature Monte Carlo simulations..... **152**

Figure 6.4.1.2. Radial probability distribution functions and distance-dependent coordination number for $Ln^{3+}(CH_3CN)_{36}$, (a) Pr, (b) Eu, (c) Tb, (d) Ho and (e) Lu. **153**

Figure 6.4.2.1. $Ln^{3+}(CH_3CN)_n$ cluster thermodynamics a) Cluster binding enthalpy, b) stepwise binding enthalpy and c) reduced cluster enthalpy vs. cluster size. The experimental heat of vaporization of acetonitrile (-7.9 kcal/mol) is represented by a dotted line [223]. All enthalpies are in kcal/mol..... **158**

Figure 6.4.2.2. Stepwise binding enthalpy vs. cluster size for $Ho^{3+}(CH_3CN)_n$ and $Ho^{3+}(H_2O)_n$ clusters (n = 1-15). All enthalpies are in kcal/mol..... **160**

LIST OF TABLES

Table 1.1.1. Cluster sizes required for obtaining bulk-like behaviour **2**

Table 1.3.1.1. Ground-state electron configurations for the rare-earth elements **6**

Table 1.3.1.2. Comparisons between the properties of Ln^{3+} and transition metal ions **8**

Table 1.3.3.1. Ionization potentials of the lanthanide ions and those of prototype solvents used in cluster studies **12**

Table 2.3.1.1. Structural features of $M^{q+}(H_2O)^a$ **26**

Table 2.3.1.2. Structural features of $M^{q+}(H_2O)_2{}^a$ **27**

Table 2.3.1.3. Electronic Properties of $M^{q+}(H_2O)_n$ **28**

Table 2.3.2.1. Binding energies (kcal/mol) of $M^{q+}(H_2O)$ **32**

Table 2.3.2.2. Binding energies (kcal/mol) of $M^{q+}(H_2O)_2$ **33**

Table 2.3.3.2. Changes in the dipole moment of water[a] in $M^{q+}(H_2O)_n$ **36**

Table 2.3.4.1. Results of Natural Population Analysis for $M^{q+}(H_2O)_n{}^{a,b}$ **38**

Table 2.3.5.1. Results of electron localization function (ELF) analysis for $M^{q+}(H_2O)_n{}^a$. **43**

Table 2.3.5.2. ELF basin covariances for V(M,O) in $M^{q+}(H_2O)^a$ **45**

Table 2.3.6.1. Results of Atoms-in-Molecules (AIM) analysis for $M^{q+}(H_2O)_n$ clusters[a]. **47**

Table 3.2.2.1. Structural, energetic and electronic properties of small $Ln^{3+}(H_2O)$ clusters[a] **61**

Table 3.2.3.1. Changes in charge distributions and water structural properties in $Ln^{3+}(H_2O)$ clusters **61**

Table 3.2.4.1. Structural, energetic and electronic properties of $Ln^{3+}(H_2O)_n$ (n=6, 8 or 9) **65**

Table 3.3.2.1. Potential parameters **68**

Table 3.4.1.1. Average first-shell coordination numbers of $Ln^{3+}(H_2O)_n$ **76**

Table 3.4.1.2. Average ion-water distance (Å) in the first coordination shell of $Ln^{3+}(H_2O)_n{}^a$ **77**

Table 4.2.2.1. Structural, energetic and electronic properties of $Ln^{3+}(H_2O)$ complexes[a] **90**

Table 4.2.3.1. Model potential parameters **92**

Table 4.3.1.1. Average ion-water distance (Å) in the first coordination shell of $Ln^{3+}(H_2O)_n$[a] **98**

Table 4.3.1.2. Average first-shell coordination numbers of $Ln^{3+}(H_2O)_n$ **99**

Table 5.2.1. Energetic Properties of $Ln^{3+}(H_2O)$ **113**

Table 5.3.3.1. O-H bond lengths of the NW[a] in the parent and transition state clusters.[b] **126**

Table 5.3.4.1. Partial atomic charges associated with the PC, TS1, MIN2, TS2 and DC structures for n = 1-9 along pathway (4).[a] **131**

Table 6.2.2.1. Structural, energetic and electronic properties of $Ln^{3+}(CH_3CN)$ clusters[a] **143**

Table 6.2.2.2. Changes in the atomic charge distribution of $Ln^{3+}(CH_3CN)$[a] **145**

Table 6.3.2.1. Acetonitrile potential parameters **148**

Table 6.3.2.2. Lanthanide potential parameters **149**

Table 6.4.1.1. Average first-shell coordination numbers of $Ln^{3+}(CH_3CN)_n$ **156**

Table 6.4.1.2. Average first-shell coordination distances (Å) for $Ln^{3+}(CH_3CN)_n$ [a] **156**

CONTRIBUTIONS OF AUTHORS

The following summarizes the contributions of each of the authors cited in this thesis. For all of the studies discussed, J.A. Capobianco and G.H. Peslherbe participated in a supervisory role. T.-N.V. Nguyen was responsible in part for the parameterization of the potentials used in Chapter 3. The acetonitrile model used in Chapter 6 was jointly developed by T.-N.V. Nguyen and S.R. Hughes.

CHAPTER 1

1.1. INTRODUCTION TO CLUSTERS

The cluster phase is defined as a state of matter that is intermediate between a small collection of atoms/molecules and bulk materials [1, 2]. A cluster is simply an agglomerate of 2-1000 atoms or molecules, although these limits are only rough guidelines for defining such an assembly [1, 2]. Cluster chemistry has been often regarded as the bridge between the traditional chemistry observed in the bulk and that of isolated atoms/molecules. This bridge is of fundamental importance to chemistry and materials science since it answers the question: how do atoms and molecules interact to create a new system with its own inherent and unique properties? As such, the study of clusters has been regarded as one of the few remaining frontiers in materials science [1, 3-7].

Clusters may possess properties that are in common, completely dissimilar or intermediate between bulk and gas phases [2]. A classic example of this phenomenon would be the properties of a nanometer-sized piece of semi-conducting material [8]. Band theory suggests that many atoms are required to bridge the band gap between the bonding and anti-bonding orbitals of a semi-conducting material and so a threshold cluster size would be required to obtain the continuum necessary for the material to conduct. In silicon-based semi-conductors, it has been determined that as few as 4-7 atoms are required to reproduce the bulk band gap of 1.1 eV [8]. However, some physical properties can only be reproduced at extremely large cluster sizes. For instance, it has been estimated that approximately 10^6 gold atoms are needed to generate cluster melting points that are even remotely similar to those of the bulk counterpart [9]. Table

1.1.1. summarizes the size regimes required to reproduce various bulk physical and chemical properties.

Table 1.1.1. Cluster sizes required for obtaining bulk-like behaviour.[a]

Property	Cluster Measurement	Cluster Size
Work function (conduction band development)	Ionization energies / electron affinity	~200 atoms
Melting points	Heating of deposited clusters	> 1 x 10^6 atoms
Coordination chemistry	Mass spectrometry (estimated from magic numbers)	~13 atoms
Bulk structure	Electron Diffraction	~2000 atoms
Ion solvation	Gas-phase Thermochemistry	~10 solvent molecules

[a] Table reproduced from Ref. [5].

As can be seen from Table 1.1.1, the hypothesis that cluster properties can converge to liquid or solid properties at large cluster sizes is widely debatable. It is also quite clear that the number of atoms or molecules required to bridge this gap is quite varied and it depends greatly on the property being probed. What can be said is that the very nature of clusters provides a convenient range of sizes that span most regimes (nano, meso) making them amenable for use in size effect studies. Unfortunately, the process of gradually monitoring any transition from the cluster phase to the bulk is not trivial.

The study of ions in solution has always been of fundamental interest to chemists. An ion can simply be defined as an atom possessing either a negative or positive charge in the absence of non-coupled electrons (to protons) [10, 11]. Ions are the quintessential basis of a multitude of substances that exist in condensed states, namely electrolytic

solutions and ionic crystals. The formal charge ultimately governs the ion's behaviour in solution, in a gas or in the solid state, particularly if it is participating as a reactive species. The properties of ions play key roles in determining the solubility of salts. They may also influence redox reactions, acid-base chemistry and phase transitions. Ions can be classified on the basis on their charge (as positive cations or negative anions) or categorized based on their electronic configuration.

One of the most pertinent questions in chemistry is 'what are the intrinsic properties of ions that owe to their reactivity'? Though this may appear to be a trivial question, more often than not, the properties of ions are coupled to or influenced by other participants in a molecular system (solvent, crystalline lattice, etc...). Studying the microsolvation of ions has proven to be an effective means of obtaining such answers to this question. The microsolvation of metal ions in the gas phase has been the focus of some intensive research over the last 3 decades and particular attention has been paid to the energetic, structural and spectroscopic properties of these systems [1-5, 7, 12-44]. Recent studies clearly illustrate that in some cases, as few as 10 solvent molecules are required to obtain bulk-like properties from ion-solvent clusters. Reproducible properties include the number of solvent molecules required to dissociate salts or acids [3, 40], bulk proton hydration enthalpies and free energies, as well as bulk band-gap energies, photoelectron spectra and absorption data for water. Even redox reactions have been mimicked under cluster conditions, as well as metal ion-mediated catalysis of various chemical reactions [3, 39, 40]. Interestingly, it has been proposed that studies of ion-solvent clusters may provide insight into metal-mediated processes in enzymes. Protein bound metal ions are in part responsible for mediating enzymatic substrate modifications

often with the aid of coordinated water molecules [1, 45, 46]. Cluster environments are quite similar to those of metal-binding sites in proteins, as they are both self-contained and isolated from the ambient environment.

The most notable advantage of cluster studies is that they provide a means for studying ion solvation at a nano-scale level without the presence of an extensive solvent continuum [41]. In this manner, direct information regarding the intermolecular forces that ultimately lead to ion solvation can be obtained. However, there do exist physical limitations regarding the cluster sizes that are experimentally manageable and so meaningful cluster-to-bulk comparisons are traditionally based on extrapolation of these properties to those in the bulk [1, 5].

1.2. EXPERIMENTAL METHODS FOR CLUSTER GENERATION

Several remarkable techniques have been developed over the last few decades that can be used to successfully generate ion-solvent clusters. For example, ionic clusters can be formed via the ionization of pre-formed neutral clusters, via the clustering of molecules about a gas-phase ion or by sputtering and vaporization of condensed materials [7]. The most popular method used today to produce ionic clusters from a neutral species is the 'pick-up' technique. This method was initially implemented by A.J. Stace and has gained tremendous popularity over the years [5, 20, 25, 33-38, 47]. The pick-up process begins with the formation of a neutral cluster. Upon formation, the clusters are subjected to electron impact (~100 eV) to produce the ionised clusters. Alternatively, one can use Fast Atom Bombardment (FAB), which is a very popular sputtering technique involving the use of a particle beam [48]. This beam is composed of neutral atoms that are projected at high velocities with sufficient energy to promote local vaporization of a

choice material. Finally, ElectroSpray Ionization (ESI) techniques provide the most efficient means of producing clusters as demonstrated extensively by Paul Kebarle [12-14, 17, 26, 28, 29, 49]. Largely responsible for introducing the popular tandem electrospray ionization /mass spectrometry (ESI-MS) technique (initially developed by Yamashita and Fenn) to the field of ion-solvent studies [50, 51], Kebarle recognised that ESI was capable of easily producing gas-phase droplets containing solvated ions from bulk solutions.

The most suitable method for detecting and characterising ion clusters is mass spectral analysis. This is not unexpected since the ion-solvent clusters can be easily discriminated on the basis of their mass/charge ratios. However, it should be noted that the detection efficiency is greatly dependent on the cluster trajectories or energies. Furthermore, the analysis must be done at low pressures (10^{-4} Torr). In the event that a high-pressure system is being monitored, the gas must be sampled by slowly letting clusters enter the mass spectrometer via molecular effusion through a small orifice. This technique is often referred to as high-pressure mass spectrometry. Coincidentally, this technique was also introduced to the area of cluster research by Kebarle and Hogg [39].

1.3. LANTHANIDE SOLVENT CLUSTERS

1.3.1. An Introduction to the Lanthanides

As was recognized by Niels Bohr in 1918, the lanthanide (Ln) family of elements has the distinction of being the first group of metals in the periodic table to possess partially filled *f*-orbitals [52, 53]. The family consists of all atoms from La to Lu inclusively. The lanthanides possess a general [Xe]$6s^2 4f^n$ electron configuration, although lanthanum possesses a $6s^2 5d^1$ ground state and cerium a $6s^2 5d^1 4f^1$ ground state

[54]. This is because the 6*s*, 5*d* and 4*f* orbitals are similar in energy for these two atoms [52]. For these reasons, it is often contested whether lanthanum should be considered a member of the lanthanide family as it formally contains no *f*-electrons, despite the fact that it possesses very similar chemical and physical properties to the other Ln atoms. However, it is included in the rare-earth family of elements, which includes the Group III transition metals Y and Sc as well as the lanthanides and actinides [52]. The ground-state electronic configurations of the rare-earth atoms are provided in Table 1.3.1.1. When ionized, the lanthanides are predominantly trivalent, however, many of them can also be found as either divalent or tetravalent ions [54].

Table 1.3.1.1. Ground-state electron configurations for the rare-earth elements.

Metal[a]	Electron Configuration[a]
Sc	[Ar]$4s^2 3d^1$
Y	[Kr]$5s^2 4d^1$
La	[Xe]$6s^2 4f^0 5d^1$
Ce	[Xe]$6s^2 4f^1 5d^1$
Pr	[Xe]$6s^2 4f^3$
Nd	[Xe]$6s^2 4f^4$
Pm	[Xe]$6s^2 4f^5$
Sm	[Xe]$6s^2 4f^6$
Eu	[Xe]$6s^2 4f^7$
Gd	[Xe]$6s^2 4f^7 5d^1$
Tb	[Xe]$6s^2 4f^9$
Dy	[Xe]$6s^2 4f^{10}$
Ho	[Xe]$6s^2 4f^{11}$
Er	[Xe]$6s^2 4f^{12}$
Tm	[Xe]$6s^2 4f^{13}$
Yb	[Xe]$6s^2 4f^{14}$
Lu	[Xe]$6s^2 4f^{14} 5d^1$

[a] Taken from Ref. [52].

The term 'rare-earth' comes from the fact that early in their discovery, the elemental form of these metals was unknown and it was difficult to extract and isolate them due to their shared properties. In fact, it was not until 1913 that chemists clearly identified that the rare-earth family constituted a novel set of elements [52, 53]. However, the name was somewhat of a misnomer as a fair number of the rare-earth elements are quite common. For instance, the abundance of Ce in the Earth's crust is approximately 60 ppm and that of Nd is approximately 30 ppm [52].

The lanthanide elements behave quite differently from the other transition metals [52, 54]. In fact, they have more in common with the alkali and alkaline earth metals than they do with most of the *d*-block elements. A comparison between the key properties of the lanthanide ions and the transition metal ions is provided in Table 1.3.1.2. Many of these differences are owing to a shielding of the valence 4*f*-orbitals by the outermost 5*s*- and 5*p*-orbitals. Since they possess a noble gas-like configuration, for all intents and purposes, the lanthanide ions behave as hard Lewis acids and as such prefer to bind to hard Lewis bases such as oxygen and fluorine [55]. They are particularly hydrophilic (and hydroscopic) and coordination complexes containing lanthanide ions complexed to N, S and halogen donors (except fluorine) tend to be unstable in aqueous media [54]. Because of the aforementioned shielding effect, they also experience little loss in energy associated with changes in their ligand field, making them virtual 'chameleons' in terms of the different coordination numbers and symmetries they adopt with their ligands. The Ln^{3+} ions are known to bind anywhere from 6-10 ligands, making them some of the most versatile ions in the periodic table. Though it was disputed for some time, most chemists agree that the lighter lanthanides prefer to bind closer to 9

ligands whereas the heavier lanthanides prefer to bind only 8 [56-62]. The average coordination numbers associated with each lanthanide ion in aqueous solution are provided in Fig. 1.3.1.1. These differences arise from a contraction in the ionic radii across the entire series due to both a poor screening of the nucleus by the *4f*-orbitals and relativistic effects that cause the valence *s*- and *p*-orbitals to experience a greater effective nuclear charge [63]. Given that they can accommodate a large range of ligands, the trivalent lanthanide ions are often used as probes of coordination sites in crystals and glasses, as well as metal-ion binding sites in proteins [64, 65].

Table 1.3.1.2. Comparisons between the properties of Ln^{3+} and transition metal ions.

Property	Lanthanides	Transition Metals
Key orbitals	4*f*	n*d*
Ionic radii	85-105 pm	60-70 pm
Common coordination numbers	6-10	4 or 6
Typical coordination polyhedra	Trigonal prism, square antiprism, dodecahedral, tri-capped trigonal prism	Square planar, tetrahedral, octahedral
Bonding	Assumed to be predominantly electrostatic, little metal-ligand orbital interaction	Strong metal-ligand orbital interaction
Bond direction	Little preference	Strong directionality
Bond strengths	Correlated with the electronegativity of the ligand	Correlated to amount of orbital overlap
Preferred ligands	F^-, OH^-, H_2O, NO_3^-, Cl^-	CN^-, NH_3, H_2O, OH^-, F^-
Solution complexes	Ionic, rapid ligand exchange	Covalent, slow ligand exchange

[a] Taken from refs. [54, 66].

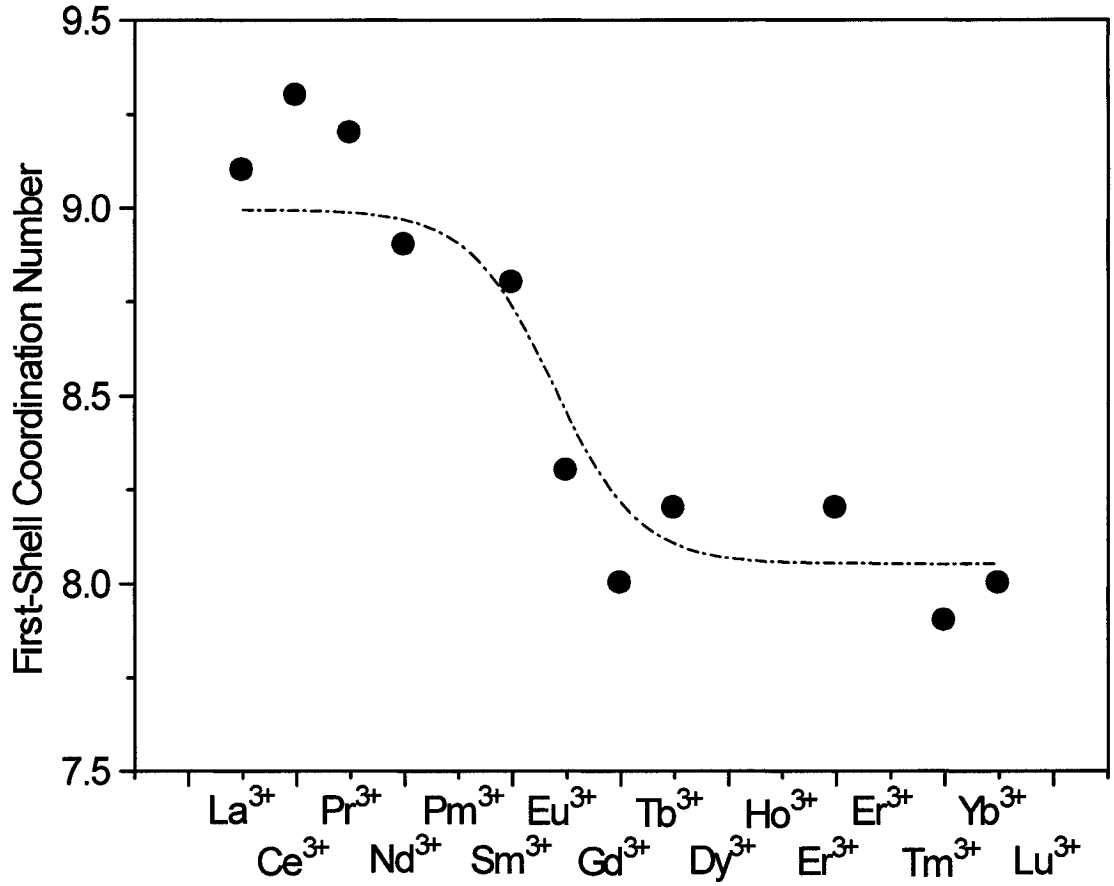

Figure 1.3.1.1. Average coordination numbers in aqueous solution for each of the trivalent lanthanide ions, taken from Ref. [58-62].

The most industrially relevant features of the lanthanide ions are their spectroscopic properties, with the exceptions of La^{3+} and Lu^{3+} which are spectroscopically 'silent' [53, 67]. The trivalent lanthanide ions absorb and emit efficiently in the UV, visible and infrared portions of the electromagnetic spectrum via *4f-4f* electronic transitions. The spectral lines associated with each lanthanide ion are well defined, and so they are convenient to use in devices that take advantage of energy transfer processes. Examples of such devices include labels in time-fluorescence spectroscopy, fluorescent probes for diagnostic or fluorescence assays (Fluorescent Resonant Energy Transfer, FRET), chemical sensors, UV dosimeters, Light Conversion Molecular Devices (LCMDs), organic light-emitting diodes, sensitizers for PhotoDynamic Therapy (PDT) and probes of *in-vivo* cellular activity [67-78]. Since the lanthanide ions also emit quite strongly in the visible region of the electromagnetic spectrum, they are often doped into solid-state materials destined for use in light-based applications. The design of new and unique Ln^{3+}-doped nanocrystalline phosphors is held in high regard, most notably in the display industry where there is an increasing demand on the market for high-resolution and energy efficient devices [79-85]. Finally, the magnetic properties of the lanthanide ions, specifically Eu^{3+} and Gd^{3+}, also make them ideal as shift agents for use in Nuclear Magnetic Resonance (NMR) and contrast agents for Magnetic Resonance Imaging (MRI) [86-89].

1.3.2. The Properties of Lanthanide Ions in Clusters

The solvation of metal ions in the cluster phase has been the focus of much of the research alluded to in section 1.2. Despite the successes associated with the study of mono- and divalent metal ion-solvent clusters, the experimental challenges associated

with the generation of triply charged metal ion-solvent clusters are well-established [5, 14, 18, 21-24, 33, 90, 91]. Many triply-charged clusters quickly become reduced to a divalent or monovalent state via dissociative electron or proton transfer processes [5, 14, 21-23]. This is because many metal ions have 2nd and 3rd ionization potentials that are higher than the IE of the complexed solvent. This promotes solvent to ion charge transfer, which may result in ligand dissociation. Product anions resulting from this dissociation can later complex the ion, thus reducing the formal charge of the cluster. Most noteworthy of such solvents is water, which like other protic solvents, can be deprotonated to produce other reactive and charged species. Not surprisingly, the issues and challenges regarding the solvation of trivalent lanthanide ions in protic solvents have been well documented in the literature [14, 18, 22, 24, 33, 90]. However, recent studies have reported the first incidence of stable $Ln^{3+}(H_2O)_n$ clusters detected from cluster generating experiments [92]. This only occurred at large cluster sizes, $n > 15$, suggesting that at large n, cluster reduction reactions may be minimized.

It should be noted that lanthanum and cerium should be good candidates to obtain trivalent lanthanide ion-protic solvent clusters, as they have 3rd ionization potentials that are comparable to the 2nd ionization potential of copper, that can readily form $Cu^{2+}(H_2O)_n$ clusters under the appropriate conditions [20]. This was demonstrated in the work of Bush *et al.* [92]. The ionization potentials of the lanthanide metals and several solvents are provided in Table 1.3.3.1.

1.4. COMPUTATIONAL CHEMISTRY

Understanding the structure and dynamics of ions in solution or in cluster phase is one of the keys to understanding their reactivity. Of particular importance is the

Table 1.3.3.1. Ionization potentials (in eV) of the lanthanides and those of prototype solvents used in cluster studies.

Metal[a]	1st IP	2nd IP	3rd IP
La	5.579	11.06	19.18
Ce	5.47	10.86	20.20
Pr	5.42	10.55	21.62
Nd	5.49	10.72	22.1
Pm	5.56	10.90	22.3
Sm	5.63	11.07	23.4
Eu	5.67	11.25	24.8
Gd	6.14	12.2	20.6
Tb	5.85	11.53	21.9
Dy	5.93	11.67	22.8
Ho	6.02	11.80	22.8
Er	6.10	11.93	22.7
Tm	6.184	12.05	23.67
Yb	6.254	12.18	25.03
Lu	5.426	13.9	20.96
Solvent	1st IP		
H_2O	12.62[b]		
CH_3CN	12.19[c]		
CH_3OH	10.85[d]		
CH_3COCH_3	9.7		

[a] Lanthanide metal ionization potentials obtained from Ref. [54].
[b] Obtained from Ref. [93].
[c] Obtained from Ref. [94].
[d] Obtained from Ref. [95].
[e] Obtained from Ref. [96].

reactivity of ions in water, as it is without question the most important and ubiquitous of all solvents used in chemistry and biology. Although many techniques are available to probe the properties of these systems, a detailed analysis of the interatomic interactions that govern these systems is unattainable by conventional experimentation. As such, molecular modeling can provide a convenient means of extracting many of the answers that experimentation cannot provide. Since the very nature of clusters is that they are small systems, they can be conveniently characterised via a wide array of computational

techniques. Various simulations of ion-solvent clusters can be found at length in the literature [3, 46, 91, 97-130].

The simulation of clusters can be accomplished using:

1) Quantum chemical methods (*ab initio* calculations, density functional methods)
2) Force fields and model potentials for use in molecular mechanics, Monte Carlo or molecular dynamics simulations
3) Hybrid methods (quantum mechanics/molecular mechanics QM/MM hybrids)

Quantum chemistry methods (QM) provide the most robust means of determining the properties of a molecular system, as its foundation is well rooted in solving complex approximations of the Schrodinger equation. In contrast, force fields and model potentials are made of much simpler, chemically-intuitive functions to describe interatomic interactions. These calculations may not provide the reliability associated with the aforementioned QM methods, however, they do provide an excellent avenue for assessing the properties of large molecular systems. The hybrid methods attempt to bridge this gap by providing some manner of quantum chemical accuracy while allowing for the sampling of large arrays of potential configurations.

The field of computational chemistry is ever growing and new developments have made simulations an ideal means for supporting experimental results or gaining new insight into chemically relevant problems. The awarding of the Nobel Prize in Chemistry to both Walter Kohn and the late John Pople in 1998 is a testament to the advances made in this field and is a reflection of its contributions to the field of chemistry as a whole.

1.5. STATEMENT OF THE PROBLEM

This thesis will address the following questions:

1) What is the nature of the metal to ligand bonding in trivalent lanthanide ion-solvent clusters?
2) What is the coordination structure of lanthanide ions in lanthanide ion-solvent clusters?
3) Why are trivalent lanthanide ion-solvent clusters so difficult to detect experimentally, particularly in protic solvents?
4) Can a link between the cluster and bulk properties of trivalent lanthanide ions be made?
5) Can one extend the present findings to other Ln^{3+}-solvent clusters?

The answers to these questions will be obtained using a combination of various molecular modelling techniques. First, a detailed survey of the structural, energetic and electronic properties of small lanthanide-water and lanthanide-acetonitrile clusters will be conducted using high-level quantum chemistry calculations. These calculations will yield the necessary information to assess the properties of lanthanide to ligand bonds in the cluster phase. The properties inherent to these lanthanide-solvent clusters will be used to develop and parameterize model potentials for use in Monte Carlo simulations of far larger ion-solvent clusters (n = 1-128). A particular emphasis will be placed on the effects of cluster size on the coordination number and structure of the lanthanide ions. Furthermore, the convergence of both the energetic and structural properties of the lanthanide ion-solvent clusters to those properties found in the bulk will be probed. Given that small, lanthanide ion-water clusters may only serve as models of solvated

lanthanide ions, as they only appear to form experimentally at large n, cluster deprotonation as the most likely pathway for the loss of the 3+ charge state of these clusters will also be investigated. This work can potentially have significant impact on the following areas:

i) Ion-solvent cluster research

ii) Modelling and design of solid state materials

iii) Modelling of metal ion binding sites in proteins

1.6. FORMAT OF THE THESIS

The layout of the thesis is as follows:

- A reproduction the paper entitled "On the Nature of Bonding Interactions in Small Metal Ion-Water Clusters" is presented in Chapter 2. This paper contains results pertaining to the structural, electronic and energetic properties of trivalent lanthanide-water dimers and trimers. These results were used as the basis for the design of model potentials. This paper is to be submitted to the Journal of Physical Chemistry A.
- The development and assessment of the aforementoned model potentials are presented in Chapters 3 and 4. Chapter 3 contains a reproduction of the paper entitled "A Theoretical Study of Trivalent Lanthanide Ion Microsolvation in Water Clusters from First Principles", originally printed in *Int. J. of Mass Spectrom.*, v. 241, 2005, pg. 283-294. Chapter 4 is a copy of the paper entitled "A Theoretical Study of the Hydration of Trivalent Lanthanide Ions Across the Series", that is to be submitted to the Canadian Journal of Chemistry. These papers report the structural and energetic features of lanthanide ion-water clusters obtained from room-temperature Monte

Carlo simulations. They also contain an assessment of the reliability of the model potentials.

- Chapter 5 contains a reproduction of the paper "Are Trivalent Europium-Water Clusters Stable Species? A Theoretical Study of the Deprotonation of $Eu^{3+}(H_2O)_n$ Clusters". This paper explores the feasibility of forming trivalent lanthanide ion-water clusters under the conditions typically used in cluster experiments and highlights many of the differences between the chemical properties of lanthanide ions in water clusters and in the bulk. This paper is to be submitted to the Journal of the American Chemical Society.
- Chapter 6 reports the simulations of lanthanide ion-acetonitrile clusters. As was the case in the study of water-based clusters, this paper focuses on the structural and energetic properties of such clusters obtained using room-temperature simulations. Entitled "Structural and Thermodynamic Properties of Lanthanide-Acetonitrile Clusters", this paper is to be submitted to the Journal of Physical Chemistry A.

At the end of each section, linking text will be provided summarizing the key points required for proceeding onto the next chapters, as well as the contributions of the various authors. Finally, conclusions and a future work section will be provided at the end of the thesis.

CHAPTER 2

On the Nature of Bonding Interactions in Small Metal Ion-Water Clusters

Sean R. Hughes, John A. Capobianco and Gilles H. Peslherbe
Centre for Research in Molecular Modeling and Department of Chemistry & Biochemistry
Concordia University
7141 Sherbrooke St. West
Montréal, Québec, Canada, H4B 1R6

Last Revised: August 2006
To be submitted to J. Phys. Chem. A.

ABSTRACT

Investigations of aqueous clusters containing metal ions, $M^{q+}(H_2O)_n$, have garnered much attention over the years. However, the nature of the bonding interaction between the metal ions and the solvent molecules in these clusters is still not thoroughly understood. These interactions are reportedly covalent in some complexes, such as Be^{2+} (H_2O) and electrostatic in others such as Na^+ (H_2O). In this article, quantum chemistry calculations and the *Atoms in Molecules* (AIM) and *Electron Localization Function* (ELF) are used to gain qualitative and quantitative insight into how water molecules bind to metal ions (Li^+, Na^+, K^+, Be^{2+}, Mg^{2+}, Ca^{2+}, Al^{3+}, Sc^{3+}, Y^{3+}, Eu^{3+}) in small clusters (n = 1, 2) and to determine the key forces that govern this interaction. The results are discussed within the framework of a detailed analysis of the cluster energetic, structural and electronic properties. Our findings indicate that those ions possessing large charge:size ratios appear to form the strongest bonds with water. Polarization effects appear to play a pivotal role in influencing the structural features of the clusters, as evidenced by the changes to the bond lengths and angles of complexed H_2O, as well as the spatial arrangement of water molecules in the cluster. ELF analyses suggest that there is little sharing of electrons in the bonds formed between the Group I or II metal

ions and water, but very slight covalent character is present in clusters containing trivalent metal ions. Results also suggest that the observed 'bent' structures for n = 2 are formed primarily from distortion of the metal subvalence shell. The AIM analysis reveals the strong closed-shell character of the metal ion-water bonds in clusters containing metal ions of low to moderate charge:size ratio. Yet, clusters containing ions with high charge:size ratios show a slight dominance of the virial field component and negative values of the local energy density at the M-O bond critical points, indicating again that there is some very slight shared-shell character to the M-O bonds in these clusters.

Keywords: Atoms in Molecules, Electron Localization Function, Cluster ions, ab initio Calculations, Charge Transfer, Polarization.

2.1. INTRODUCTION

Studies of aqueous clusters containing metal ions have garnered much attention over the last few years both from a theoretical [46, 100-102, 104, 105, 109-112, 114, 116, 119-122, 124, 126, 128, 129, 131, 132] and experimental standpoint [12-17, 27-30, 34, 37, 133]. Cluster research has provided means for understanding the fundamental interactions that give rise to bulk solutions [134], that affect phase transitions [134] and that govern metal-ligand interactions in complex environments, for example in proteins [46, 105, 119, 121]. Several theoretical studies [100, 101, 109-112, 122] have dealt with the solvation of metal ions in small clusters. A typical feature of clusters containing large metal ions and 2 water molecules, for example $Ca^{2+}(H_2O)_2$, is that the O-M-O bond angle is less than 180°, resulting in a bent cluster structure with C_s or C_2 symmetry, in sharp contrast to the 'linear' D_{2d} structures obtained in clusters containing small metal ions, such as Li^+. The C_2 and D_{2d} configurations are depicted in Fig. 2.1.1.

It has been previously suggested that both polarization and covalent bonding play prominent roles in the O-M-O bending motif observed in both monovalent and divalent metal ion-water clusters [104, 105, 110-112, 119, 121, 122, 126]. The partial covalent character of the metal-solvent bonds was surmised from observed solvent-to-metal charge transfer phenomena. However, reasons for interpreting charge transfer as evidence for covalent bonding, and not simply as charge transfer were not discussed in any detail.

The nature of bonding interactions in metal ion-water clusters depends on several key factors. Most light ions are considered to be 'hard' ions, preferentially associating with other 'hard', non-polarizable ligands [135, 136]. These interactions are presumed to be electrostatic in nature although some ions may form dative covalent bonds with water

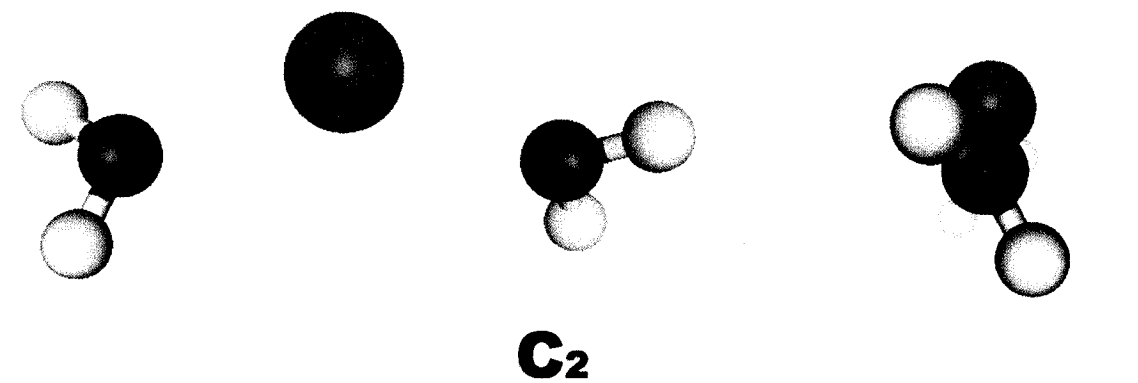

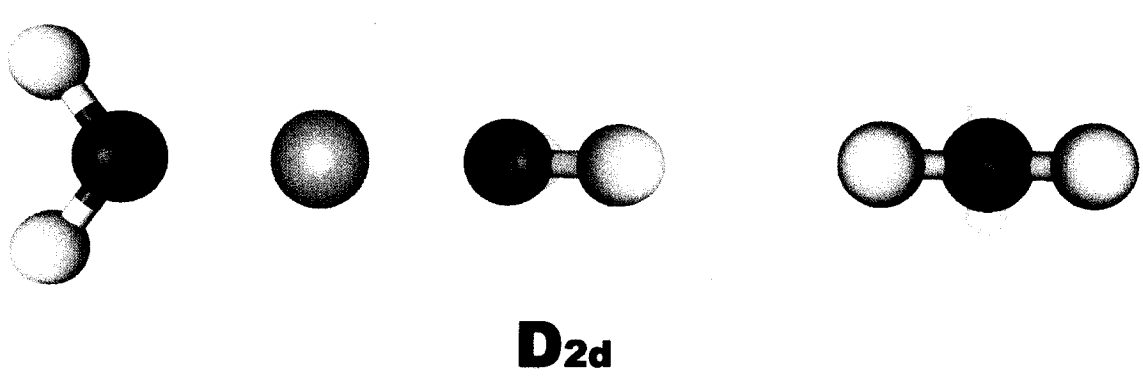

Figure 2.1.1. Typical C_2 and D_{2d} $M^{q+}(H_2O)_2$ structures.

[104, 105, 114]. For instance, the binding energy of the sodium ion to water is ~25 kcal/mol, and the sodium ion-water interaction is traditionally thought to be an electrostatic interaction [17]. In contrast, the Be^{2+} to water binding energy has been predicted to be ~150 kcal/mol [104] and the Be^{2+}-water interaction is considered to be of the dative covalent type. It has been shown that clusters containing ions with high charge:size ratios exhibit appreciable charge transfer between the cation and bound water molecule, whereas this transfer appears minimal in clusters containing larger, monovalent ions [104, 105, 112, 119, 121, 122, 126]. Again, this has been interpreted as a sign of increased covalency in the metal ion to water interaction for metal ions with high charge:size ratios.

Several advanced theoretical methods have proven remarkably effective in yielding both qualitative and quantitative information regarding the nature of chemical bonding in molecules. For example, the Natural Bond Orbital theory of Weinhold and co-workers [137], the Electron Localization Function (ELF), derived by Becke and Edgecombe [138, 139], and the theory of Atoms-in-Molecules (AIM), developed by Bader and co-workers [140, 141], are all rigorous and reputable methods capable of classifying different types of bonding interactions. To our knowledge, these methods have only been applied sparingly to the analysis of metal ion-solvent clusters [130, 142, 143].

The goal of this work is to characterize the various interactions that govern the energetics and structures of small metal ion-water clusters, $M^{q+}(H_2O)_n$, where n = 1 and 2. The metal ions used in this study include all Group I metals from Li^+ to K^+, as well as all Group II metals from Be^{2+} to Ca^{2+}. Furthermore, a variety of trivalent ions, notably

Al^{3+}, Sc^{3+}, Y^{3+} and Eu^{3+} ions have also been considered. The metal ion-water binding energies and several key structural features of the clusters have been predicted using quantum chemistry calculations, and subsequent atomic point charge analyses were used to determine the extent of charge transfer in each of these systems. Furthermore, we have made use of Natural Bond Orbital (NBO) theory [144, 145] to assess metal ion valence orbital occupancies and Natural Resonance Theory (NRT) [146, 147] to determine the amount of electrostatic and covalent character inherent to the metal ion-water bonds in these clusters. Where available, we have made comparisons between our aforementioned studies and those found in the literature. We also present a topological and quantitative analysis of the electron density using both the AIM and ELF analyses in order to ascertain the nature of the metal ion-water bonds.

2.2. COMPUTATIONAL PROCEDURES

All ground-state quantum chemistry calculations were performed using the Gaussian 98 program [148], employing either Becke's three parameter, Lee, Yang, Parr hybrid density functional (B3LYP) [149, 150] or second-order Møeller-Plessett (MP2) perturbation theory [151]. The 6-31G+(2d,p) basis set [152] was used for all atoms with the exception of Y and Eu. These ions were represented by Stuttgart-Dresden-Bonn (SDD) [153, 154] pseudopotentials and valence basis sets; the large core pseudopotentials (LC) were used for Eu. Ground and transition state geometries were characterized by frequency analysis. The metal ion-water binding energies were corrected for zero-point energy and for Basis-Set Superposition Error (BSSE) using the Counterpoise method [155].

Mulliken [156] and Electrostatic Potential (ESP) [157] atomic point charges were determined using Gaussian98 [148], while Atoms-in-Molecules (AIM) [140] charges were calculated with the AIMPAC [158] and AIM2000 [159, 160] packages, and Natural Bond Orbital [144, 145] charges were obtained with the NBO 4.0 package [161]. The NBO 4.0 set of programs was also used for our Natural Population Analysis (NPA) and Natural Resonance Theory (NRT) calculations [146, 147, 161]. Molecular dipole moments were estimated based on the charge distributions and the water geometries in the cluster.

An in-depth derivation of the electron localization function (ELF) has been given by Becke and Edgecombe, to which the reader is referred to for a more detailed account of the methodology [138, 139]. The ELF is related to the pair probability of two same-spin electrons in space and is expressed as:

$$\eta(r) = \left[1 + \left(\frac{D_\sigma}{D_\sigma^0}\right)^2\right]^{-1}, \qquad 3.2.1.1.$$

where D_σ is the excess local kinetic energy density due to Pauli repulsion and D_σ^o is the Thomas-Fermi kinetic energy density. When η(r) = 1, there is perfect localization of an electron and a value of η(r) = 0.5 is equivalent to the localization of an electron in a homogeneous electron gas (representative of delocalization). Regions possessing ELF values close to unity are termed attractors and are regions of high electron density. The ELF can be divided into basins by tracing the path of steepest ascent from each attractor, identifying regions containing core, valence or 'bonding' electrons. The terms mono-, di- and polysynaptic are used to reflect the connectivity of the basins. For example, a bonding basin representative of a single bond between two atoms is termed disynaptic

since it 'connects' two attractors. Basins containing only a proton are called protonated valence basins. Basin populations, N(Ω), can be estimated by integrating the electron density over the basin volume, Ω, and the basin fluctuation, λ(Ω), which is representative of the electron delocalization, is expressed from the statistical population variance, $\sigma(N,\Omega)$, as:

$$\lambda(\Omega) = \frac{\sigma^2(N,\Omega)}{N(\Omega)}. \qquad 3.2.1.2.$$

In this work, the ELF was calculated using the ToPMoD package developed by Noury *et al.* [162] and visualized with the SciAN program [163]. The ToPMoD set of programs provides a quantitative analysis of the ELF. The topological features of the gradient vector field of the ELF were obtained with the ToP_GRID program using a stepsize of 0.10 Å for the dimers (n = 1) and a stepsize between 0.15-0.20 Å for the trimers (n = 2). The basin analysis was done using the default settings of the ToP_BAS program. The threshold for basin integration used in the ToP_POP program was 10^{-7}, which was used to determine the basin populations.

As in the ELF formalism, AIM theory also divides the electron density of a molecule such that an atom is assigned an attractor and a surrounding basin [140]. Atomic basins are obtained by following the gradient vector field of the charge density, $\nabla\rho$, in a manner much akin to ELF. Furthermore, the (de-)localization of charge can be monitored via a topological analysis of the Laplacian, $\nabla^2\rho$. The resulting molecular graphs yield a variety of interconnected paths arising from so-called critical points, that correspond to maxima, minima or saddle points of ρ. These points are assigned a rank, ω, and a signature, σ, which are the number of non-zero curvatures in ρ and the sum of

their signs, respectively. For instance, a (3,-1) bond critical point (BCP) identifies a region where the gradient vector field becomes zero between two atoms. An interaction line or 'bond' path can be traced through this point and the two aforementioned nuclei, constituting a line of maximum electron density. A gradient vector field line perpendicular to this line and passing through the BCP defines the basin boundaries of the two atoms. The rank and signature of atomic nuclei are (3,-3) and those of ring and cage critical points are (3,+1) and (3,+3) points, respectively.

AIM theory has a successful history of yielding both the quantitative and qualitative characteristics of electrostatic, covalent, van der Waals and hydrogen bonding [141]. AIM calculations were performed for both the B3LYP and MP2 wave functions and electronic densities, but only the MP2 results will be reported as B3LYP yields essentially similar results.

2.3. RESULTS AND DISCUSSION

2.3.1. Structures

Tables 2.3.1.1. and 2.3.1.2. list the structural features of the dimer and trimer structures determined from B3LYP and MP2 calculations, where they are compared with previous studies. Clearly, the larger ions have a tendency to bind less closely to water. Water binds least tightly to Cs^+ at a distance of ~3 Å while the shortest metal ion-water distance is in the $Be^{2+}(H_2O)$ cluster at ~1.5 Å. The metal ion-water distances appear to be shortest for clusters containing small metal ions with high charge:size ratios, namely Be^{2+}, Al^{3+}, Li^+, Sc^{3+} and Mg^{2+}. These charge:size ratios are presented in Table 2.3.1.3. Other ions with high charge:size ratios, for example, Y^{3+} and Eu^{3+}, involve larger ion-water distances, due to their relatively larger ionic sizes. For instance, the larger alkali

Table 2.3.1.1. Structural features of $M^{q+}(H_2O)$.[a]

Structure	r_{M-O}	r_{O-H}	$\angle_{H-O-H}$	Δr_{O-H}	$\Delta\angle_{H-O-H}$	Method
H_2O	-	0.96	105.2	-	-	b
	-	0.96	104.7	-	-	c
$Li^+(H_2O)$	1.84	0.97	106.1	0.01	0.9	b
	1.88	0.97	105.7	0.01	1.0	c
$Na^+(H_2O)$	2.22	0.97	105.2	0.00	0.1	b
	2.28	0.96	104.7	0.00	0.0	c
	2.27	0.96	104.5	-	-	[129]
$K^+(H_2O)$	2.65	0.97	104.7	0.01	-0.5	b
	2.68	0.96	104.1	0.00	-0.6	c
	2.62	0.96	104.0	0.00	-0.7	[122]
$Rb^+(H_2O)$	2.81	0.96	104.0	0.00	-0.9	[122]
$Cs^+(H_2O)$	3.00	0.96	103.8	0.00	-0.9	[122]
$Be^{2+}(H_2O)$	1.49	1.00	108.5	0.04	3.3	b
	1.51	0.99	108.6	0.03	3.9	c
	1.51	0.99	107.8	0.03	5.3	[104]
$Mg^{2+}(H_2O)$	1.92	0.98	106.3	0.02	1.1	b
	1.95	0.98	105.7	0.02	1.0	c
	1.94	0.97	105.7	~0.01	~1.0	[111]
$Ca^{2+}(H_2O)$	2.29	0.98	104.2	0.01	-1.0	b
	2.30	0.97	103.8	0.01	-0.9	c
	2.25	0.97	103.5	-0.01	-1.5	[122]
$Sr^{2+}(H_2O)$	2.45	0.95	104.2	0.00	-0.5	[122]
$Al^{3+}(H_2O)$	1.75	1.02	108.4	0.06	3.1	b
	1.75	1.02	107.7	0.06	3.0	c
	1.72	1.02	106.5	0.06	2.4	[132]
$Sc^{3+}(H_2O)$	1.94	1.02	105.3	0.06	0.1	b
	1.99	1.01	104.6	0.05	-0.1	c
	1.94	1.01	103.0	0.05	-1.7	[122]
$Y^{3+}(H_2O)$	2.16	1.00	104.0	0.04	-1.3	d
	2.17	1.00	103.3	0.04	-1.4	e
	2.15	0.99	102.0	0.04	-2.5	[122]
$La^{3+}(H_2O)$	2.37	0.99	102.0	0.03	-2.7	[122]
$Eu^{3+}(H_2O)$	2.24	1.00	103.7	0.03	-1.5	d
	2.26	0.99	103.0	0.03	-1.7	e

[a] Distances in Å and angles in degrees [b] Quantum chemistry calculations performed with B3LYP/6-31+G(2d,p) as discussed in the text [c] Quantum chemistry calculations performed with MP2/6-31+G(2d,p) [d] Quantum chemistry calculations performed with B3LYP/6-31+G(2d,p)/SDD [e] Quantum chemistry calculations performed with MP2/6-31+G(2d,p)/SDD.

Table 2.3.1.2. Structural features of $M^{q+}(H_2O)_2$.[a]

Structure	Sym.	r_{M-O}	r_{O-H}	$\angle_{H-O-H}$	$\angle_{O-M-O}$	Δr_{O-H}	$\Delta\angle_{H-O-H}$	Method
H_2O	C_{2v}	-	0.96	105.2	-	-	-	b
	C_{2v}	-	0.96	104.7	-	-	-	c
$Li^+(H_2O)_2$	D_{2d}	1.85	0.97	106.0	180.0	0.01	0.8	b
	D_{2d}	1.88	0.96	105.6	180.0	0.00	0.9	c
$Na^+(H_2O)_2$	D_{2d}	2.23	0.97	105.2	180.0	0.00	0.0	b
	D_{2d}	2.29	0.96	104.7	180.0	0.00	0.0	c
	D_{2d}	2.30	0.96	104.5	180.0	-	-	[129]
$K^+(H_2O)_2$	D_{2d}	2.68	0.97	104.7	180.0	0.01	0.0	b
	C_2	2.64	0.96	104.1	113.9	0.00	-0.6	c
	C_s	2.69	-	-	180.0	-	-	[122]
$Cs^+(H_2O)_2$	C_s	3.03	-	-	113.3	-	-	[122]
$Be^{2+}(H_2O)_2$	D_{2d}	1.52	0.99	108.4	180.0	0.03	3.2	b
	D_{2d}	1.53	0.98	108.5	180.0	0.02	3.8	c
	D_{2d}	1.52	0.98	108.1	180.0	0.02	5.6	[126]
$Mg^{2+}(H_2O)_2$	D_{2d}	1.94	0.98	106.0	180.0	0.02	0.8	b
	D_{2d}	1.96	0.98	105.6	180.0	0.02	0.9	c
	D_{2d}	1.96	0.96	105.8	180.0	~0.01	~1.0	[111]
$Ca^{2+}(H_2O)_2$	C_2							b
	C_2	2.32	0.97	103.8	129.3	0.01	-0.9	c
	C_2	2.32	0.96	104.3	132.6	~0.01	~1.0	[111]
	C_s	2.29	-	-	141.0	-	-	[122]
$Sr^{2+}(H_2O)_2$	C_2	2.49	0.96	104.4	116.3	~0.01	~1.0	[111]
	C_s	2.46	-	-	117.5	-	-	[122]
$Al^{3+}(H_2O)_2$	D_{2d}	1.76	1.01	107.2	180.0	0.04	2.0	b
	D_{2d}	1.77	1.00	107.0	180.0	0.04	2.3	c
$Sc^{3+}(H_2O)_2$	C_2	1.99	1.00	104.9	119.6	0.04	-0.3	b
	C_2	2.03	0.99	104.5	114.1	0.03	-0.2	c
	C_s	2.02	-	-	116.5	-	-	[122]
$Y^{3+}(H_2O)_2$	C_2	2.20	0.99	104.1	112.7	0.03	-1.1	d
	C_2	2.20	0.99	103.5	110.5	0.03	-1.2	e
	C_s	2.24	-	-	112.2	-	-	[122]
$La^{3+}(H_2O)_2$	C_2	2.44	-	-	107.0	-	-	[122]
$Eu^{3+}(H_2O)_2$	C_2	2.29	0.99	103.2	108.0	0.02	-1.5	d

[a] Distances in Å and angles in degrees [b] Quantum chemistry calculations performed with B3LYP/6-31+G(2d,p) as discussed in the text [c] Quantum chemistry calculations performed with MP2/6-31+G(2d,p) [d] Quantum chemistry calculations performed with B3LYP/6-31+G(2d,p)/SDD [e] Quantum chemistry calculations performed with MP2/6-31+G(2d,p)/SDD.

Table 2.3.1.3. Electronic Properties of $M^{q+}(H_2O)_n$.

n = 1															
Metal	r[a]	q:r[b]	α[c]	q_M[d]				q_O[d]				q_H[d]			
				Mulliken	ESP	AIM	NBO	Mulliken	ESP	AIM	NBO	Mulliken	ESP	AIM	NBO
Li^+	0.47	2.1	0.02	0.85	1.00	0.97	0.99	-0.69	-1.12	-1.29	-1.12	0.42	0.56	0.66	0.56
Na^+	0.87	1.1	0.25	0.97	1.00	0.97	1.00	-0.79	-1.04	-1.26	-1.09	0.41	0.52	0.64	0.55
K^+	1.22	0.820	1.2	0.98	0.99	0.99	1.00	-0.78	-0.92	-1.30	-1.07	0.40	0.47	0.66	0.54
Be^{2+}	0.11	18	-	1.37	1.86	1.90	1.92	-0.41	-1.37	-1.41	-1.25	0.52	0.76	0.76	0.66
Mg^{2+}	0.54	3.7	0.10	1.79	1.95	1.93	1.96	-0.74	-1.31	-1.36	-1.20	0.47	0.68	0.71	0.62
Ca^{2+}	0.90	2.2	1.1	1.92	1.96	1.94	1.98	-0.83	-1.13	-1.37	-1.16	0.45	0.58	0.71	0.59
Al^{3+}	0.35	8.6	0.06	2.45	2.81	2.80	2.81	-0.55	-1.56	-1.40	-1.25	0.55	0.86	0.79	0.72
Sc^{3+}	0.58	5.2	0.86	2.59	2.82	2.79	2.69	-0.66	-1.31	-1.36	-1.07	0.53	0.75	0.79	0.69
Y^{3+}	0.75	4.0	-	2.69[e]	2.85[e]	-	2.86[e]	-0.72[e]	-1.19[e]	-1.38[e]	-1.18[e]	0.51[e]	0.67[e]	0.76[e]	0.66[e]
Eu^{3+}	0.86	3.5	1.6	2.84[e]	2.84[e]	-	-	-0.85[e]	-1.13[e]	-1.37[e]	-	0.51[e]	0.65[e]	0.76[e]	-
n = 2															
Li^+	0.48	2.1	0.02	0.75	1.07	0.95	0.97	-0.71	-1.18	-1.33	-1.10	0.42	0.57	0.68	0.56
Na^+	0.89	1.1	0.25	1.00	1.08	0.96	0.99	-0.81	-1.12	-1.31	-1.09	0.41	0.54	0.67	0.55
K^+	1.24	0.806	1.2	0.96	0.98	0.97	1.00	-0.78	-0.91	-1.29	-1.07	0.40	0.46	0.65	0.54
Be^{2+}	0.13	15	-	1.64	1.58	1.85	1.82	-0.82	-1.13	-1.45	-1.21	0.50	0.67	0.76	0.65
Mg^{2+}	0.56	3.6	0.10	1.84	1.89	1.88	1.94	-0.85	-1.23	-1.40	-1.19	0.47	0.64	0.73	0.61
Ca^{2+}	0.92	2.2	1.1	1.87	1.94	1.91	1.98	-0.83	-1.12	-1.36	-1.16	0.45	0.58	0.70	0.59
Al^{3+}	0.77	3.9	0.06	2.39	2.48	2.73	2.69	-0.78	-1.21	-1.46	-1.24	0.54	0.73	0.80	0.70
Sc^{3+}	0.59	5.1	0.86	2.35	2.76	2.68	2.79	-0.70	-1.29	-1.37	-1.21	0.51	0.73	0.77	0.66
Y^{3+}	0.80	3.8	-	2.47[e]	2.91[e]	-	2.88[e]	-0.73[d]	-1.39[e]	-1.38[e]	-1.22[e]	0.50[e]	0.73[e]	0.75[e]	0.64[e]
Eu^{3+}	0.89	3.4	1.6	2.71[e]	2.78[e]	-	-	-0.84[d]	-1.16[e]	-1.38[e]	-	0.49[e]	0.65[e]	0.74[e]	-
Water	-		-	-	-	-	-	-0.74	-0.77	-1.24	-1.01	0.37	0.39	0.51	0.62

[a] Ionic radii (in Å) estimated by subtracting from the M-O bond distance a universal value of 1.40 Å, which is representative of the Pauling ionic radius of O^{2-} [164]; [b] Charge:size ratio of the ion (in e $Å^{-1}$); [c] Polarizabilities (in $Å^3$) obtained from ref. [135]; [d] Partial atomic charges (in e) obtained using MP2/6-31+G(2d,p) and the various methods;[e] Calculated using MP2/6-31+G(2d,p)/SDD.

metal ions bind at very large distances, ranging from ~2.5 Å to ~3.0 Å. Similar trends are seen in the metal ion-water distances of the trimer structures, however, these are larger than those for the dimer by ~0.05 Å. This can be attributed to the solvent-solvent repulsions and a screening of the coordinated ion by the presence of additional solvent molecules.

Tables 2.3.1.1. and 2.3.1.2. also list the ground-state geometries of both the uncomplexed and complexed water. Our calculations predict a gradual shrinking of the H-O-H bond angle proceeding down the clustered alkali metal ion series. A similar behavior is observed for $Ca^{2+}(H_2O)$, but it is not conserved for $Be^{2+}(H_2O)$ and $Mg^{2+}(H_2O)$, where breathing of the H-O-H bond angle is observed instead. This may be due to polarization of the electron density of water, as has been shown previously for the Mg^{2+} -water bond [111]. The polarization of water is greater for the $Be^{2+}(H_2O)$ cluster given that Be^{2+} has a higher charge:size ratio. This is reflected by much larger bond angle breathing for $Be^{2+}(H_2O)$ (3.7° versus 1.0°). Similar features are found for $Al^{3+}(H_2O)$, where the bond angle breathing is intermediate between that of $Mg^{2+}(H_2O)$ and $Be^{2+}(H_2O)$, which is not surprising since the Al^{3+} ion has an intermediate charge:size ratio between Be^{2+} and Mg^{2+}.

The O-H bond distances listed in Table 2.3.1.1. also increase upon ion complexation, most notably in $Be^{2+}(H_2O)$, $Al^{3+}(H_2O)$ and $Mg^{2+}(H_2O)$, implying that once again polarization of the metal ion-oxygen bond is of paramount importance in the overall structure of the cluster. On the other hand, the Group I metal ion-water clusters exhibit little changes in the O-H bond lengths since these ions are only weakly polarizing.

Though O-H bond lengthening is observed in $Sc^{3+}(H_2O)$, $Y^{3+}(H_2O)$ and $Eu^{3+}(H_2O)$, it is interesting to note that the H-O-H bond angle decreases by as much as ~2°, which contrasts our previous observation that ions with high charge:size ratios tend to induce H-O-H bond angle breathing. These ions all share similar charge:size ratios, between 3.5 and 5.5. *e*/Å, and relatively more polarizable than the other metal ions studied. Based on our data, the ionic size and polarizability of the metal ion appear to affect primarily the H-O-H bond angle, while the charge:size ratio mostly influences the O-H bond lengths.

Similar changes of the O-H bond lengths and the H-O-H bond angles are found for the metal ion-water trimers, but these effects are less pronounced. This is due to an increased shielding of the ion's charge by the presence of the additional solvent molecule, which results in longer metal ion-water distances and thus, weaker ion-solvent interactions. Given that these structural changes appear largely influenced by short-range polarization effects, it is not surprising that these taper off with increasing ion-solvent distances [165].

As reported previously [110, 111, 122], linear D_{2d} structures (see Fig. 2.1.1.) prevail for all trimers containing light metal ions, namely Li^+, Na^+, Be^{2+}, Mg^{2+} and Al^{3+}, with the exception of K^+, which according to the MP2 results, predicts that the linear conformation is a 1^{st}-order saddle-point structure and the C_2-like structure to be more stable. On the other hand, the B3LYP model chemistry predicts that the D_{2d} structure is most stable. It should be noted that Kaupp *et al.* [122] have found that both C_s and C_2-like structures are iso-energetic with the D_{2d} structure using an MP2/SDD model chemistry.

The O-M-O bond angles listed in Table 2.3.1.2. distort substantially from 180° in $Mg^{2+}(H_2O)_2$ to ~130° for $Ca^{2+}(H_2O)_2$, and shrinks to as low as 108° for $Eu^{3+}(H_2O)_2$. The O-M-O bond angles become smaller as one moves across a period, for example, the O-M-O bond angle is reduced by 10.6° from $Ca^{2+}(H_2O)_2$ to $Sc^{3+}(H_2O)_2$. These features have been reported previously for similar clusters and our values vary by at most ~5.0° with respect to previously reported calculated data [110, 111, 121, 122]. The only glaring deviation is with respect to the O-Ca-O bond angle, which was reported previously to be ~141° [122]. However, our results are comparable to those of Kaufman-Katz *et al.* (124.5°) and Bauschlicher *et al.* (125.5°) [101, 121].

2.3.2. Energetics

Tables 2.3.2.1. and 2.3.2.2. list the binding energies of the metal ion-water dimers and trimers, respectively, where they are compared to literature values [110, 111, 122, 126, 128, 132]. The dimer binding energies decrease down the groups. The Group I metal ion-water binding energies decrease by as much as 20 kcal/mol, while a far more significant gap is observed for clusters containing Group II metal ions. For example, the Be^{2+} and Sr^{2+} ion-water binding energies differ by ~95 kcal/mol, in agreement with the larger metal ion-water bond distances reported in Table 2.3.1.1. The strongest binding energy is that of $Al^{3+}(H_2O)$ at ~200 kcal/mol and the weakest is for $Cs^{+}(H_2O)$ at ~14 kcal/mol [110, 111, 122, 126, 128, 132]. Our calculations agree quite well with the previous predictions listed in Tables 2.3.2.1. and 2.3.2.2.

On account of the larger metal ion-water distances in the trimer structures, the second stepwise binding energies are smaller than those for the dimers. The largest differences between the first and second stepwise binding energies are observed for

Table 2.3.2.1. Binding energies (kcal/mol) of $M^{q+}(H_2O)$.

Structure	D_o	Method
$Li^+(H_2O)$	34.6	a
	33.3	b
	34.4	[110]
$Na^+(H_2O)$	24.8	a
	23.6	b
	21.1	[129]
$K^+(H_2O)$	17.9	a
	18.3	b
	18.8	[110]
$Rb^+(H_2O)$	16.1	[110]
$Cs^+(H_2O)$	14.0	[110]
$Be^{2+}(H_2O)$	146.1	a
	138.5	b
	150.0	[126]
$Mg^{2+}(H_2O)$	82.5	a
	77.8	b
	78.8	[111]
$Ca^{2+}(H_2O)$	53.9	a
	52.3	b
	53.7	[111]
$Sr^{2+}(H_2O)$	47.2	[111]
$Al^{3+}(H_2O)$	204.5	a
	191.7	b
	199.6	[132]
$Sc^{3+}(H_2O)$	162.0	a
	133.5	b
	141.2	[122]
$Y^{3+}(H_2O)$	112.9	c
	102.5	d
	109.9	[122]
$La^{3+}(H_2O)$	87.8	[122]
$Eu^{3+}(H_2O)$	103.1	c
	90.7	d

[a] Quantum chemistry calculations performed with B3LYP/6-31+G(2d,p).
[b] Quantum chemistry calculations performed with MP2/6-31+G(2d,p).
[c] Quantum chemistry calculations performed with B3LYP/6-31+G(2d,p)/SDD.
[d] Quantum chemistry calculations performed with MP2/6-31+G(2d,p)/SDD.

Table 2.3.2.2. Binding energies (kcal/mol) of $M^{q+}(H_2O)_2$.

Structure	D_0	Symmetry	Method
$Li^+(H_2O)_2$	30.4	D_{2d}	a
	29.9	D_{2d}	b
	29.9	D_{2d}	[110]
$Na^+(H_2O)_2$	22.5	D_{2d}	a
	21.9	D_{2d}	b
	20.1	D_{2d}	[129]
$K^+(H_2O)_2$	16.2	C_2	a
	17.6	C_2	b
	16.9	D_{2d}	[110]
$Rb^+(H_2O)_2$	14.6	C_2	[110]
	15.1	C_s	[122]
$Cs^+(H_2O)_2$	12.7	C_2	[110]
$Be^{2+}(H_2O)_2$	117.9	D_{2d}	a
	114.6	D_{2d}	b
	124.2	D_{2d}	[126]
$Mg^{2+}(H_2O)_2$	72.7	D_{2d}	a
	70.2	D_{2d}	b
	70.6	D_{2d}	[111]
$Ca^{2+}(H_2O)_2$	48.0	C_2	a
	48.6	C_2	b
	48.5	C_2	[111]
$Sr^{2+}(H_2O)_2$	42.2	D_{2d}	[111]
$Al^{3+}(H_2O)_2$	167.1	D_{2d}	a
	162.0	D_{2d}	b
$Sc^{3+}(H_2O)_2$	115.1	C_2	a
	107.1	C_2	b
	107.8	C_s	[122]
$Y^{3+}(H_2O)_2$	91.6	C_2	c
	86.2	C_2	d
	88.8	C_2	[122]
$La^{3+}(H_2O)_2$	75.7	C_s	[122]
$Eu^{3+}(H_2O)_2$	78.3	C_2	d

[a] Quantum chemistry calculations performed with B3LYP/6-31+G(2d,p) model chemistry.
[b] Quantum chemistry calculations performed with the MP2/6-31+G(2d,p) model chemistry.
[c] Quantum chemistry calculations performed with the B3LYP/6-31+G(2d,p)/SDD model chemistry.
[d] Quantum chemistry calculations performed with the MP2/6-31+G(2d,p)/SDD model chemistry.

$Be^{2+}(H_2O)_n$, as well as the trivalent metal ion–water clusters (~25 kcal/mol). In contrast, the difference between the first and second stepwise binding energies is smallest for clusters where the charge:size ratio of the ion is very small. For example, a difference of 2 kcal/mol is observed in the stepwise binding energies of $K^+(H_2O)$ and $K^+(H_2O)_2$ clusters. Optimizations of trimers containing larger ions resulted in D_{2d} first-order saddle point structures, which is likely a transition state associated between two mirror-image C_2 structures. Clusters that exhibited this behaviour included Ca^{2+}, Sc^{2+}, Eu^{3+}, Y^{3+} and $K^+(H_2O)_2$ clusters. The binding energy differences between the ground state and saddle point structures were found to be as low as 0.1 kcal/mol for the D_{2d} and C_2 structures of $K^+(H_2O)_2$ and $Ca^{2+}(H_2O)_2$), and as high as 4 kcal/mol for those of $Y^{3+}(H_2O)_2$ and $Eu^{3+}(H_2O)_2$.

2.3.3. Charge Analysis

Table 2.3.1.3. lists the ionic sizes, charge:size ratios and polarizabilities of the metal ions, and the calculated, partial atomic charge distributions in the dimers and trimers determined from Mulliken, ESP, NBO and AIM analyses. The Mulliken-derived atomic point charges, which have also been used in previous work [104, 105, 119, 121, 126], appear to be overestimated, compared to those obtained from ESP, NBO and AIM analyses for the smaller metal ions studied. For example, the charge of the Be^{2+} ion in the dimer is reduced by 0.60*e* according to the Mulliken analysis, but the ESP, NBO and AIM charge analyses predict a reduction of only 0.12, 0.07 and 0.05*e*, respectively. Similarly, the Mulliken charge of the Li^+ ion is much smaller than that determined by other methods. This leads us to question the validity of the Mulliken approach for estimating charge transfer in such a system as was done previously [104, 105, 119, 121,

126]. This is not a surprising result, given the well-known limitation of the Mulliken analysis [156].

Regardless of the charge analysis method employed, the metal ions with high charge:size ratios experience a significant charge reduction when bound to water. The ions whose charges are most reduced are Sc^{3+} and Be^{2+}, which lose 10% and 7% of their formal charge, respectively. The charges of the Al^{3+} and Y^{3+} ions are also reduced significantly by ~6% each. In contrast, the alkali earth metals do not undergo a significant loss of positive atomic charge upon complexation. Of note is that the partial atomic charges of the metal ions are, in general, less positive than those obtained in the dimer calculations, simply due to the fact that two water molecules charge transfer now to the ion.

The partial atomic charges of the oxygen atoms become more negative in dimers where the metal ion has a high charge:size ratio, despite the significant transfer of negative charge from the water molecule to the metal ion. The positive charge of the hydrogen atoms obviously increase accordingly. Charge transfer effects appear to be exaggerated by the ESP analysis compared to the AIM and NBO results. Nevertheless, the charge analyses suggest a strong distortion of the electron distribution of water upon complexation with a metal ion that is accompanied by the structural changes in water that were discussed in the previous section. For trimers, the charges of the oxygen atoms become even more negative at the expense of the hydrogens' positive charges. The clusters for which charge transfer is most prominent are those containing the trivalent metal ions and Be^{2+}. However, it is interesting to note that Be^{2+}, which has the highest charge:size ratio has a less reduced charge than Sc^{3+}.

The changes in the dipole moments of the complexed water molecules are listed in Table 2.3.3.2. According to the ESP charge analysis, the dipole moment of the complexed water molecule increases the most for $Al^{3+}(H_2O)$, by 2.32 D. In contrast, the smallest increase is observed for $K^{+}(H_2O)$, where the dipole moment of water increases by only 0.45 D. Once again, these effects are less pronounced in both the AIM and NBO results. According to the NBO analysis, the dipole moments of water increase by only 0.78 D for $Al^{3+}(H_2O)$ and 0.23 D for $K^{+}(H_2O)$, leading us to question the validity of the ESP charge analysis method for investigating polarization in metal ion-water clusters. As expected, the induced dipole moments of water increase for the trimers.

Table 2.3.3.2. Changes in the dipole moment of water[a] in $M^{q+}(H_2O)_n$.

Metal	Δμ					
	ESP[b]		AIM[b]		NBO[b]	
	n = 1	n = 2	n = 1	n = 2	n = 1	n = 2
Li^{+}	1.11	1.16	0.11	0.33	0.31	0.25
Na^{+}	0.86	1.05	0.04	0.32	0.26	0.26
K^{+}	0.45	0.48	0.18	0.28	0.23	0.22
Be^{2+}	1.64	1.00	0.41	0.61	0.69	0.51
Mg^{2+}	1.59	1.39	0.35	0.59	0.57	0.57
Ca^{2+}	1.11	1.06	0.43	0.54	0.53	0.47
Al^{3+}	2.32	1.35	0.53	0.80	0.78	0.72
Sc^{3+}	1.64	1.67	0.53	0.64	0.38	0.73
Y^{3+}	1.30[b]	1.67[b]	0.38[b]	0.37[b]	0.69[b]	0.49[b]
Eu^{3+}	1.28[b]	1.14[b]	0.49[b]	0.48[b]	-	-

[a] Change in the water dipole moment upon complexation (Debye), based on calculated partial atomic charges. The sum of the water atomic charges is not exactly zero, and the origin was chosen as the midpoint between the hydrogens in the calculation of the dipole moments. All dipole moments were obtained from MP2/6-31+G(2d,p) calculations except for [b] Calculated using MP2/6-31+G(2d,p)/SDD.

2.3.4. Natural Bond Orbital (NBO)

Kaupp *et al.* [122] proposed earlier that the metal ion-water bonds in the trimers may possess some covalent character due to σ-bonding between the vacant d_z orbitals of

the metal ions and the oxygen atoms of water, resulting in O-M-O bending. In addition, π-interactions arising from ligand bonding via the vacant d_{xz} and d_{yz} orbitals of the metal ions may contribute to the D_{2d} structures observed in small metal ion-water clusters [122].

The present natural population analysis (NPA) does indicate that the alkali metal cations receive negligible charge transfer from water and that the trivalent metal ions exhibit a significant population of their valence *s*- and *d*-orbitals. As shown in Table 2.3.4.1., the vacant *s*-orbital populations are highest among light metal ions that received the most charge transfer, namely Al^{3+}, Be^{2+} and Mg^{2+}. On the other hand, the larger trivalent ions, Sc^{3+} and Y^{3+}, have preferential occupation of their *d*-orbitals upon charge transfer. The larger Group I and II metals, such as K^+ and Ca^{2+}, exhibit no population of the *d*-orbitals, despite the fact that the bent symmetries are energetically more favorable than the D_{2d} symmetries. A similar behavior is observed for the Group I metal ion-water clusters, namely in $K^+(H_2O)_2$, $Rb^+(H_2O)_2$ and $Cs^+(H_2O)_2$ [122]. Thus, the O-M-O bending in some of the monovalent and divalent metal ion-water trimers does not appear to be greatly correlated with covalent interactions.

Only in the case of $Al^{3+}(H_2O)$ and $Al^{3+}(H_2O)_2$ were metal ion-oxygen bond orbitals actually found in the NBO analysis. These bond orbitals were made up mostly from contributions of the oxygen atomic hybrids, making up 94.72% and 93.62% of the bond orbitals in the dimer and trimers, respectively. Interestingly, the valence p-orbitals of the Al^{3+} ion are significantly populated in the dimer and this occupation is increased in the trimers. These results suggest that the metal ion-water bond interaction has partial

covalent character, which correlates well with the cluster binding energies being the largest among the set studied here.

Table 2.3.4.1. Results of Natural Population Analysis for $M^{q+}(H_2O)_n$.[a,b]

Metal	*s*	d_{xy}	d_{xz}	d_{yz}	$d_{x^2y^2}$	d_{z^2}	Natural Bond Orders	
							Ionic	Covalent
n = 1								
Li^+	0.000	-	-	-	-	-	0.003	0.000
Na^+	0.000	-	-	-	-	-	0.001	0.000
K^+	0.000	-	-	-	-	-	0.000	0.000
Be^{2+}	0.032	-	-	-	-	-	0.021	0.001
Mg^{2+}	0.017	-	-	-	-	-	0.009	0.000
Ca^{2+}	0.003	-	-	-	-	-	0.003	0.000
Sc^{3+}	0.008	0.000	0.042	0.003	0.000	0.070	-	-
Y^{3+}	0.005	0.000	0.021	0.001	0.000	0.036	-	-
n = 2								
Li^+	0.000	-	-	-	-	-	0.007	0.000
Na^+	0.000	-	-	-	-	-	0.003	0.000
K^+	0.000	-	-	-	-	-	0.001	0.000
Be^{2+}	0.142	-	-	-	-	-	0.036	0.002
Mg^{2+}	0.051	-	-	-	-	-	0.013	0.000
Ca^{2+}	0.011	-	-	-	-	-	0.004	0.000
Sc^{3+}	0.029	0.077	0.024	0.011	0.038	0.026	0.051	0.002
Y^{3+}	0.019	0.044	0.019	0.010	0.013	0.014	0.029	0.000
	s	p_x	p_y	p_z			Natural Bond Orders	
n = 1								
Al^{3+}	0.091	0.015	0.000	0.015	-	-	0.059	0.005
n = 2								
Al^{3+}	0.175	0.022	0.022	0.087	-	-	0.076	0.004

[a] NAO metal valence populations and M^{q+}-O natural bond order contributions obtained from NRT, in electrons.
[b] Results obtained for MP2 calculations.

Natural Resonance Theory (NRT) was used to determine the natural bond order of each of the metal ion to oxygen interactions, specifically to assess the degree of electrostatic (electrovalency) versus covalent character, in the ion-water bonds. The results of this analysis are summarized in Table 2.3.4.1. In all cases, it can be seen that

the metal ion-water bonds have a predominantly ionic bond order, with little or no contribution from covalent interactions. For example, the NRT analysis shows that even the Al-O bond order in $Al^{3+}(H_2O)_n$, for which a bond orbital was detected in the NBO analysis, is primarily electrostatic. The metal ions with large charge:size ratios also appear to have both electrostatic and covalent character, but the latter is quite negligible in most cases (< 0.001). The electrostatic character appears to increase in the trimers, as the larger ion-water distances restrict the possibility of any orbital overlap.

2.3.5. Electron localisation function (ELF)

Presented in Fig. 2.3.5.1. are the ELF isosurfaces and contour plots for $Na^{+}(H_2O)$, $Be^{2+}(H_2O)$, $Al^{3+}(H_2O)$ and $Sc^{3+}(H_2O)$. Each of the 3-D surfaces represents an irreducible representation of the ELF, whereas each contour plot is a slice along the plane perpendicular to the H-O-H plane. $Be^{2+}(H_2O)$ is the only species for which two bonding basins are found between Be and O [V(Be,O)], in addition to two other basins representing oxygen lone pairs [V(O)]. Basin analyses of $Na^{+}(H_2O)$, $Al^{3+}(H_2O)$ and $Sc^{3+}(H_2O)$ showed that the lone pairs originating from oxygen were bound to the metal ion and thus were formally identified as V(M,O) disynaptic basins, a feature that was found for all complexes.

The contour plots of the ELF yield remarkable qualitative insight into how the polarization of the water molecule occurs by the presence of the various metal ions. For instance, the single bonding basin for $Be^{2+}(H_2O)$ simply arises from the strong polarization of the oxygen electron distribution by the Be^{2+} ion. The contour plot bisecting the plane of the lone pairs clearly demonstrates this phenomenon: the ELF

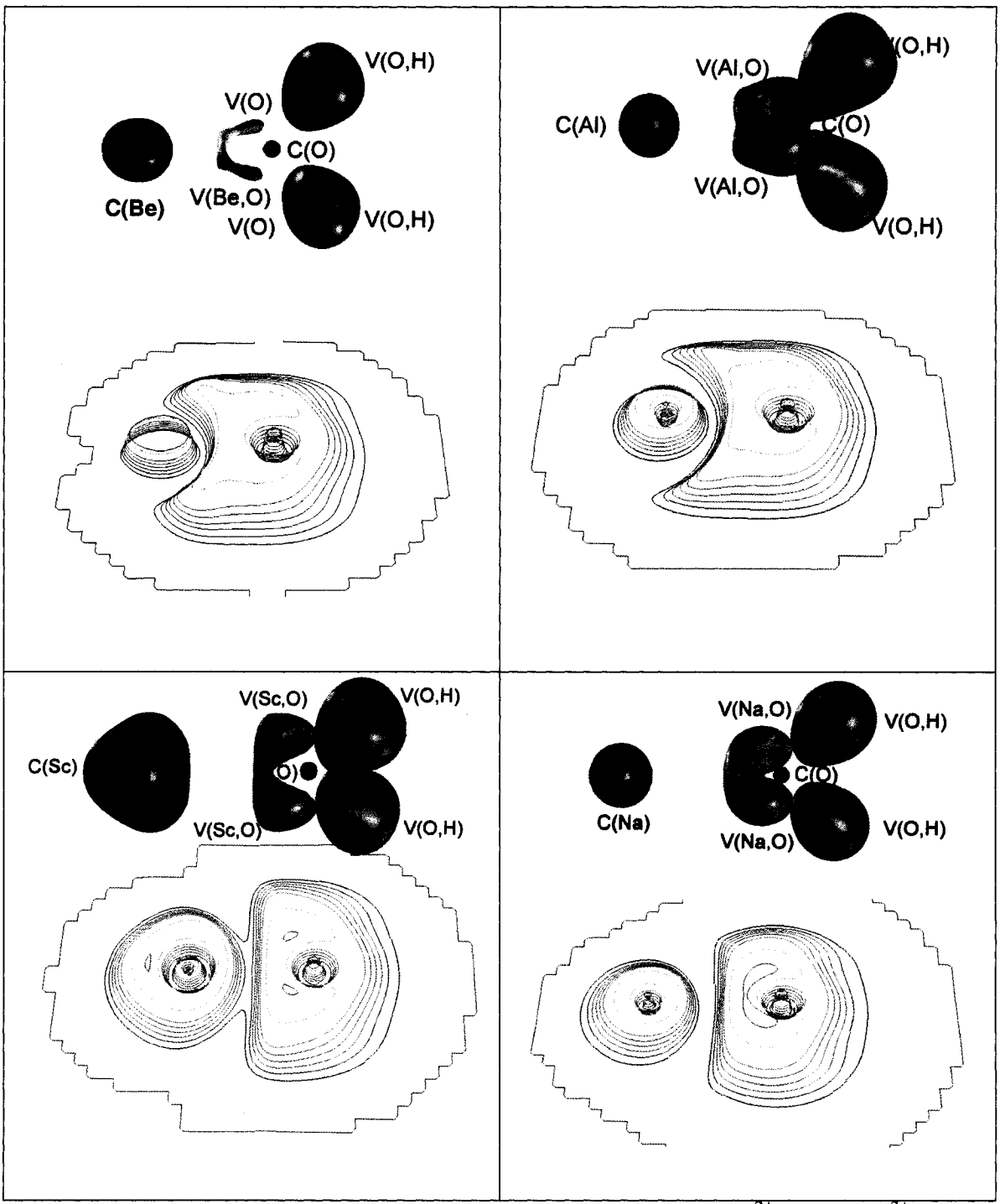

Figure 2.3.5.1. ELF isosurfaces and contour diagrams for $Be^{2+}(H_2O)$, $Al^{3+}(H_2O)$, $Sc^{3+}(H_2O)$ and $Na^{+}(H_2O)$ clusters. Each contour plot is the plane containing the V(M,O), C(M) and C(O) basins. The ELF values for each plot are $\eta(r) = 0.89$, 0.85, 0.86 and 0.85 respectively. The ELF was determined using B3LYP wavefunctions.

basins surrounding the oxygen atom are greatly distorted, whereas those of the Be^{2+} ion are unperturbed. Likewise, this feature is present, but to a lesser extent in the $Al^{3+}(H_2O)$, $Li^{+}(H_2O)$ and $Mg^{2+}(H_2O)$ contour plots (not shown), but not in those for $Na^{+}(H_2O)$ and in the other complexes.

With respect to the structural and energetic features discussed earlier, the ELF clearly highlights how small metal ions with high charge:size ratio cause H-O-H bond angle breathing, whereas the larger ions cause H-O-H bond angle shrinking. For $Be^{2+}(H_2O)$, the ELF localized around the oxygen atom is greatly distorted towards the metal ion, thus reducing the amount of lone-pair to H repulsions in water. This results in the hydrogen atoms being able to move further apart from each other, thus resulting in the observed H-O-H bond breathing upon complexation to the metal ion. In contrast, the $Sc^{3+}(H_2O)$ ELF is not distorted around the oxygen. This is likely due to the very diffuse C(Sc) core basin repelling the lone pairs of oxygen and hydrogen atoms, consequently reducing the H-O-H bond angle. This large C(M) basin is also present in the ELF of $Y^{3+}(H_2O)$ and $Eu^{3+}(H_2O)$, which all possess similar charge:size ratios and polarizabilities to Sc^{3+}.

The results of the population analysis for each basin are listed in Table 2.3.5.2. With the exception of $Be^{2+}(H_2O)$, each V(M,O) bonding basin contains a population of approximately 2.10 electrons. This is not unexpected, given that these basins represent the lone pairs of oxygen. Furthermore, the average population variations of the V(M,O) basins for all the clusters are of the order of 0.50, implying that 50% of the electrons occupying these basins can be localized into other, neighbouring basins. Not surprisingly, the population variations are highest for those clusters containing metal ions

with high charge:size ratios, as these can be correlated to the amount of charge transfer that was received by these ions, as shown in Table 2.3.3.1. In the unique case of $Be^{2+}(H_2O)$, the V(Be,O) basin populations are 0.90 *e* and may be reflective of the large charge transfer received from water (see Table 2.3.1.3.). The neighbouring V(O) basins have a population of 1.29 *e*, which make up the remainder of the 4 electrons of the lone pairs of oxygen. It should be noted that the population variation is also quite high for the V(Be,O) basin, indicating that electron delocalization is significant.

Despite the strong distortion of the ELF bonding basins for $Al(H_2O)^{3+}$ and $Be(H_2O)^{2+}$, these basins do not overlap with the C(M) core , since the ELF reaches zero in the region between these basins in the contour plots of Fig 2.3.5.1. The basin co-variances associated with the V(M,O) bonding basins were also determined and are presented in Table 2.3.5.3. In general, the V(M,O) bonding basins correlate moderately well with both the other V(M,O) and V(O,H) basins (~35% and 27% respectively), but do not with the C(O) core basins. In clusters containing metal ions with low to moderate charge:size ratio, no significant cross contribution can be observed with the C(M) core basin, but this contribution becomes more significant with an increase in the charge:size ratio of the metal ion. Nevertheless, this increase is not significant enough to suggest any dominant shared-shell character of the M-O bonds in these clusters.

The ELF associated with the trimer structures are also plotted in Fig. 2.3.5.2. in order to understand the O-M-O bending motif observed in clusters containing large ions. A greater distortion of the C(M) basin occurs in the cluster as the metal ion becomes larger, as seen for $Al^{3+}(H_2O)_2$ and $Sc^{3+}(H_2O)_2$ in Fig. 2.3.5.2. No distortion of the C(Al) basin is apparent in the contour plot of $Al^{3+}(H_2O)_2$. Yet, for $Sc^{3+}(H_2O)_2$, the C(Sc) basin

Table 2.3.5.1. Results of electron localization function (ELF) analysis for $M^{q+}(H_2O)_n$.[a]

Ion	Prop.	C(O)[d]		C(M)[e]		V(O,H)[f]		V(M,O)[g]		V(O)[h]	
		n = 1	n = 2	n = 1	n = 2	n = 1	n = 2	n = 1	n = 2	n = 1	n = 2
Li^+	N^b	2.12	2.13	2.01	2.02	1.75	1.69	2.12	2.24		
	λ^c	0.16	0.16	0.02	0.04	0.45	0.46	0.48	0.48		
Na^+	N^b	2.12	2.14	10.01	10.02	1.74	1.67	2.13	2.25		
	λ^c	0.16	0.17	0.00	0.01	0.45	0.47	0.48	0.49		
K^+	N^b	2.12	2.13	18.01	18.00	1.72	1.72	2.14	2.22		
	λ^c	0.16	0.17	0.00	0.01	0.46	0.46	0.48	0.49		
Be^{2+}	N^b	2.12	2.09	2.02	2.03	1.72	1.74	1.74	1.59	1.33	1.40
	λ^c	0.16	0.17	0.03	0.07	0.46	0.46	0.54	0.59	0.72	0.60
Mg^{2+}	N^b	2.11	2.13	10.02	9.99	1.77	1.73	2.10	2.20		
	λ^c	0.16	0.17	0.01	0.02	0.45	0.46	0.49	0.48		
Ca^{2+}	N^b	2.12	2.09	18.02	18.07	1.75	1.71	2.11	2.24		
	λ^c	0.16	0.17	0.00	0.01	0.45	0.46	0.49	0.49		
Al^{3+}	N^b	2.13	2.10	10.04	9.99	1.70	1.72	2.15	2.23		
	λ^c	0.16	0.17	0.01	0.02	0.47	0.47	0.49	0.49		
Sc^{3+}	N^b	2.12	2.12	18.15	18.36	1.76	1.75	2.04	2.09		
	λ^c	0.16	0.17	0.01	0.03	0.46	0.46	0.51	0.51		
Y^{3+}	N^b	2.12	2.12	2.09	8.28	1.74	1.73	2.09	2.15		
	λ^c	0.16	0.16	0.02	0.06	0.46	0.46	0.50	0.50		
Eu^{3+}	N^b	2.12	2.12	32.10	8.14	1.76	1.76	2.06	2.15		
	λ^c	0.16	0.16	0.01	0.02	0.45	0.46	0.50	0.50		

[a] All results obtained with the ToPMoD package [162]. [b] Basin populations (electrons). [c] Basin fluctuations (electrons). [d] Core basin of oxygen atom. [e] Core basin of metal ion. [f] Bonding basin between oxygen and hydrogen. [g] Bonding basin between metal ion and oxygen. [h] Valence basin of oxygen.

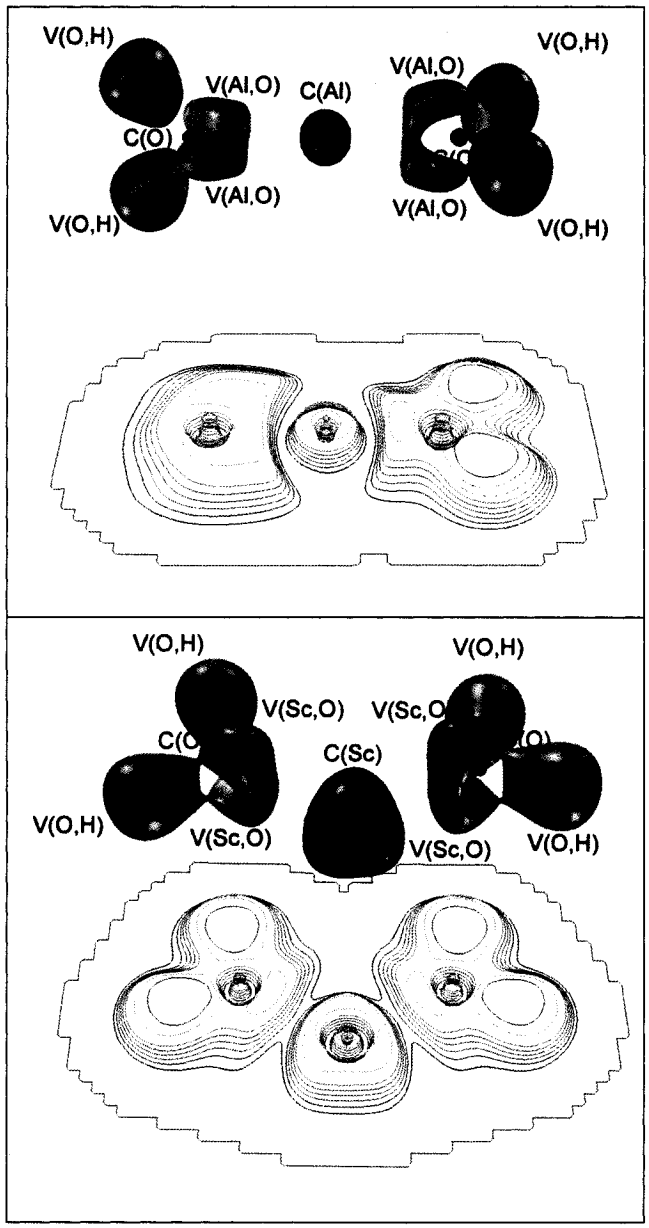

Figure 2.3.5.2. ELF isosurfaces and contour diagrams for $Al^{3+}(H_2O)_2$ and $Sc^{3+}(H_2O)_2$. Each contour plot is a slice through the plane defined by the O-M-O bond angle. The ELF values for each plot are $\eta(r) = 0.86$ and 0.83, respectively, and were determined using B3LYP wavefunctions.

Table 2.3.5.2. ELF basin covariances for V(M,O) in $M^{q+}(H_2O)$.[a]

Basin[b]	$C(O)_1$[c]	C(M)[d]	$V(O,H)_1$[e]	$V(M,O)_2$[f]
V(Li,O)	10.7	1.9	28.2	35.9
V(Na,O)	10.7	1.9	28.2	35.9
V(K,O)	10.6	1.9	27.9	35.6
V(Be,O)	7.4	5.3	16.0	-
V(Mg,O)	10.7	2.9	27.2	34.6
V(Ca,O)	10.7	3.9	27.2	35.0
V(Al,O)	9.4	4.7	27.4	34.9
V(Sc,O)	9.7	9.7	26.2	32.0
V(Y,O)	9.6	7.7	27.0	32.7
V(Eu,O)	9.7	7.8	25.2	33.0

[a] All results obtained with ToPMoD package [162].
[b] Metal ion to oxygen bonding basins.
[c] Core basin of oxygen atom.
[d] Core basin of metal ion.
[e] Bonding basin between oxygen and hydrogen.
[f] Bonding basin between metal ion and oxygen.
[g] Valence basin of oxygen.

appears to take on a wedge-like shape. This is due to the mutual distortion of the C(M) basin by each water molecule, in keeping with the predominant role of the metal ion subvalence shell in determining the O-M-O bending motif [122, 166, 167]. The greater distortion at the polarized end of the metal ion results in weaker ion-water repulsions, and thus closer and stronger associations result between the metal ions and water [122, 166, 167]. This was evidenced in the work of Glendening *et al.*, where the bent conformers have smaller metal ion-oxygen distances than the linear conformers [111]. Furthermore, the O-M-O bending is more pronounced in clusters containing metal ions with the larger charge:size ratios of this subset, since these ions have closer interactions with water and result in greater distortions of the C(M) basins. Thus polarization is what ultimately governs the extent of O-M-O bending in large ion-water clusters. This agrees well with previous ELF studies of metal dioxides containing d^0 Group IV metals [168].

From the geometrical arrangement of the water molecules, it could be inferred that hydrogen bonding may contribute to the bending of the O-M-O bond in the trimers of C_2 symmetry. This inter-ligand H-bonding has been observed in $I^-(CH_3CN)_2$ clusters [169], however, no basins arising from hydrogen bonds were found in the present analysis. This is to be expected, since the large inter-ligand distances clearly do not favour this type of interaction [the shortest O-O distance is 3.43 Å in $Sc^{3+}(H_2O)_2$].

2.3.6. Atoms in Molecules (AIM)

Figure 2.3.6.1. shows contour plots of both the electron density, ρ, and the Laplacian, $\nabla^2\rho$, for $Be^{2+}(H_2O)$, $Al^{3+}(H_2O)$ and $Na^+(H_2O)$. Analysis of ρ for all dimers generates a set of four (3,-3) critical points for each atom and three (3,-1) bond critical points (BCP), one of which is a bond interaction line between the metal and the oxygen atom of water. The most interesting qualitative features are found in the Laplacian, $\nabla^2\rho$, that defines regions of high or low charge concentration. Careful observation of the contour plot of $\nabla^2\rho$ for $Be^{2+}(H_2O)$ reveals the absence of any charge localization in the region between the water molecule and the Be^{2+} ion, suggesting that there is little or no sharing of electrons between both species. Another striking feature is the distortion of $\nabla^2\rho$ associated with the oxygen atom, which is reminiscent of the distortions of the V(M,O) basins observed in the ELF contour plots due to the polarization of the water molecule by the ion. This is also a feature of $\nabla^2\rho$ for $Al^{3+}(H_2O)$, but this is not apparent for $Na^+(H_2O)$. It should be noted that no other system aside from the Be^{2+} and Al^{3+} dimers exhibited this distortion, contrasting with the previous ELF results which suggested that the Li^+ and Mg^{2+} dimers should exhibit similar properties. This may be due to the fact that the ELF was determined from B3LYP calculations wavefunctions,

Table 2.3.6.1. Results of Atoms-in-Molecules (AIM) analysis for $M^{q+}(H_2O)_n$ clusters.[a]

n = 2							
BCP	ρ^b	$\nabla^2\rho^c$	$\lvert\lambda_1\rvert/\lambda_3{}^d$	v^e	G^f	G/ρ^g	H^h
Li-O	0.0330	0.264	0.166	-0.041	0.053	1.62	1.27×10^{-2}
Na-O	0.0220	0.148	0.147	-0.024	0.030	1.37	6.73×10^{-3}
K-O	0.0197	0.099	0.153	-0.017	0.021	1.07	3.68×10^{-3}
Be-O	0.1070	0.820	0.215	-0.219	0.211	1.97	-7.30×10^{-3}
Mg-O	0.0509	0.414	0.149	-0.076	0.090	1.77	1.36×10^{-2}
Ca-O	0.0406	0.225	0.167	-0.046	0.051	1.26	5.12×10^{-3}
Al-O	0.0936	0.687	0.173	-0.178	0.175	1.87	-3.38×10^{-3}
Sc-O	0.0978	0.449	0.229	-0.138	0.125	1.28	-1.31×10^{-2}
Y-O	0.0729	0.351	0.193	-0.093	0.091	1.24	-2.68×10^{-3}
Eu-O[i]	0.0847	0.390	0.200	-0.113	0.105	1.24	-7.59×10^{-3}
n = 3							
BCP	ρ^b	$\nabla^2\rho^c$	$\lvert\lambda_1\rvert/\lambda_3{}^d$	v^e	G^f	G/ρ^g	H^h
Li-O	0.0323	0.252	0.170	-0.039	0.051	1.58	1.21×10^{-2}
Na-O	0.0208	0.140	0.147	-0.022	0.029	1.39	6.53×10^{-3}
K-O	0.0187	0.094	0.152	-0.016	0.020	1.07	3.55×10^{-3}
Be-O	0.0988	0.764	0.214	-0.192	0.191	1.93	-2.20×10^{-4}
Mg-O	0.0494	0.400	0.152	-0.073	0.086	1.74	1.35×10^{-2}
Ca-O	0.0360	0.197	0.165	-0.039	0.044	1.23	5.04×10^{-3}
Al-O	0.0912	0.668	0.178	-0.171	0.169	1.85	-2.38×10^{-3}
Sc-O	0.0804	0.393	0.212	-0.107	0.103	1.28	-4.53×10^{-3}
Y-O	0.0660	0.328	0.186	-0.082	0.082	1.24	-1.73×10^{-4}

[a] AIM properties determined using the AIMPAC [158] and AIM2000 [159, 160] software packages based on MP2 derived wavefunctions.
[b] Electronic density at the BCP in $e/a_o{}^3$.
[c] Value of the Laplacian at the BCP.
[d] Ratio of the curvatures, λ_1 and λ_3, at the BCP.
[e] Virial field at the BCP.
[f] Kinetic energy density at the BCP.
[g] Kinetic energy per electron at the BCP.
[h] Energy density at the BCP.

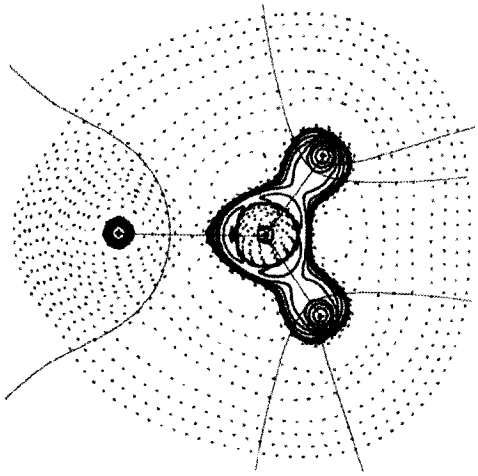

$Be^{2+}(H_2O)$

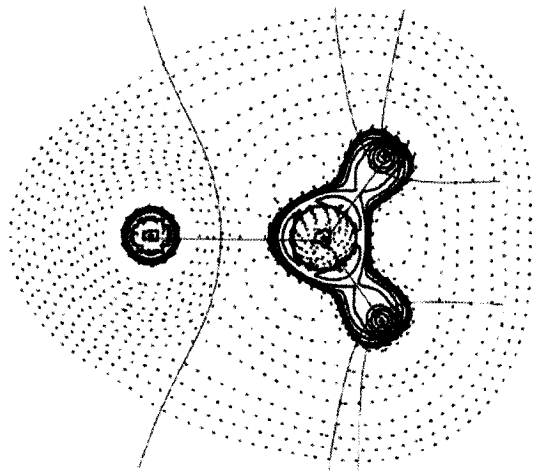

$Al^{3+}(H_2O)$

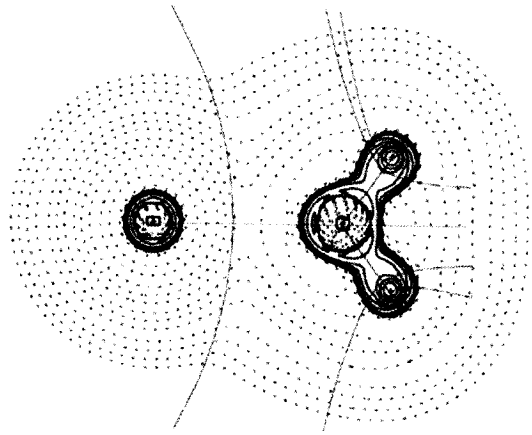

$Na^{+}(H_2O)$

Figure 2.3.6.1. AIM contour plots of the Laplacian for $Be^{2+}(H_2O)$, $Al^{3+}(H_2O)$, and $Na^{+}(H_2O)$. All plots are based on MP2 wave functions.

that predicted slightly stronger metal ion-water binding energies than did the MP2 calculations, thus enhancing this effect. AIM analyses based on the B3LYP wavefunctions (not shown) suggest values of ρ slightly higher and values of $\nabla^2\rho$ marginally smaller at the M-O BCPs, in keeping with the greater metal ion-water binding energies shown in Table 2.3.2.1.

The nature of a bond can be inferred from the analysis of the values of ρ, $\nabla^2\rho$, the eigenvalues of the Hessian (λ_1, λ_2, λ_3, also termed curvatures), the kinetic energy density, G(r), the virial field, v(r) and the local energy density, H(r), at a BCP. Typically, a 'shared-shell' interaction between two atoms is characterized by large values of ρ, negative values of $\nabla^2\rho$, a ratio greater than 1 for $|\lambda_1|/\lambda_3$ and the predominance of the kinetic energy density at the BCP with respect to the virial field [141, 170]. The features of electrostatic bonds, hydrogen bonds, and van der Waals interactions are antipodal to those of 'shared-shell' interactions and are termed 'closed-shell'. These are typically dominated by the virial field component, which is directly related to the potential energy density at the BCP [141, 170].

The calculated values for each of these AIM properties at the M-O bond critical points of each cluster are listed in Table 2.3.6.1. Trimers containing metal ions with high charge:size ratios, such as Be^{2+}, Al^{3+} and Sc^{3+}, possess relatively higher ρ at the M-O BCPs than the other ions, and thus, bind water with slightly more shared-shell character. However, all the values of ρ are less than 1, implying that charge localization at the BCP is low, as evidenced from the topology of $\nabla^2\rho$ between the metal ions and the oxygen atoms in each of the clusters. For ions with small charge:size ratio, the values of ρ at the BCP are quite similar to those obtained for other (traditionally) ionic compounds such as

NaF (0.0500 a.u.), NaCl (0.0310 a.u.) [170] and LiF (0.0760 a.u.) [141]. However, Be^{2+}, Al^{3+} and Sc^{3+}-O bonds have BCP densities that resemble those obtained for Cl-Cl interactions (0.1270 a.u.) [170].

The values of $\nabla^2\rho$ are positive for each of the metal ion-water bonds, implying a predominant closed-shell character. However, no real trend can be discerned from these results. Similarly, the $|\lambda_1|/\lambda_3$, presents no real trend, however they are all below 1, implying that there exists a predominance of closed-shell character to the metal ion to oxygen interaction. However, this criterion provides an unreliable description of closed or shared-shell character, particularly in the aforementioned case of the Cl-Cl bond where it has been reported that $|\lambda_1|/\lambda_3$ also exhibits closed-shell character (0.460 a.u.) [170].

The values of the kinetic energy density per electron at the M-O BCP, G(r)/ρ, in Table 2.3.6.1. appear to be quite similar to those reported for other closed-shell compounds [170]. For example, the NaF G(r)/ρ has a value of 1.94 a.u., which is similar to that for the largest value of G(r)/ρ in this work, 1.97 a.u. for the Be^{3+}-O bond. This feature lends further support for strong, closed-shell interactions in the M-O bonds. The local energy density, H, at the Be^{2+}, Al^{3+}, Sc^{3+}, Y^{3+} and Eu^{3+}-O BCPs are all negative, in sharp contrast with those for other metal ion-water dimers, where the values of H are distinctly positive. However, the negative values are quite small, implying that the shared-shell character of the Be^{2+}, Al^{3+}, Sc^{3+}, Y^{3+} and Eu^{3+}-O bonds may be minimal, and only moderately significant.

M-O BCP properties were also evaluated for the trimer structures. No additional BCPs were found that could be linked to some hydrogen bonding, once again ruling out its role in the O-M-O bending, as discussed previously. As in the dimers, the plots in Fig.

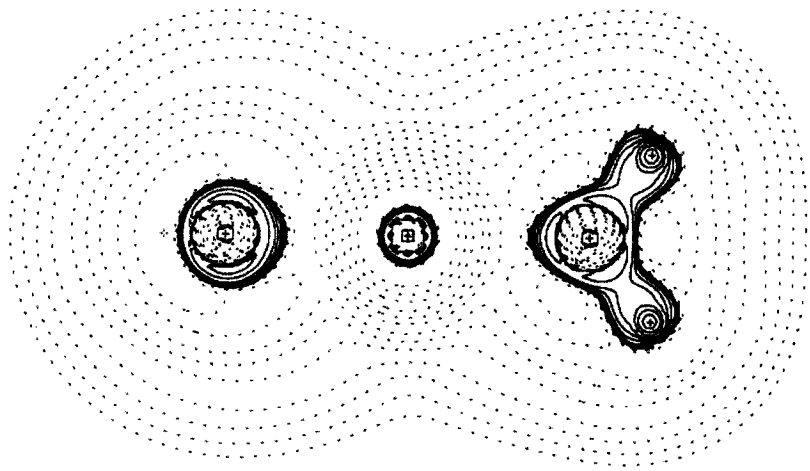

$Al^{3+}(H_2O)$

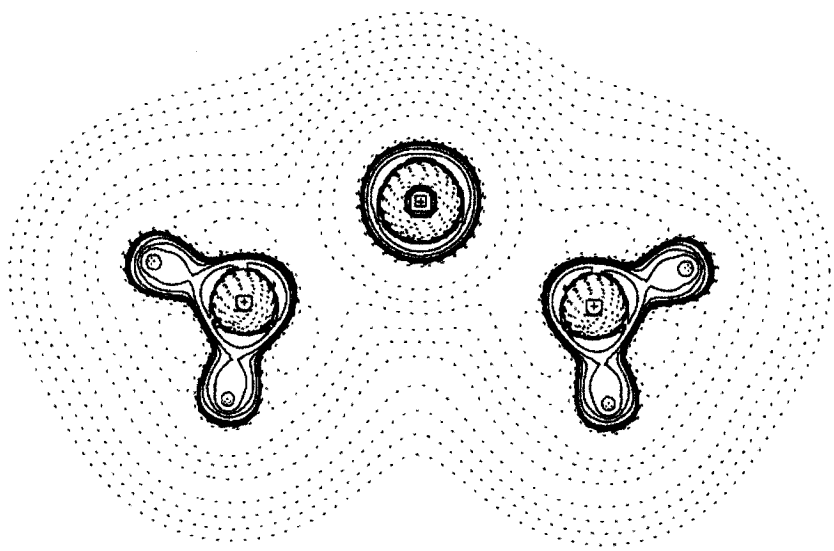

$Sc^{3+}(H_2O)_2$

Figure 2.3.6.2. AIM contour plots of the Laplacian for $Al^{3+}(H_2O)_2$ and $Sc^{3+}(H_2O)_2$. All plots are based on MP2 wavefunctions.

2.3.6.2. for the trimers show no distortion of $\nabla^2\rho$ in clusters containing large ions such as K^+ and Sc^{3+}. From a qualitative standpoint, this feature does not agree with the assessment that polarization of the metal subvalence shell dominates the O-M-O bond angle bending as evidenced in the ELF analyses. However, the quantitative analysis does reveal that the metal ion-oxygen bonds in these clusters have predominantly closed-shell character. As can be seen in Table 2.3.6.1., the properties at the BCP in the dimer structures are similar to those obtained in the trimers. In the trimers, the more positive values of *H* for those M-O bonds that exhibited slight covalent character in the dimers are a direct reflection of the weaker metal ion-water binding energies and the longer M-O bonds found for these structures.

2.4. CONCLUSIONS

An extensive analysis of the bonding interactions in a wide range of different metal ion-water clusters has been performed. The nature of the bonds between the metal ions and water is clearly electrostatic. The main factor governing the structural and energetic features of these clusters, particularly in clusters containing Group I and II metal ions, are polarization effects. These effects are evidenced by the ELF analysis of trimers, where distortion of the metal ion subvalence shell, due to both polarization of the metal ion by water and the electronic repulsions between the C(M) and V(M,O) basins, provide a more favourable bonding interaction with a second water molecule. This was shown in the 3-D surfaces and contour plots of the ELF of $Be^{2+}(H_2O)$, $Al^{3+}(H_2O)$ and $Sc^{3+}(H_2O)$. Changes in the structural properties and in the net dipole moments of water also agree with this assessment.

The electrostatic character of the M-O bonds is demonstrated by the ELF and AIM analyses. According to the ELF analysis, the formation of the metal ion-water bond arises from interaction of the oxygen lone pairs with the metal ion. Furthermore, the ELF yields a clear picture of polarization effects on the cluster structural properties, namely the H-O-H and O-M-O bond angle motifs. The AIM analysis provides a complementary representation of the charge distribution in the clusters. Not only is there distinct localization of charge in both the light and heavy metal ion clusters, but the metal ion also appears to distort the charge distribution of water, particularly in clusters containing small metal ions with high charge:size ratios such as Be^{2+} and Al^{3+}.

In the case of clusters containing trivalent metal ions or Be^{2+}, the metal to oxygen bonds have some slight covalent character, but not enough to influence the structure of the cluster. The NBO analysis shows that only the Al^{3+}-O bond possesses any significant covalent character. Quantitative features of the ELF for these clusters indicate that the V(M,O) bonding basin delocalizes into both the C(M) and C(O) bonding basins, implying that some sharing of electrons occurs between both atoms. This very slight covalent character is also apparent from the AIM analysis, where negative values of the local energy density are found at the M-O BCPs. However, charge localization is restricted to either the ion or to the water molecule, showing once again that any covalent character is modest at best.

The charge analyses showed that negative charge transfer from the solvent to the ion increases with cluster size. It has been shown that this increase continues gradually with increasing cluster size in several other ion-solvent clusters, such as in $Eu^{3+}(H_2O)_n$, but it was shown to taper off at $n > 5$ [118]. Most of the previous work on metal ion

water clusters employed Mulliken charge analyses, and so a re-visitation of these charge transfer trends using a combined charge, ELF and AIM analysis is certainly warranted. It should be noted that ESP and Mulliken analyses did not yield the same quantitative picture as AIM or NBO analyses. However, the deviations seen in the Mulliken analyses were by far the most erroneous of the set of analyses used.

AUTHOR'S NOTES AND SIGNIFICANCE OF PAPER TO THESIS

This work served primarily as a validation of the model chemistry to be used in the parameterization of our model potentials. In addition, it was used to determine the form of the model potential to be employed in our Monte Carlo simulations. Given that polarization effects played a prominent role in influencing the structural, electronic and energetic properties of ion-solvent clusters, it was quite clear that such interactions needed to be considered in the functional form of the potentials.

The following chapter summarizes our initial foray into the development of model potentials for lanthanide ion-water cluster simulations and overviews the key structural and thermodynamic properties of these clusters with increasing cluster size.

CHAPTER 3

A Theoretical Study of Trivalent Lanthanide Ion Microsolvation in Water Clusters from First Principles

Sean R. Hughes, Tao-Nhân Nguyen, John A. Capobianco and Gilles H. Peslherbe*
Centre for Research in Molecular Modeling (CERMM)
And Department of Chemistry & Biochemistry
Concordia University
7141 Sherbrooke St. West
Montréal, Québec, Canada, H4B 1R6

Received 2 December, 2004; accepted 15 December 2004
Dedicated to Bill Hase on the occasion of his 60th birthday.

ABSTRACT

Although metal ion-water clusters $M^{m+}(H_2O)_n$ have been widely studied for many singly charged metal ions, thermodynamic and structural studies of di- or trivalent metal ion-water clusters remain relatively rare. We have investigated the structural and thermodynamic properties of $Ln^{3+}(H_2O)_n$ clusters (Ln^{3+} = Nd^{3+}, Eu^{3+}, Er^{3+} and Yb^{3+}) by means of Monte Carlo simulations using newly-developed, polarizable model potentials parameterized on the basis of ab initio calculations for small clusters. We report stepwise cluster binding enthalpies predicted by our simulations, which have yet to be determined experimentally. Our results also indicate that Ln^{3+} ions exhibit a well-defined interior solvation shell structure. At small cluster sizes (n = 6-12), the first-shell coordination numbers are close to 6 or 7, whereas convergence towards bulk-like coordination numbers seems to be achieved at cluster size $n \geq 24$. In contrast, convergence of the thermodynamic properties towards bulk values only occurs at much larger cluster sizes, $n \geq 64$.

Keywords: Cluster ions; Lanthanide; Model Potentials; Coordination Structure; Thermodynamics; Monte Carlo Simulations

---

3.1. INTRODUCTION

The microsolvation of metal ions in the gas phase has been the focus of intensive research over the last twenty years [123, 125, 128, 129]. Particular attention has been paid to the energetic, structural and spectroscopic properties of ionic clusters containing monovalent metal ions. However, despite advances in electrospray ionization/mass spectrometry techniques that allow for the generation of multiply charged, solvated metal ion clusters [12, 14, 18, 19, 21-24, 30, 31, 33, 37, 90, 108], they have not been studied extensively, especially those clusters containing trivalent metal ions [14, 18, 21-24, 90]. Understanding the fundamental interactions involved in the formation of these clusters, such as the metal-to-ligand bond, can yield insight into the properties of larger clusters or even bulk solutions [98, 171]. One of the most pertinent solvents is obviously water, which is ubiquitous in chemistry and biology.

In an effort to probe the interactions between trivalent metal ions and water, we have opted to investigate $Ln^{3+}(H_2O)_n$ clusters, paying particular attention to their structural and thermodynamic properties. The lanthanides are particularly interesting due to their rather unique binding properties, which contrast with their transition metal counterparts [70]. Despite large, ion-ligand binding energies [106-108, 116, 172-174], the lanthanide ions are believed to form predominantly ionic complexes with their ligands. This is owed to the shielding of the 4f-orbitals by the outermost 5p and 5s electrons, which prevents them from participating in metal to ligand covalent binding [70]. In addition, these ions exhibit a flexible coordination chemistry, binding anywhere from 6 to 10 ligands. Even though the preferential coordination numbers of lanthanide ions in solution had been the subject of a heated debate in the past, it is now widely

accepted that the coordination numbers are closer to nine for the lighter lanthanide ions and eight for the heavier ions. This phenomenon is attributed to 'lanthanide contraction', or the reduction in ionic size across the lanthanide series [58-62, 175, 176]. Because of these features, lanthanide ions provide the foundation for many electro-luminescent devices [70].

Despite sustained efforts, there has been little success in detecting trivalent lanthanide-solvent in small clusters with protic solvents, in particular water [14, 22, 24, 33]. It has been revealed that the trivalent lanthanide metals are prone to dissociative electron or proton transfer, resulting in the production of either $M^{2+}X(HOR)_n$ or $M^{2+}OR(HOR)_n$ species [22]. The reasons for this have yet to be elucidated given that the third ionization potentials of some lanthanide metals, such as La and Ce, are lower than the second ionization potential of Cu, which forms stable $Cu^{2+}(H_2O)_n$ clusters [22]. Recently, work by Bush *et al.* has shown that $Ln^{3+}(H_2O)_n$ clusters containing either Ce, Eu or La, can in fact form stable clusters, but only at large cluster sizes, $n > 15$ [92]. Presumably, at this size, cluster deprotonation reactions are minimized. Prior to this, only Shvartsburg had reported the successful retention of the 3+ state of lanthanide metals in clusters containing a protic solvent, namely Ln^{3+}-diacetone alcohol clusters [22]. However, this depended on maintaining a minimum cluster size, which ranged from n = 5-8 along the series. On the other hand, it has been shown that the 3+ state can be readily conserved in clusters containing aprotic solvents such as acetonitrile, acetone, dimethyl formamide and DMSO [14, 18, 21, 23, 33, 90]. Similarly, Shvartsburg has reported minimum cluster sizes of n = 1-3 in those containing acetonitrile [23] and n = 2-5 in clusters containing DMSO [21]. More interesting, however, is the detection of stable

Ho^{3+}-acetonitrile clusters by Walker *et al.* [33]. The most stable cluster size determined in these experiments was n = 6.

In the past, a variety of electrostatic potential models have been proposed to describe lanthanide ions in solution. Meier *et al.* proposed one of the earliest models [172], which was able to reproduce the experimental coordination number of La^{3+} in water, as reported by Habenschuss and Spedding [58]. However, this study failed to address other lanthanide ions and, thus, did not deal with the well known 'lanthanide shift' in coordination number [61, 62]. Subsequent work by Helm and Merbach's groups [177-181], not only reproduced the observed trends in coordination across the series, but also determined the solvent exchange rates and coordination equilibria for Nd^{3+}, Sm^{3+} and Yb^{3+} in solution [180, 181]. Furthermore, they were the first group to stress the importance of polarization for these systems, and they accounted for it by scaling the dipole moments of the solvent molecules in the first coordination shell. However, these models predicted bulk hydration enthalpies in poor agreement with experimental values [174, 176]. More recent potentials for Ln^{3+} solutions proposed by Floris *et al.* [173] yield structural results in good agreement with experiment, but fail to account for the appropriate coordination numbers of the late ions of the lanthanide series, namely Yb^{3+}. Finally, Derepas *et al.* [108] recently reported a model for $La^{3+}(H_2O)_n$ clusters up to size n = 9. Their findings indicated the preferential formation of 7+1 and 7+2 coordination structures as opposed to purely 8 or 9 coordinated species.

We have constructed a new, rigorous model potential, parameterized to reproduce properties of small ion-water clusters derived from quantum chemistry calculations. This is in contrast with the models presented earlier, which were geared towards bulk, aqueous

solvation. We have made use of our model potential to carry out room-temperature simulations of $Ln^{3+}(H_2O)_n$ clusters, specifically those involving Nd^{3+}, Eu^{3+}, Er^{3+}, and Yb^{3+}, in order to evaluate the structural and thermodynamic features of these clusters. These ions were chosen since they are characteristic of the trends in coordination across the series, in addition to their relevance as it relates to luminescence activity [15]. The outline of this article is as follows: we first discuss the results of quantum chemistry calculations for small $Ln^{3+}(H_2O)$ clusters. The latter serve as the basis for parameterization of our model potentials, which are presented in the following section along with the computational details of our simulations. The cluster structural features and thermodynamics resulting from our simulations are then presented and discussed. Concluding remarks follow immediately.

3.2. QUANTUM CHEMISTRY CALCULATIONS FOR SMALL $Ln^{3+}(H_2O)_n$ CLUSTERS

3.2.1. Computational Details

Small, ground-state $Ln^{3+}(H_2O)_n$ clusters were characterized by quantum chemistry calculations using the Gaussian 98 program [148]. Minimum energy structures were optimized without symmetry constraint using either the unrestricted Hartree-Fock (HF) method [151], Becke's three parameter Lee-Yang-Parr (B3LYP) hybrid density functional theory [149, 150] and second-order Møller-Plessett (MP2) perturbation theory [151]. Energies were also calculated with the Quadratic Configuration Interaction method [182] with single, double and linearized triple excitations [QCISD(T)] for MP2 optimized geometries. All minimum energy structures were characterized by a vibrational frequency analysis and the energies were corrected for zero-point energy. The

6-31G+(2d,p) basis set was employed for water [152], as this basis set generates a rather accurate structure and a reasonable dipole moment for gas phase water at the MP2 level of theory. Lanthanide ions were represented by Stuttgart-Dresden-Bonn (SDD) large-core pseudopotentials and valence basis sets [153, 183], which allow for an extensive description of the valence space and yields relatively accurate interaction energies [153, 183].

3.2.2. $Ln^{3+}(H_2O)$ - Structural and Energetic Properties

Table 3.2.2.1. outlines the features of the minimum energy structures obtained from our quantum chemistry calculations. All ion-water dimers possess C_{2v} symmetry. Most of the model chemistries yield similar ion-water distances and binding energies, all of which agree well with those reported in the literature [106-108, 116, 172, 173]. Typically, the lanthanide ion will bind to oxygen at a distance of 2.30 Å in the case of Nd^{3+} and 2.15 Å for Yb^{3+} according to our MP2 calculations. As expected, the cluster binding energy is seen to increase across the series, from 88.7 kcal/mol for the Nd^{3+}-water dimer to 106.2 kcal/mol for the Yb^{3+}-water dimer according to our QCISD(T) calculations. The shifts in equilibrium ion-water distance are not surprising given that the heavier atoms possess an increased charge to size ratio and, thus, are more prone to inductive effects. Furthermore, the repulsive character of the interaction is reduced across the series due to the decrease in ionic size, leading to more favorable association between the ligand and ions. We note that the popular B3LYP method yields binding energies systematically overestimated by as much as 10 kcal/mol, compared to the more rigorous MP2 or QCISD(T) values. This is consistent with our previous findings for anionic clusters [169, 184].

Table 3.2.2.1. Structural, energetic and electronic properties of small $Ln^{3+}(H_2O)$ clusters.[a]

Ion	Property	HF	B3LYP	MP2	QCISD(T)	Model[e]
Nd^{3+}	r_{Ln-O}[b]	2.32	2.29	2.30	2.30	2.36
	D_o[c]	85.5	98.0	87.3	88.7	88.7
	μ_{H_2O}[d]			3.27		6.03
Eu^{3+}	r_{Ln-O}[b]	2.27	2.24	2.26	2.26	2.34
	D_o[c]	90.5	103.7	92.3	94.3	92.7
	μ_{H_2O}[d]			3.37		6.17
Er^{3+}	r_{Ln-O}[b]	2.19	2.15	2.17	2.17	2.27
	D_o[c]	99.2	113.2	101.2	103.4	103.3
	μ_{H_2O}[d]			3.43		6.54
Yb^{3+}	r_{Ln-O}[b]	2.16	2.13	2.15	2.15	2.22
	D_o[c]	102.4	116.7	104.7	106.2	106.4
	μ_{H_2O}[d]			3.52		6.96

[a] Quantum chemistry calculations are performed with the 6-31+G(2d,p)/SDD basis set as discussed in the text.
[b] Lanthanide to oxygen distance (Å).
[c] Binding energy (kcal/mol) corrected for zero-point energy.
[d] Dipole moment (Debye) of water based on calculated, electrostatic potential (ESP) charges [157].
[e] Prediction of model potentials.

Table 3.2.3.1. Changes in charge distributions and water structural properties in $Ln^{3+}(H_2O)$ clusters.

Ion	Δq_{Ln}[a]	Δq_O[a]	Δq_H[a]	$\Delta\mu$[b]	Δr_{O-H}[c]	$\Delta\angle_{H-O-H}$[d]
Nd^{3+}	-0.15	-0.35	+0.25	1.16	0.03	-1.8
Eu^{3+}	-0.15	-0.39	+0.27	1.26	0.03	-1.7
Er^{3+}	-0.15	-0.44	+0.30	1.32	0.03	-1.5
Yb^{3+}	-0.16	-0.44	+0.30	1.41	0.03	-1.5

[a] Change in the atomic charge (*e*) upon complexation, based on calculated ESP charges [157].
[b] Change in the water dipole moment (Debye) upon complexation, based on calculated ESP charges [157]. The sum of the water atomic charges is not exactly zero, and the origin was chosen as the midpoint between the hydrogens in the calculation of the dipole moments.
[c] Change in water O-H distance (Å) upon complexation.
[d] Change in water angle (degrees) upon complexation.

3.2.3. $Ln^{3+}(H_2O)$ - Electronic Properties

In order to evaluate induction effects, we calculated the partial, atomic charges of each atom in the dimer clusters and the resulting dipole moments. The changes in atomic charges and dipole moments upon complexation are listed in Table 3.2.3.1. The first, notable feature is that the positive partial charges of the lanthanide ions decrease in the dimer, indicating some (slight) electron transfer from the solvent. A significant distortion of the electronic distribution of the water molecule occurs due to the polarizing nature of the lanthanide ion, which pulls some negative charge from the oxygen atom. The extent of charge transfer from oxygen to the lanthanide ion is of the order of 0.15*e* for all ions studied. The electronic changes are accompanied by slight structural changes in the water molecule: the O-H bonds are elongated by 0.03Å and the water bond angle shrinks by an average ~1.6°. These results are in agreement with the trends previously reported by Hengrasmee *et al.* [116]. Induction effects result in a significant increase in the dipole moment of water, of the order of ~1.2-1.4 D, which is substantially larger than the increase observed in clusters of smaller charge:size ratios [109, 111]. These results clearly demonstrate the need to incorporate polarization into any model that accurately describes Ln^{3+}-water interactions.

3.2.4. Larger $Ln^{3+}(H_2O)_n$ Clusters (n =6,8,9)

In addition to our benchmark with cluster dimers, we will compare the predictions of our model against quantum chemistry calculations for a select number of larger clusters. Based on the fact that B3LYP seemed to systematically overestimate binding energies for the dimers by as much as 10% (cf. Table 3.2.2.1.), we opted to perform HF calculations for the larger clusters. Even though HF lacks electron correlation, it yielded

dimer structural and energetic properties comparable to those predicted by the high-level QCISD(T) and, as such, HF calculations may provide respectable estimates of the properties of large $Ln^{3+}(H_2O)_n$ clusters.

In previous work by Walker *et al.* [33], $Ho^{3+}(H_2O)_n$ were reportedly not found in electrospray mass spectrometry experiments employing the pick-up technique, but it was shown that metal-solvent clusters of various sizes containing acetonitrile or acetone could be generated. In particular, $Ho^{3+}(CH_3CN)_6$ and $Ho^{3+}(C_3H_6O)_6$ appeared to be preferentially formed. Accordingly, we have attempted to probe the characteristics of hexa-coordinated Ln^{3+} complexes via quantum chemistry calculations. An octahedral symmetry was assumed to be the initial structure, given that it is the preferential coordination of the lanthanide ions with 6 ligands [61]. An example of a minimized structure can be seen in Fig. 3.2.4.1.a and properties of these clusters are collected in Table 3.2.4.1.. Similar trends are observed as for the dimer. For instance, the bond distances shorten from an average 2.50 Å in $Nd^{3+}(H_2O)_6$ to 2.33 Å in $Yb^{3+}(H_2O)_6$. Furthermore, the total cluster binding energies increase, from 371.0 kcal/mol to 431.2 kcal/mol for the same clusters.

We have also optimized the structures of $Ln^{3+}(H_2O)_8$ and $Ln^{3+}(H_2O)_9$, since these clusters correspond to the preferential coordination numbers of lanthanide ions in solution [58-62]. We assumed a square anti-prism (SQA) and a tri-capped trigonal prism (TCTP) for the 8 and 9-coordinated clusters, respectively (see Figs. 3.2.4.1.b and 3.2.4.1.c), as they appear to be the preferred orientations of water in solution [58-62].

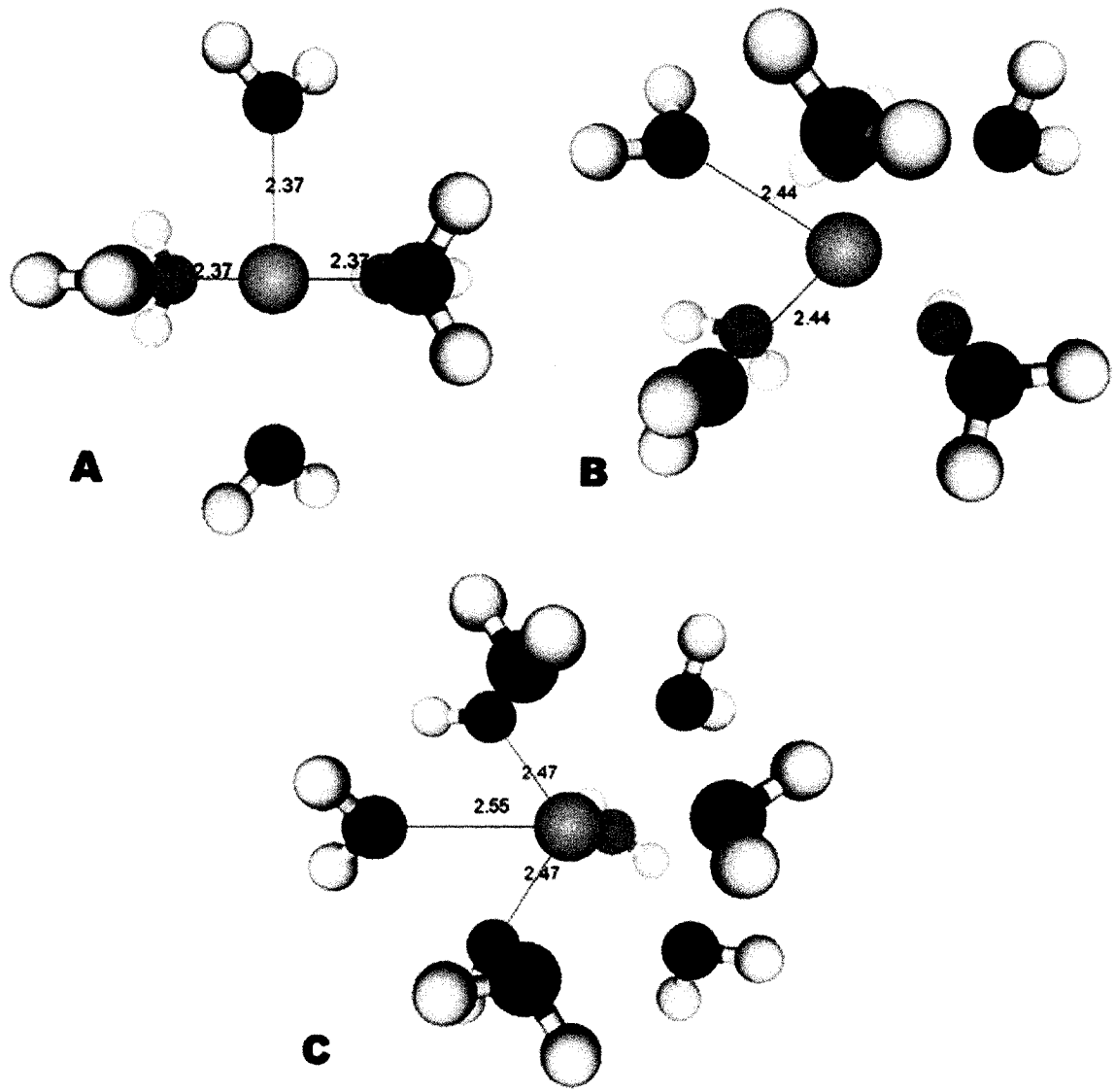

Figure 3.2.4.1. Minimum energy $Er^{3+}(H_2O)_n$ cluster structures for a) n = 6, b) n = 8 and c) n = 9 obtained from quantum chemistry calculations with the HF/SDD/6-31+G(2d,p) model chemistry. Distances are in Å.

Table 3.2.4.1. Structural, energetic and electronic properties of $Ln^{3+}(H_2O)_n$ (n=6, 8 or 9).

Ion	Property	6-coordinated		8-coordinated		9-coordinated	
		HF[d]	Model[e]	HF[d]	Model[e]	HF[d]	Model[e]
Nd^{3+}	r_{Ln-O}[a]	2.50	2.63	2.54	2.74	2.59 / 2.61	2.78 / 2.84
	U[b]	371.0	351.5	431.2	403.9	451.0	424.8
	μ_{H_2O}[c]	3.24	4.10	3.08	3.60	2.99 / 3.10	3.35 / 3.50
	q_{Nd}[c]	+2.8	+3.0	+2.9	+3.0	+3.0	+3.0
Eu^{3+}	r_{Ln-O}[a]	2.45	2.63	2.53	2.72	2.55 / 2.58	2.75 / 2.82
	U[b]	389.4	364.0	449.1	416.9	467.7	438.4
	μ_{H_2O}[c]	3.34	4.10	3.14	3.60	3.07 / 3.11	3.37 / 3.53
	q_{Eu}[c]	+2.8	+3.0	+3.1	+3.0	+3.2	+3.0
Er^{3+}	r_{Ln-O}[a]	2.36	2.63	2.44	2.67	2.47 / 2.54	2.69 / 2.78
	U[b]	419.4	392.2	477.4	451.9	493.7	471.3
	μ_{H_2O}[c]	3.27	4.10	3.09	3.70	3.11 / 3.16	3.37 / 3.56
	q_{Er}[c]	+2.8	+3.0	+2.9	+3.0	+2.8	+3.0
Yb^{3+}	r_{Ln-O}[a]	2.33	2.50	2.42	2.66	2.44 / 2.53	2.68 / 2.80
	U[b]	431.2	406.0	487.5	441.9	502.9	459.5
	μ_{H_2O}[c]	3.26	4.20	3.10	3.71	3.10 / 3.14	3.33 / 3.59
	q_{Yb}[c]	+2.8	+3.0	+2.9	+3.0	+3.0	+3.0

[a] Lanthanide to oxygen distance (Å). For 9-coordinated species, the values listed correspond to the axial and equatorial ligand properties, respectively.
[b] Binding energy (kcal/mol) corrected for zero-point energy.
[c] Dipole moment (Debye) of water and atomic charges of Ln^{3+} (*e*) based on calculated ESP charges [157]. For 9-coordinate species, the values listed correspond to the axial and equatorial ligand properties, respectively.
[d] Quantum chemistry calculations are performed with the 6-31+G(2d,p)/SDD basis set as discussed in the text.
[e] Predictions of model potentials.

The features of these clusters are also collected in Table 3.2.4.1. Our structural results compare well with those of Cosentino *et al.*, who reported the features of several global minimum energy structures for $Nd^{3+}(H_2O)_8$, $Yb^{3+}(H_2O)_8$ and $Gd^{3+}(H_2O)_9$ clusters [106, 107]. In addition our energetic results are in the range of those reported by Hengrasmee *et al.*, though their calculations assumed a cubic structure for $Ln^{3+}(H_2O)_8$ as opposed to the SQA structure [116]. HF calculations for the $Ln^{3+}(H_2O)$ dimer seemed to underestimate the cluster binding energies by a consistent ~4 kcal/mol (approximately 4%), compared to the QCISD(T) predictions. Thus, the HF energies listed in Table 3.2.4.1. may also be underestimated by a similar 4%.

3.3. MODEL POTENTIAL AND SIMULATIONS/PROCEDURE

3.3.1. Functional form of the Model Potentials

The model chosen to represent ion-water and water-water interactions is a sum of Coulombic, induction and repulsion-dispersion terms:

$$U = U_{Coulomb} + U_{Induction} + U_{Repulsion-dispersion}. \quad (1)$$

The Coulombic energy simply reflects the interactions between permanent charges:

$$U_{Coulomb} = \sum_{i,j} q_i q_j / r_{ij}, \quad (2)$$

where i and j represent different sites in the system separated by a distance r_{ij} and the q's are the static point charges of the metal ion and the water atoms. The induction energy is expressed as

$$U_{Induction} = -\frac{1}{2}\sum_i \vec{E}_i^o \vec{\mu}_i, \quad (3)$$

where E_{ij} is the electric field at site i arising from the permanent charges:

$$\vec{E}_i^o = \sum_j q_j \cdot \vec{r}_j \Big/ \left|\vec{r}_i - \vec{r}_j\right|^3, \tag{4}$$

and the induced dipoles, μ_{ij}, are evaluated as a linear response to the total electric field:

$$\vec{\mu}_i = \alpha_i \cdot \vec{E}_i = \alpha_i \left[\vec{E}_i^o + \sum_{i \neq j} T_{ij} \cdot \vec{\mu}_j \right], \tag{5}$$

where α_i is the polarizability of site i and T_{ij} is the dipole tensor [185]. The polarizable sites in the induced dipole problem of Eqs. (3) to (5) account for the mutual polarization of the solvent molecules and the lanthanide ion. In cluster simulations, the low dimensionality of the problem yields a straight-forward solution of the set of linear equations in Eq. (5) in matrix form [186], which is obtained by LU decomposition and back substitution [187] in this work. The repulsion-dispersion interactions are represented by a generalized 12-8-6 Lennard-Jones potential:

$$U_{Repulsion-Dispersion} = \sum_{i,j} \left[A_{ij} r_{ij}^{-12} + B_{ij} r_{ij}^{-8} - C_{ij} r_{ij}^{-6} \right], \tag{6}$$

where A_{ij}, B_{ij} and C_{ij} are adjustable parameters.

3.3.2. Parameterization of the Model Potentials

The parameters for the polarizable model include the point charges (q_i), the polarizabilities (α_i) and the repulsion-dispersion parameters (A_{ij}, B_{ij}, C_{ij}). The lanthanide ions are assigned a +3 charge and a polarizability of 2.8 Å^3. The latter is larger than the experimental polarizability of La^{3+} (1.6 Å^3) [135] and should be more representative of that for the early ions in the lanthanide series. The point charges and polarizability of water are those of our OPCS model [128, 129]. The parameters are listed in Table 3.3.2.1.. Briefly, the OPCS model is a rigid, 5-site model, with 4 permanent charge sites, one induced dipole site on the oxygen atom and repulsion sites on the hydrogen atoms.

Of the 4 permanent charges, 2 positive charges are positioned on the hydrogen atoms, while 2 negative charges are located in the vicinity of the oxygen atom towards the hydrogen atoms, out of plane from the water symmetry axis. It should be noted that this model employs a water molecule with a rigid gas-phase geometry (r_{OH} = 0.9572 Å, $\angle_{HOH}$ = 104.52° [188]) and reproduces the gas-phase water dipole moment [189]. The repulsion-dispersion parameters for the solvent-solvent interactions were fit to reproduce the water dimer geometry and binding energy [128]. The ion-solvent interactions were fit to reproduce the equilibrium ion-water distance, the binding energy and the dipole moment of water molecules as predicted by quantum chemistry calculations for the ion-water dimer. This fitting was performed using a non-linear least-squares algorithm based on the Marquardt-Levenberg method [187].

Table 3.3.2.1. Potential parameters.

	A_{ij}[a]	B_{ij}[a]	C_{ij}[a]
Nd^{3+}-O	0	92 665	7099
Eu^{3+}-O	0	93 199	7871
Er^{3+}-O	0	92 488	9327
Yb^{3+}-O	0	77 694	6794
O-O[b]	1 152 921	0	1074
H-H[b]	10^{5}[c]	5.5[c]	
	α[d]	q[e]	
Nd^{3+}	2.8	3.00	
Eu^{3+}	2.8	3.00	
Er^{3+}	2.8	3.00	
Yb^{3+}	2.8	3.00	
O[b]	1.45	-0.569	
H[b]	-	0.569	
	$r_{O\text{-}M}$[f]	$\theta_{H2O\text{-}M}$[g]	
Water	0.342	43.4	

[a] Repulsion-dispersion parameters: A_{ij} (kcal·mol Å^{-12}), B_{ij} (kcal·mol Å^{-8}), C_{ij} (kcal·mol Å^{-6}); [b] From references 1-2; [c] Repulsion parameters between hydrogen atoms: the functional form of this interaction is a Born-Mayer term, $A_{ij}e^{-Bijr}$, with parameters A_{ij} (kcal/mol) and B_{ij} (Å^{-1}) [128]; [d] Polarizability (Å^{3}); [e] Permanent point charges (e); [f] Distance between oxygen and its charge sites (Å) [128]; [e] Angle defining each oxygen charge site with respect to the molecular plane of water (°).

Table 3.2.2.1. lists the structural, energetic and electronic properties of the ion-water dimer minimum energy structure predicted by the model potentials. We note that the binding energies of the dimers are reproduced very well by our model potentials, with little or no deviation with respect to the QCISD(T) values. The ion-water bond distances differ from the MP2 value by at most 0.08 Å, which constitutes an overall error of only 3% with respect to the quantum chemistry reference. The water dipole moments predicted by our model potentials follow the trend predicted by our quantum chemistry calculations, i.e. they are significantly larger than that of gas-phase water in the presence of lanthanide ions, and lighter lanthanide ions have a smaller effect on the induced dipole than heavier ions. However, the water dipole moments in $Ln^{3+}(H_2O)$ clusters are grossly overestimated by our model potential when compared to the quantum chemistry results. Improving the water dipole moments predicted by the model potentials could only be done at the expense of the cluster structure and binding energy. This overestimate of solvent polarization in the dimer may be attributed to the neglect of charge transfer in the functional form of the potential, but as will be discussed shortly, it will be less of an issue for larger clusters.

The predictions of our model potentials for a select number of larger $Ln^{3+}(H_2O)_n$ clusters (n = 6, 8, 9) are summarized in Table 3.2.4.1., where they are compared to the results of quantum chemistry calculations. It can be seen that the water dipole moments decrease significantly compared to their value in the cluster dimer, and in general decrease with cluster size increase. This is due to the ion making multiple associations with solvent molecules and an increased number of solvent-solvent repulsions, which result in structures with the ion located at a larger distance from the water molecules. For

instance, the average ion-oxygen distance is ~0.2 Å longer for cluster size 6 when compared to those for cluster size 1, and the larger distances between the ion and the solvent molecules naturally lead to a decrease of mutual polarization. In addition, it can be seen from Table 3.2.4.1. that the atomic charge of the lanthanide ion increases with cluster size, regaining the full +3 charge by cluster size 9. This clearly indicates that charge transfer is not an issue for larger clusters and that, even though polarization effects may be overestimated for smaller clusters, they will be quantitatively described by our model potential for medium-size to large clusters. Furthermore, this is consistent with the experimental observations of Shvartsburg, where minimum clusters sizes of n = 5-8 were required to maintain the 3+ charge of the cations in clusters containing diacetone alcohol [22]. However, it has been proposed that the stabilization of the 3+ state was dependent on the bidendate nature of diacetone alcohol and on the ion-ligand distance, which, in clusters containing diacetone alcohol, may be much longer than in water (though this has not been confirmed). At n = 6, 8 and 9, the water molecules are located at much larger distances from the ion with respect to those seen in the dimer (~0.2 Å further). For this reason, the charge transfer mechanism becomes less probable and thus, is minimized in our calculations of larger clusters.

Finally, inspection of Table 3.2.4.1. reveals that the model potentials seem to properly account for many-body interactions, yielding cluster binding energies underestimated by only 6% compared to the quantum chemistry values for intermediate cluster sizes 6, 8 and 9. Together with the fact the HF quantum chemistry results underestimated the binding energies predicted by high-level QCISD(T) calculations by

4%, this suggests an error bar of ~10% for energetic properties predicted by our model potentials for medium-size clusters.

3.3.3. Monte Carlo Simulations

Monte Carlo simulations were used to investigate the thermodynamic and structural properties of $Ln^{3+}(H_2O)_n$ clusters at 300K. The detailed procedure has been reported previously [125] and only the key features are summarized here. A random-walk approach is used to generate new configurations, which involves the random translation of a water molecule in Cartesian space and its rotation around the Euler angles. The maximum allowed translations were set to 0.15 Å and the range of angular movements was set to 15°. The resulting configurations were accepted or rejected according to the Metropolis algorithm [190]. Because we are simulating clusters and not the bulk liquid, no periodic boundary conditions were imposed. As a consequence, evaporation of the solvent molecules from the cluster is possible and it was closely monitored. Any water molecule that is found beyond 20 Å from the ion for cluster sizes $n < 64$ and 35 Å for clusters sizes $64 \leq n < 128$ are considered evaporated from the cluster. Markov chains containing configurations with evaporated solvent molecules were discarded from the overall sampling so as to define a representative, equilibrium ensemble for a given cluster size. A periodic heating and cooling of the system was used to avoid trapping in local minima. In general, each run entailed at least $2x10^6$ configurations for equilibration, followed by an equal amount of steps for data collection. The acceptance ratios obtained ranged between 35% and 45%.

Cluster enthalpies were calculated from the average energy $<U>$ of the canonical ensembles of configurations as

$$\Delta H_n = \Delta U + \Delta(PV) = \langle U \rangle + nRT, \tag{8}$$

and the stepwise binding enthalpies, which represent the enthalpy gain associated with the addition of one solvent molecule to the cluster, were calculated as

$$\Delta H_{n,n-1} = \Delta H_n - \Delta H_{n-1}. \tag{9}$$

The structural properties of the clusters were analyzed in terms of a distance-dependent coordination number $N_{coord}(r)$, and its derivative, $P(r)$, which is the normalized radial probability distribution function:

$$P(r) = {dN_{coord}(r)}/{dr} = \frac{n4\pi r^2 g(r)}{\int_0^\infty 4\pi r^2 g(r) dr}. \tag{10}$$

It should be noted that $P(r)$ differs from the radial distribution function $g(r)$ used in liquid structure theory by a factor of $4\pi r^2$ and it is normalized to the number of solvent molecules in the cluster.

3.4. RESULTS AND DISCUSSION

3.4.1. Structural Data

Fig. 3.4.1.1. shows some representative structures of $Eu^{3+}(H_2O)_n$ clusters obtained from room-temperature Monte Carlo simulations. The ion is clearly coordinated to the water oxygen atoms and the clusters exhibit an interior solvation shell structure. The latter finding is further ascertained from the probability distribution functions shown in Fig. 3.4.1.2., where clear peaks are indicative of a well-defined ion solvation shell structure. The interior solvation structure is due to the fact that the loss in free energy associated with the disruption of the solvent network is compensated by the formation of much stronger ion-solvent bonds. This is not surprising given the very large ion binding energies discussed earlier for $Ln^{3+}(H_2O)$, of the order of 100 kcal/mol, compared to a

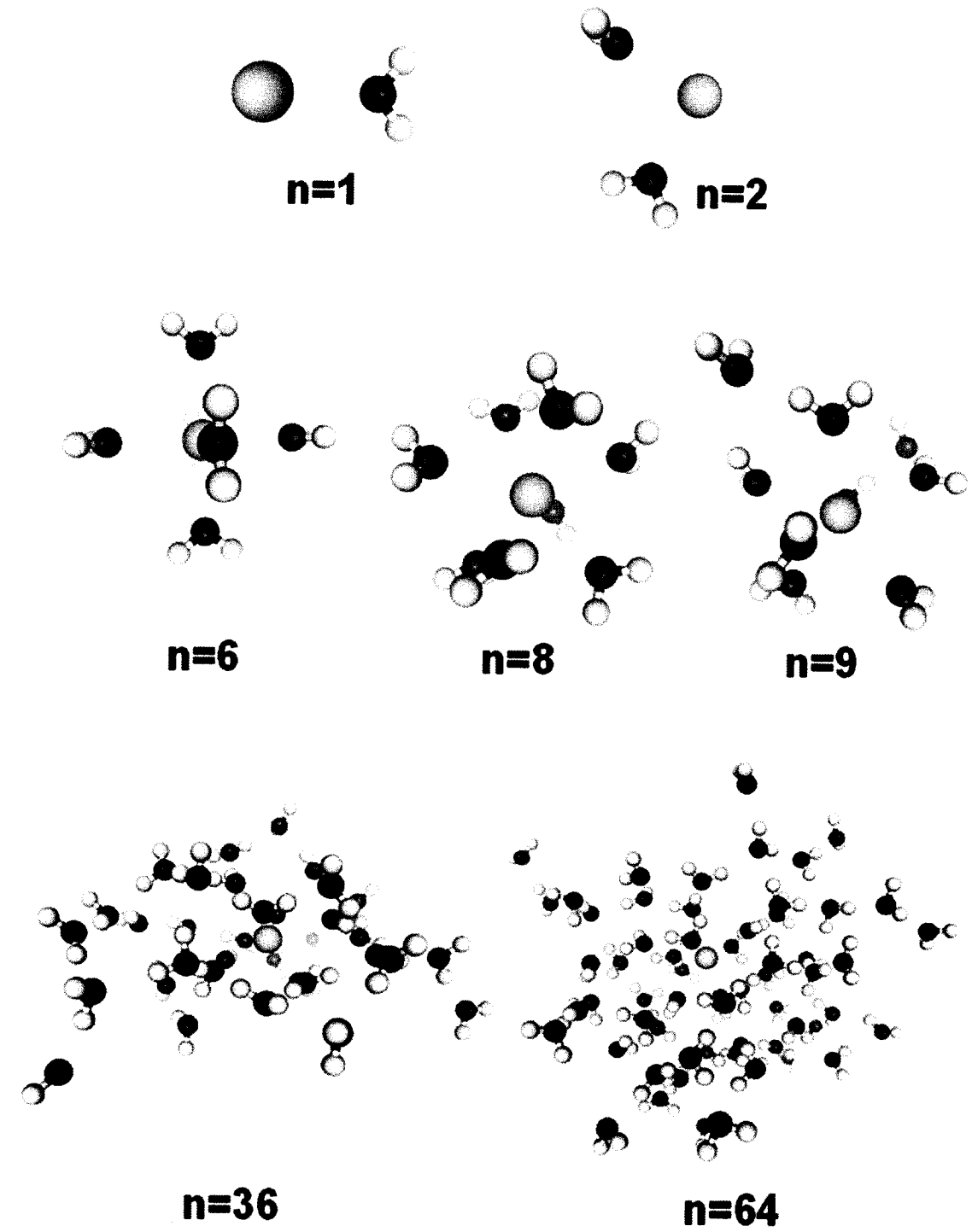

Figure 3.4.1.1. Representative structures obtained for $Eu^{3+}(H_2O)_n$ clusters from Monte Carlo simulations with model potentials.

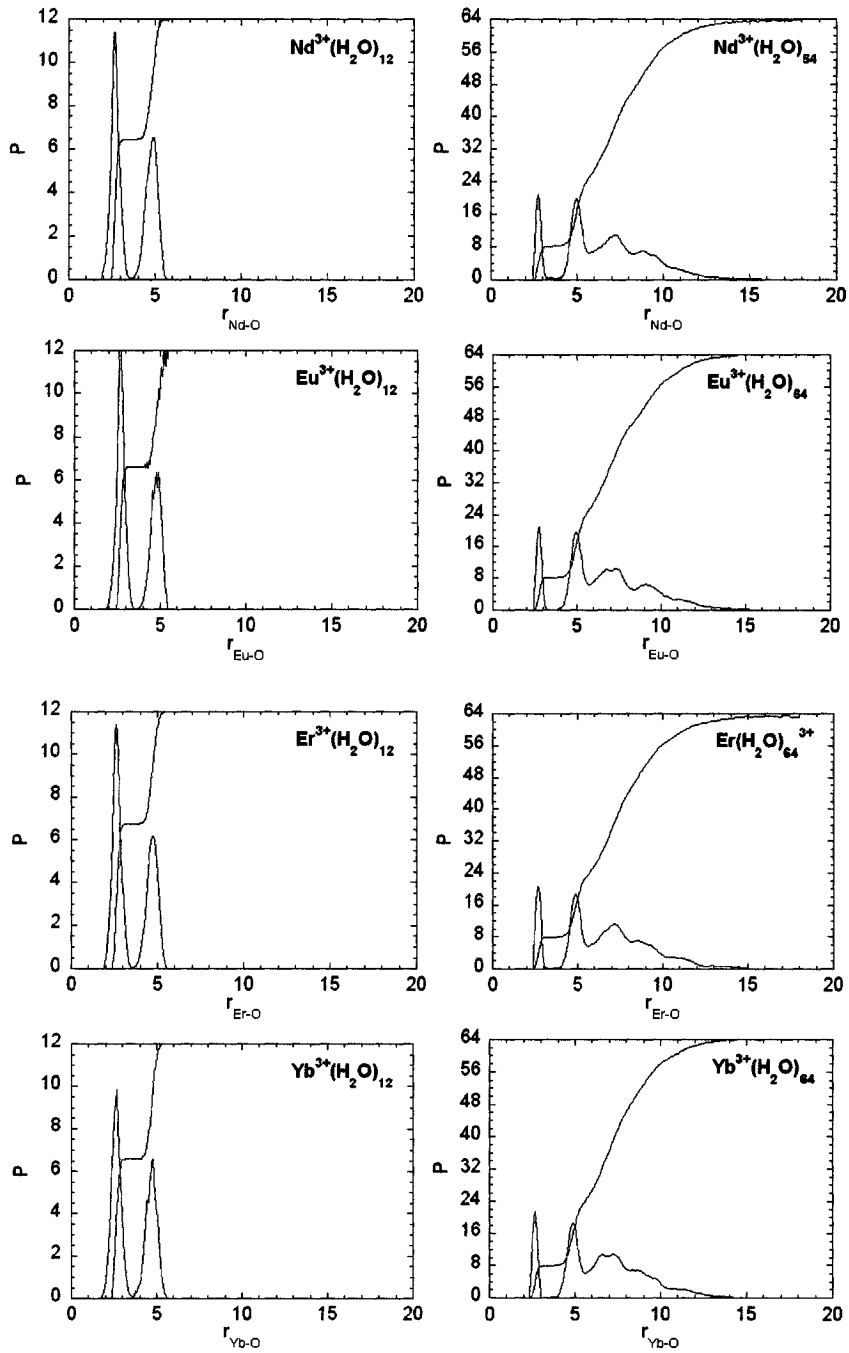

Figure 3.4.1.2. Radial probability distribution functions and cumulative radial probability distribution functions vs. Ln^{3+}-O distance for $Ln^{3+}(H_2O)_{12}$ and $Ln^{3+}(H_2O)_{64}$ (Ln^{3+} = Nd^{3+}, Eu^{3+}, Er^{3+} and Yb^{3+}). First-shell coordination numbers derived from the cumulative functions are listed in Table 3.4.1.1. and average ion-oxygen distances in Table 3.4.1.2.

water-water interaction energy of ~5 kcal/mol [128]. Evidence of a second, loose, coordination shell can be seen for large clusters such as $Ln^{3+}(H_2O)_{64}$ from the second peak at ~5 Å. This is a reflection of the long-range influence of the ion on the solvent and indicates that the ion-solvent interactions ultimately govern the cluster structure.

The probability distribution functions shown for $Ln^{3+}(H_2O)_{64}$ are representative of those observed for all clusters $n \geq 24$ for each ion studied. In the case of Eu^{3+}, where the average first-shell coordination number lies between 8 and 9, simulation results point to a purely 8 or 9-coordinated first hydration shell structure. Furthermore, the fact that the probability distribution function, P(r), goes to zero in between the two peaks representing the first and second coordination shells indicates that solvent molecules are not found in between the coordination shells, in agreement with the low residence times for water previously reported by Kowall *et al.* [180, 181].

The average first-shell coordination numbers of the lanthanide ions are listed in Table 3.4.1.1. for a number of cluster sizes. When approaching cluster size 64, the coordination numbers derived from our simulations agree well with those obtained from X-ray and neutron diffraction experiments of $LnCl_3$ solutions [58-62], and changes in coordination numbers along the series are consistent with solution experimental data. The relatively slow convergence of the coordination numbers to the bulk values contrasts with what was observed in our previous work on cesium and sodium-water clusters [125, 128, 129], for which the coordination numbers are comparable to those observed in the bulk at very small cluster sizes ($n < 12$). This difference is due to the low charge:size ratio of the monovalent ions, which results in weaker ion-water interaction energies. For instance, the $Na^{+}(H_2O)$ binding energy is ~24 kcal/mol, whereas that of $Yb^{3+}(H_2O)$ is

~106 kcal/mol. As a result, first-coordination shell water molecules can be found at a larger distance from the ion and from each other, and solvent-solvent repulsions in the first coordination shell are minimized in monovalent ion-water clusters.

Table 3.4.1.1. Average first-shell coordination numbers of $Ln^{3+}(H_2O)_n$.

n	6	7	8	9	12	24	36	64	128	Exp[a]
Nd^{3+}	6.0	6.6	6.5	6.5	6.4	8.0	8.0	8.2	8.6	8.9
Eu^{3+}	6.0	7.0	7.0	6.9	7.0	8.0	8.0	8.2	8.4	8.3
Er^{3+}	6.0	6.9	7.1	7.0	6.7	7.8	8.0	8.0	8.0	8.2
Yb^{3+}	6.0	6.3	7.3	6.6	7.1	7.9	7.9	7.9	8.4	7.9

[a] Bulk solution data [58-62].

The distances between the ions and the oxygen atoms of the water molecules in the first coordination shell are listed in Table 3.4.1.2. for a number of cluster sizes. Experimental, bulk values from diffraction studies of $LnCl_3$ salt solutions are also provided in Table 3.4.1.2. for comparison [58-62]. The cluster ion-water distances, even for very large clusters, are larger than those for bulk solutions by 0.25 Å. These deviations could be attributed to the absence of counter-ions in our clusters, which may drive the solvent to coordinate more tightly to the cations due to repulsions. Compared to the previous model of Floris *et al.* [173], our model reproduces the decrease of the coordination number across the series, but apparently at the expense of the ion-water distances. Both the models of Floris *et al.* [173] and Kowall *et al.* [180] failed to describe the solvation of Yb^{3+} in solution appropriately. The former failed to reproduce the experimental coordination number and the latter, the ion-water distance in the bulk. Our model not only manages to reproduce the appropriate coordination number of Yb^{3+}, but the trend in the Yb^{3+}-O distance predicted for large clusters by our model also is consistent with the experimental bulk values [58-62]. Our model is thus capable of

consistently describing the qualitative differences in lanthanide coordination across the series.

Table 3.4.1.2. Average ion-water distance (Å) in the first coordination shell of $Ln^{3+}(H_2O)_n$.[a]

n	24	36	64	128	Exp[b]
Nd^{3+}	2.74	2.73	2.75	2.77	2.51
Eu^{3+}	2.72	2.71	2.71	2.74	2.45
Er^{3+}	2.65	2.66	2.66	2.65	2.37
Yb^{3+}	2.64	2.64	2.63	2.67	2.32

[a] Average lanthanide to oxygen distance from Monte Carlo simulations. The cut-off radius for the first coordination shell was determined from the probability distribution functions.
[b] Bulk solution data [58-62].

Solvation in smaller clusters differs somewhat from that for larger clusters. Inspection of Table 3.4.1.1. indicates that the model predicts either 6+2 or 7+1, and either 6+3 or 7+2 coordination for cluster sizes 8 and 9, respectively. The +1, +2 and +3 refer to solvent molecules that reside outside the first coordination shell, indicating the beginning of a second hydration shell formation. This trend is observed for all clusters in the range of n = 8-12. This is not a surprising result since no solvent network is present to confine the additional solvent molecules in the first solvation shell. At larger cluster sizes, additional solvent molecules may drive the ion coordination numbers towards bulk values. Similar behavior has been reported by Derepas *et al.* [108] for small $La^{3+}(H_2O)_n$ clusters.

3.4.2. Thermodynamic Data

Cluster enthalpies for $Ln^{3+}(H_2O)_n$ clusters are shown as a function of clusters size in Fig. 3.4.2.1. We note that since our model potentials are likely to underestimate the cluster binding energies by ~10% for medium-sized clusters (cf. Sec. 4.3.2), the total

cluster enthalpies are likely to be underestimated by a similar 10%. Stepwise binding enthalpies for cluster sizes n = 1-9 are shown in Fig. 3.4.2.1.a, where a gradual decrease of the stepwise binding enthalpy can be observed upon addition of each solvent molecule. A remarkable feature of the stepwise binding enthalpies is the more pronounced decrease occurring between $\Delta H_{5,6}$ and $\Delta H_{6,7}$, which coincides with the completion of the first hydration shell in small clusters as shown in Fig. 3.4.1.2. (top panels) and discussed earlier. Since the solvation of Ln^{3+} ions in both water and acetonitrile in the bulk follow similar trends [57], a similar behavior may be expected for small clusters, and these findings are consistent with the experimental observations of only $Ho^{3+}(C_3H_6O)_6$ and $Ho^{3+}(CH_3CN)_6$ clusters [33].

Total cluster enthalpies and reduced cluster enthalpies are shown in Fig. 3.4.2.1.b and 4c, respectively, as a function of cluster size. The thermodynamic properties follow the energetic trends observed earlier, with the lighter lanthanide ions having smaller cluster enthalpies than the heavier ions. For example, the $Nd^{3+}(H_2O)_{128}$ cluster has a total enthalpy of ~1492 kcal/mol, whereas the $Yb^{3+}(H_2O)_{128}$ cluster has a total enthalpy of ~1556 kcal/mol. At a cluster size $n \geq 36$, the total cluster enthalpies start to increase almost linearly. This may reflect the decreasing influence of the ion interaction with the outermost solvent molecules and indicate that the change in stabilization enthalpy of the cluster arises primarily from additional H_2O-H_2O interactions. This is reflected in the plateau observed in the reduced cluster enthalpy shown in Fig. 3.4.2.1.c. The latter converges to the heat of vaporization of water, whose experimental value is around 9.7 kcal/mol [191], as the reduced cluster enthalpy naturally approaches the average amount of energy necessary to vaporize one solvent molecule from the cluster in the large cluster

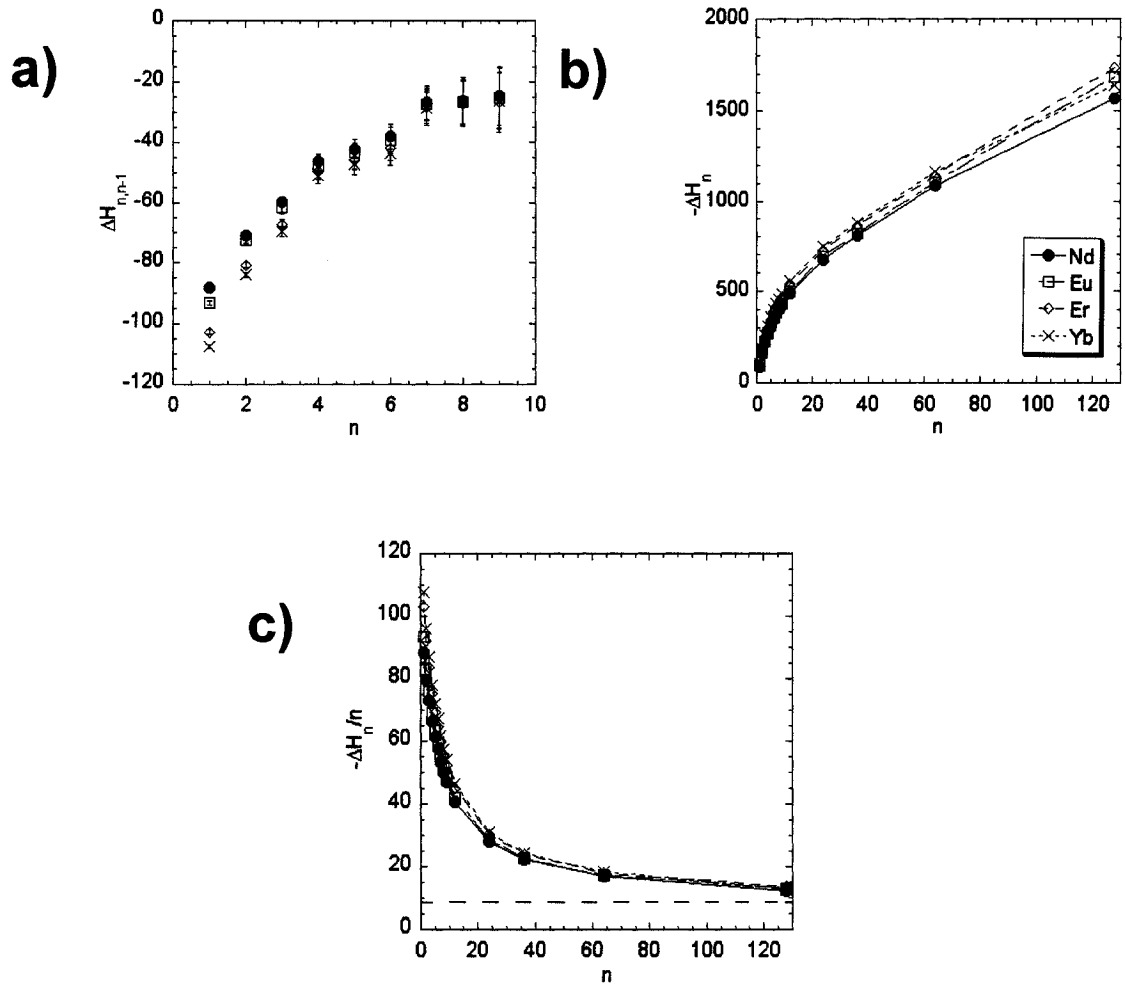

Figure 3.4.2.1. a) Stepwise binding enthalpy vs. cluster size for $Ln^{3+}(H_2O)_n$ clusters (n = 1-9); b) reduced cluster enthalpy vs. cluster size for Ln^{3+} $(H_2O)_n$ clusters (n = 1-128). The experimental heat of vaporization of bulk water, shown as a dashed line, has a value of -9.7 kcal/mol; c) total cluster enthalpy vs. cluster size for $Ln^{3+}(H_2O)_n$ clusters (n = 1-128). All enthalpies are in kcal/mol.

regime [125]. The reduced cluster enthalpies for $Ln^{3+}(H_2O)_n$ are ~17.0 kcal/mol for n = 64 and ~13.0 kcal/mol for n = 128. Interestingly, the convergence of the reduced cluster enthalpy towards the heat of vaporization of water occurs at a far faster rate in clusters containing smaller monovalent metal ions than in those containing trivalent lanthanides. For instance, the $Na^+(H_2O)_{36}$ reduced cluster enthalpy lies only within ~2 kcal/mol of the heat of vaporization of water [125]. This is once again a reflection of the long-range influence of the trivalent lanthanide ion interaction with the surrounding solvent molecules beyond the first coordination shell.

3.5. CONCLUSIONS

In this work, we have investigated the structural and thermodynamic properties of $Ln^{3+}(H_2O)_n$ clusters by means of room-temperature Monte Carlo simulations. These calculations made use of a rigorous model potential containing an explicit polarization term that was fitted to quantum chemistry predictions of the energetic, structural and electronic properties of small Ln^{3+}-water clusters.

An interior solvation shell structure is observed for all $Ln^{3+}(H_2O)_n$ clusters, and peaks in the probability distribution functions indicate a well-defined solvation shell structure. For all clusters, the following trends are observed in going across the lanthanide series: ion-water binding energies increase, while ion-water distances decrease. Smaller clusters (n = 8-12) tend to adopt 6 or 7-coordinated structures due to the absence of a solvent network, which influences the coordination number via induction effects. At large cluster sizes, the lighter lanthanide ions (e.g. Nd^{3+}) show a preference for forming 9-coordinated structures with their ligands, whereas the heavier lanthanides

(e.g. Yb^{3+}) yield 8-coordinated structures, in agreement with what is observed experimentally for bulk solution [58-62].

Since there has been little experimental work on multiply charged ion aqueous clusters, we have calculated thermodynamic quantities related to the binding of water molecules to Ln^{3+} ions to guide possible, future experiments. The predicted stepwise binding enthalpies are quite large, even for small cluster sizes. A more pronounced decrease of the stepwise binding enthalpies occurs between n = 6 and 7, reflecting the completion of the first coordination shell in small clusters and indicating the higher stability of hexa- and hepta-coordinated clusters, a feature consistent with experimental observations with other solvents [33]. The total cluster enthalpies show that the lighter lanthanides bind less tightly to the solvent than do the heavier ions. At larger cluster sizes, the increase in the cluster enthalpies is attributed to interactions of the additional (outermost) water molecules with other solvent molecules that solvate the ion. As a result, the reduced cluster enthalpies converge to the heat of vaporization of liquid water but the rate of convergence for $Ln^{3+}(H_2O)_n$ is much slower than what was observed for monovalent ion aqueous clusters [123, 125, 128, 129], a feature consistent with the strong, long-range interaction of Ln^{3+} ions with solvent molecules.

Previous simulations of monovalent metal ion aqueous clusters, following the same procedure and employing similar model potentials as in this work, yielded stepwise binding energies in excellent agreement with available experimental data [123, 125, 128, 129]. This gives confidence in the predicted thermodynamic quantities reported in this work, which in turn could serve as benchmarks for future mass spectrometry experiments. This work is being extended to explore the solvation of Ln^{3+} metal ions

with other solvents, such as acetonitrile, for which a stable hexa-coordinated cluster has been reported [33]. The model potentials are also being refined to account for charge transfer between ions and solvent molecules via the incorporation of fluctuating charges [192], and by improving the treatment of polarization.

3.7. AUTHOR'S NOTES AND SIGNIFICANCE OF PAPER TO THESIS

This paper is core to one of the central themes of this thesis: how does one progress from the cluster phase to the bulk? Unlike the case of $Na^+(H_2O)_n$ clusters, the convergence of the structural and thermodynamic properties of the $Ln^{3+}(H_2O)_n$ cluster system requires a far greater number of solvent molecules (n ~ 128 molecules in contrast to 6.) This clearly indicates that the properties of the ion have a substantial effect on the size limits at which bulk-like properties can be produced in a cluster. This paper also illustrates another aspect of ion dependency, namely that the lighter lanthanide ions will converge towards a 9-coordinate first solvation shell structure, whereas those of the heavier lanthanides converge to an 8-coordinate structure. This is remarkable given the fact that the lanthanide ions studied in this paper have very similar properties. However, the key difference between them is their ability to polarize water. The heavier lanthanides do so more efficiently by virtue of their smaller charge:size ratios, resulting in shorter ion-water bonds. This creates greater solvent-solvent repulsions, which ultimately govern the solvation properties.

In the following paper, we will complete this study with regards to the remaining ions.

CHAPTER 4

A Theoretical Study of the Hydration of Trivalent Lanthanide Ions Across the Series

Sean R. Hughes, John A. Capobianco and Gilles H. Peslherbe
Centre for Research in Molecular Modeling (CERMM)
And Department of Chemistry & Biochemistry
Concordia University
7141 Sherbrooke St. West
Montréal, Québec, Canada, H4B 1R6

Last Revised: August 2006
To be submitted to Can. J. Chem.

ABSTRACT

Model potentials have been developed for simulating the structural and thermodynamic properties of lanthanide ions (Ln^{3+}) in aqueous environments. The model potentials were parameterized based on the properties of small $Ln^{3+}(H_2O)$ complexes that were obtained from high-level quantum chemistry calculations. The results obtained from Monte Carlo simulations with these potentials clearly show that the lanthanide ions adopt a well-defined interior solvation shell structure, with first-shell coordination numbers that depend on clusters up to size 36, where they begin to reach bulk-limit values. Total cluster enthalpies also approach the experimental bulk heats of hydration around cluster size 36, but reduced cluster enthalpies only slowly converge to the experimental heat of vaporization of water, a feature consistent with the significant long-range interactions between the trivalent lanthanide ions and the surrounding water molecules. This work suggests that $Ln^{3+}(H_2O)_n$ complexes may serve as an adequate model for investigating the microsolvation of Ln^{3+} ions in hydrated environments.

Keywords: Cluster ions; Lanthanide; Model Potentials; Coordination Structure; Thermodynamics; Monte Carlo Simulations

---

4.1. INTRODUCTION

Although it has been the subject of extensive research over the last two decades, the production of stable, multiply-charged, solvated metal ion clusters still poses many experimental challenges [12-14, 18, 21-24, 28, 29, 33, 34, 37, 90]. For instance, numerous difficulties are reportedly associated with forming trivalent lanthanide metal ion-solvent clusters using various laser vaporization or electrospray/mass spectrometry techniques [18, 21-24, 33, 90]. A limited number of studies have been devoted to the hydration of lanthanide ions in clusters since these are prone to dissociative electron or proton transfer processes that hinder the metal ion's ability to maintain its overall 3+ charge at small cluster sizes [33, 92]. This remains an intriguing problem, given that the third ionization potentials of La and Ce, are lower than the second ionization potential of Cu, which is known to form stable, divalent metal ion-water clusters, $Cu^{2+}(H_2O)_n$ [18, 21-24, 37]. In contrast, it was shown that the 3+ state of lanthanide metal ions can be preserved in clusters of aprotic solvents, such as acetonitrile, acetone, dimethyl formamide and DMSO [14, 18, 21, 23, 24, 33, 90]. Interestingly, Walker *et al.* were able to detect stable $Ho^{3+}(CH_3CN)_6$ and $Ho^{3+}(C_3H_6O)_6$ clusters, suggesting a preferred cluster size for microsolvated lanthanide ions that presumably corresponds to the completion of a first coordination shell [33]. However, this has recently been refuted based on recent work by Shvartsburg [23].

The properties of the lanthanides are rather unique compared to those of other metals, in particular transition metals. First, they form predominantly electrostatic bonds with their ligands, in sharp contrast to several non-d^0 block transition metals [52, 70, 193, 194], as a result of shielding by the more diffuse *p*- and *s*-orbitals which impede ligands

from interacting with the valence 4*f*-orbitals. The lanthanide ions are used ubiquitously for probing the structure of solid-state materials and proteins because of their flexible coordination chemistry. They bind as many as 6 to 10 ligands, but it is widely accepted that their first-shell coordination numbers are closer to 9 for the lighter lanthanide ions and 8 for the heavier ions in water [56, 58-62, 175, 179, 195-197]. This trend in the lanthanide ion first-shell coordination numbers follows an 'S-shaped' dependence, with the average coordination numbers of the mid-series lanthanides is intermediate between 8 and 9 ligands. This phenomenon is a direct consequence of the gradual reduction of the lanthanide ion size across the series.

Several model potentials have been previously developed with the purpose of simulating lanthanide ions in solution. The model of Meier *et al.* is capable of reproducing the experimental coordination number of La^{3+} in water at different salt concentrations, but no analogous model potentials were developed for the remaining lanthanide ions [172]. Helm *et al.* developed polarizable model potentials for the purpose of determining solvent exchange rates and the average first-shell coordination numbers in $LnCl_3$ solutions, but these models fell short of accurately predicting bulk, experimental hydration enthalpies [177, 178, 180, 181, 198]. Chaussedent and Monteil developed model potentials to investigate the hydration of Eu^{3+} and the influence of the resulting coordination sphere on the ion's electronic spectra, but again this work did not extend beyond Eu^{3+} [199, 200]. van Veggel and Reinhoudt also proposed model potentials that accurately predict the free energy of hydration of Ln^{3+} in salt solutions, but both the first-shell coordination numbers and the Ln^{3+}-O distances were consistently overestimated with respect to experimental values [201]. Floris *et al.* developed 'ab initio effective pair

potentials' based on quantum chemistry calculations of small $Ln^{3+}(H_2O)_n$ clusters embedded in a polarizable continuum model, but these models failed to account for the first-shell coordination numbers of the late lanthanide ions, namely Yb^{3+} [173]. Finally, Derepas *et al.* developed a model for $La^{3+}(H_2O)_n$ cluster simulations, which revealed the preferential formation of 7+1 and 7+2 coordination structures, as opposed to purely 8 or 9 coordinated species, for cluster sizes n = 1-9, but again, other lanthanide ions were not considered [108].

Our goal is to develop model potentials for simulating lanthanide ions in aqueous environments across the lanthanide series. We recently simulated via Monte Carlo simulations the structural and thermodynamic properties of trivalent lanthanide ion-water clusters, $Ln^{3+}(H_2O)_n$, using newly-derived polarizable model potentials parameterized to high-level quantum chemistry calculations for small clusters [118]. In this work, we extend our investigation to the remaining lanthanide ions. The model potentials were developed using the methodology described earlier [118] and are employed in room-temperature Monte Carlo simulations to evaluate the structural and thermodynamic features of large clusters (n = 1-128). The outline of this article is as follows. In section 4.2, we will briefly discuss the features of our model potentials, the results of the quantum chemistry calculations used to parameterize these models and the details of our Monte Carlo simulation procedure. We will then present the results of these simulations focusing on the structural and thermodynamic properties of the clusters in section 4.3. A summary and concluding remarks follow in Section 4.4.

4.2. COMPUTATIONAL PROCEDURE

4.2.1. Model Potentials

The model potential [118, 129] used to describe lanthanide ion-water and water-water interactions is a sum of Coulombic, polarization and repulsion-dispersion terms:

$$U = U_{Coulomb} + U_{Polarization} + U_{Repulsion-dispersion}. \qquad 4.2.1.1.$$

The Coulombic energy simply reflects the interactions between permanent point charges:

$$U_{Coulomb} = \sum_{i,j} \frac{q_i q_j}{r_{ij}}, \qquad 4.2.1.2.$$

where i and j represent different interaction sites separated by a distance r_{ij}, and the q's are site permanent point charges. The polarization energy is expressed as

$$U_{Polarization} = -\tfrac{1}{2}\sum_{i} \vec{E}_i^{\,o}\vec{\mu}_i, \qquad 4.2.1.3.$$

where E_j^o is the electric field at site i arising from the surrounding set of permanent charges:

$$\vec{E}_i^{\,o} = \sum_{j} \frac{q_j \cdot \vec{r}_j}{\left|\vec{r}_i - \vec{r}_j\right|^3}, \qquad 4.2.1.4.$$

and the induced dipoles, μ_i, are evaluated as a linear response to the total electric field:

$$\vec{\mu}_i = \alpha_i \cdot \vec{E}_i = \alpha_i\left[\vec{E}_i^{\,o} + \sum_{i \neq j} T_{ij} \cdot \vec{\mu}_j\right], \qquad 4.2.1.5.$$

where α_i is the polarizability of site i and T_{ij} is the dipole tensor [185]. The set of linear equations in Eq. 4.2.1.5. is simply solved in matrix form using LU decomposition and back substitution [186, 187]. Finally, the repulsion-dispersion interactions are represented by a generalized 12-8-6 Lennard-Jones potential:

$$U_{Repulsion-Dispersion} = \sum_{i,j}\left[A_{ij}r_{ij}^{-12} + B_{ij}r_{ij}^{-8} - C_{ij}r_{ij}^{-6}\right]. \qquad 4.2.1.6.$$

where A_{ij}, B_{ij} and C_{ij} are adjustable parameters. This model potential accounts for the mutual polarization of the solvent molecules and the lanthanide ion.

The point charges and molecular polarizability of water are those of the optimized potential for cluster simulations (OPCS) water model [129]. In short, the OPCS water model employs the gas-phase geometry of water (r_{OH} = 0.9572 Å, $\angle_{HOH}$ = 104.52°) [188], and includes a set 2 positive charge and repulsion sites on the hydrogen atoms, 2 negative charge sites near the oxygen atom, and an induced dipole and repulsion-dispersion site on the oxygen atom. The water repulsion-dispersion parameters were fit to reproduce the water dimer geometry and binding energy [129]. The remaining parameters for the ion-water interactions were derived by fitting to properties of Ln^{3+}-H_2O complexes from quantum chemistry calculations, which are the object of the next section.

4.2.2. Quantum Chemistry Calculations of Ln^{3+}-complexes

Ground-state Ln^{3+}-H_2O complexes were characterized with quantum chemistry calculations using the Gaussian 98 program [148]. Minimum energy structures were optimized without symmetry constraints using second-order Møller-Plessett (MP2) perturbation theory [151]. The 6-31G+(2d,p) basis set [152] was employed for water while Stuttgart-Dresden-Bonn (SDD) large-core pseudopotentials and valence basis sets were used for lanthanide ions [153, 183, 202]. Binding energies were also calculated with the Quadratic Configuration Interaction method using single, double and linearized triple excitations [QCISD(T)] for MP2 optimized geometries [182]. All minimum energy structures were characterized by a vibrational frequency analysis and binding energies were corrected for zero-point energy and basis-set superposition error (BSSE) via the

Counterpoise method [155]. Atomic charges were evaluated with the electrostatic potential (ESP) method and served as the basis for calculating solvent dipole moments in clusters [157].

Listed in Table 4.2.2.1. are the structural and energetic features of the minimum energy structures obtained from our quantum chemistry calculations of Ln^{3+}-H_2O complexes [203]. The present lanthanide ion-water distances and binding energies are within 0.01 Å and 3 kcal/mol, respectively, of results previously reported in the literature [106, 107, 116, 172, 173]. According to the MP2 calculations, the largest ion-oxygen distance is obtained for La^{3+}-H_2O (2.37 Å), while the shortest one is obtained for Lu^{3+}-H_2O (2.14 Å). This is not surprising since the ionic size decreases across the lanthanide series, resulting in smaller ion-oxygen distances in clusters. For similar reasons, the binary complex binding energy increases across the lanthanide series, as an increased charge:size ratio results in larger ligand polarization effects [136]. The binding energies range from 80.8 kcal/mol for La^{3+}-H_2O to 105.6 kcal/mol for Lu^{3+}-H_2O. These binding energies are comparable to those predicted for $[Mg(H_2O)]^{2+}$ and $[Y(H_2O)]^{3+}$ clusters, which involve metal ions with similar charge:size ratios to the trivalent lanthanide ions [111, 117, 122]. The increase of polarization effects across the lanthanide series is obvious from the dipole moments of water in the Ln^{3+}-complexes listed in Table 4.2.2.1., which increase with charge:size ratio from La^{3+} to Lu^{3+}. The dipole moments induced by the ions on the water molecules are significant (~1.0-1.4 D), in keeping with the generally accepted idea that polarization accounts for nearly one third of the Ln^{3+}-H_2O binding energy [116]. The induced dipole moments are also substantially larger than those reported for complexes of water with other metal ions [109-111, 117]. These

Table 4.2.2.1. Structural, energetic and electronic properties of $Ln^{3+}(H_2O)$ complexes.[a]

Ion	Property	MP2	QCISD(T)	Model[e]	Ion	Property	MP2	QCISD(T)	Model[e]
La^{3+}	r_{Ln-O}[b]	2.37	-	2.50	Gd^{3+}	r_{Ln-O}[b]	2.23	-	2.38
	D_o[c]	79.6	80.8	80.8		D_o[c]	92.7	93.9	93.9
	μ_{H_2O}[d]	3.12	-	5.52		μ_{H_2O}[d]	3.31	-	6.04
Ce^{3+}	r_{Ln-O}[b]	2.34	-	2.48	Tb^{3+}	r_{Ln-O}[b]	2.22	-	2.36
	D_o[c]	81.7	82.9	82.9		D_o[c]	94.3	95.5	95.5
	μ_{H_2O}[d]	3.13	-	5.59		μ_{H_2O}[d]	3.34	-	6.12
Pr^{3+}	r_{Ln-O}[b]	2.32	-	2.47	Ho^{3+}	r_{Ln-O}[b]	2.19	-	2.34
	D_o[c]	83.7	84.9	84.9		D_o[c]	97.8	98.9	98.9
	μ_{H_2O}[d]	3.21	-	5.66		μ_{H_2O}[d]	3.39	-	6.25
Nd^{3+}	r_{Ln-O}[b]	2.30	-	2.44	Er^{3+}	r_{Ln-O}[b]	2.17	-	2.33
	D_o[c]	85.7	86.9	86.9		D_o[c]	99.5	101.0	101.0
	μ_{H_2O}[d]	3.27	-	5.75		μ_{H_2O}[d]	3.43	-	6.23
Sm^{3+}	r_{Ln-O}[b]	2.27	-	2.40	Yb^{3+}	r_{Ln-O}[b]	2.15	-	2.32
	D_o[c]	89.1	90.2	90.2		D_o[c]	103.0	104.4	104.4
	μ_{H_2O}[d]	3.27	-	5.94		μ_{H_2O}[d]	3.52	-	6.50
Eu^{3+}	r_{Ln-O}[b]	2.26	-	2.39	Lu^{3+}	r_{Ln-O}[b]	2.14	-	2.30
	D_o[c]	90.7	90.5	90.7		D_o[c]	104.4	105.6	107.1
	μ_{H_2O}[d]	3.37	-	5.97		μ_{H_2O}[d]	3.47	-	6.42

[a] Quantum chemistry calculations are performed with the 6-31+G(2d,p)/SDD basis set as discussed in the text.
[b] Lanthanide ion-to-oxygen distance (Å).
[c] Binding energy (kcal/mol) corrected for zero-point energy and basis set superposition error.
[d] Dipole moment (D) of water, based on calculated ESP charges [157].
[e] Prediction of model potentials.

results clearly indicate that polarization must be accounted for in any model potential whose goal is to accurately describe Ln^{3+}-water interactions.

4.2.3. Parameterization of the Model Potentials

The parameters employed in the model potential are the point charges (q_i), the polarizabilities (α_i) and the repulsion-dispersion parameters (A_{ij}, B_{ij}, C_{ij}). These are available in Table 4.2.3.1. The lanthanide ions are characterized by a +3 charge and a polarizability of 2.8 $Å^3$, which lies around the upper limit of the reported polarizabilities of the Ln^{3+} ions [135, 204]. We assume this universal polarizability as this property only varies appreciably across the lanthanide series [La^{3+} (2.2 $Å^3$), Ce^{3+} (2.4 $Å^3$) and Yb^{3+} (1.6 $Å^3$)] [135, 204]. The repulsion-dispersion sites for the ion-solvent interactions were fit to reproduce the binary complex equilibrium ion-water distance, its binding energy and the dipole moment of the complexed water molecules reported in Table 4.2.2.1. This fitting was performed using a non-linear least-squares algorithm based on the Marquardt-Levenberg method [187].

Table 4.2.2.1. lists the energetic and structural properties of the Ln^{3+}-H_2O complexes predicted by the model potentials along with the quantum chemistry data. Binding energies of the complexes are well reproduced by the model potentials, with essentially no deviation from the QCISD(T) values except for the Lu^{3+}-H_2O complex, for which the model potentials predict a binding energy 2.6 kcal/mol lower than the QCISD(T) value, but still within the range of the accepted accuracy of quantum chemistry. The lanthanide ion-water distances predicted by the model potentials for Ln^{3+}-H_2O complexes differ from the MP2 values by, at most, 0.15 Å, which represents a maximum 6% error. The water dipole moments predicted by the model potentials

Table 4.2.3.1. Model potential parameters.

	A_{ij}[a]	B_{ij}[a]	C_{ij}[a]
La^{3+}-O	0	133 097	12 243
Ce^{3+}-O	0	130 537	12 363
Pr^{3+}-O	0	129 083	12 557
Nd^{3+}-O	0	113 405	13 878
Sm^{3+}-O	0	112 015	10 772
Eu^{3+}-O	0	110 247	10 561
Gd^{3+}-O	0	113 194	11 667
Ho^{3+}-O	0	110 205	11 418
Tb^{3+}-O	0	108 035	11 597
Er^{3+}-O	0	115 907	13 380
Yb^{3+}-O	0	101 958	11 310
Lu^{3+}-O	0	106 261	11 919
O-O[b]	1 152 921	0	1074
H-H[b,c]	10^5	5.5	-
	α[d]	q[e]	
Ln^{3+}	2.8	3.00	
O[b]	1.45	-0.569	
H[b]	-	0.569	
	$r_{O\text{-}M}$[f]	$\theta_{H2O\text{-}M}$[g]	
Water	0.342	43.4	

[a] Repulsion-dispersion parameters: A_{ij} (kcal·mol^{-1} Å^{-12}), B_{ij} (kcal·mol^{-1} Å^{-8}), C_{ij} (kcal·mol^{-1} Å^{-6}).
[b] From references [128, 129].
[c] Repulsion parameters between hydrogen atoms: the functional form of this interaction is a Born-Mayer term, $A_{ij}e^{-Bijr}$, with parameters A_{ij} (kcal/mol) and B_{ij} (Å^{-1})[128].
[d] Polarizability (Å^3).
[e] Permanent point charges in units of *e*.
[f] Distance between oxygen and its charge sites (Å).
[g] Angle defining the position of each oxygen charge site with respect to the molecular plane of water along the water bisector (°).

significantly overestimate the quantum chemistry estimates [205]. These deviations may be due to an overestimation of the solvent polarization energy arising from the neglect of solvent to metal ion charge transfer in the model potential, which in fact reduces the ion-charge by 10% according to quantum chemistry calculations [109, 117]. In any case, predictions of the model potential for the water dipole moment do not appear to be an issue for larger clusters, as was shown in our previous work [118].

Note that the minimum binding energies predicted by this current set of model potentials are a slight improvement over those predicted by the model potentials we designed previously for Nd^{3+}, Eu^{3+}, Er^{3+} and Yb^{3+} ion-water clusters [118]. As was previously reported, the minimum binding energy of $Eu^{3+}(H_2O)_8$ clusters predicted by reference Hartree-Fock (HF) calculations is approximately -449.1 kcal/mol, whereas the model potential used here predicts a binding energy of approximately -433.4 kcal/mol [118]. Factoring in the inaccuracy of the HF results versus what is obtained using QCISD(T) methods at smaller cluster sizes, we estimate that the cluster energies predicted by our model potentials are to within ~7% of those determined from quantum chemistry calculations, whereas our old model potentials predicted energies to within only 10%.

4.2.4. Monte Carlo Simulations

Monte Carlo simulations are used to investigate the thermodynamic and structural properties of $Ln^{3+}(H_2O)_n$ clusters (n = 1-128) at 300K. A random-walk approach is used to generate trial configurations, which involves the random translation of a water molecule in Cartesian space and rotations about its Euler angles. The Metropolis algorithm was used to accept or reject the new configuration [190]. No periodic

boundary conditions are imposed over the course of cluster simulations, but solvent evaporation is closely monitored. Solvent molecules found from 20 ($n \leq 64$) and 40 Å ($n = 128$) away from the ion were considered as evaporated from the cluster and any configuration containing evaporated solvent was excluded from the Markov chain used for further analysis. Periodic heating (up to 600K) and cooling steps were also implemented during the simulations so as to sample the configuration space as uniformly as possible. In general, each run entailed at least $1x10^7$ configurations for equilibration, followed by an equal number of steps for data collection. The maximum allowed displacements were set to 0.15 Å for translation and 15° for rotation in order to ensure acceptance ratios between 30% and 40%.

Cluster enthalpies were calculated from the average energy $<U>$ obtained from the canonical ensembles of configurations as:

$$\Delta H_n = \Delta U + \Delta(PV) = \langle U \rangle + nRT, \qquad 4.10.3.1.$$

Finally, the structural properties of the clusters were analyzed in terms of the radial probability distribution, $P(r)$, which is simply evaluated from the configurations as the probability of finding a water molecule (oxygen atom) at a distance r from the ion. The latter is normalized so that its integration yields a distance-dependent coordination number, $N_{coord}(r) = \int_o^r P(r')dr'$, which converges to the number, n, of solvent molecules in the cluster.

4.3. RESULTS AND DISCUSSION

4.3.1. Structural Data

Representative cluster structures obtained from room temperature Monte Carlo simulations are shown in Fig. 4.3.1.1. Lanthanide ions are clearly located near the center of the cluster and adopt an interior solvation shell structure, due to the strong lanthanide ion-water interactions that compensate for the disruption of the stable, hydrogen-bonded water network. The coordination shell structure is evidenced by sharp peaks located at ~2.6-2.7 Å in the probability distribution functions plotted in Fig. 4.3.1.2. (n = 64), which characterize the ion's first coordination shell. The probability distribution functions go to zero at approximately 3.0 Å, and the location of this minimum in *P(r)* is consistent with that observed in *g(r)* obtained experimentally for bulk solutions and in other simulations [58-60, 172, 173, 177, 178, 180, 197, 199, 200]. The peak located at ~5 Å is representative of a second coordination shell. The relative ordering of the water molecules beyond the first coordination shell reflects the long range nature of the ion-water interactions and the strong influence of the ion on the structure of the surrounding solvent. This feature contrasts, for instance, the arrangement of solvent molecules in $Na^+(H_2O)_n$ clusters, where there is no ordering evident in the second coordination shell [125].

The average first-shell coordination (Ln^{3+}-O) distances are listed in Table 4.3.1.1. as a function of cluster size. The first-shell ion-oxygen coordination distances increase slightly with cluster size, a feature that reflects both the increasing importance of solvent-solvent repulsions between the water molecules in the first coordination shell and the mutual attraction between first and second coordination shell water molecules. The latter

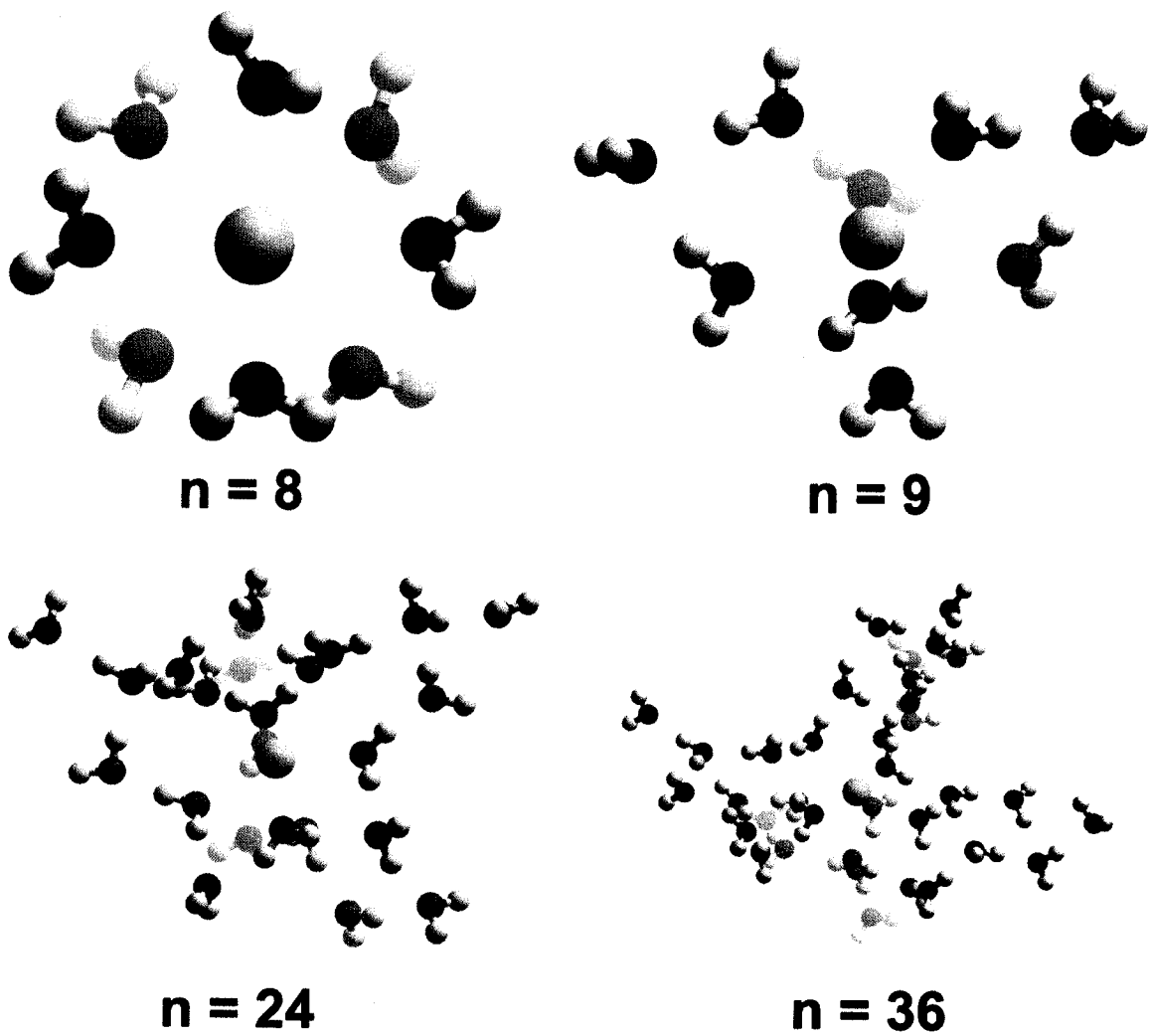

Figure 4.3.1.1. Representative $La^{3+}(H_2O)_n$ cluster structures obtained from room temperature Monte Carlo simulations using model potentials.

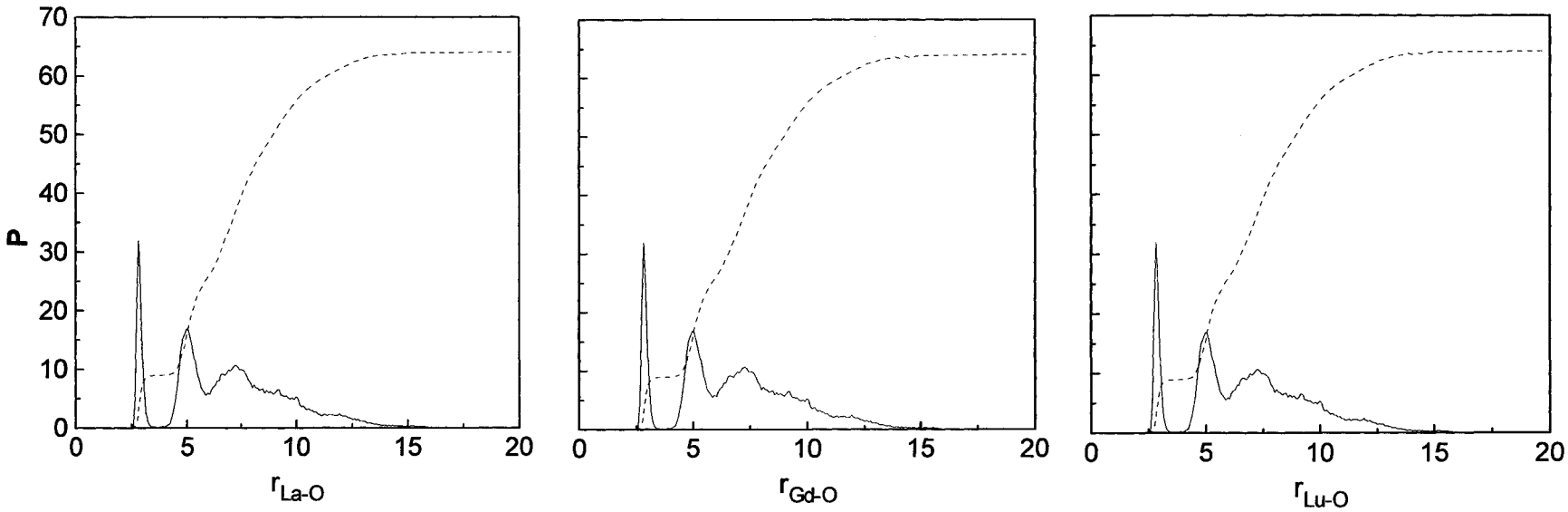

Figure 4.3.1.2. Radial probability distributions (–) of Ln^{3+}-O distances for select $Ln^{3+}(H_2O)_{64}$ clusters (Ln^{3+} = La^{3+}, Gd^{3+}, Lu^{3+}). Also shown is the distance-dependent coordination (- - -) obtained by integration of the radial probability distribution. The first-shell Ln^{3+}-O distances and coordination numbers are listed in Tables 4.3.1.1. and 4.3.1.2., respectively. All r_{Ln-O} distances in Å.

are quite favorable, given the large dipole moments induced on solvent molecules in the first coordination shell. The predicted cluster ion-oxygen distances overestimate bulk values by a consistent margin of ~0.30 Å, a feature that might be associated with the lack of counter-ions in this study, with the varying conditions under which the X-ray/neutron diffraction data were obtained, and with the parameterization of the model potential as discussed in Sect. 4.2. [56, 58-62, 175, 179, 196, 197].

Table 4.3.1.1. Average ion-water distance (Å) in the first coordination shell of $Ln^{3+}(H_2O)_n$[a].

n	24	36	64	128	Exp[b]
La^{3+}	2.80	2.86	2.83	2.83	2.58
Ce^{3+}	2.78	2.82	2.80	2.81	2.52
Pr^{3+}	2.79	2.77	2.77	2.80	2.54
Nd^{3+}	2.76	2.76	2.77	2.78	2.51
Sm^{3+}	2.73	2.75	2.74	2.74	2.47
Eu^{3+}	2.73	2.74	2.76	-	2.45
Gd^{3+}	2.71	2.71	2.73	2.72	2.37
Tb^{3+}	2.71	2.69	2.68	2.69	2.41
Ho^{3+}	2.68	2.67	2.67	2.70	-
Er^{3+}	2.67	2.68	2.71	2.69	2.37
Yb^{3+}	2.65	2.65	2.65	2.68	2.32
Lu^{3+}	2.64	2.65	2.65	2.68	2.34

[a] Average lanthanide ion-to-oxygen distance from Monte Carlo simulations (Å). The cut-off radius for the first coordination shell was determined from the probability distribution functions.
[b] Bulk solution data from ref. [56, 58-62, 175, 196, 197].

The simulated average first-shell coordination numbers are listed in Table 4.3.1.2. as a function of increasing cluster size. The first-shell coordination numbers are cluster-size dependent, as their values only converge towards those obtained in bulk solutions at very large cluster sizes, n > 36 [56, 58-62, 175, 179, 195-197]. This feature reflects the

fact that an extensive solvent network is required in order to reproduce bulk features. This sharply contrasts with what has been reported for other ion-solvent clusters, where it was shown that as few as 10 solvent molecules are necessary to obtain bulk-like hydration [40]. For example, bulk-like coordination numbers were obtained at much smaller cluster sizes, $n < 12$, in simulations of $Na^+(H_2O)_n$ and $Cs^+(H_2O)_n$ clusters, presumably due to the relatively smaller ion-water binding energies and the longer ion-water distances which cause a reduction of solvent-solvent repulsions within the first coordination shell [125, 128, 129].

Table 4.3.1.2. Average first-shell coordination numbers of $Ln^{3+}(H_2O)_n$.

n	24	36	64	128	Exp[a]
La^{3+}	8.1	8.6	8.9	9.0	9.1
Ce^{3+}	8.0	8.9	8.6	9.0	9.3
Pr^{3+}	8.4	8.3	8.4	9.0	9.2
Nd^{3+}	7.9	8.2	8.7	8.9	8.9
Sm^{3+}	8.0	8.4	8.3	8.9	8.8
Eu^{3+}	8.0	8.4	8.5	-	8.3
Gd^{3+}	8.0	8.3	8.4	8.4	8.0
Tb^{3+}	8.2	8.0	8.0	8.0	8.2
Ho^{3+}	8.0	8.0	8.1	8.0	-
Er^{3+}	8.0	8.2	8.2	8.2	8.2
Yb^{3+}	8.0	8.1	8.1	8.4	7.9
Lu^{3+}	8.0	8.2	8.2	8.2	8.0

[a] Bulk solution data from ref. [56, 58-62, 175, 196, 197].

As can be seen from Fig. 4.3.1.3., in the bulk limit (n = 128), the 'S-shaped' dependence of the first-shell hydration numbers for the lanthanide series is in excellent accord with experiment [56, 58-62, 175, 179, 195-197]. As evidenced from the integrated distribution functions in Fig. 4.3.1.2., the intermediate set of lanthanide ions

(Gd^{3+} to Tb^{3+}) possess bulk-limit equilibrium first-shell coordination numbers between 8 and 9 water molecules. Our simulations indicate that these clusters mainly adopt a purely 8- or 9-coordinate structure, given that *P(r)* is effectively zero between the peaks corresponding to the first and second coordination shells. This feature is in excellent agreement with the work of Helm *et al.* [177, 179-181, 198, 206, 207]. It should be noted, however, that at cluster size 128, the coordination number of Yb^{3+} is not well-reproduced by our model potentials.

Second shell coordination numbers for the lanthanides were also from the obtained probability distribution functions for each cluster size $n \geq 64$. The second coordination shell contains 17 water molecules for the La^{3+}-Sm^{3+} ions and 15 solvent molecules for the Tb^{3+}-Lu^{3+} series. Gd^{3+} appears to be the only ion with a second-shell coordination number of 16. Clearly, the second-shell coordination numbers are influenced by the size of the ion, as the heavier lanthanides have smaller first-shell coordination shells than the lighter ions. Overall, these values are in excellent agreement with the results of previous simulations and experimental studies on the hydration of Y^{3+}, an ion which possesses similar properties as for the lanthanide ions [173, 180, 208].

4.3.2. Thermodynamic Data

The cluster enthalpies obtained from our simulations are plotted in Fig. 4.3.2.1. as a function of cluster size. As expected on the basis of what was observed in the quantum chemistry calculations, the cluster enthalpies increase steadily across the lanthanide series. The cluster binding enthalpies of $Ln^{3+}(H_2O)_n$ clusters shown in Fig. 4.3.2.1.a are relatively large, compared to those reported for other ion-water clusters. For instance, $Na^{+}(H_2O)_{36}$ only has a cluster enthalpy on the order of -210 kcal/mol whereas the

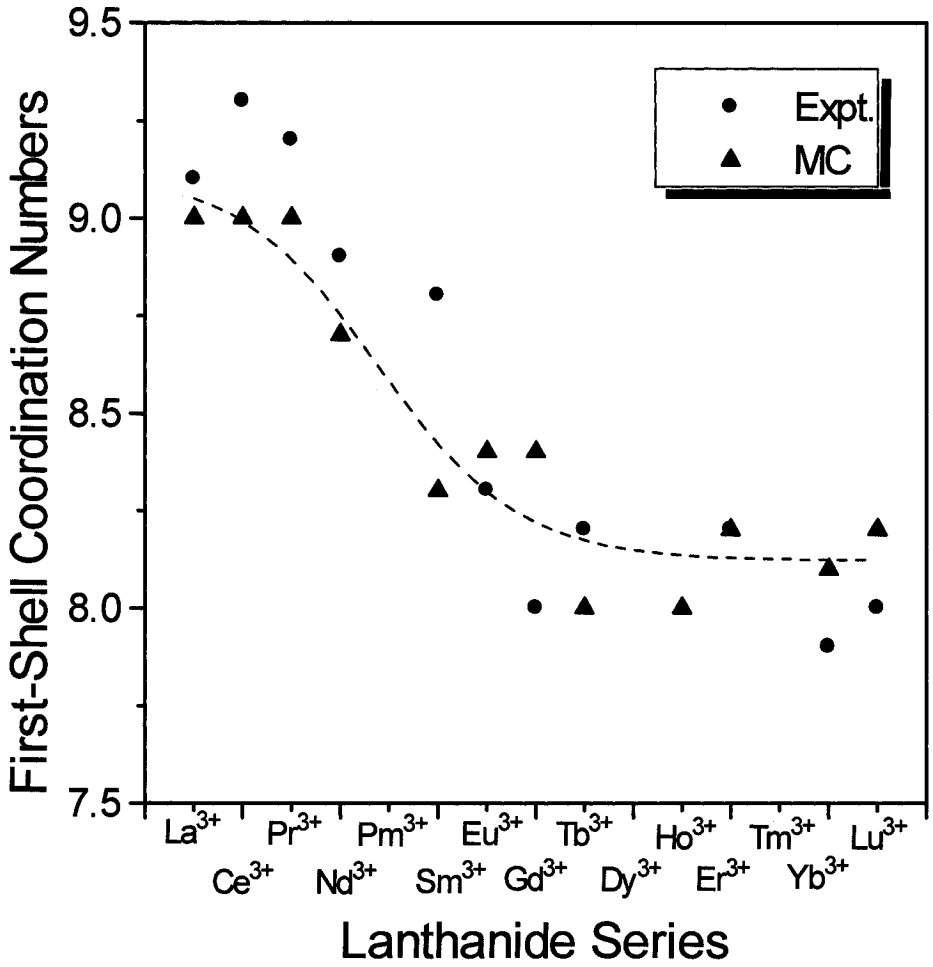

Figure 4.3.1.3. Average first-shell coordination numbers obtained from Monte Carlo simulations of $Ln^{3+}(H_2O)_{128}$ (▲) and those obtained from bulk solution data (●).

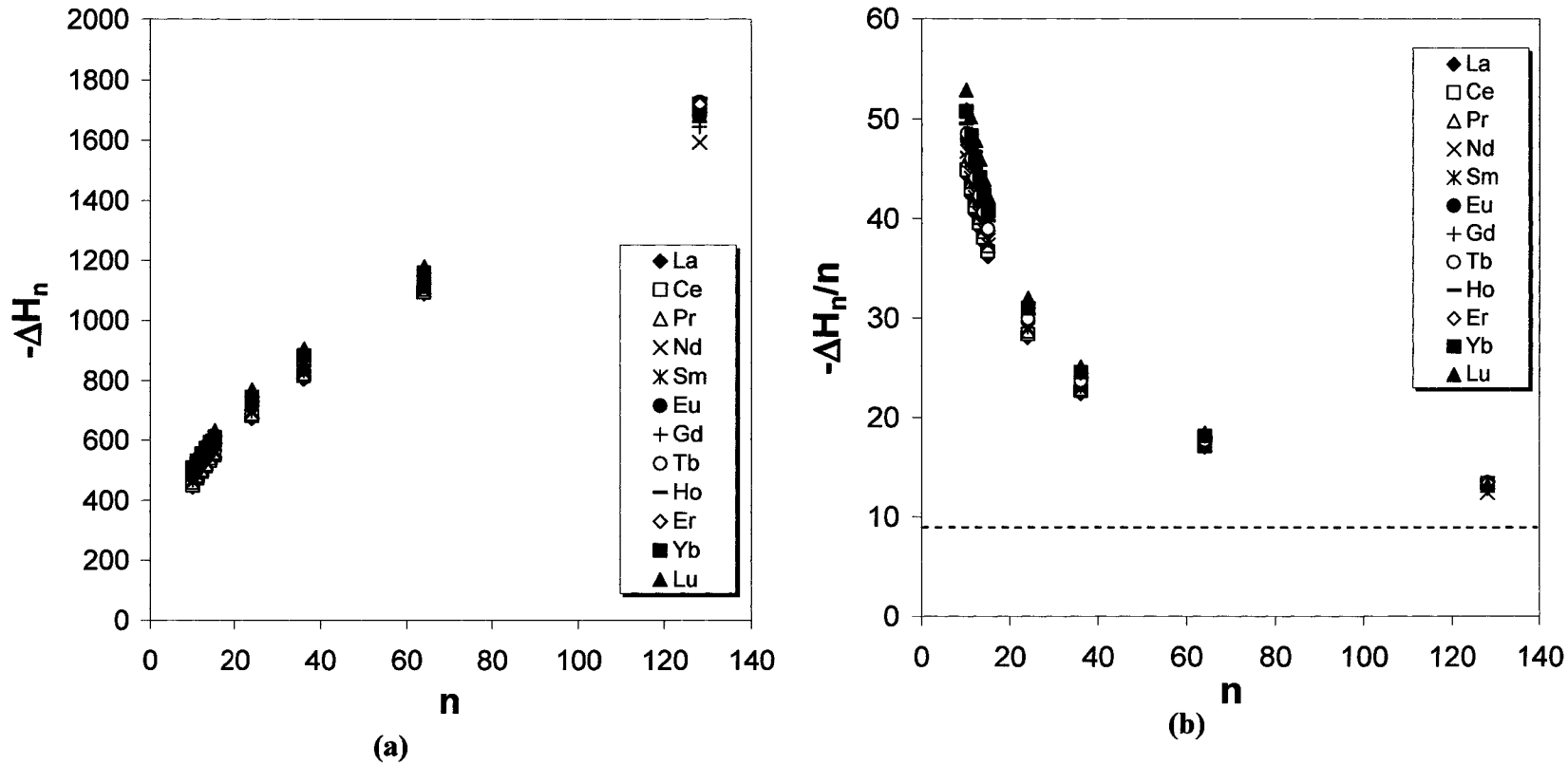

Figure 4.3.2.1. a) Cluster enthalpy and b) the reduced cluster enthalpy vs. cluster size for $Ln^{3+}(H_2O)_n$. The heat of vaporization of water (-9.7 kcal/mol) is indicated on the plot with a dashed line. All enthalpies are in kcal/mol.

$La^{3+}(H_2O)_{36}$ cluster has a cluster enthalpy of -804 kcal/mol [125]. These results clearly illustrate the high interaction energies associated with the lanthanide ion-water interactions.

The fact that the cluster enthalpy becomes increasingly dependent with cluster size on solvent-solvent interactions as opposed to metal-ion solvent interactions can be inferred from Fig. 4.3.2.1.b where the reduced binding enthalpy, the cluster enthalpy per solvent molecule $\Delta H_n/n$, is plotted as a function of cluster size. It can be clearly seen that the reduced binding enthalpy decreases exponentially with increasing cluster size. The reduced binding enthalpies of $Ln^{3+}(H_2O)_n$ clusters, ~13 kcal/mol at n = 128, approach the heat of vaporization of bulk water of -9.7 kcal/mol. This constitutes a deviation of approximately 30%, implying that the cluster has yet to reach the bulk limit at n = 128. The fact that the convergence is slow with cluster size unlike in the case of $Na^+(H_2O)_n$ clusters, is again indicative of the long-range interactions between the lanthanide ion and the solvent molecules [125].

4.4. CONCLUSIONS

We have investigated and characterized the structural and thermodynamic properties of $Ln^{3+}(H_2O)_n$ clusters through the lanthanide series using room-temperature Monte Carlo simulations, as an extension of previous work on Nd^{3+}, Eu^{3+}, Er^{3+} and Yb^{3+}-water clusters [118]. With the exception of the Th^{3+}, Dy^{3+} and the radioactive Pm^{3+} ions, we have now developed model potentials for nearly the entire lanthanide series. These model potentials have proven to yield precise, and in most cases accurate structural and energetic properties with respect to either the quantum chemistry calculations reported here or to available, experimental results. For instance, the trends in lanthanide ion-

oxygen distances obtained in X-ray and neutron diffraction studies of bulk solutions are fairly reproduced, with any errors in these distances being systematic across the entire set of lanthanides studied (an error of 0.30 Å) [56, 58-62, 175, 196, 197]. The first and second-shell coordination numbers were also in agreement with those obtained from both X-ray/neutron diffraction studies and those reported from other simulations [56, 58-62, 175, 196, 197]. Of particular interest is the fact that simulations with our model potentials reproduce the S-shaped trend in coordination numbers across the lanthanide series, namely that the early Ln^{3+} ions (La^{3+}-Pr^{3+}) are surrounded by ~9 water molecules, the later set of ions (Ho^{3+}-Lu^{3+}) by 8 water molecules, and the intermediate ions (Sm^{3+}-Tb^{3+}) tend to have coordination numbers that reflect the relative distribution of 8 or 9-coordinated species in the course of the simulations. Furthermore, the coordination numbers obtained for smaller cluster sizes were in agreement with those obtained in other simulations and were quite similar to the stable cluster sizes observed experimentally for other lanthanide ion-solvent clusters [33, 108, 118].

In addition to our investigation of the structural properties of these clusters, we had also focused our attention on determining the thermodynamic properties of the $Ln^{3+}(H_2O)_n$ clusters. The appropriate trends in cluster enthalpies, namely that water molecules are less tightly bound to that the lighter lanthanide ions than to the heavier ones, were obtained in our simulations and the results were in keeping with the range of energies established from previous quantum chemistry calculations and previous simulations of liquid systems [106-108, 112, 116-118, 122]. The cluster binding enthalpies greatly depend on ion-solvent interactions for small cluster sizes ($n < 24$), whereas the cluster enthalpy is mainly governed by solvent-solvent interactions at larger

sizes. The latter was reflected by the manner in which the total cluster enthalpies increased linearly for $n \geq 36$, and by the convergence of the reduced binding enthalpies towards the heat of vaporization of bulk water at $n = 64$ and 128.

Previous simulations of monovalent metal ion-water clusters using similar model potentials and the same simulation procedure yielded stepwise binding energies in excellent agreement with experimental data [123, 125, 128, 129]. Although no experimental data is available regarding the thermodynamics of the clusters studied in this paper, we estimate that the cluster binding enthalpies reported here are probably accurate to within 7%, which is a marked improvement over the predictions of our previously published model potentials [91, 103, 118, 209].

As detailed in the introduction, much of the experimental issues hindering the study of $Ln^{3+}(H_2O)_n$ clusters include solvent-to-ion electron transfer and deprotonation of the cluster. A systematic study of these processes is underway for relatively small cluster sizes. Furthermore, our studies of the microsolvation of lanthanide ions is currently being extended to other solvents, such as in acetonitrile, for which stable 3+ clusters have been observed experimentally [23, 24, 33, 90].

AUTHOR'S NOTES AND SIGNIFICANCE OF PAPER TO THESIS

Prior to publication of the work in Chapter 3, it was strongly suggested by one reviewer that it is not possible to form $Ln^{3+}(H_2O)_n$ clusters experimentally. Given that our simulations seemed to imply that the formation of these clusters was quite favourable, it was clear that a more thorough investigation into the stability of these clusters was warranted. As our model potentials are not amenable to such a study, we chose to use quantum chemical calculations as a means of probing cluster reduction in $Ln^{3+}(H_2O)_n$.

As will be described in the following chapter, cluster reduction can occur via 3 different mechanisms, 1) proton transfer, 2) electron transfer and 3) heterolytic cleavage. We have decided to focus on the most likely of these pathways, namely the proton transfer mechanisms.

CHAPTER 5

Are Trivalent Europium-Water Clusters Stable Species? A Theoretical Study of the Deprotonation of $Eu^{3+}(H_2O)_n$ Clusters

Sean R. Hughes, John A. Capobianco and Gilles H. Peslherbe*
Centre for Research in Molecular Modeling (CERMM)
And Department of Chemistry & Biochemistry
Concordia University
7141 Sherbrooke St. West
Montréal, Québec, Canada, H4B 1R6

Last Revised: August 2006
To be submitted to JACS.

ABSTRACT

The difficulties associated with producing stable, multiply-charged, solvated metal ion clusters using traditional spray techniques have been well documented in the literature. Of particular note have been issues pertaining to conserving the 3+ state of clusters containing trivalent lanthanide metal ions and protic solvents, such as $Ln^{3+}(H_2O)_n$ even though the third ionization potentials of several lanthanide metals are lower than the second ionization potential of Cu, which is known to form stable divalent metal ion-water clusters, $Cu^{2+}(H_2O)_n$. We present a preliminary study of deprotonation mechanisms in $Eu^{3+}(H_2O)_n$ clusters as a tentative explanation for the shortcomings associated with these experiments. Our results indicate that the parent clusters (PC) are more stable than the resultant deprotonated clusters (DC) for cluster sizes ≥ 3 and that this relative stability increases with cluster size. However, the predicted dissociation energies reveal that the deprotonation of the cluster is highly exothermic (-50 to -150 kcal/mol) even for relatively large cluster sizes. Our calculations reveal that the most likely pathway for cluster deprotonation for sizes $n < 6$ is via the ejection of an H_3O^+ ion from the cluster, while pathways producing solvated H_3O^+ ions appear to be the most likely candidates for

cluster dissociation at larger sizes. The reaction paths and transition states associated with the dissociation and deprotonation of clusters have been characterized. Clusters smaller than n = 6 dissociate via a one step mechanism whereas clusters of size n = 6-8 dissociate via a two step mechanism involving migration of a water molecule from the first to the second coordination shell, followed by hydrolysis of another inner-sphere water molecule. The barrier heights associated with these dissociation processes are at least 25 kcal/mol lower in energy than the barriers associated with simple ligand loss from the cluster. These results would imply that $Eu^{3+}(H_2O)_n$ clusters with $n < 9$ cannot be isolated under conventional spray conditions.

Keywords: Cluster ions, lanthanide, deprotonation, europium, water

---

5.1. INTRODUCTION

Despite sustained efforts, experimentalists have encountered varying success in creating and detecting multiply-charged, solvated metal ion clusters [12-14, 19, 21-24, 28, 29, 31, 33, 34, 37, 90]. Of particular interest are the issues associated with the formation and detection of stable clusters containing trivalent lanthanide metal ions in protic solvents using various combined laser or electrospray/mass spectrometry based techniques [14, 19, 24, 33, 90]. These problems are likely due to dissociative (1) electron or (2) proton transfer processes that hinder the cluster's ability to maintain the 3+ condition [14, 19, 24, 33, 90, 103, 209]. The mechanisms associated with these processes are as follows:

$$M^{3+}L_n \rightarrow M^{2+}L_{n-1} + L^+, \quad (1)$$

$$M^{3+}(LH)_n \rightarrow M^{2+}L(LH)_{n-2} + LH_2^+, \quad (2)$$

where L is the solvent, or donor, ligand and M is the complexed metal ion. In general, clusters of the form $M^{2+}X(LH)_n$ (where X is a counter ion) or $M^{2+}L(LH)_n$ can be formed quite readily using conventional electrospray/pick-up techniques, however, most clusters of the form $M^{3+}(HOR)_n$ cannot be detected even following 'mild' spray conditions [14]. This presents a quandary to experimentalists since the third ionization potentials of most lanthanide metals are similar, if not lower than the second ionization potential of Cu, which has been shown to form stable $Cu^{2+}(H_2O)_n$ clusters [12, 13, 37].

Recently, it has been reported that stable $Ln^{3+}(H_2O)_n$ clusters can only be formed in large clusters when the metal ion is either La^{3+}, Ce^{3+} or Eu^{3+} [92]. At smaller sizes, only products associated with the aforementioned proton or electron transfer processes are observed. Apart from water, only diacetone alcohol appears to form stable 3+

clusters with lanthanide ions [22]. In contrast, it has been shown that the 3+ state of the lanthanide-solvent cluster can be conserved when the solvent is aprotic, for example in clusters containing acetonitrile, acetone, dimethyl formamide and DMSO [14, 21, 23, 24, 90]. The minimum cluster sizes required to maintain this 3+ state were n = 1-3 for acetonitrile clusters and n = 2-5 for DMSO clusters [21, 23]. In contrast, the minimum cluster sizes required to retain this state in diacetone alcohol ranged from 5-8 solvent molecules, and a minimum of 16 molecules were required to conserve this charge in water clusters, clearly showing that large cluster sizes are required to maintain 3+ clusters containing protic solvents [22, 92].

A previous quantum chemistry study by Beyer *et al.* revealed that the deprotonation of $M^{2+}(H_2O)_2$ clusters (M = Be, Mg, Ca, Sr, and Ba) potentially occurs via a salt-bridge mechanism [103]. This process begins with the migration of a first coordination shell solvent molecule in the parent cluster (PC) to the second solvation shell. A subsequent proton transfer to the second shell water from the nearest, first-shell, water (NW) molecule results in both the formation of H_3O^+ and the dissociated cluster (DC), both of which separate via Coulomb explosion. A total of two transition state structures were observed. The first, TS1, involves the displaced water (DW) lying in close proximity to the NW. This DW then proceeds to move completely into the second shell yielding the MIN2 local minimum energy structure. Finally, the formation of a salt-bridge due to the proton exchange defines the second transition state, TS2, which then gives rise to the deprotonated cluster products. It was shown that these deprotonation reactions can compete with single ligand loss (SLL) from the cluster as both processes are virtually isoenergetic. This is because the activation barriers for both TS1 and TS2

are quite low, depending on the nature of the complexed metal ion. In the aforementioned work, clusters containing metal ions with small charge:size ratios were found to be prone to SLL whereas those with high charge:size ratios preferentially underwent deprotonation. Later, studies by Vitorge and Masella revealed that Be^{2+} undergoes a similar hydrolysis mechanism at larger cluster sizes (n = 3-6) [209]. The calculated free energies of the deprotonated clusters were much larger than those obtained for the bulk counterparts.

This paper contains recent findings regarding the deprotonation of $Eu^{3+}(H_2O)_n$ clusters. Specifically, we have characterized using quantum chemistry calculations the following pathways:

$$Eu^{3+}(H_2O)_n \rightarrow Eu^{2+}OH(H_2O)_{n-1} + H^+, \quad (3)$$

$$Eu^{3+}(H_2O)_n \rightarrow Eu^{2+}OH(H_2O)_{n-2} + H_3O^+, \quad (4)$$

$$Eu^{3+}(H_2O)_n \rightarrow Eu^{2+}OH(H_2O)_{n-3} + H_3O^+H_2O, \quad (5)$$

$$Eu^{3+}(H_2O)_n \rightarrow Eu^{2+}OH(H_2O)_{n-4} + H_3O^+(H_2O)_2, \quad (6)$$

up to a parent cluster size of 8. Comparisons will be made between the relative stabilities of the parent cluster versus the deprotonated cluster. Furthermore, we will compare the exothermicity of the various deprotonation pathways and discuss their impact on the formation of trivalent lanthanide ion-water clusters. Finally, we will characterize both the activation barriers and transition state structures associated with pathway (4) and assess its competitiveness with single ligand loss.

5.2. METHODS

Quantum chemistry calculations were performed using the Gaussian98 program [148]. The Stuttgart-Dresden (SDD) effective core potential (ECP) and basis set were

used for europium and the 6-31+G(2d,p) basis set was used to represent all other atoms [152, 153, 183, 202]. The level of theory chosen for this study was the hybrid G96PL density functional theory method as it appeared to best reproduce the cluster binding energies obtained from high-level MP2/6-31+G(2d,p)/SDD // QCISD(T)/6-31+G(2d,p)/SDD calculations reported previously [118, 182, 210, 211].

The performance of our model chemistry with respect to other DFT calculations with the same basis sets and ECP can be compared in Table 5.2.1. As can be clearly seen, the model chemistry employing the G96PL hybrid functional outperforms the other DFT calculations in terms of CPU time used and the resultant, calculated binding energies are in fair agreement with those reported from our previous QCISD(T) calculations [118, 182, 210, 211]. However, we do acknowledge they overestimate the QCISD(T) binding energies by ~7%.

All cluster optimizations were done using no symmetry constraints and transition state calculations were done using the Opt=TS keyword in Gaussian98. Both the transition state and minimum energy structures were characterized using a frequency analysis and the various energies were corrected for zero-point energy contributions.

Finally, atomic point charge analyses were done for each configuration using ElectroStatic Potential (ESP) derived charges [157]. These were calculated using the aforementioned model chemistry with the Gaussian98 program.

5.3. RESULTS AND DISCUSSION

5.3.1. Structures

Figure 5.3.1.1. depicts the minimum energy structures associated with the PCs, $Eu^{3+}(H_2O)_n$, obtained from our quantum chemistry calculations. The Ln^{3+}-O distances

Table 5.2.1. Energetic Properties of $Ln^{3+}(H_2O)$.

Level of Theory[a]	D_o[b]	Time[c]
QCISD(T)	90.5	04:22.2
G96PL	97.3	00:52.0
G96VWN5	97.3	00:52.8
G96VWN	97.7	01:05.7
BHandLYP	99.6	00:58.9
mPWP81	100.7	01:35.7
mPWVWN5	100.7	01:09.2
mPWVWN	101.1	00:54.2
G96PW91	101.7	01:33.0
B3PW91	101.8	01:38.4
G96LYP	102.1	01:48.8
mPW1PW91	102.2	00:54.6
PW91P81	102.3	01:12.8
PW91VWN5	102.3	00:59.2
PW91VWN	102.7	01:08.2
BPW91	103.7	01:28.5
B3LYP	103.7	01:30.5
mPWPW91	105.1	00:57.8
mPWLYP	105.5	00:59.3
PBE1PBE	105.5	00:59.0
PBEPBE	106.3	00:54.8
PW91PW91	106.8	00:55.3
PW91LYP	107.1	00:51.0
PW91P86	108.1	00:52.3

[a] Quantum chemistry calculations are performed with the 6-31+G(2d,p)/SDD basis set as discussed in the text.
[b] Binding energies (kcal/mol).
[c] CPU times were based on single point calculations using the aforementioned model chemistries. These calculations were run on a computer equipped with a Pentium III 1.2 GHz processor and 1 GB of RAM.

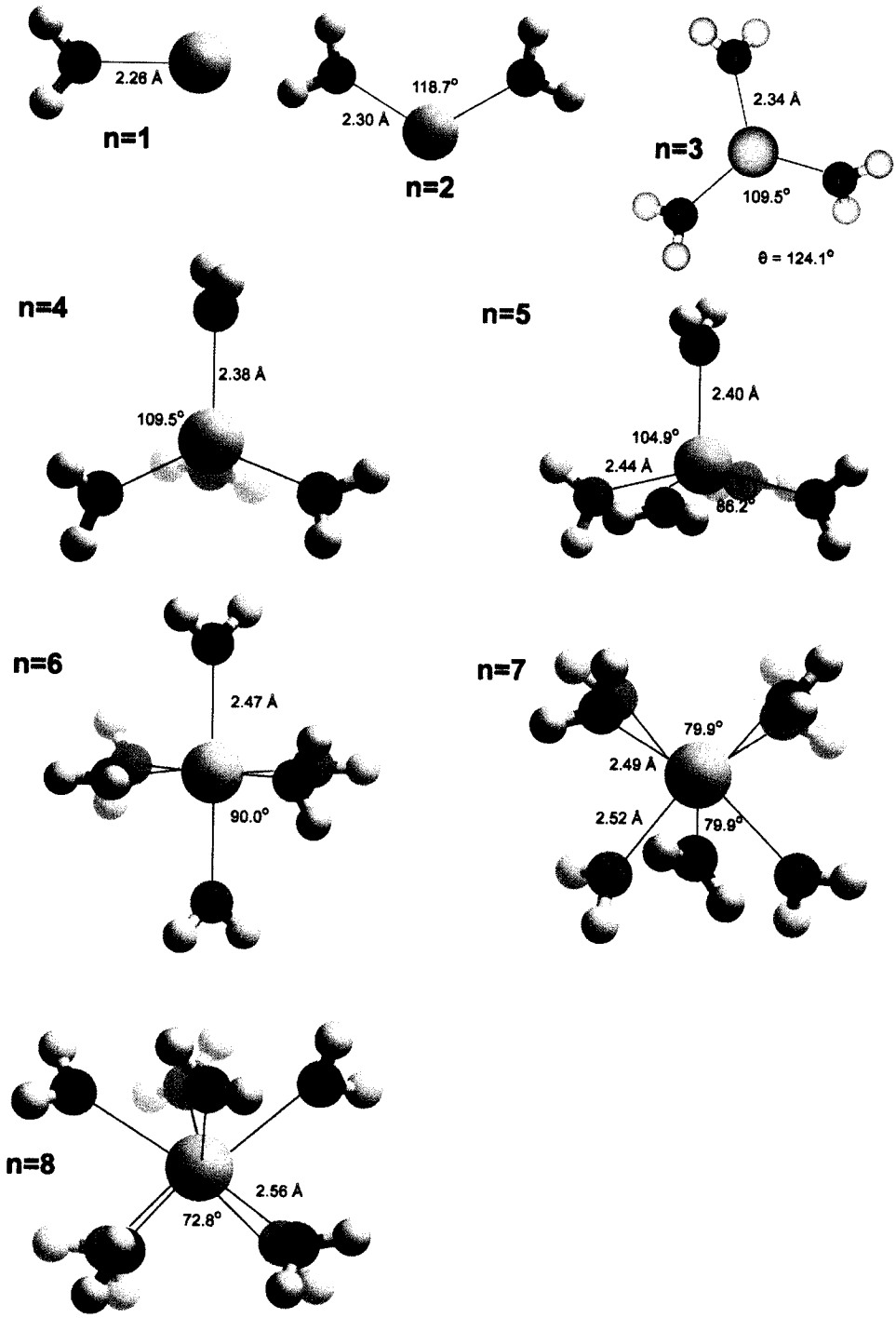

Figure 5.3.1.1. Minimum energy structures associated with the parent clusters (PC), $Eu^{3+}(H_2O)_n$.

increase with increasing cluster size, as would be expected based on the increased shielding of the Eu^{3+} ion by the surrounding solvent. The bent structure of the cluster at n = 2 is due to a mutual polarization on the same side of the lanthanide ion by both ligands [109-112, 117, 122, 168]. This complex has a C_2-like symmetry such that the water molecules are tilted out of the plane defined by the O-Eu-O bond angle. This configuration is not uncommon and has been described in calculations of other large metal ion-solvent clusters [109-112, 117, 122, 168]. At n = 3, the coordinating solvent molecules form a trigonal pyramid. This structure has been observed as the minimum energy structure in other calculations of similar clusters containing heavy metal ions such as Cs^+ and Rb^+ [108, 212]. At this size, the energy gain due to the mutual polarization of the Eu^{3+} ion by all three water molecules favors the trigonal pyramidal arrangement of the ligands as opposed to the more common trigonal planar structure. Attempts to optimize the latter using our simulation procedure resulted in convergence to the trigonal pyramidal structure. At n = 4, the tetrahedral symmetry was found to be favored over a square-based pyramidal arrangement (where the Eu^{3+} ion is capping). This is favored since the solvent-solvent repulsions outweigh the benefits from mutual polarization of the Eu^{3+} ion at the same end. However, these repulsions are lessened at n = 5 due to the longer Eu-O bond lengths (~0.06 Å longer), and so a square-based pyramidal symmetry is obtained. It should be noted that the capping water molecule at n =5 is located closer to the metal ion at a distance of 2.40 Å, whereas the remaining ligands are located 2.44 Å away. Similar minimum energy structures have been reported for $Mg^{2+}(H_2O)_5$ and $Ba^{2+}(H_2O)_5$ clusters [105, 111, 121]. At cluster size n = 6, an octahedral symmetry is favored by the cluster resulting in equidistant Eu-O bonds [213, 214]. The cluster

symmetry obtained at n = 7 is that of a distorted capped trigonal prism, with the capping water molecule located 2.54 Å from the Eu^{3+} ion and the remaining ligands located approximately 2.50 Å away [121, 126]. Such a structure has been observed in $Ca^{2+}(H_2O)_7$ clusters, and it is well documented that the Ca^{2+} ion shares similar trends in coordination to the europium ion [64, 121, 126]. At n = 8, the square antiprism symmetry around the Eu^{3+} ion is adopted by the cluster. This symmetry is preferred by most octa-coordinated trivalent lanthanide metal ions in solution and such a symmetry has also been reported for $Ca^{2+}(H_2O)_8$ clusters [58-62, 106, 107, 121, 126].

Similar geometries to the PCs were obtained for the DCs, $Eu^{2+}OH(H_2O)_{n-1}$, as shown in Figure 5.3.1.2. for sizes n = 1-8. The OH^- ligand generated by cluster deprotonation binds far closer to the Eu^{3+} ion than do the water molecules. For example, at n = 1 the Eu-OH bond distance is 1.95 Å whereas the Eu-water bond is far longer at 2.38 Å. For the most part, the symmetries adopted by the DCs closely resemble those of the PCs with only slight differences in the positions of the ligands. For instance, the O-Eu-OH bond angles are smaller than the O-Eu-O angles found in the PC at most cluster sizes. For instance, at n = 4, the HO-Eu-O bond angle is 112.5° whereas the O-Eu-O bond angle is 109.5° in the corresponding PC. This is not surprising given that the hydroxide-water repulsions are far weaker than the water-water repulsions. Only two exceptions to these trends are apparent in our calculations: at n = 6 and 7, the DCs fully retain their parent octahedral and distorted trigonal prismatic symmetries.

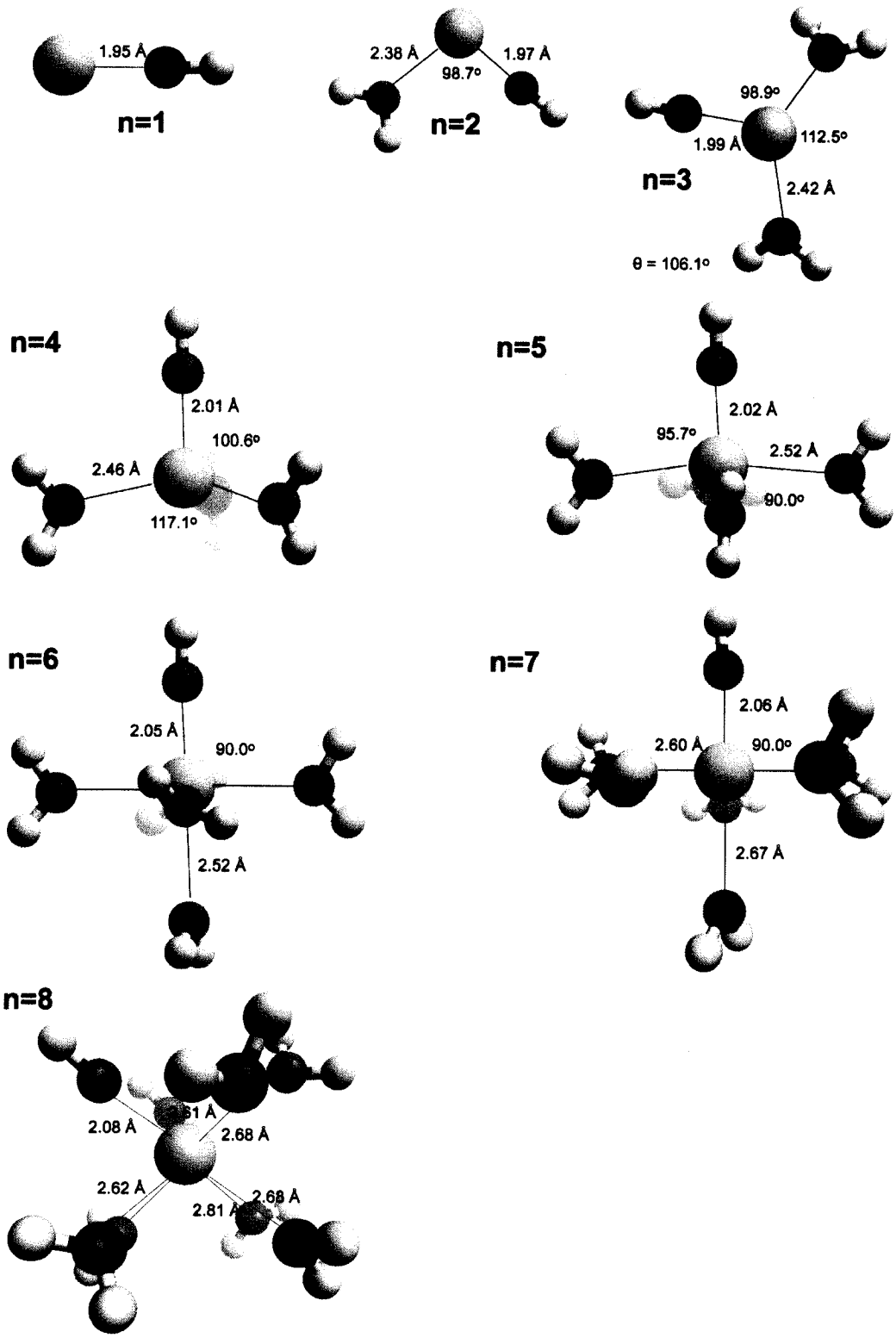

Figure 5.3.1.2. Minimum energy structures associated with the dissociated clusters (DC), $Eu^{2+}OH(H_2O)_{n-1}$.

5.3.2. Energetics

Figure 5.3.2.1. contains plots of the total cluster energies and the stepwise binding energies of the PC as a function of increasing cluster size. The cluster binding energies were determined to be:

$$\Delta D_n = D_o^{PC} - D_o^{Eu^{3+}} - nD_o^{H_2O} \tag{7}$$

where D_o represents the various zero-point corrected energies for the superscripted structure. The stepwise binding energies are calculated to be:

$$\Delta D_{n,n-1} = D_n - D_{n-1}\,. \tag{8}$$

It should be noted that the reverse process of Eq. (8) yields the dissociation energies associated with single ligand loss (SLL) from the cluster.

The PC cluster binding energies are very large. For example, the cluster binding energy at n = 6 is approximately -387 kcal/mol, which is much lower than the binding energy associated with $Ca^{2+}(H_2O)_6$ (-235 kcal/mol) and $Mg^{2+}(H_2O)_6$ (-305 kcal/mol) clusters [111, 121, 126]. Consequently, the PC stepwise binding energies are also quite high. For instance, the first stepwise binding energy is -97 kcal/mol, which is somewhat comparable in magnitude to the first stepwise binding energies for $Mg^{2+}(H_2O)_n$ and $Y^{3+}(H_2O)_n$ complexes (-75 and -110 kcal/mol respectively) [111, 117, 122]. Even at large cluster sizes the stepwise binding energies are quite high, with values of -20 kcal/mol for cluster sizes 6-8. These energies would suggest that the formation of trivalent lanthanide ion-water clusters appears to be highly exothermic. However, these clusters do not form experimentally and thus a competing process leading to cluster dissociation must exist.

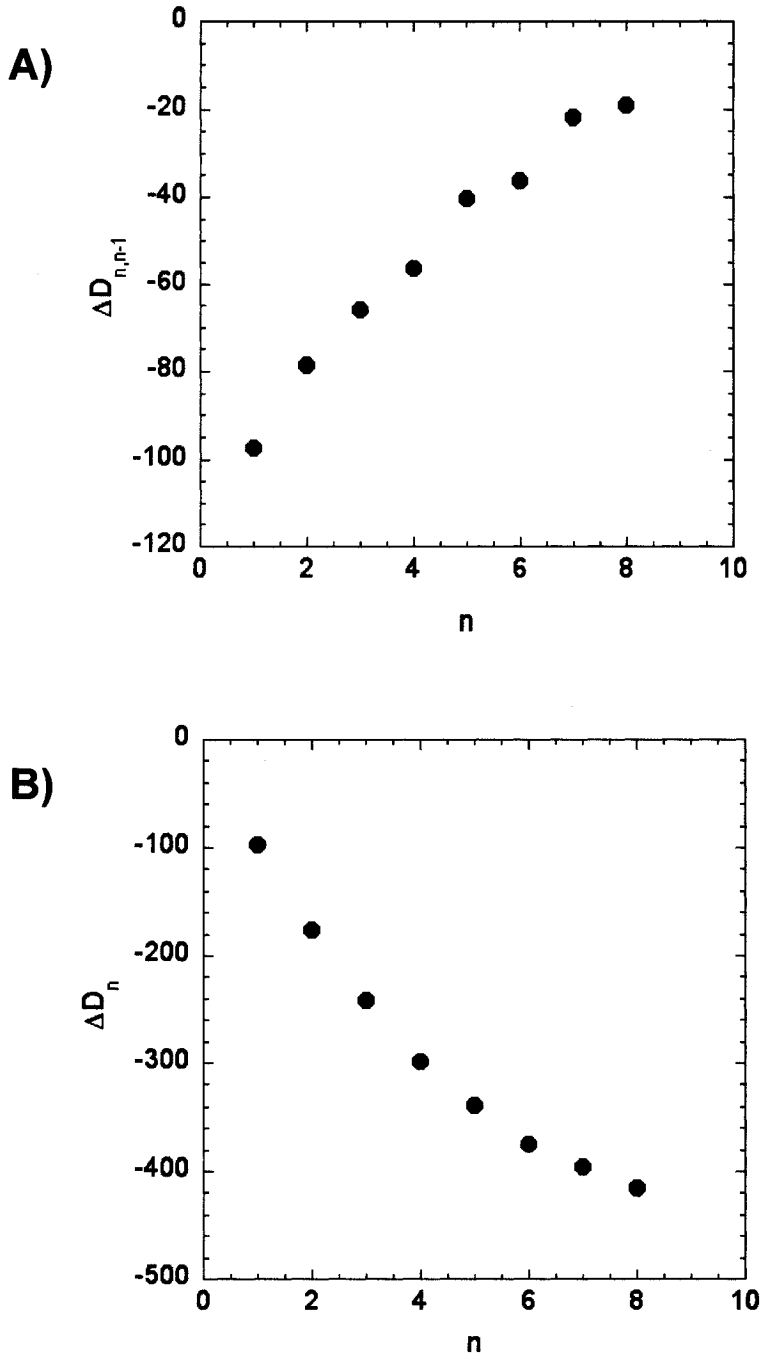

Figure 5.3.2.1. a) Parent cluster (PC) stepwise binding energies, b) PC cluster binding energies. All energies are in kcal/mol.

In Figure 5.3.2.2., we have plotted the dissociation energies associated with the four pathways presented earlier (in Eqs. 3-6) versus cluster size:

$$\Delta D_{deprotonation} = D_{Eu^{3+}(H_2O)_n} - D_{products}. \quad (9)$$

It is quite clear from the figure that the least exothermic pathway is (3). Beyond cluster size n = 2, the cluster dissociation becomes endothermic and less favorable with cluster size increase. This is concomitant with the shorter O-H bond distances of the NW observed with cluster size increase. However, the fact that the PC can readily dissociate at n = 1, 2 is quite a remarkable feature since it suggests that no trivalent clusters of these sizes can be formed. For instance, the deprotonation of $Eu^{3+}(H_2O)$ is highly exothermic with a deprotonation energy of -49.5 kcal/mol. These sizes are similar to the experimentally determined minimum cluster sizes at which other Eu^{3+}-protic solvent clusters can no longer maintain a 3+ charge [21-23].

In contrast, pathways leading to the production of H_3O^+ are highly preferred. At small cluster sizes n < 5, the most preferred pathway for PC dissociation is via pathway (4). For example, the deprotonation energy of $Eu^{3+}(H_2O)_2$ is -142.0 kcal/mol whereas the deprotonation energy using pathway (3) is only -11.9 kcal/mol. At larger cluster sizes, the pathways involving the production of partially solvated H_3O^+ ions (Eqs. 5, 6) become the most energetically favored routes for cluster deprotonation. These cluster products are consistent with those previously proposed for other ion-solvent clusters [5, 14, 24, 33, 90]. This finding is further supported by the fact that this size range represents the point where solvation of the H_3O^+ ion is energetically more favorable than the solvation of $Eu^{2+}OH$. The solvation energies of both ions are shown in Figure 5.3.2.3. for comparison. The H_3O^+ solvent stepwise binding energies are -30.3 kcal/mol and -16.2

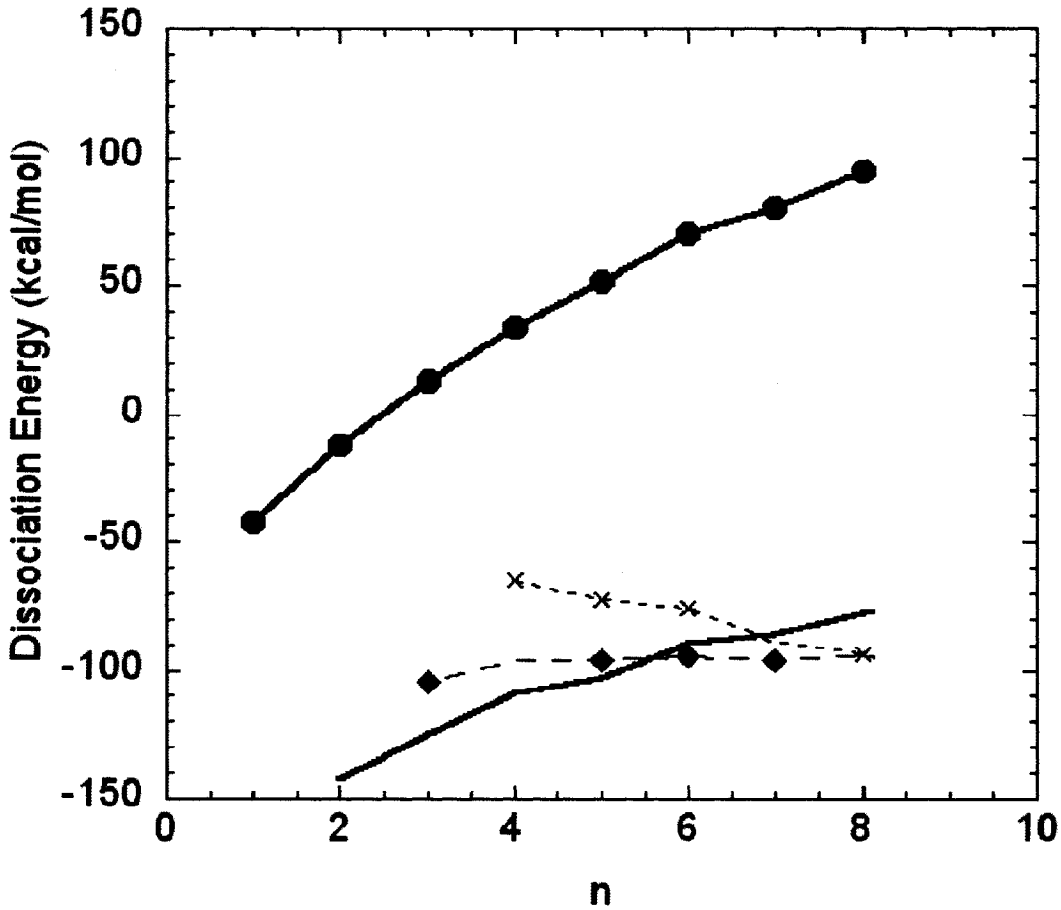

Figure 5.3.2.2. Parent cluster (PC) dissociation energies as a function of cluster size for pathways 3 (solid line with •), 4 (solid line), 5 (long-dashed line with ◆) and 6 (short-dashed line with ×). All energies are in kcal/mol.

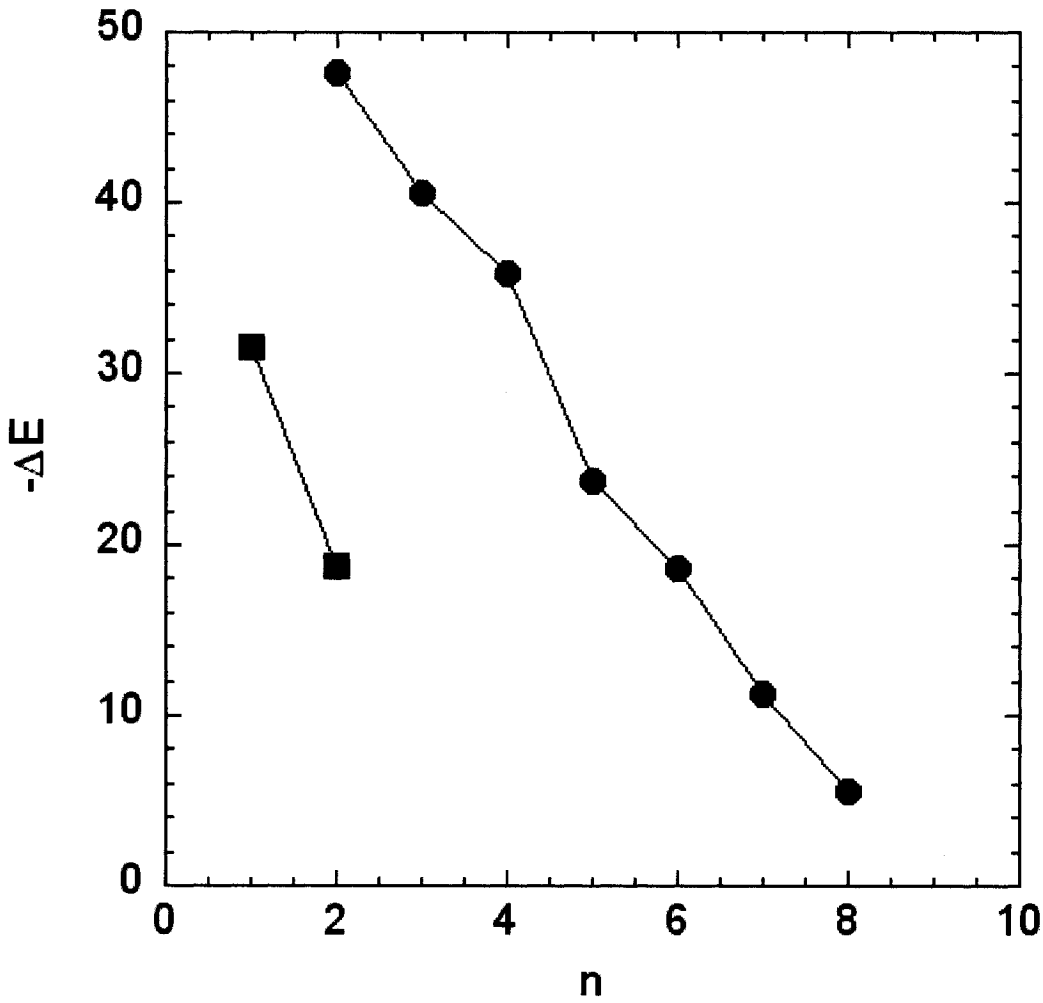

Figure 5.3.2.3. Dissociated cluster (DC, •) and H_3O^+ (■) stepwise solvation energies as a function of cluster size. All energies are in kcal/mol.

kcal/mol at n = 1 and 2, respectively. These predictions are similar in magnitude to experimentally determined enthalpies and are in excellent agreement with previous quantum chemistry calculations [26]. At n = 1, the solvation energy of H_3O^+ is lower than the stepwise binding energies of $Eu^{2+}OH(H_2O)_n$ of sizes $n \geq 5$, and at n = 2, it is lower than the stepwise binding energies for clusters with $n \geq 6$. Not surprisingly, these sizes correspond to the cluster sizes at which pathways (5) and (6) are favored over (4), as evidenced from Figure 5.3.2.2.

The dissociation reactions associated with pathways (5) and (6) are highly exothermic with dissociation energies ranging from 50 to 150 kcal/mol, depending on cluster size. For instance at n = 8, the dissociation energies associated with pathways (4), (5) and (6) are –77.9 kcal/mol, -94.7 kcal/mol and –93.2 kcal/mol, clearly indicating that the production of solvated H_3O^+ is highly preferred at these sizes. It is interesting to note that the deprotonation energies of pathways (5) and (6) are very similar at this size because the solvation of H_3O^+ by two water molecules can compensate for the loss in energy associated with loss of two water molecules from the PC.

5.3.3. Reaction Mechanism for Pathway (4)

Figures 5.3.3.1. and 5.3.3.2. contain the transition state structures for the TS1 and TS2 complexes, respectively, associated with pathway (4). Recall that the TS1 structures result from the displacement of one solvent molecule from the first coordination shell into the second coordination shell. In these structures, the NW is closer to the Eu^{3+} ion and the resultant Eu-O distance is similar to that of the Eu-OH bond distances in the DCs. Furthermore, it can be seen that the remaining H_2O molecules are arranged such that the

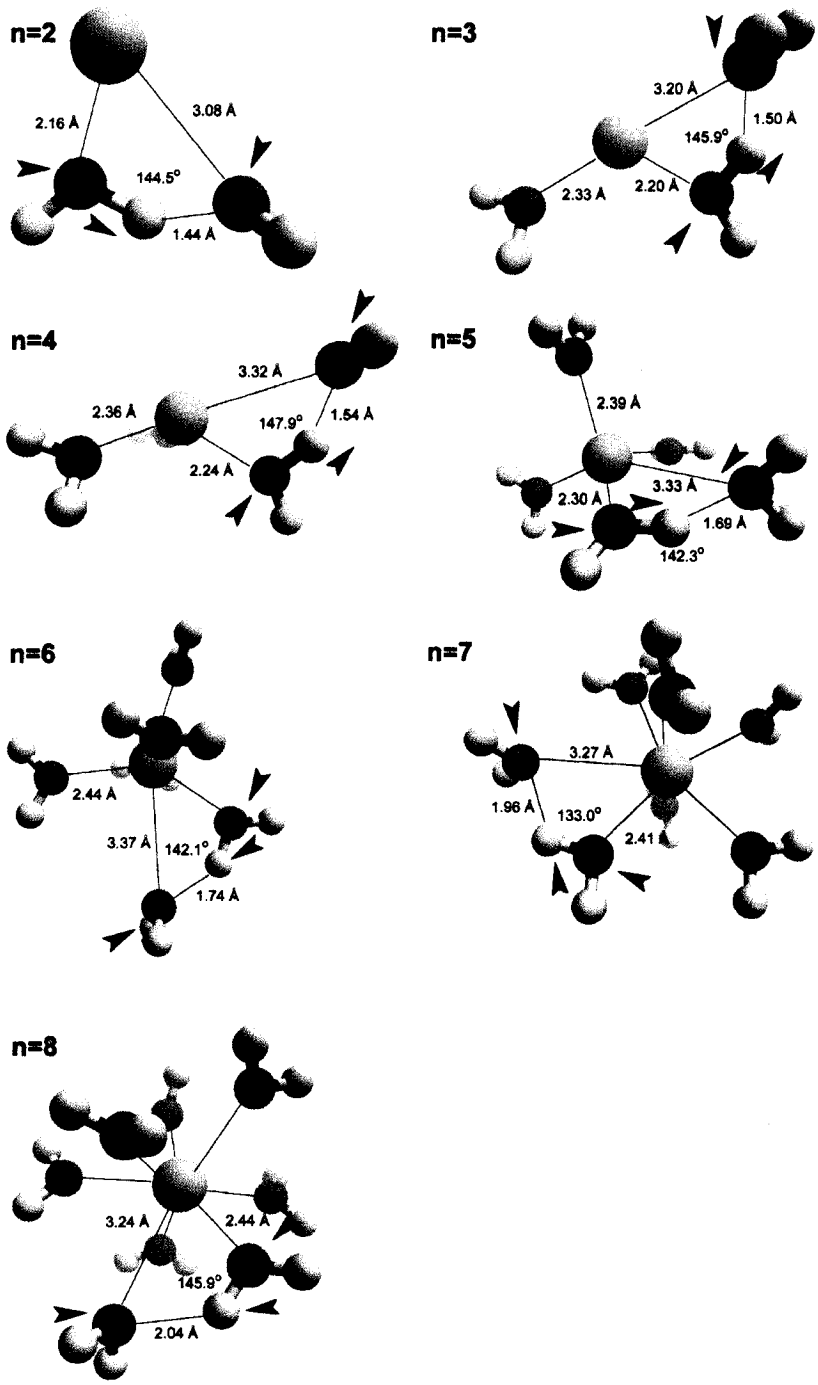

Figure 5.3.3.1. Minimum energy structures associated with the TS1 transition state clusters, $Eu^{3+}(H_2O)_n$. Arrows represent the vibrational mode associated with the imaginary frequency of the transition state.

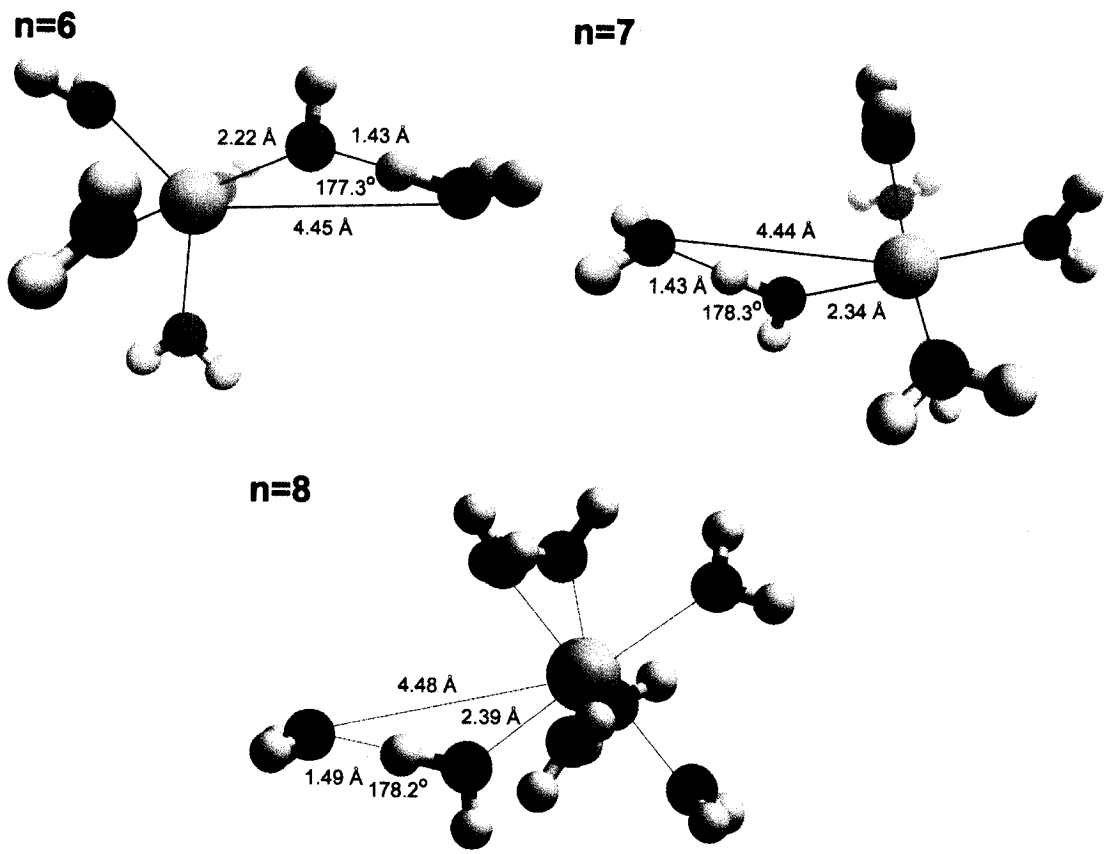

Figure 5.3.3.2. Minimum energy structures associated with the MIN2 intermediate clusters, $Eu^{3+}(H_2O)_{n-1}H_2O$.

Table 5.3.3.1. O-H bond lengths of the NW[a] in the parent and transition state clusters.[b]

n	PC[c]	TS1[d]	Δr_{O-H}
2	0.99	1.07	0.08
3	0.99	1.05	0.06
4	0.98	1.02	0.04
5	0.98	1.02	0.04
6	0.98	1.01	0.03
7	0.98	0.99	0.01
8	0.97	0.98	0.01
n	PC[c]	MIN2[e]	Δr_{O-H}
6	0.98	1.43	0.45
7	0.98	1.43	0.45
8	0.97	1.49	0.52
n	PC[c]	TS2[f]	Δr_{O-H}
6	0.98	2.11	1.13
7	0.98	2.36	1.38
8	0.97	2.50	1.53

[a] Water molecule nearest the 'displaced' water molecule (DW) that is localized in the second solvation shell as in the TS1 structure, see Figure 5.3.3.1. and text for details.
[b] Quantum chemistry calculations are performed with the G96PL/6-31+G(2d,p)/SDD basis set as discussed in the text. O-H bond distances reported in Å.
[c] Parent cluster, $Eu^{3+}(H_2O)_n$.
[d] 1st transition state structure.
[e] 2nd minimum energy configuration.
[f] 2nd transition state structure, $Eu^{2+}(H_2O)_{n-2}H_3O^+$.

cluster geometry shifts from that in the PC to that found in the DC. This is clearly done to minimize solvent-solvent repulsions.

To gain insight into the extent of PC dissociation at the TS1 stage, the changes in the O-H bond distances of the NW for both the PC and the TS1 structures were monitored. These values are listed in Table 5.3.3.1. The O-H bond length of the NW is longer in the TS1 structure compared to that in the corresponding PC at each cluster size. For example, in $Eu^{3+}(H_2O)_2$ the O-H bond length changes from 0.99 Å in the PC to 1.07

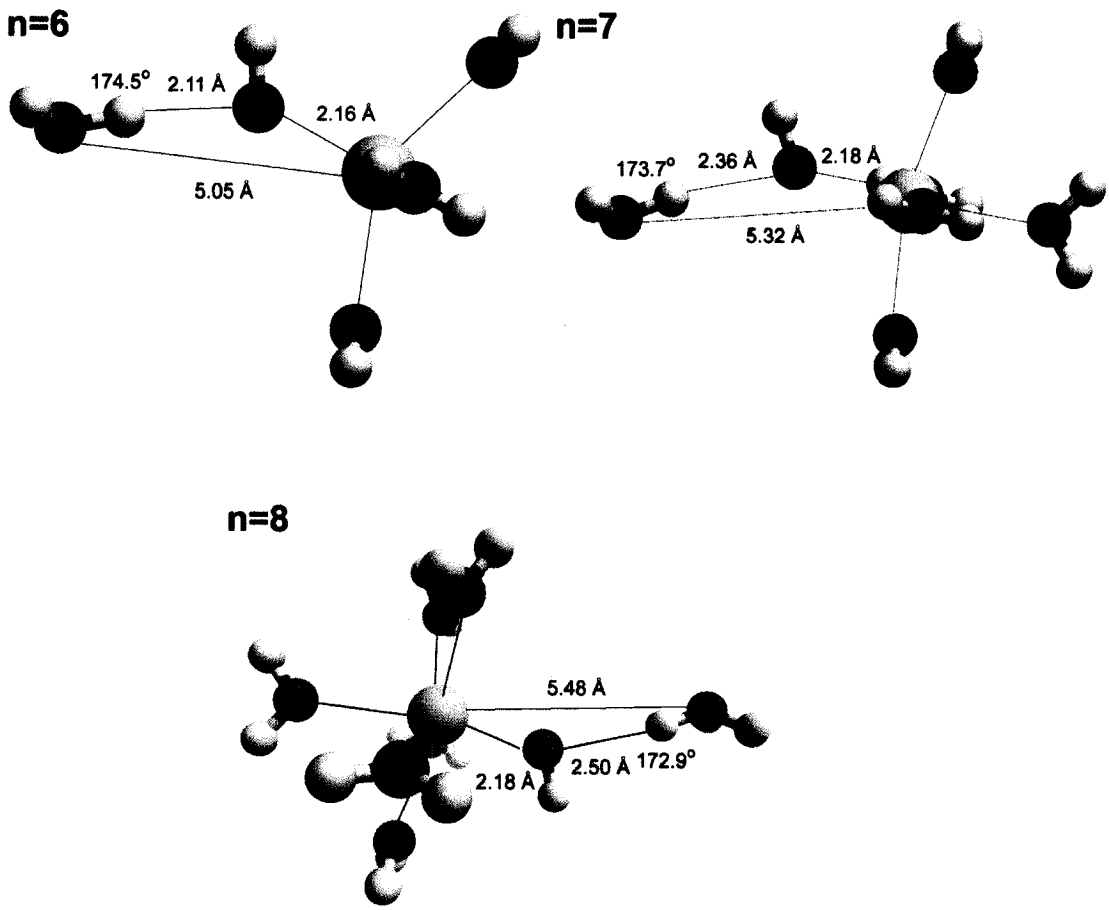

Figure 5.3.3.3. Minimum energy structures associated with the TS2 transition state clusters, $Eu^{2+}OH(H_2O)_{n-2}H_3O^+$.

Å in TS1, constituting a change of +0.08 Å. This change is the same as that reported for the NW in $Mg^{2+}(H_2O)_2$, $Ca^{2+}(H_2O)_2$ and $Sr^{2+}(H_2O)_2$ TS1 clusters [103].

Most importantly, the changes in the O-H bond distance become smaller with cluster size increase. This is due to the fact that the DW is situated further away from the NW in the TS1 structure of larger clusters and thus, the O-H bond is not polarized as extensively. This feature would imply that the formation of H_3O^+ may become increasingly difficult with increasing cluster size, corroborating what has been seen experimentally [92].

Figure 5.3.3.2. contains the intermediate minimum energy structures, MIN2 ($Eu^{3+}(H_2O)_{n-1}H_2O$), that are associated with the complete displacement of the DW to the second coordination shell for cluster sizes n = 6-8. The DW at this stage is located at a distance approximately 4.5 Å away from the metal ion, corresponding to the distance associated with the second coordination shell of the Eu^{3+} ion in solution [60]. For smaller cluster sizes, attempts to minimize structures similar to the respective TS1 states resulted in convergence towards the separated products from pathway (4), implying that in small complexes, the NW is distorted sufficiently in the TS1 state to allow for donation of the proton to the 2nd solvation shell. This is strongly supported by the large Δr_{OH} values reported in Table 5.3.3.1. for small clusters (n = 2-5). In the MIN2 structures, we note that the values of Δr_{OH} are sufficiently large enough to promote proton transfer.

The TS2 structures obtained at cluster sizes n = 6-8 are presented in Figure 5.3.3.3. As stated earlier, these structures are defined by a salt bridge, HO---H---OH_2, which is representative of the proton transfer between the NW and the DW. It is clear from Figure 5.3.3.3. that the O-H-O bond angle is quasi-linear for each of these clusters

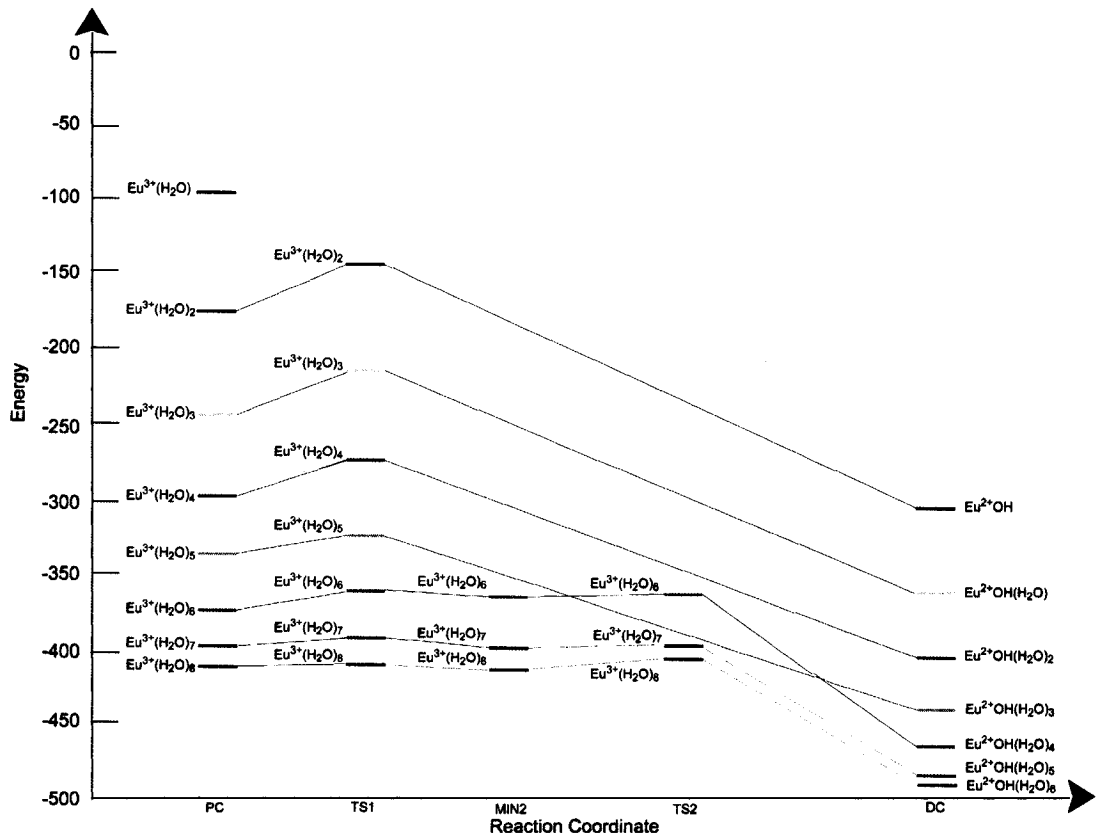

Figure 5.3.3.4. A comparison of the energetics associated with parent cluster (PC) dissociation via pathway (4) with single ligand loss (SLL) for cluster sizes n = 2-9. TS1 and TS2 structures represent transition states along the reaction path, MIN2 structures are reaction intermediates associated with the displacement of one solvent molecule from the first to the second coordination shell and DC is the deprotonated cluster of the form $Eu^{2+}OH(H_2O)_{n-2}$. All energies are in kcal/mol.

with angles of ~170-175°. More importantly, the normal modes associated with the imaginary frequencies indicate that the proton from the NW moves towards the DW. Finally, the larger Δr_{OH} values for these structures compared to the TS1 structures would indicate that the proton is being shared by both parties explicitly.

Pathway (4) was further probed by determining the reaction path intermediates for each cluster size and their respective activation energies. The complete reaction pathway associated with loss of H_3O^+ from the cluster is compared to the dissociation energies associated with SLL from the cluster in Figure 5.3.3.4. As was proposed earlier, the dissociation occurs via a two-step mechanism involving the TS1 and TS2 structures found in Figs. 5.3.3.1. and 5.3.3.2. [103]. Recall that the dissociation of smaller clusters, $n < 6$, only involves the TS1 intermediate.

In general, the activation energies are quite low. For example, the highest TS1 relative energy is that of the $Eu^{3+}(H_2O)_2$ cluster at 27.7 kcal/mol. This activation energy is comparable to that found for the TS1 structure in $Mg^{2+}(H_2O)_2$ clusters [103]. As shown in Figure 5.3.3.4., the activation energies become smaller with cluster size increase. This is attributed to the transition state complex becoming increasingly stabilized by the surrounding solvent relative to the PC. The energy barriers associated with TS2 are much smaller than those for the TS1 states. For example, the activation energy associated with TS1 for the $Eu^{3+}(H_2O)_6$ cluster is -10.9 kcal/mol whereas that for the TS2 barrier is effectively zero.

The reverse activation energy barriers associated with MIN2 are smaller than those for the forward reactions. For instance, the energy barrier for the reaction involving MIN2 back to TS1 in $Eu^{3+}(H_2O)_6$ is -5.0 kcal/mol, compared to -10.9 kcal/mol for the

Table 5.3.4.1. Partial atomic charges associated with the PC, TS1, MIN2, TS2 and DC structures for n = 1-9 along pathway (4).[a]

n	Type	q_{Eu}	$q_{O\text{-}NW}$	$q_{H\text{-}NW}$	$q_{H\text{-}DP}$	$q_{O\text{-}DW}$	$q_{H\text{-}DW}$	$q_{H\text{-}DW}$
2	PC[b]	+2.66	-1.10	+0.61	+0.65	-1.10	+0.61	+0.65
	TS1[c]	+2.62	-1.02	+0.60	+0.65	-1.08	+0.60	+0.62
	DC[d]	+2.34	-0.93	+0.59	-	-	-	-
3	PC[b]	+2.59	-1.10	+0.60	+0.64	-1.10	+0.60	+0.64
	TS1[c]	+2.57	-1.03	+0.61	+0.62	-1.13	+0.62	+0.59
	DC[d]	+2.31	-1.00	+0.59	-	-	-	-
4	PC[b]	+2.65	-1.17	+0.63	+0.63	-1.17	+0.63	+0.63
	TS1[c]	+2.54	-1.02	+0.60	+0.59	-1.12	+0.59	+0.59
	DC[d]	+2.29	-1.04	+0.60	-	-	-	-
5	PC[b]	+2.58	-1.12	+0.59	+0.59	-1.06	+0.58	+0.58
	TS1[c]	+2.62	-1.16	+0.63	+0.60	-0.99	+0.53	+0.53
	DC[d]	+2.39	-1.06	+0.58	-	-	-	-
6	PC[b]	+2.67	-1.09	+0.57	+0.57	-1.09	+0.57	+0.57
	TS1[c]	+2.61	-1.07	+0.59	+0.56	-1.00	+0.53	+0.53
	MIN2[e]	+2.57	-1.09	+0.46	+0.52	-0.61	+0.49	+0.49
	TS2[f]	+2.33	-0.99	+0.41	+0.44	-0.49	+0.50	+0.50
	DC[d]	+2.70	-1.09	+0.58	-	-	-	-
7	PC[b]	+2.70	-1.07	+0.55	+0.57	-1.05	+0.55	+0.55
	TS1[c]	+2.59	-1.28	+0.56	+0.52	-1.14	+0.57	+0.57
	MIN2[e]	+2.62	-1.10	+0.49	+0.59	-0.82	+0.48	+0.48
	TS2[f]	+2.49	-1.08	+0.42	+0.50	-0.50	+0.50	+0.50
	DC[d]	+2.48	-1.13	+0.57	-	-	-	-
8	PC[b]	+2.71	-1.03	+0.54	+0.54	-1.03	+0.54	+0.54
	TS1[c]	+2.56	-1.00	+0.55	+0.50	-0.92	+0.48	+0.48
	MIN2[e]	+2.63	-1.05	+0.49	+0.55	-0.82	+0.47	+0.47
	TS2[f]	+2.48	-1.04	+0.40	+0.46	-0.48	+0.49	+0.49
	DC[d]	+2.42	-1.24	+0.60				
	Molecule	q_O	q_H					
	H_2O	-0.72	+0.36	-	-	-	-	-
	H_3O^+	-0.44	+0.48	-	-	-	-	-

[a] Electrostatic potential (ESP) charges determined using the G96PL/6-31+G2d,p/SDD model chemistry [157]. [b] Parent cluster, $Eu^{3+}(H_2O)_n$. [c] 1st transition state structure, see Figure 5.3.3.4. and text for details. [d] Dissociated cluster, $Eu^{2+}OH(H_2O)_{n-2}$. [e] Intermediate minimum energy structure, $Eu^{3+}(H_2O)_{n-1}H_2O$. [f] 2nd transition state structure, $Eu^{2+}(H_2O)_{n-2}H_3O^+$, see Figure 5.3.3.4. and text for details.

complimentary forward reaction. However, the smaller energy barrier between MIN2 and TS2 clearly favors progression of the reaction towards cluster deprotonation. It is also clear from Figure 5.3.3.4. that SLL (first column) cannot compete with the deprotonation process.

5.3.4. Charge Analysis

The calculated atomic point charges of the Eu, O and H atoms for each of the cluster sizes and types studied are collected in Table 5.3.4.1. It is interesting to note that the positive point charges associated with the Eu^{3+} ion, q_{Eu}, decrease from +2.66 at n = 1 to a low of +2.58 at n = 5, then steadily increase again up to +2.71 at n = 8 in the PC. This is because at smaller cluster sizes, the solvent molecules are quite close to the Eu ion that is surrounded by an increasing number of potential charge donors, whereas at larger cluster sizes this process is slowly minimized due to the increasingly larger r_{Eu-O} distances. Accompanying the decreases in q_{Eu} are increases in the negative charge of the oxygen atoms, q_O, and increases in the positive charge of the hydrogen atoms, q_H, with respect to those determined in the uncomplexed water molecule (also shown in Table 5.3.4.1.). These changes in the charge distribution of water are a reflection of the strong polarization of the water molecules by the Eu^{3+} ion.

In order to assess whether or not charge transfer is one of the driving forces for the various deprotonation processes, a comparison between the partial atomic charges of each atom associated with each cluster type has been made. For reference, the point charges associated with the NW and DW have the appropriate subscripts and the hydrogen atom involved in the deprotonation process is labelled H-DP. A comparison of the various point charges obtained from the TS1 and PC structures reveals that as the DW

moves into the second coordination shell, the NW begins to transfer slightly more charge to Eu, due to the fact that the NW to Eu distance shrinks (see Figs. 5.3.1.1. and 5.3.3.1.). The same can be said for the remaining H_2O molecules in the first coordination shell. On the other hand, $q_{O\text{-}DW}$ and $q_{H\text{-}DW}$ become more positive and negative, respectively, since their interactions with the metal ion are lessened, thus restoring to some extent the atomic point charges seen in the uncomplexed water. At cluster sizes n = 2-4, the $q_{O\text{-}DW}$ in the TS1 complex is more negatively charged than $q_{O\text{-}NW}$. This results in a stronger attraction between the H-DP to the O-DW, thus providing an electrostatic rationale for the proton transfer. This is not the case for cluster sizes n = 5-8 where the driving force may be the increased attraction of the NW to the Eu ion. Due to the shorter Eu-O bond length, the H-DP may become repelled and drawn to the DW. The loss of energy associated with this transfer is more than compensated for by the gain in energy associated with the formation of the much stronger Eu-OH bond.

5.4. CONCLUSIONS

We have investigated with quantum chemistry calculations the deprotonation of $Eu^{3+}(H_2O)_n$ clusters via 4 different mechanisms. Despite the high exothermicity associated with the formation of $Eu^{3+}(H_2O)_n$ clusters, the dissociation of these complexes into $Eu^{2+}OH(H_2O)_n$ is even more favorable. At $n \geq 3$, H_2O must accompany the loss of H^+ in order for the deprotonation process to be feasible. At $n > 6$, the dissociation of the parent cluster is most favorable when water molecules accompany loss of H_3O^+ from the cluster, this due to the greater H_3O^+ solvation energy with respect to that of $Eu^{2+}OH$. It bears mentioning that this study constitutes an initial foray into investigating the mechanism behind $Ln^{3+}(H_2O)_n$ cluster deprotonation. To our knowledge, no other study

associated with this phenomenon as it relates to this cluster type has been presented in the literture.

Given the wide array of configurations that are possible at larger cluster sizes, n > 8, an in-depth study beyond that presented here would be required to probe the sizes at which the deprotonation process is quenched and more bulk-like properties are obtained. This would appear to be at cluster size n = 16 according to recently published, experimental data [92]. It is well-documented that Eu^{3+} ions have large pKas and act as weak acids in solution [54, 61, 62]. Based on this analysis and the scarce experimental evidence available, it would appear that the acid-base properties of Eu^{3+}, and perhaps the other lanthanide ions, are substantially different in cluster phase until, presumably, a cluster size of 16 solvent molecules.

Our calculations clearly shed light onto the issues regarding the detection of $Eu^{3+}(H_2O)_n$ clusters under spray conditions. The results for pathway (4) indicate that the activation energies associated with parent cluster deprotonation are not high and that this process is increasingly favorable with increasing cluster size. This is a clear illustration of how the immediate environment of the ion influences the dissociation process. All the deprotonation activation energies are lower in energy, compared to the energies associated with single ligand loss from the cluster.

Though it was not explicitly investigated in this study, no curve-crossing exists was assumed between between these two pathways, as was the case in the work of Beyer *et al.* on other metal ion-solvent clusters [103]. In their study, it was shown that the MIN2 to TS2 energy barrier for Mg^{2+}, Ca^{2+} and $Sr^{2+}(H_2O)_2$ clusters is higher in energy

than that of single ligand loss from the cluster. However, akin to the system studied here, such a crossing did not occur in the $Be^{2+}(H_2O)_2$ clusters.

In terms of future work, it would be worthwhile to monitor the electron transfer pathways alluded to earlier, though this would appear to be unfavourable based on previous calculations of other ion-solvent calculations [103]. In the work of Beyer *et al.*, it was shown that the formation of DCs was more energetically favoured over the production of $M^+(H_2O)$ species (and H_2O^+) from $M^{2+}(H_2O)_2$ clusters. It must be stressed that other reduced cluster products, such as $Eu^+(H_2O)(OH)_2$, can also result from these cluster generation experiments and so some investigation into the energetics involved in these reactions warrants investigation.

AUTHOR'S NOTES AND SIGNIFICANCE OF PAPER TO THESIS

This paper reflects upon the reasons why $Ln^{3+}(H_2O)_n$ clusters cannot be formed at small cluster sizes using current cluster generating techniques. Our findings have profound implications on cluster research as they effectively show that lanthanide ions have very different chemical properties in the cluster phase compared to in the bulk. For instance, the Eu^{3+} ion in the microsolvated cluster plays a pivotal role in producing hydronium ions that ultimately lead to charge reduced clusters. However, this behaviour rarely occurs in the bulk where the europium ion acts as a weak acid at best.

It should be noted that this work was in preparation prior to the publishing of Bush *et al.*'s article in the International Journal of Mass Spectrometry in June 2006. Remarkably, our work in this chapter clearly illustrates why such clusters could not be formed in their experiments at smaller cluster sizes than 16.

CHAPTER 6

Structural and Thermodynamic Properties of Lanthanide-Acetonitrile Clusters

Sean R. Hughes, Tao-Nhân Nguyen, John A. Capobianco and Gilles H. Peslherbe*
Centre for Research in Molecular Modeling (CERMM)
And Department of Chemistry & Biochemistry
Concordia University
7141 Sherbrooke St. West
Montréal, Québec, Canada, H3G 1M8

To be submitted to the Journal of Physical Chemistry A, last revised August 2006

ABSTRACT

Model potentials based on quantum chemistry calculations of small trivalent lanthanide ion-acetonitrile clusters, $Ln^{3+}(CH_3CN)_n$ (Ln = Pr, Eu, Tb, Ho, Lu) were developed in order to predict the thermodynamic and structural properties of these clusters at room temperature, based on Monte Carlo simulations. The model potentials account for polarization and make use of a newly developed rigid model for acetonitrile. The simulations show that the ion-solvent intermolecular distances depend on the ion size and are in keeping with the trends obtained from X-ray crystallographic studies of lanthanide ion-acetonitrile complexes and from previous simulations. The average first-shell coordination numbers are found to depend on the size of the metal ion and that of the cluster, where convergence to the bulk limit, at around cluster size n = 36, coincides with the completion of a second coordination sphere. The stepwise binding enthalpies of $Ln^{3+}(CH_3CN)_n$ are very large in magnitude, reflecting the strong influence of the Ln^{3+} ion on the coordinated acetonitrile molecules, a feature strongly contrasting what has been observed in other $M^{q+}(CH_3CN)_n$ clusters, such as those containing Na^+. The cluster enthalpies are also quite large and the reduced cluster enthalpy converges slowly to the acetonitrile bulk heat of vaporization with cluster size (approximately n = 52). The

thermodynamic quantities presented in this article have not been determined experimentally and we anticipate that these results can serve as benchmarks for future experimentation. They also suggest that the formation of these clusters is quite favorable, as has been observed in cluster formation experiments.

Keywords: Cluster ions; Lanthanide; Model Potentials; Thermodynamics; Monte Carlo Simulations; Acetonitrile

---

6.1. INTRODUCTION

Microsolvation of ions in clusters has received considerable attention over the past few years, and most recently, emphasis has been placed on creating and characterizing multivalent ion-solvent clusters [1, 3, 5-7, 12, 13, 20, 31, 32, 34, 35, 37, 40, 42, 46]. Several methods, for instance the pick-up technique and tandem electrospray/mass spectrometry, have proven to be effective means for generating such clusters, in particular those containing trivalent lanthanide ions [5, 14, 18, 21-24, 49, 90, 91, 97, 99, 108, 117, 118]. This family of elements would appear to provide good candidate ions for such an endeavor as they possess ionization potentials (IP) that lie below ~25 eV and are comparable to the IPs of other ions, such as Cu^{2+}, which are known to form stable, divalent ion-solvent clusters, most notably with water [20, 37]. Unfortunately, lanthanide ions have difficulty retaining their 3+ charge in small clusters containing protic solvents [22]. This may be due to the fact that these clusters are prone to deprotonation, which results in $Ln^{2+}(OH)(H_2O)_{n-2}$ species [91]. Indeed, at small cluster sizes, deprotonation of the trivalent ion-solvent clusters was found to be a highly exothermic process that competes quite effectively against single ligand loss from the cluster [91]. In contrast, aprotic solvents can stabilize a trivalent ion in a cluster by eliminating the tendency for this proton transfer to occur, however, cluster reduction can still occur via charge transfer from solvent or via heterolytic cleavage of one of the solvent molecules, as has been demonstrated in collision-induced dissociation experiments [23]. The former is evidenced from studies involving the formation of clusters under 'gentle' spray conditions whereas the latter was observed in collision induced dissociation experiments [23, 33, 90]. Trivalent lanthanide ion-solvent clusters

have been detected successfully with aprotic solvents such as acetone, DMSO, dimethyl formamide and acetonitrile [14, 18, 21, 23, 24, 90].

Acetonitrile is a versatile organic solvent that is capable of solvating both hydrophilic and hydrophobic species, and its complexation to lanthanide ions in clusters has been studied in moderate detail. Stewart *et al.* were capable of isolating $Pr(CH_3CN)_n$ clusters using electrospray methods [90]. Using a similar technique, Walker *et al.* found that $Ho^{3+}(CH_3CN)_6$ was the most stable species formed using the pick-up technique [33]. Later, Shvartsburg isolated similar clusters for the remainder of the lanthanide series and determined a set of minimum cluster sizes at which these ions could retain their 3+ charge, and he disregarded the existence of any 'magic numbers' as had been suggested by Walker *et al.* [23]. However, despite all this work, very little is known about the structure of the clusters produced in these experiments or the thermodynamics involved in their formation.

The lanthanide ions are particularly interesting due to their rather unique ligand-binding properties. Despite large ion-ligand binding energies, the lanthanide ions form predominantly electrostatic complexes with their ligands [52, 54, 91, 97, 117, 118], owing to a shielding of the valence 4*f*-orbitals by the larger 5*p* and 5*s* orbitals [52, 54]. In addition, these ions exhibit a flexible coordination chemistry, binding anywhere from 6 to 10 ligands [52, 54]. Even though the preferential coordination numbers of the lanthanide ions in solution had been the subject of a heated debate in the past, it is now widely accepted that the coordination numbers are closer to nine for the lighter lanthanide ions and eight for the heavier ions [54, 57-62, 175, 176, 215]. This phenomenon is attributed to the reduction in the size of the lanthanide ions across the series [52, 54]. This effect

also results in stronger ion-ligand interactions and shorter ion-ligand distances for heavier lanthanide ion-ligand complexes.

To our knowledge, the only experimental studies geared towards characterizing Ln^{3+} solvation in bulk acetonitrile are those by Deacon *et al.* and Bünzli *et al.* [57, 215]. The former involved estimation of the first-shell coordination numbers and ion-acetonitrile distances using data obtained from crystallized $Ln(CH_3CN)_{8,9}(AsF_6)_3$, whereas the latter involved estimation of these properties from FTIR spectra and fluorimetric data for similar complexes. Given this lack of experimental data, several research groups had opted to use computer simulations to assess the properties of these systems. Simulations of both lanthanide ion-acetonitrile solutions and $Ln^{3+}(CH_3CN)_n$ clusters (n = 1-15) have been performed previously by Baaden *et al.* using a polarizable form of the AMBER force field [99]. The simulations reproduced, in part, the first-shell coordination numbers of La^{3+}, Eu^{3+} and Yb^{3+}, however, the total shift in the first-shell coordination numbers was found to be two ligands, as opposed to only one. Furthermore, the stepwise binding enthalpies predicted by the model for small cluster sizes were far lower than those determined from reference quantum chemistry calculation for $Eu^{3+}(CH_3CN)$ (by ~60 kcal/mol). Later simulations by Kim on the bulk solvation of Ln^{3+} by acetonitrile using a model made simply of Coulombic and 'Lennard-Jones 12-6' repulsion-dispersion interaction terms, revealed a similar trend in coordination, with the larger lanthanide ions binding approximately 12 solvent molecules in the first coordination shell, and the smaller ions binding as few as 8 molecules [216-218]. However, it has been observed that polarization plays a prominent role in the lanthanide-ligand interactions and so this model appears to be too simplistic, as evidenced, for

example, by the overestimation of the coordination number of larger Ln^{3+} ions [116, 117, 173, 180, 181].

Our group has reported a new polarizable model for gas-phase acetonitrile, which has been successfully employed in simulations of $Na^+(CH_3CN)_n$, $I^-(CH_3CN)_n$ and $NaI(CH_3CN)_n$ clusters [130]. This new model is used here in an attempt to predict the structural and energetic properties of room temperature, $Ln^{3+}(CH_3CN)$ clusters using Monte Carlo simulations. The outline of this article is as follows. First we present the computational procedure, which includes details concerning reference quantum chemistry calculations that were used to parameterize model potentials for use in Monte Carlo simulations. Section 6.3. summarizes the structural and thermodynamic properties of $Ln^{3+}(CH_3CN)$ clusters obtained from these simulations and where possible, comparison is made to experimental and reported simulations. Particular attention is paid to possible cluster-to-bulk transitions and to determining the thermodynamic properties of these clusters, as these have yet to be determined experimentally [99]. Finally, comparisons are made to previous simulations of $Ln^{3+}(H_2O)_n$ clusters [97, 118].

6.2. METHODS

6.2.1. Computational Details

Small, ground-state $Ln^{3+}(CH_3CN)_n$ (n = 1-2) clusters were characterized by quantum chemistry calculations using the Gaussian03 program [219]. Minimum energy structures were optimized without symmetry constraint using second-order Møller-Plessett (MP2) perturbation theory [151]. The 6-31G+(2d,p) basis set was employed for the acetonitrile atoms, as this basis set generates a rather accurate structure and a reasonably accurate dipole moment for gas-phase acetonitrile [152, 220]. Lanthanide

ions were described by Stuttgart-Dresden-Bonn (SDD) large-core pseudopotentials and valence basis sets, which allow for an extensive description of the valence space and yield relatively accurate interaction energies [153, 183]. All minimum energy structures were characterized by a vibrational frequency analysis and the energies were corrected for both zero-point energy and basis-set superposition error via the Counterpoise approach [155]. All dipole moments were estimated using point charges determined from calculations based on the ElectroStatic Potential (ESP) [157].

6.2.2. $Ln^{3+}(CH_3CN)_{1,2}$ - Structural and Energetic Properties

Table 6.2.2.1. lists the structural, energetic and electronic properties of $Ln^{3+}(CH_3CN)_{1,2}$ complexes obtained from MP2 calculations. All of the binary complexes possess C_3 symmetry with the ion coordinated to the nitrogen of the acetonitrile molecule. The Ln-N bond distance decreases from 2.29 Å in $Pr^{3+}(CH_3CN)$ to 2.12 Å in $Ho^{3+}(CH_3CN)$. This is not surprising as both experimental data and ion-ligand calculations suggest that the lanthanide elements at the heavier end of the series bind more strongly and closely to their ligands than the lighter ions [57, 99, 118]. The ion-solvent binding energies of the binary complexes can be found in Table 6.2.2.1., which shows the binding energies increasing from 128.9 kcal/mol for $Pr^{3+}(CH_3CN)$ to 157.2 kcal/mol for $Lu^{3+}(CH_3CN)$. These binding energies are similar to that of $Mg^{2+}(CH_3CN)$ [221].

The observed increase of the binding energy across the series is coupled to an increase in the dipole moment of the complexed acetonitrile molecules in the cluster, this

Table 6.2.2.1. Structural, energetic and electronic properties of $Ln^{3+}(CH_3CN)$ clusters.[a]

Ion	r_{Ln-N}[b]	r_{N-C}[b]	r_{C-Cm}[b]	D_o[c]	μ_{CH3CN}[d]	θ_{N-Ln-N}[d]
$Pr^{3+}(CH_3CN)$	2.29 (2.30)	1.19 (1.17)	1.43 (1.46)	128.9 (128.9)	6.13 (10.00)	
$Eu^{3+}(CH_3CN)$	2.23 (2.24)	1.19 (1.17)	1.43 (1.46)	136.8 (136.8)	6.36 (10.23)	
$Tb^{3+}(CH_3CN)$	2.19 (2.20)	1.19 (1.17)	1.43 (1.46)	143.6 (143.6)	6.40 (10.42)	
$Ho^{3+}(CH_3CN)$	2.16 (2.17)	1.19 (1.17)	1.43 (1.46)	148.2 (148.2)	6.70 (10.56)	
$Lu^{3+}(CH_3CN)$	2.12 (2.12)	1.19 (1.17)	1.43 (1.46)	157.2 (157.2)	7.00 (10.80)	
$Pr^{3+}(CH_3CN)_2$	2.37 (2.35)	1.18 (1.17)	1.44 (1.46)	228.8 (235.8)	6.11 (9.16)	108.6 (112.7)
$Eu^{3+}(CH_3CN)_2$	2.30 (2.29)	1.18 (1.17)	1.44 (1.46)	243.1 (249.5)	6.30 (9.34)	109.6 (116.4)
$Tb^{3+}(CH_3CN)_2$	2.26 (2.25)	1.18 (1.17)	1.44 (1.46)	253.2 (261.1)	6.36 (9.48)	110.1 (116.9)
$Ho^{3+}(CH_3CN)_2$	2.23 (2.22)	1.18 (1.17)	1.44 (1.46)	261.0 (268.9)	6.61 (9.59)	110.9 (118.3)
$Lu^{3+}(CH_3CN)_2$	2.18 (2.18)	1.18 (1.17)	1.44 (1.46)	277.3 (284.2)	6.89 (9.76)	112.3 (123.2)
CH_3CN	-	1.17 (1.17)	1.46 (1.46)	-	3.93 (3.93)	-

[a] Determined from MP2 calculations and from model potentials (in parentheses).
[b] Interatomic distances (Å), C_m indicates the methyl carbon in acetonitrile.
[c] Binding energy (kcal/mol) corrected for both zero-point energy and basis set superposition error.
[d] Dipole moment (D) of acetonitrile based on electrostatic potential (ESP) charges.
[e] Nitrogen-lanthanide-nitrogen bond angle (°).

due to increase in the charge:size of the ion. Solvent polarization by the ion is very significant, resulting in very large solvent molecular dipole moments in the cluster, nearly twice as much as that of the uncomplexed acetonitrile molecule. The acetonitrile molecular dipole moments in $Ln^{3+}(CH_3CN)_n$ clusters are much larger than those in alkali ion-acetonitrile clusters [125]. For example, the total dipole moment of acetonitrile is 5.4 D for $Na^+(CH_3CN)$ whereas it is 7.00 D for $Lu^{3+}(CH_3CN)$, this owing to the larger

charge:size ratio and greater polarizing ability of the Ln^{3+} ions. Similar polarization of the solvent has also been observed in $Ln^{3+}(H_2O)$ clusters, but to a lesser extent, most likely because of the weaker solvent polarizability (1.45 $Å^3$ for water versus 4.45 $Å^3$ for acetonitrile) [117, 118]. Polarization of the solvent contributes significantly to the ion-solvent complex stabilization (or binding) energy. Since polarization effects are less significant for water than acetonitrile, ion-water binding energies are typically smaller in $Ln^{3+}(H_2O)$ versus $Ln^{3+}(CH_3CN)$. For example, the binding energy of the $Eu^{3+}(H_2O)$ complex is approximately -90 kcal/mol, which is 40 kcal/mol weaker than that of $Eu^{3+}(CH_3CN)$ [118].

Slight structural changes are observed for the complexed acetonitrile molecule as a result of solvent polarization, as seen from the data in Table 6.2.2.1. The N-C bonds lengthen sparingly (+0.01 Å) whereas the carbon to methyl carbon (C_m) distances shorten slightly (-0.03 Å). Changes associated with the atomic point charge distribution of acetonitrile also reflect the polarization of acetonitrile molecule due to Ln^{3+} ions. The atomic point charge of the nitrogen atoms, listed in Table 6.2.2.2., decrease upon ion complexation and become more negative across the lanthanide ion series. On the other hand, both carbon atoms become more positive, as do the hydrogens. This electron density redistribution is reflective of the strong polarization of acetonitrile induced by the lanthanide ion. Charge transfer from acetonitrile to the lanthanide ion also appears to be significant, as evidenced by the data in Table 6.2.2.2., where it can be seen that there is a uniform reduction of 0.32 *e* in the atomic point charge of the clustered lanthanide ion. Similar trends were observed in previous calculations of lanthanide ion-water complexes but charge transfer was found to be far less extensive (~0.15 *e*) [118]. This may be due to

the fact that nitrogen is less electronegative than oxygen and is thus more prone to charge transfer interactions.

Table 6.2.2.2. Changes in the atomic charge distribution of $Ln^{3+}(CH_3CN)$.[a]

Ion	q_{Ln}[b]	q_N[c]	q_C[d]	q_{Cm}[e]	q_H[f]
Dimers					
$Pr^{3+}(CH_3CN)$	+2.68	-0.72	+0.65	-0.43	+0.27
$Eu^{3+}(CH_3CN)$	+2.68	-0.78	+0.71	-0.45	+0.28
$Tb^{3+}(CH_3CN)$	+2.68	-0.80	+0.74	-0.48	+0.29
$Ho^{3+}(CH_3CN)$	+2.68	-0.83	+0.77	-0.50	+0.29
$Lu^{3+}(CH_3CN)$	+2.68	-0.87	+0.81	-0.52	+0.30
$Pr^{3+}(CH_3CN)_2$	+2.54	-0.74	+0.66	-0.48	+0.27
$Eu^{3+}(CH_3CN)_2$	+2.54	-0.78	+0.70	-0.50	+0.27
$Tb^{3+}(CH_3CN)_2$	+2.55	-0.80	+0.72	-0.50	+0.27
$Ho^{3+}(CH_3CN)_2$	+2.55	-0.80	+0.72	-0.50	+0.27
$Lu^{3+}(CH_3CN)_2$	+2.55	-0.81	+0.73	-0.50	+0.27
CH_3CN	-	-0.49	+0.46	-0.52	+0.18
Ln	+3.00	-	-	-	-

[a] All charges from ESP calculations based on MP2/6-31+G(2d,p) calculations.
[b] Atomic point charge of the lanthanide ion (fractions of *e*).
[c] Atomic point charge of the acetonitrile nitrogen atom in acetonitrile (fraction of *e*).
[d] Atomic point charge of the acetonitrile carbon atom in acetonitrile (fraction of *e*).
[e] Atomic point charge of the acetonitrile methyl carbon atom in acetonitrile (fraction of *e*).
[f] Atomic point charges of the acetonitrile hydrogen atoms in acetonitrile (fraction of *e*).

All $Ln^{3+}(CH_3CN)_2$ clusters investigated possess C_{2v} symmetry, a structural motif not uncommon in trimers involving large metal ions, and any attempt to obtain a linear C_3 structure resulted in the cluster converging to the C_{2v} geometry [110-112, 117, 122]. This symmetry is likely the result of several factors. First, the lanthanide ion is polarized mutually at the same end by both acetonitrile molecules, thus allowing for closer and more favorable ion-solvent interactions than would be obtained in the linear C_3 structure [117]. Second, the longer ion-acetonitrile distances compared to those found in the

dimers are the result of the ion being incapable of polarizing both acetonitrile molecules as efficiently due to a screening of the ion's charge. This results in less enhancement of the acetonitrile dipole moments, and consequently lower Ln^{3+}-CH_3CN interaction energies than in the dimer. For instance, the bond lengths and binding energies are 2.37 Å and 228.8 kcal/mol in $Pr^{3+}(CH_3CN)_2$ and 2.29 Å and 128.9 kcal/mol in $Pr^{3+}(CH_3CN)$. Across the lanthanide series, the tendency for the larger ions to bind less tightly than the smaller ions to acetonitrile is conserved. Furthermore, the N-Ln-N bond angles increase across the series, this owed to slightly increased inter-solvent repulsions resulting from the observed decreases in the ion-solvent distances (c.f. Table 6.2.2.1.).

6.3. MODEL POTENTIALS AND SIMULATIONS/PROCEDURE

6.3.1. Functional Form of the Model Potentials

The model potential employed in the simulations consists of a sum of Coulombic, polarization and repulsion-dispersion terms:

$$U = U_{Coulomb} + U_{Polarization} + U_{\mathrm{Re}\,pulsion-Dispersion}. \qquad 6.3.1.1.$$

The ion and solvent molecules are represented by point charge distributions, induced dipoles and repulsion-dispersion forces. The Coulombic energy is simply:

$$U_{Coulomb} = \sum_{i,j} \frac{q_i q_j}{r_{ij}}, \qquad 6.3.1.2.$$

where q_i and q_j are static point charges carried by ionic and molecular sites located at a distance r_{ij} from each other. The polarization energy, which reflects the mutual polarization of the solvent molecules and the lanthanide ion, accounts for the interactions between induced dipoles (μ_i) and the electric field, E_i^o, felt at site i arising from the static point charge distribution:

$$U_{Polarization} = -\frac{1}{2}\sum_i \vec{E}_i^o \vec{\mu}_i \,, \qquad 6.3.1.3.$$

$$\vec{E}_i^o = \sum_j \frac{q_j \cdot \vec{r}_j}{\left|\vec{r}_i - \vec{r}_j\right|^3} \,. \qquad 6.3.1.4.$$

The induced dipoles are evaluated as a linear response to the total electric field:

$$\vec{\mu}_i = \alpha_i \cdot \vec{E}_i = \alpha_i \left[\vec{E}_i^o + \sum_{i \neq j} T_{ij} \cdot \vec{\mu}_j \right], \qquad 6.3.1.5.$$

where α_i is the polarizability at site i and T_{ij} is the dipole tensor [185]. In cluster simulations, the low dimensionality of the problem allows for a straightforward solution of the set of linear equations in Eq. 6.3.1.3.-6.3.1.5. in matrix form, which is obtained via LU decomposition and back substitution [186, 187]. Finally, the repulsion-dispersion energy is obtained using a generalized 12-8-6 Lennard-Jones potential:

$$U_{Repulsion-Dispersion} = \sum_{i,j} \left[A_{ij} r_{ij}^{-12} + B_{ij} r_{ij}^{-8} + C_{ij} r_{ij}^{-6} \right], \qquad 6.3.1.6.$$

where A_{ij}, B_{ij} and C_{ij} are adjustable parameters. A_{ij} sites were only used for atoms involved in acetonitrile-acetonitrile interactions whereas B_{ij} were only used for atoms involved in Ln-acetonitrile interactions. C_{ij} sites were used for all interatomic interactions.

The acetonitrile model used in this study is that developed in recent work [130]. Briefly, the CH_3CN model employs a gas-phase equilibrium structure. The acetonitrile charge distribution is assigned on the basis of atomic point charges obtained from high-level quantum chemistry calculations that reproduced the molecular dipole moment of gas-phase acetonitrile (3.9 D). In addition, the model contains a set of distributed polarizabilities on the N, C and methyl C (C_m) atoms, and repulsion-dispersion sites on

each atom. On the other hand, the lanthanide ions carry point-charge, polarizability and repulsion-dispersion sites.

6.3.2. Parameterization of the Model Potentials

The parameters used in the polarizable model potential include effective atomic point charges, atomic polarizabilities ($Å^3$) and repulsion-dispersion parameters, A_{ij} (kcal/mol $Å^{-12}$), B_{ij} (kcal/mol $Å^{-8}$) and C_{ij} (kcal/mol $Å^{-6}$). The lanthanide ions carry a point charge of +3 and polarizabilities based on the work of Saxena *et al.*, while a set of atomic polarizabilities on the N, C and methyl C (C_m) sites was fitted under the constraint of reproducing the molecular polarizability of 4.45 $Å^3$ [222]. The repulsion-dispersion parameters were fitted to reproduce solute-solvent and solvent-solvent binding energies and interaction distances, as well as solvent molecular dipole moments for a number of pure solvent and ion-solvent clusters [130]. The fitting was performed using a non-linear least-squares fit based on the method proposed by Marquardt and Levenberg [187]. The parameters are listed in Tables 6.3.2.1. and 6.3.2.2.

Table 6.3.2.1. Acetonitrile potential parameters.

	A_{ij}[a]	C_{ij}[b]
N-N	92287	-945
N-C	1365181	-11058
N-H	79804	-1142
C-C	86030	-1046
C-H	2578	-124
H-H	1	-1
	α[c]	q[d]
N	1.14	-0.49
C	1.18	+0.48
C_m	2.00	-0.56
H	-	+0.19

[a] Repulsion-dispersion parameter (kcal/mol $Å^{-12}$).
[b] Repulsion-dispersion parameter (kcal/mol $Å^{-6}$).
[c] Site polarizability ($Å^3$).
[d] Atomic point charge (fraction of *e*).

Table 6.3.2.2. Lanthanide potential parameters.

Parameter	Pr	Eu	Tb	Ho	Lu
B_{ij}[a]					
Ln-N	90194	78093	71584	66227	59662
Ln-C	67107	68970	69186	69842	69860
Ln-H	63262	64665	64651	64418	64761
C_{ij}[b]					
Ln-N	-10832	-9963	-9334	-8796	-8521
Ln-C	-10000	-7786	-9709	-9530	-7837
Ln-H	-5118	-6265	-7651	-124	-7767
α[c]	1.76	1.44	1.33	1.22	1.04[e]
q[d]	+3.00	+3.00	+3.00	+3.00	+3.00

[a] Repulsion-dispersion parameter (kcal/mol $Å^{-8}$).
[b] Repulsion-dispersion parameter (kcal/mol $Å^{-6}$).
[c] Site polarizability ($Å^3$) based on ref [222].
[d] Atomic point charge (fraction of *e*).
[e] Estimated from trends provided in ref [222].

The structural, energetic and electronic properties of the minimum energy $Ln^{3+}(CH_3CN)_{1,2}$ complexes obtained with the model potentials are listed in Table 6.2.2.1. The model potentials accurately reproduce the various Ln-N interaction distances and generate fair estimates of the minimum binding energies for the binary complexes. However, the acetonitrile dipole moments are grossly overestimated by ~2-3 D with respect to those obtained from our quantum chemistry calculations. However, the model does reproduce the ability of the heavier lanthanide ions to induce larger solvent dipole moments than the lighter ions. Similarly, the features of the trimer structures are adequately reproduced by the model potentials, with the largest deviation in the interaction distances being ~0.01 Å with respect to the quantum chemistry estimates. However, the N-Ln-N bond angles are not. Though the trend associated with the N-Ln-N bond angle increasing across the series is reproduced, the extent to which the bond breathing increases is not. For example, the difference between the N-Ln-N bond angles in $Pr^{3+}(CH_3CN)_2$ and $Lu^{3+}(CH_3CN)_2$ obtained from the quantum chemistry calculations is

only 3.7°, whereas this difference is approximately 10.5° according to the model potentials. Additionally, the binding energies obtained with the model potential are slightly overestimated for this cluster size, but by no more than a 3% error with respect to the quantum chemistry calculations. Finally, the solvent molecular dipole moments in the trimers are smaller than those predicted for the binary complex, as is the case in the quantum chemistry calculations. This again reflects a decrease in the ion's propensity to polarize ligand molecules with cluster size because of the ion charge being screened by the other ligands.

6.3.3. Monte Carlo Simulations

Monte Carlo simulations were used to investigate the thermodynamic and structural properties of $Ln^{3+}(CH_3CN)_n$ clusters at 300K. A random-walk approach was used to generate new configurations by both randomly translating the acetonitrile molecules in Cartesian space and rotating them about their Euler angles. The maximum allowed translations were set to 0.25 Å and the range of angular displacements was set to 25° which resulted in acceptance ratios between 35-45%. The resulting configurations were accepted or rejected according to the Metropolis algorithm [190]. Since clusters are being simulated and not a bulk liquid, no periodic boundary conditions were imposed on the system. As a consequence, evaporation of the solvent molecules from the cluster was closely monitored such that any solvent molecule detected beyond 20 and 40 Å at cluster sizes $n < 36$ and $n = 36$, respectively, was considered evaporated from the cluster. Markov chains containing configurations with evaporated solvent molecules were discarded from the overall sampling so as to define a representative, equilibrium ensemble for a given cluster size. Periodic heating and cooling of the system was

performed to avoid trapping in local minima of configurational space. In general, each run entailed at least $1x10^6$ configurations for equilibration, followed by an equal number of steps for data collection.

Cluster enthalpies were calculated from the average energy $<U>$ of the canonical ensembles of configurations as

$$\Delta H_n = \Delta U + \Delta(PV) = \langle U \rangle + nRT . \qquad 3.7.$$

Stepwise binding enthalpies, which represent the enthalpy gain associated with the addition of one solvent molecule to the cluster, were calculated as

$$\Delta H_{n,n-1} = \Delta H_n - \Delta H_{n-1} . \qquad 3.8.$$

The structural properties of the clusters were analyzed in terms of a distance-dependent coordination number $N_{coord}(r)$, and its derivative, $P(r)$, which is the normalized radial probability distribution function:

$$P(r) = \frac{dN_{coord}(r)}{dr} = \frac{n4\pi r^2 g(r)}{\int_0^\infty 4\pi r^2 g(r) dr} . \qquad 3.9.$$

It should be noted that $P(r)$ differs from the radial distribution function $g(r)$ used in liquid structure theory by a factor of $4\pi r^2$ and it is normalized to the number of solvent molecules in the cluster.

6.4. RESULTS AND DISCUSSION

6.4.1. Structural Data

Figure 6.4.1.1. contains representative $Ln^{3+}(CH_3CN)_n$ clusters obtained from the Monte Carlo simulations at room temperature. The ion is coordinated to acetonitrile by the nitrogen atom and they are found in the interior of the cluster for each size studied. This interior solvation shell structure is the result of the strong Ln-CH_3CN interactions,

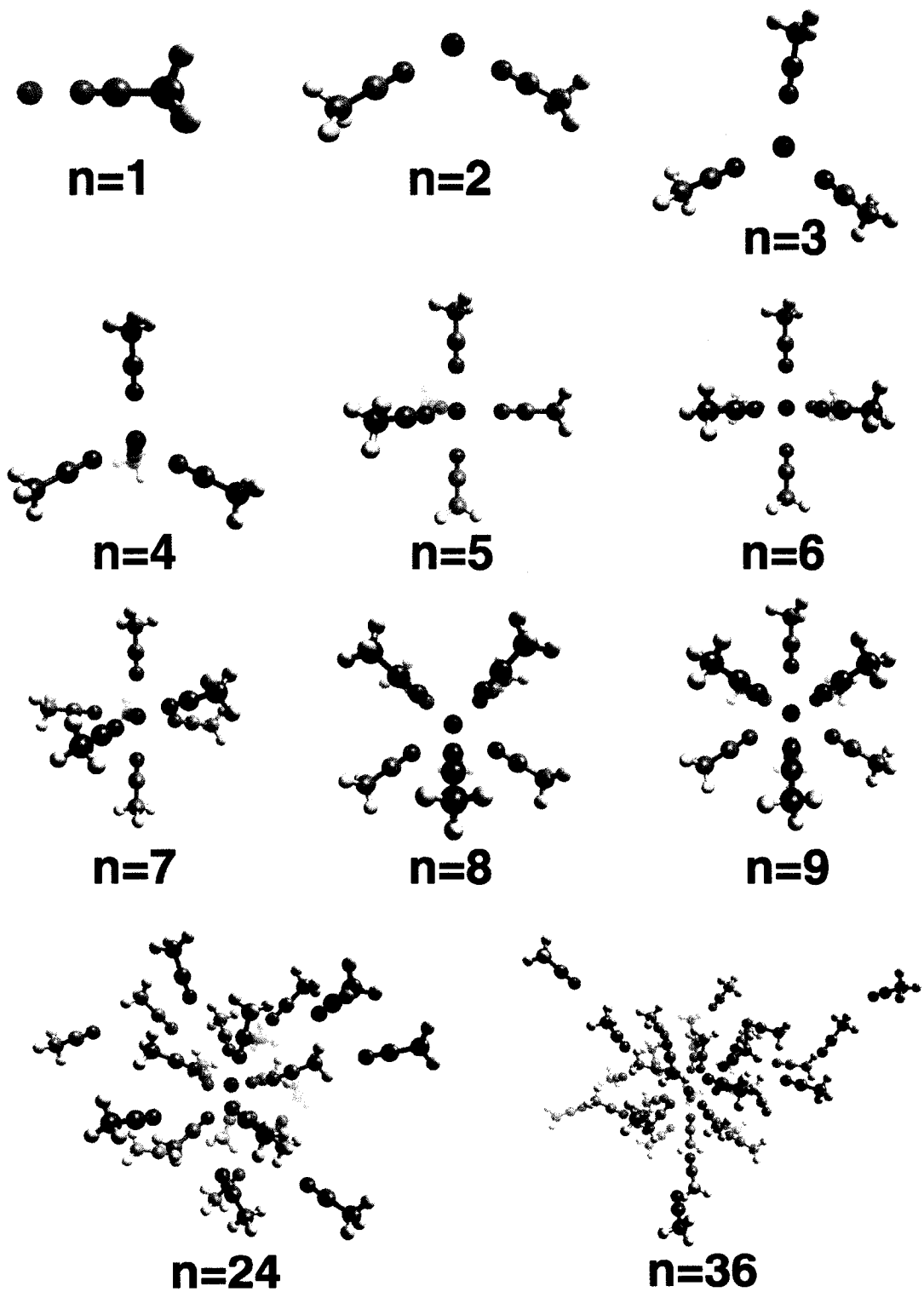

Figure 6.4.1.1. Representative structures of $Lu^{3+}(CH_3CN)_n$ clusters obtained from room temperature Monte Carlo simulations.

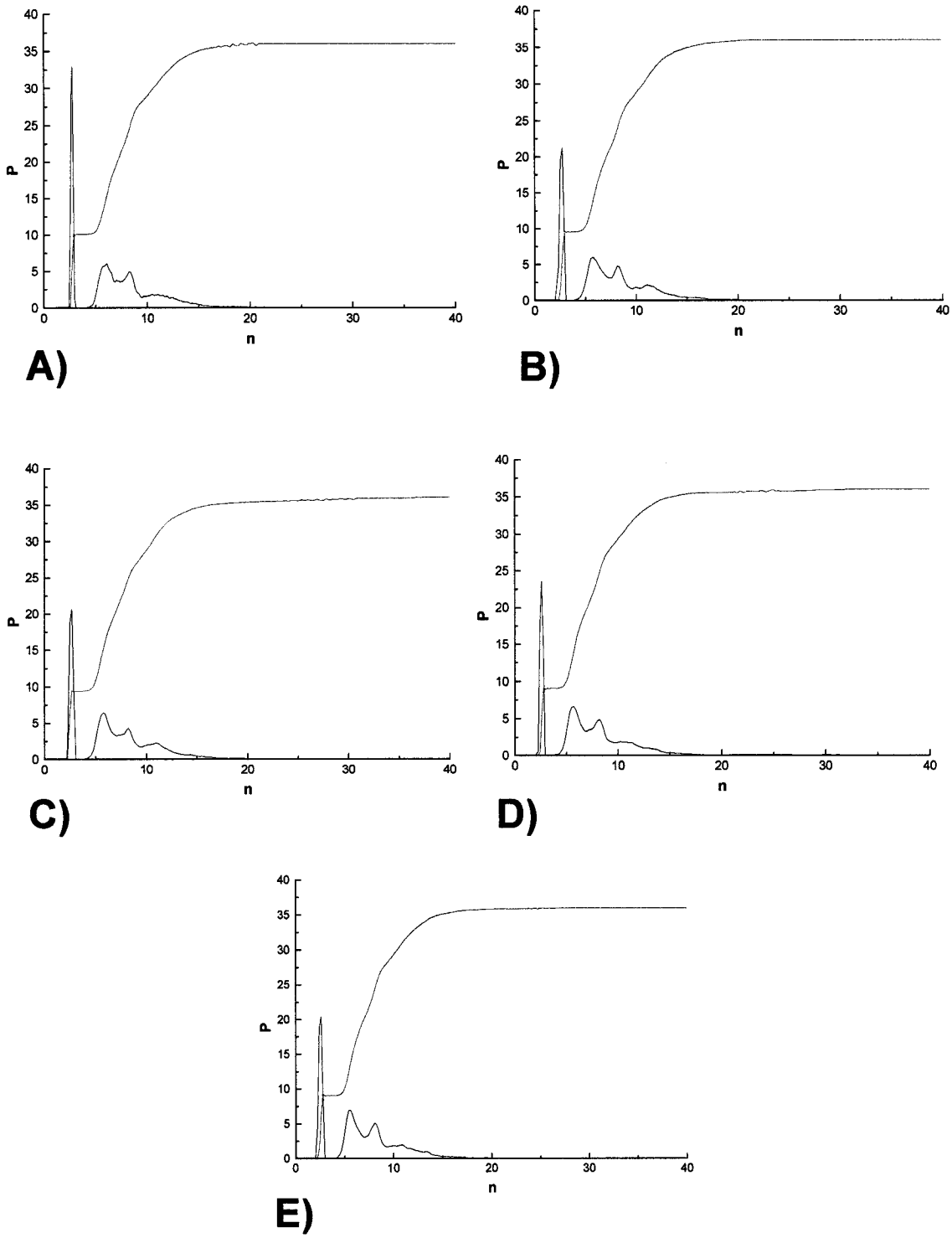

Figure 6.4.1.2. Radial probability distribution functions and distance-dependent coordination number for $Ln^{3+}(CH_3CN)_{36}$, (a) Pr, (b) Eu, (c) Tb, (d) Ho and (e) Lu.

which are far stronger (by orders of magnitude) than the CH_3CN-CH_3CN interaction energies (cf. Table 6.2.2.1.) and the solvent molecules organize around the ion rather than into a solvent dipole-bound network. As can be seen from the probability distribution functions (PDFs) shown in Fig. 6.4.1.2., two prominent peaks representing the first and second coordination shells are present at large n. At n = 36, the first coordination shell is quite sharp and is located approximately 2.5-2.6 Å away from the ion, whereas the second coordination shell is fairly diffuse and is located at ~5.5 Å. The locations of the first coordination shells in our simulations are consistent with those found in the bulk studies, whereas those of the second shell is at slightly shorter distances than what is predicted by the Baaden model (6.0 Å) [57, 99]. The sharpness of the first peak in the PDF implies that the solvent molecules are well ordered in the first coordination shell, however, the second peak in the PDF is broad, indicating poor ordering of the second coordination shell. This contrasts our previous studies of lanthanide ion-water clusters, where long-range ordering of the solvent was suggested by the PDFs [97, 118]. This difference can be explained by the fact that acetonitrile molecules do not form strong, ordered hydrogen-bonded networks like water and that the acetonitrile molecules bind less tightly than water to the Ln^{3+} ion with increasing cluster size, most likely due to the larger size of the acetonitrile molecule which results in larger first solvation shells. This consequently results in weaker interactions between second coordination shell molecules and the ion, thus leading to less ordering of the solvent. This would appear to be the case since in large $Ln^{3+}(H_2O)_n$ clusters, the second coordination shell is located at only 5 Å from the ion, i.e. 0.5 Å closer than the second shell acetonitrile molecules. Furthermore, broad distributions of solvent molecules in the second coordination shell have been

observed in previous studies of $Ln^{3+}(CH_3CN)_n$, $Na^+(CH_3CN)_n$ and $Cs^+(CH_3CN)_n$ clusters, and so this appears to be a feature inherent to most metal ion-acetonitrile clusters [99, 125].

The average first-shell coordination number of the ion obtained from the PDFS of lanthanide ion-solvent clusters at $n < 24$ are consistent with approximately 9 acetonitrile molecules for all lanthanide ions. These are shown in Table 6.4.1.1. However, for $n \geq 24$, the first-shell coordination numbers gradually increase for the lighter ions, and the typical trend associated with lanthanide ion bulk coordination across the series, that the lighter ions bind more ligands than the heavier ones, is reproduced by cluster size 36. The formation of the second coordination shell is obviously necessary for the cluster to adopt a first coordination shell similar to that in the bulk. As opposed to the more traditionally accepted 9-8 shift in coordination, the trend in acetonitrile clusters suggests a 10- to 9-coordinate shift [57, 215]. Similar coordination numbers were reported by Baaden *et al.* and Kim [99, 216-218], however, it should be noted that only the simulations presented here predict a net change of only one ligand, which is consistent with the traditional shift in lanthanide ion coordination across the series. The second coordination sphere contains approximately 10-12 molecules for $n = 36$, in good agreement with the observations of Baaden *et al.* [99]. Finally, it should be noted that the probability distribution function goes to zero between the peaks corresponding to the first and second coordination shells, suggesting that no solvent molecule resides in between the solvation shells and that any migration to or out of the first solvation shell is only transient, in agreement with the low population of solvent in the interstitial region found by Baaden *et al.* [99].

Table 6.4.1.1. Average first-shell coordination numbers of $Ln^{3+}(CH_3CN)_n$.

	n				Baaden[a]	Kim[b]	Exp[c]
	12	15	24	36			
La^{3+}	-	-	-	-	9.8, 9.9	12	9
Pr^{3+}	9.0	9.2	9.8	10.0	-	-	9
Eu^{3+}	9.0	9.0	9.9	9.5	9.1, 9.2	10.0, 9.6	9
Tb^{3+}	9.0	9.0	9.5	9.4	-	-	-
Ho^{3+}	9.1	9.1	9.1	9.0	-	-	-
Lu^{3+}	9.0	9.0	9.0	9.0	-	-	-
Yb^{3+}	-	-	-	-	8.8, 8.7	8.3	6

\[a] Simulated data from both Ln^{3+}-acetonitrile solutions and $Ln^{3+}(CH_3CN)_{15}$ clusters, taken from Ref. [99].
[b] Simulated data from Refs. [216-218]
[c] Bulk data obtained from crystalline $Ln(CH_3CN)_n(AlX_m)_3$, Refs. [57] and [215].

Table 6.4.1.2. Average first-shell coordination distances (Å) for $Ln^{3+}(CH_3CN)_n$.[a]

	N				Baaden[b]	Kim[c]	Exp[d]
	12	15	24	36			
La^{3+}	-	-	-	-	2.70, 2.70	2.9	2.63
Pr^{3+}	2.62	2.64	2.67	2.70	-	-	2.59
Eu^{3+}	2.57	2.57	2.62	2.66	2.50	2.6, 2.6	2.54
Tb^{3+}	2.53	2.53	2.58	2.63	-	-	-
Ho^{3+}	2.50	2.51	2.52	2.58	-	-	-
Lu^{3+}	2.46	2.46	2.48	2.53	-	-	-
Yb^{3+}	-	-	-	-	2.30, 2.30	2.4	2.39

[a] Average lanthanide to nitrogen distances were obtained from Monte-Carlo simulations. The cut-off radius for the first coordination shell was determined from the probability distribution functions in Fig. 6.4.1.2.
[b] Simulated data from both Ln^{3+}-acetonitrile solutions and $Ln^{3+}(CH_3CN)_{15}$ clusters, taken from Ref. [99].
[c] Simulated data from Refs. [216-218].
[d] Mean Ln-N distances obtained from crystalline $Ln(CH_3CN)_n(AlX_m)_3$, Refs. [57] and [215].

The average first-shell ion-acetonitrile coordination distances are listed in Table 6.4.1.2. as a function of cluster size. The ion-N distances increase with cluster size, as would be expected on the basis an increased shielding of the Ln ion's charge by the large

number of solvent molecules in the first coordination shell. Furthermore, the ion-N distances decrease across the lanthanide series, a feature consistent with the trends in lanthanide ion-ligand binding described earlier. These distances at large cluster sizes are slightly larger than those predicted by Baaden *et al.* for $Ln^{3+}(CH_3CN)_{15}$, as well as those reported from crystallographic data and simulations of bulk solutions [57, 99, 215-218]. The Ln-N distances are expected to be larger in clusters than those obtained in the solid state because of the lack of confinement in the cluster case.

6.4.2. Thermodynamic Data

The cluster enthalpies and the stepwise binding enthalpies of $Ln^{3+}(CH_3CN)_n$ clusters for sizes n = 1-15 are shown in Fig. 6.4.2.1. The cluster enthalpies increase rapidly for all lanthanide ion-acetonitrile clusters until a cluster size of approximately n = 15, at which point the enthalpy starts increasing linearly. This feature occurs at much larger cluster sizes, n = ~36, in water clusters, because acetonitrile molecules residing beyond the first coordination shell bind less tightly to the Ln^{3+} ion than do water molecules in this region. The $Ln^{3+}(CH_3CN)_n$ cluster enthalpies increase across the lanthanide series. For instance, the cluster enthalpy for $Pr^{3+}(CH_3CN)_{15}$ is -713.3 kcal/mol whereas it is -796.4 kcal/mol for $Lu^{3+}(CH_3CN)_{15}$. These values are consistent with the range of binding enthalpies proposed by Baaden *et al.* for similar clusters [99]. For example, the minimum cluster enthalpy predicted by the Baaden model for the $Eu^{3+}(CH_3CN)_{15}$ cluster is -797 ± 11 kcal/mol whereas our prediction is -738.2 ± 3.6 kcal/mol. We believe that the estimates present in this work are more reliable since the Baaden model does not account for the appropriate binding energies of small clusters.

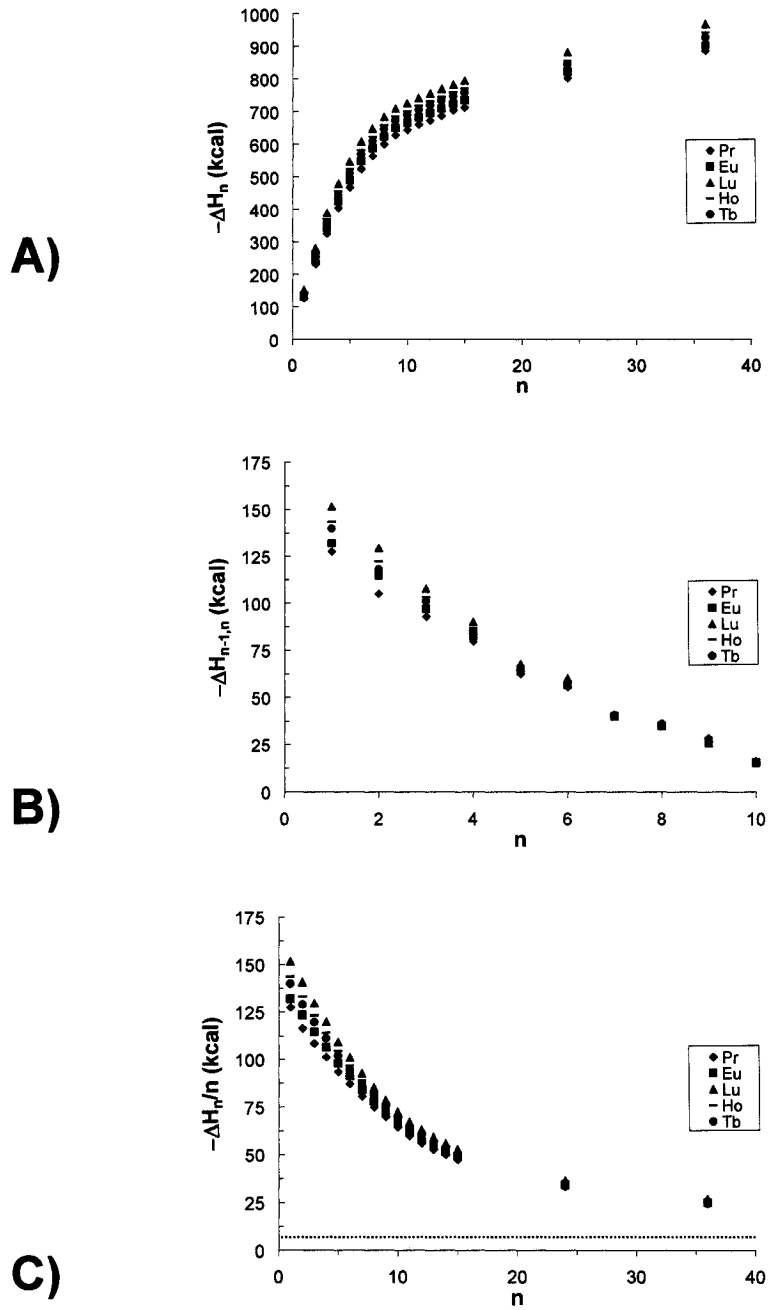

Figure 6.4.2.1. $Ln^{3+}(CH_3CN)_n$ cluster thermodynamics a) Cluster binding enthalpy, b) stepwise binding enthalpy and c) reduced cluster enthalpy vs. cluster size. The experimental heat of vaporization of acetonitrile (-7.9 kcal/mol) is represented by a dotted line [223]. All enthalpies are in kcal/mol.

The stepwise binding enthalpies (Fig. 6.4.2.1.b) increase steadily for n = 1-9 before plateauing, reflecting the completion of the first coordination shell (see first-shell coordination numbers of the $Ln^{3+}(CH_3CN)_{12,15}$ clusters in Table 6.4.1.1.). The stepwise binding enthalpies are largest for the heavier lanthanide ion-solvent clusters, which again is consistent with the trends in ion-solvent interaction energies seen in Table 6.2.2.1. Finally, this convergence occurs at an n much larger than those in $Na^+(CH_3CN)_n$ and $Cs^+(CH_3CN)_n$ clusters [97, 118, 125]. This is a result of the stronger ion-solvent interactions present in the lanthanide ion-solvent clusters compared to monovalent alkali metal ion-acetonitrile clusters. For example, the $Na^+(CH_3CN)$ binding enthalpy is only approximately -20 to -30 kcal/mol, which is close to 5 times smaller than that of $Ln^{3+}(CH_3CN)$.

The stepwise binding enthalpies of $Ho^{3+}(CH_3CN)_n$ and $Ho^{3+}(H_2O)_n$ are shown in Fig. 6.4.2.2. as a function of cluster size, in order to compare the thermodynamics associated with the gradual solvation of the lanthanide ion. The stepwise binding enthalpies of the small $Ho^{3+}(CH_3CN)_n$ clusters are much larger in magnitude than those of $Ho^{3+}(H_2O)_n$ clusters, mostly due to the stronger ion-acetonitrile interaction energies, again attributed to greater polarization effects. But by cluster size 9, the size corresponding to completion of the first coordination shell, the stepwise binding energies become smaller in magnitude for the acetonitrile clusters than for the water clusters [118]. This can be explained by the fact that the acetonitrile molecules are located further away from the ion than water molecules in this same region.

As expected, the reduced cluster enthalpy converges towards the heat of vaporization of acetonitrile (ΔH_{vap} = -7.9 kcal/mol) at large cluster sizes, but very slowly,

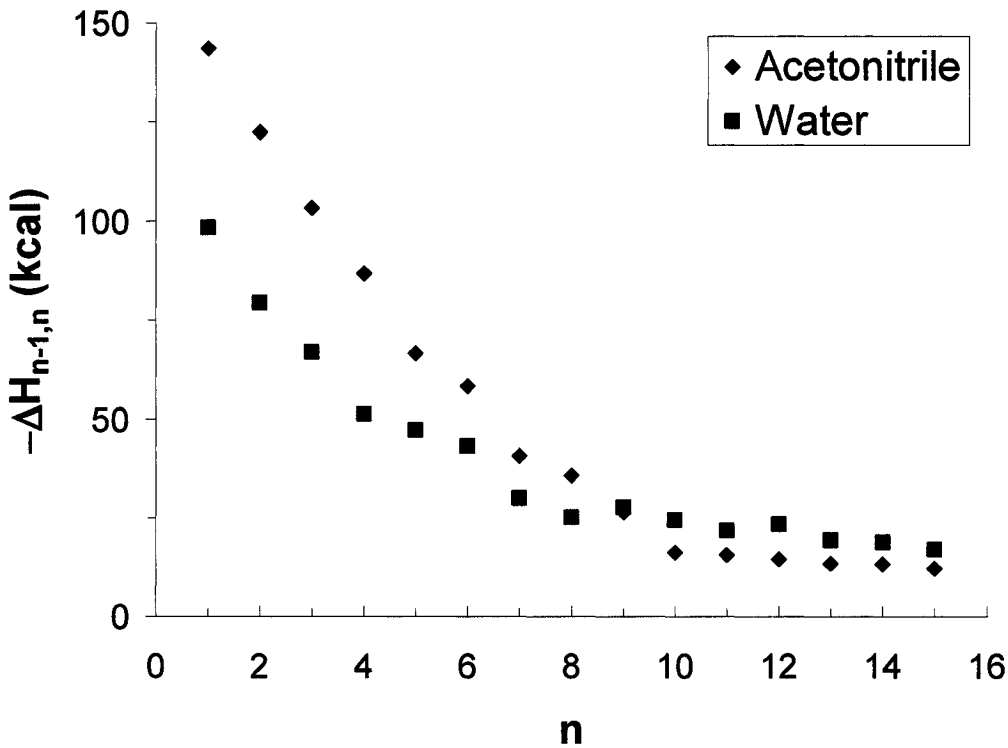

Figure 6.4.2.2. Stepwise binding enthalpy vs. cluster size for $Ho^{3+}(CH_3CN)_n$ and $Ho^{3+}(H_2O)_n$ clusters (n = 1-15). All enthalpies are in kcal/mol.

as shown in Fig. 6.4.2.1.c [223]. The reduced binding enthalpy decreases to an average of -25 kcal/mol for n = 36 for each of the lanthanide ion-acetonitrile clusters studied. In principle, the reduced binding enthalpy should underestimate the heat of vaporization of acetonitrile at the large cluster limit, because of cluster edge effects. A simple, exponential extrapolation of the reduced binding enthalpy suggests that convergence occurs for the heat of vaporization at approximately n = 52, a value far smaller than that found for $Ln^{3+}(H_2O)_n$ clusters (n > 128) [27]. Again, this reflects the weaker ion-solvent and solvent-solvent interactions beyond the first coordination shell in $Ln^{3+}(CH_3CN)_n$ clusters.

6.5. CONCLUSIONS

Model potentials were developed to study the properties of $Ln^{3+}(CH_3CN)_n$ clusters, in order to gain insight into the stability of multivalent clusters under experimental conditions. These model potentials were parameterized to the structural, energetic and electronic properties of small $Ln^{3+}(CH_3CN)_n$ model systems and were later used to propagate the simulations of larger clusters using Monte Carlo techniques. These simulations made use of a recently developed model for gas-phase acetonitrile and so this work also serves as a means of determining the effectiveness of this model in the simulating the behaviour of acetonitrile molecules in ion-solvent cluster simulations.

The cluster enthalpies of $Ln^{3+}(CH_3CN)_n$ predicted by the simulations are found to be large and negative, and much larger than those of simple monovalent ion-acetonitrile clusters, such as $Na^+(CH_3CN)_n$ which are known to form stable species. Thus the results suggest that $Ln^{3+}(CH_3CN)_n$ clusters can be formed as stable species in the absence of

heterolytic cleavage and both proton and electron transfer processes, as would be the case under 'gentle' spray conditions.

The model potentials developed in this work and the simulations reproduce many of the trends associated with the subset of lanthanide ions considered in this work. For instance, the stepwise binding enthalpies are strongest for the heavier lanthanide ion-acetonitrile clusters, as would be expected on the basis of the higher charge:size ratios of these ions. For small cluster sizes, the cluster enthalpy is influenced predominantly by strong ion-solvent interactions, while in large clusters these interactions are far less predominant beyond the first coordination shell. It must be stressed that the stepwise binding enthalpies determined with the model potentials are quantities that have yet to be determined experimentally and thus these results can serve as benchmarks for future experimentation. Using a similar simulation protocol, the thermodynamics associated with several other metal and halide ion-solvent clusters have been reproduced [125, 128, 130].

Also of interest is the convergence of cluster properties to bulk-like values at large cluster sizes. The probability distribution functions (PDF) indicate a clear ion solvation shell structure at large n. The lanthanide ions seem to influence the ordering of the acetonitrile solvent molecules effectively beyond the first coordination shell, but not to the same extent as in water-based clusters. At large cluster sizes, the positions of the first and second coordination shells in our simulations of $Ln^{3+}(CH_3CN)_n$ clusters are similar to those reported in other cluster simulations [99]. At large cluster sizes, the first-shell coordination numbers are 10 for the light ions and 9 for the heavier ions, which is consistent with what has been reported in other simulations. However, only our model

reproduces the traditional shift of only one coordinating ligand across the lanthanide series. With respect to cluster thermodynamics, the reduced cluster binding enthalpies slowly approach the heat of vaporization of bulk acetonitrile with increasing cluster size, converging at cluster size n = 52, which is much larger than what is observed for other ion-acetonitrile clusters because of the larger ion-solvent interaction energies.

It must be noted that cluster properties converge to bulk-like values very differently in $Ln^{3+}(H_2O)_n$ and $Ln^{3+}(CH_3CN)_n$ clusters. In summary, coordination numbers and thermodynamic properties of $Ln^{3+}(CH_3CN)_n$ clusters converge to bulk-like values at cluster sizes that are more than twice as small as those obtained for $Ln^{3+}(H_2O)_n$ clusters. For example, bulk-like first shell coordination numbers are obtained at size n = 64 in $Ln^{3+}(H_2O)_n$ clusters, whereas this occurs at n = 24 in $Ln^{3+}(CH_3CN)_n$ clusters. In addition, the heat of vaporization of water is only achieved at n = 128 for $Ln^{3+}(H_2O)_n$ clusters, which is in sharp contrast to what occurs in acetonitrile clusters. This is again due to the fact that acetonitrile molecules beyond the first coordination shell do not bind as tightly to the central ion as do water molecules, nor do they form strong hydrogen-bonded networks in this region.

Immediate future work will involve parameterizing the remaining set of lanthanide ions and determining whether or not the same trends across the lanthanide ion series will be conserved for other ions. Additionally, a thorough quantum chemistry analysis of the bonding interactions present in $Ln^{3+}(CH_3CN)_n$ clusters, akin to what we have performed previously for water-based clusters, may provide insight into their cluster reduction mechanisms at small cluster sizes [91, 117].

AUTHOR'S NOTE AND SIGNIFICANCE OF PAPER TO THESIS

This paper served several purposes. First, it aided us in determining whether or not similar cluster-to-bulk transitions observed in $Ln^{3+}(H_2O)_n$ clusters could occur in other lanthanide ion-solvent clusters. This appears to be the case, but progression from cluster to bulk properties is clearly dependent on the nature of the ion-solvent interactions. Second, this paper provided insight into the structural and thermodynamic properties of $Ln^{3+}(CH_3CN)_n$ clusters, which have yet to be determined experimentally. These clusters appear to be stable and exhibit similar structural features to those observed in water-based clusters. Finally, the study of $Ln^{3+}(CH_3CN)_n$ clusters provides an ideal means for characterizing interactions between Ln^{3+} ions and N-donor ligands. These findings can be extended to the modeling of other environments where lanthanide ions are ligated to nitrogen atoms, such as in protein metal-binding sites.

CHAPTER 7

7.1. CONCLUSIONS

The primary goal of this thesis was to characterize the structural, electronic and thermodynamic properties of $Ln^{3+}(solvent)_n$ clusters using a vast array of quantum chemistry and statistical mechanics techniques, with the ultimate purpose of identifying the fundamental interactions that govern lanthanide ion-ligand interactions and the possible transition from cluster to bulk properties. From each of the preceding chapters, one can conclude that:

- In both lanthanide ion-water and acetonitrile clusters, the metal to solvent bonding is predominantly electrostatic. This character was demonstrated for small, $Ln^{3+}(H_2O)_n$ complexes using a combination of structural, atomic point charge, Natural Bond Orbital (NBO), Electron Localization Function (ELF) and Atoms-in-Molecules (AIM) analyses, and for $Ln^{3+}(CH_3CN)_n$ clusters using only structural and atomic point charge distribution analysis. Furthermore, a significant amount of charge transfer from the solvent to the lanthanide ion was found to occur upon complexation, the extent of which depends on the hardness of the ligating atom (nitrogen in acetonitrile versus oxygen in water). The predominant feature in Ln^{3+}-solvent bonding was found to arise from the mutual polarization of the ion and the solvent, which governs the cluster structure.
- The coordination structure around the lanthanide ions depends on numerous factors. These include the strength of the ion-solvent interactions, the strength of the solvent-solvent interactions, the cluster size and most importantly, the

charge:size ratio of the ion. The 'S-shaped trend' in Ln^{3+} ion coordination numbers that is observed experimentally was reproduced by our simulations.

- $Ln^{3+}(H_2O)_n$ clusters are predicted to be only metastable species, and thus should not be detected experimentally at small cluster sizes, $n < 9$, due to energetically favourable, intracluster deprotonation processes, which compete with single ligand loss from the cluster. Depending on the cluster size, it dissociates via one or two-step mechanisms, the latter making use of a salt-bridge intermediate arising from the exchange of a proton between a first and second-shell water molecule.
- Model potentials parameterized for $Ln^{3+}(solvent)_n$ clusters do reproduce bulk-like properties at large cluster sizes. Such properties include the solvation shell structure inferred by the radial probability distribution functions, first and second-shell coordination numbers and trends in ion-ligand distances. Therefore, $Ln^{3+}(solvent)_n$ clusters may serve as good models for the bulk, and model potentials developed for small, $Ln^{3+}(H_2O)_n$ clusters may be used to simulate the properties of larger clusters or even bulk solvation.
- Finally, the thermodynamic properties of $Ln^{3+}(solvent)_n$ clusters predicted in this work have yet to be determined experimentally. Our results may prove to be useful benchmarks for future experimentation in this field.

7.2 FUTURE WORK

As discussed earlier, assessing the effects of cluster size on the deprotonation processes is of particular importance. Characterizing stationary points for clusters of increasing size with quantum chemistry calculations may turn out to be a daunting task;

one may instead employ biased ab initio molecular dynamics to simulate such reactions. In this approach, the atomic motion is propagated using a molecular dynamics routine guided by the forces calculated from single-point quantum chemistry calculations at each time step, which makes it very computationally expensive. The deprotonation process could not be monitored with simulations employing our model potentials, since the latter make use of a rigid water model that does not account for water deprotonation. This could potentially be done using a variety of hybrid methods. One avenue would be to use Atom-centered Density Matrix Propagation methods which are easily amenable to density function theory (DFT)-based calculations [224-226]. One might also consider semi-empirical DFT models such as the Self-Consistent Charge Density-Functional Tight Binding (SCC-DFTB) method, which is computationally very efficient [226, 227]. However, these methods have yet to be developed for lanthanide-based systems. This work would be instrumental in confirming the cluster sizes at which deprotonation stops being the most favourable pathway and stable clusters can be observed experimentally, as reported by Bush *et al.* in a very recent paper (June 2006) [92].

Similar to the work on $Ln^{3+}(H_2O)_n$ clusters, a thorough assessment of the electronic properties of $Ln^{3+}(CH_3CN)_n$ clusters using NBO, ELF and AIM analyses is required to properly determine whether or not covalent bonding plays a role in the ion-acetonitrile interactions. We note, however, that it is unlikely that this is the case considering that several $M^{q+}(H_2O)_n$ complexes have similar cluster binding energies to those found for $Ln^{3+}(CH_3CN)_n$ clusters that the ion-solvent distances are similar for both types of clusters, and that the ion-water bonds in these clusters did not possess any

significant covalent character. This study may also lend insight into potential cluster reduction mechanisms for this system.

Other future work would involve the determination of the spectroscopic properties of Ln^{3+} ions in water and acetonitrile clusters. As one of the central goals of the Capobianco group is to determine the spectroscopic properties of Ln^{3+} ions in a variety of different host environments, it should be established 1) whether the model potentials are capable of producing an ensemble of large clusters whose structures result in the electronic transitions of Ln^{3+} ions observed in bulk solution and 2) how the ion's spectra evolves with cluster size. Given that Eu^{3+} has a simple set of energy levels, initial development of the spectroscopic model should be geared towards reproducing spectra in large solvent clusters. As it stands, we are currently modifying versions of the BNMGENE and SPECTRO programs developed by Stéphane Chaussedent at l'Université d'Angers such that it can be coupled to a home-grown program called SPECTRA2 [199, 200, 228]. The first two programs produce the necessary crystal field parameters and ultimately the Stark levels and transition probabilities, whereas the last program calculates line intensities, crystal field strength and produces the spectral envelope. Once the program is capable of reproducing bulk-like spectra for large $Ln^{3+}(solvent)_n$ clusters, the spectral properties of smaller clusters can then be characterized.

It should be noted that the BNMGENE program is based on a simple point-charge model and as such only accounts for perturbations to the electronic levels of lanthanide ions arising from a field of point charges [52, 68, 229]. However, our studies have shown that polarization is an important component of the lanthanide ion-ligand interaction, and

so modification of the BNMGENE program so as to include multipolar effects is necessary. This modification may enhance the overall predictions of the electronic energy levels of the Ln^{3+} ion in clusters, and likely in other environments.

Future work may involve the modelling of more complex environments, such as nanocrystals, sol-gels and proteins where the ion-solvent cluster parameters can provide insight into the treatment of Ln^{3+}-O or Ln^{3+}-N interactions, particularly within the first coordination shell and in the immediate environment. In the case of water, the OPCS model can be used to account for the effects of hydration on spectroscopic properties. In the case of nanocrystals and sol-gels, it is well-documented that water is often trapped in these materials during their synthesis or is adsorbed to their surface post-synthesis, and the strong vibrational modes of water thus decrease their overall luminescence [84, 85]. Additionally, water often acts as a coordinating ligand in the metal-binding sites of proteins [65]. In all three cases, the metal-binding site is a self-contained environment and so the OPCS model may yield improved structural and spectroscopic properties of these various materials/complexes, compared to what may be obtained using other water models designed for liquid or solution studies, since this environment is cluster-like.

Finally, to test the range of applicability of the water and acetonitrile models, liquid simulations should be performed to assess whether or not bulk liquid properties can be reproduced. Interestingly, it has recently been shown that highly polarizable ions can accumulate at the air-water interface, a finding that is in sharp contrast to what has been traditionally believed about the solvation of ions in solution [230, 231]. Using liquid simulations with our recently developed model potentials, we could potentially predict the behaviour of Ln^{3+} ions at such an interface and correlate our findings with

what has been obtained from first sum frequency generation experiments [230, 231]. One means of doing so is by implementing our model potential into the TINKER software package, which already possesses a framework for performing liquid simulations [232].

REFERENCES

1. A.J. Stace, *Cluster Solutions.* Science, 2001. **294**: p. 1292-1293.

2. G. González-Moraga, *Cluster Chemistry - Introduction to the Chemistry of Transition Metal and Main Group Element Molecular Clusters*. 1993, New York, NY: Springer-Verlag.

3. J.V. Coe, *Fundamental Properties of Bulk Water From Cluster Ion Data.* Int. Rev. Phys. Chem., 2001. **20**: p. 33-58.

4. S. Sugano and H. Koizumi, *Microcluster Physics*. 2nd ed. Springer Series in Materials Science, ed. J.P. Toennies, et al. 1998, New York, NY: Springer-Verlag.

5. A.J. Stace, *Metal Ion Solvation in the Gas Phase: The Quest for Higher Oxidation States.* J. Phys. Chem. A, 2002. **106**: p. 7993-8005.

6. A.W. Castleman_Jr. and R.G. Keesee, *Clusters: Bridging the Gas and Condensed Phases.* Acc. Chem. Res., 1986. **19**: p. 413-419.

7. A.W. Castleman_Jr. and R.G. Keesee, *Ionic Clusters.* Chem. Rev., 1986. **86**: p. 589-618.

8. V. Kumar, K. Esfarjani, and Y. Kawazoe, *Ab Initio Simulations on Microclusters*, in *Clusters and Nanomaterials: Theory and Experiment*, Y. Kawazoe, T. Kondow, and K. Ohno, Editors. 2002, Springer-Verlag: New York, NY.

9. P. Buffat and J.-P. Borel, *Size Effect on the Melting Temperature of Gold Particles.* Phys. Rev. A, 1976. **13**: p. 2287-2298.

10. S.S. Zumdahl and S.A. Zumdahl, *Chemistry*. 6th ed. 2003, Boston, MA: Houghton Mifflin Company.

11. G.A. Krestov, *Thermodynamics of Solvation: Solution and Dissolution, Ions and Solvents, Structure and Energetics*, ed. T.J. Kemp. 1991, New York, NY: Ellis Norwood.

12. A.T. Blades, P. Jayaweera, M.G. Ikonomou, and P. Kebarle, *Studies of Alkaline Earth and Transition Metal M^{++} Gas Phase Ion Chemistry.* J. Chem. Phys., 1990. **92**(10): p. 5900-5906.

13. A.T. Blades, P. Jayaweera, M.G. Ikonomou, and P. Kebarle, *Ion-Molecule Clusters Involving Doubly Charged Metal Ions (M^{2+}).* Int. J. Mass Spectrom., 1990. **102**: p. 251-267.

14. A.T. Blades, P. Jayaweera, M.G. Ikonomou, and P. Kebarle, *First Studies of the Gas Phase Ion Chemistry of M^{3+} Metal Ion Ligands.* Int. J. Mass. Spectrom: Ion Processes, 1990. **101**: p. 325-336.

15. S.B. Nielsen, M. Masella, and P. Kebarle, *Competitive Gas-Phase Solvation of Alkali Metal Ions by Water and Methanol.* J. Phys. Chem.B, 1999. **103**: p. 9891-9898.

16. T.F. Magnera, D.E. David, D. Stulik, R.G. Orth, H.T. Jonkman, and J. Michl, *Production of Metal Ions by Fast Ion or Atom Beam Sputtering. Collision-induced Dissociation and Successive Hydration Energies of Gaseous Cu^+ with 1-4 Water Molecules.* J. Am. Chem. Soc., 1989. **111**: p. 5036-5043.

17. I. Dzidic and P. Kebarle, *Hydration of the Alkali Ions in the Gas Phase. Enthalpies and Entropies of Reactions $M^+(H_2O)_{n-1} + H_2O = M^+(H_2O)_n$.* J. Phys. Chem., 1970. **74**: p. 1466-1474.

18. T. Kojima, I. Kudaka, T. Sato, T. Asakawa, R. Akiyama, V. Kawashima, and H. Kiraoka, *Observation of Triply Charged Metal Ion Clusters by Electrospray and Laser Spray.* Rapid Commun. Mass Spectrom., 1999. **13**(2090-2097).

19. D. Vukomanovic and J.A. Stone, *A Low-Energy CAD Study of the Ions $MOH(H_2O)^+$ (M = Mn, Co, Ni, Cu, Zn) and $[M(H_2O_2)]^+$ (M = Cr, Fe, La, Pr).* Int. J. Mass. Spec., 2000. **202**: p. 251-259.

20. A.J. Stace, N.R. Walker, and S. Firth, *$[Cu\cdot(H_2O)_n]^{2+}$ Clusters: The First Evidence of Aqueous Cu(II) in the Gas Phase.* J. Am. Chem. Soc., 1997. **119**: p. 10239 - 10240.

21. A.A. Shvartsburg, *DMSO Complexes of Trivalent Metal Ions: First Microsolvated Trications Outside of Group 3.* J. Am. Chem. Soc., 2002. **124**: p. 12343-12351.

22. A.A. Shvartsburg, *Gas-Phase Trications in Protic Solvent Complexes.* J. Am. Chem. Soc., 2002. **124**: p. 7910-7911.

23. A.A. Shvartsburg, *Acetonitrile Complexes of Triply Charged Metal Ions: Are Ligated Trications Intrinsically More Prone to Charge Reduction than Dications.* Chem. Phys. Lett., 2002. **360**: p. 479-486.

24. Z.L. Cheng, K.W.M. Siu, R. Guevremont, and S.S. Berman, *Solvent-Derived Metal Oxides in Electrospray Mass Spectrometry of Metal Salt Solutions.* Org. Mass. Spectrom, 1992. **27**: p. 1370-1376.

25. M.P. Dobson and A.J. Stace, *The Chemistry of Sr^{2+} in Association with Propanol Clusters.* Int. J. Mass Spectrom. Ion Processes, 1990. **165/166**: p. 5-12.

26. Y.K. Lau, S. Ikuta, and P. Kebarle, *Thermodynamics and Kinetics of the Gas-Phase Reactions: $H_3O^+(H_2O)_{n-1} + H_2O = H_3O^+(H_2O)_n$.* J. Am. Chem. Soc., 1982. **104**: p. 1462-1469.

27. T.F. Magnera, D.E. David, and J. Michl, *Gas-Phase Water and Hydroxyl Binding Energies for Monopositive First-Row Transition-Metal Ions.* J. Am. Chem. Soc., 1989. **111**: p. 4100-4101.

28. M. Peschke, A.T. Blades, and P. Kebarle, *Hydration Energies and Entropies for Mg^{2+}, Ca^{2+}, Sr^{2+}, and Ba^{2+} from Gas-Phase Ion-Water Molecule Equilibria.* J. Phys. Chem. A, 1998. **102**: p. 9978-9985.

29. M. Peschke, A.T. Blades, and P. Kebarle, *Formation, Acidity and Charge Reduction of the Hydrates of Doubly Charged Ions M^{2+} (Be^{2+}, Mg^{2+}, Ca^{2+}, Zn^{2+}).* Int. J. Mass Spectrom., 1999. **185/186/187**: p. 685-699.

30. S.E. Rodriquez-Cruz, R.A. Jockusch, and E.R. Williams, *Binding Energies of Hexahydrated Alkaline Earth Metal Ions, $M^{2+}(H_2O)_6$, M = Mg, Ca, Sr, Ba: Evidence of Isomeric Structures for Magnesium.* J. Am. Chem. Soc., 1999. **121**: p. 1986-1987.

31. A.J. Stace, *Metal Ions in Hydrogen Bonded Solvents: a Gas Phase Perspective.* Phys. Chem. Chem. Phys., 2001. **3**: p. 1935-1941.

32. Z. Vager, R. Naamen, and E.P. Kanter, *Structures of Molecules and Clusters as Determined by Coulomb Explosions*, in *Ion and Cluster Ion Spectroscopy and Structure*, J.P. Maier, Editor. 1989, Elsevier: New York, NY. p. 1-26.

33. N.R. Walker, R.R. Wright, A.J. Stace, and C.A. Woodward, *Cluster Ion Studies of Ho^{2+} and Ho^{3+} Solvation in the Gas Phase.* Int. J. Mass. Spec., 1999. **188**: p. 113-119.

34. N. Walker, M.P. Dobson, R.R. Wright, P.E. Barran, J.N. Murrell, and A.J. Stace, *A Gas-Phase Study of the Coordination of Mg^{2+} and Oxygen- and Nitrogen-Containing Ligands.* J. Am. Chem. Soc., 2000. **122**: p. 11138-11145.

35. C.A. Woodward, M.P. Dobson, and A.J. Stace, *Intracluster Charge-Transfer Chemistry in $[Mg\cdot(C_3H_7OH)_n]^{2+}$ Complexes.* J. Phys. Chem., 1996. **100**: p. 5605-5607.

36. C.A. Woodward, M.P. Dobson, and A.J. Stace, *Chemistry of Mg^+ and Mg^{2+} in Association with Methanol Clusters.* J. Phys. Chem. A, 1997. **101**: p. 2279-2287.

37. R.R. Wright, N.R. Walker, S. Firth, and A.J. Stace, *Coordination and Chemistry of Stable Cu(II) Complexes in the Gas Phase.* J. Phys. Chem. A, 2001. **105**: p. 54-64.

38. H. Cox, G. Akibo-Betts, R.R. Wright, N.R. Walker, S. Curtis, B. Duncombe, and A.J. Stace, *Solvent Coordination in Gas-Phase $[Mn(H_2O)_n]^{2+}$ and $[Mn(ROH)_n]^{2+}$ Complexes: Theory and Experiment.* J. Am. Chem. Soc., 2003. **125**: p. 233-242.

39. P. Kebarle and A.M. Hogg, *Heats of Hydration and Solvation by Mass Spectrometry.* J. Chem. Phys., 1965. **42**: p. 798-799.

40. V.E. Bondybey and M.K. Beyer, *How Many Molecules Make a Solution?* Int. Rev. Phys. Chem., 2002. **21**: p. 277-306.

41. R.G. Keesee and A.W. Castelman_Jr., *Structure of Solvated Ion Clusters*, in *Ion and Cluster Ion Spectroscopy and Structure*, J.P. Maier, Editor. 1989, Elsevier: New York, NY. p. 275-329.

42. J.M. Lisy, *Spectroscopy and Structure of Solvated Alkali-Metal Ions.* Rev. Phys. Chem., 1997. **16**: p. 267-289.

43. G. Niedber-Schatteburg and V.E. Bondybey, *FT-ICR Studies of Solvation Effects in Ionic Water Clusters.* Chem. Rev., 2000. **100**: p. 4059-4066.

44. C. Dedonder-Lardeux, G. Grégoire, C. Jouvet, S. Martrenchard, and D. Solgadi, *Charge Separation in Molecular Clusters: Dissolution of a Salt in a Salt-$(Solvent)_n$ Cluster.* Chem. Rev., 2000. **100**: p. 4023-4037.

45. J.J.R. Fraústo_da_Silva and R.J.P. Williams, *The Biological Chemistry of the Elements: The Inorganic Chemistry of Life.* 2nd ed. 2001, New York, NY: Oxford University Press.

46. T. Dudev, J.A. Cowen, and C. Lim, *Competitive Binding in Magnesium Coordination Chemistry: Water versus Ligands of Biological Interest.* J. Am. Chem. Soc., 1999. **121**: p. 7665-7673.

47. P.G. Lethbridge and A.J. Stace, *Reactivity-structure Correlations in Ion Clusters: A Study of the Unimolecular Fragmentation Patterns of Argon Ion Clusters, Ar_n^+, for n in the Range 30-200.* J. Chem. Phys., 1988. **89**: p. 4062-4073.

48. M. Barber, R.S. Bordoli, G.J. Elliott, R.D. Sedgewick, and A.N. Tyler, *Fast Atom Bombardment Mass Spectrometry.* Anal. Chem., 1982. **54**: p. 645A-657A.

49. P. Kebarle and L. Tang, *From Ions in Solution to Ions in Gas Phase: The Mechanism of Electrospray Mass Spectrometry.* Anal. Chem., 1993. **65**: p. 972-986.

50. M. Yamashita and J.B. Fenn, *Electrospray Ion Source. Another Variation on the Free-Jet Theme.* J. Phys. Chem., 1984. **88**: p. 4451-4459.

51. M. Yamashita and J.B. Fenn, *Negative Ion Production with the Electrospray Ion Source.* J. Phys. Chem., 1984. **88**: p. 4671-4675.

52. C.J. Jones, *d and f-block Chemistry.* 2001, Cambridge, UK: Royal Society of Chemistry.

53. G.H. Dieke, *Spectra and Energy Levels of Rare Earth Ions in Crystals.* 1968, New York, NY: Interscience Publishers.

54. J.E. Huheey, E.A. Keiter, and R.L. Keiter, *Inorganic Chemistry: Principles of Structure and Reactivity.* 4th ed. 1993, New York, NY: HarperCollins College.

55. G.R. Choppin, *Factors in Ln(III) Complexation.* J. Alloys and Compd., 1997. **249**: p. 1-8.

56. P.G. Allen, J.J. Bucher, D.K. Shuh, N.M. Edelstein, and I. Craig, *Coordination Chemistry of Trivalent Lanthanide and Actinide Ions in Dilute and Concentrated Chloride Solutions.* Inorg. Chem., 2000. **39**: p. 595-601.

57. G.B. Deacon, B. Görtler, P.C. Junk, E. Lork, R. Mews, J. Petersen, and B. Zemva, *Syntheses of Some Homoleptic Acetonitrile Lanthanoid(III) Complexes.* J. Chem. Soc. Dalton Trans., 1998. **22**(3887-3891).

58. A. Habenschuss and F.H. Spedding, *The Coordination (Hydration) of Rare Earth Ions in Aqueous Chloride Solutions from X-Ray Diffraction. II. $LaCl_3$, $PrCl_3$ and $NdCl_3$.* J. Chem. Phys., 1979. **70**: p. 3758-3763.

59. A. Habenschuss and F.H. Spedding, *The Coordination (Hydration) of Rare Earth Ions in Aqueous Chloride Solutions from X-Ray Diffraction. I. $TbCl_3$, $DyCl_3$, $ErCl_3$, $TmCl_3$ and $LuCl_3$.* J. Chem. Phys., 1979. **70**: p. 2797-2805.

60. A. Habenschuss and F.H. Spedding, *The Coordination (Hydration) of Rare Earth Ions in Aqueous Chloride Solutions from X-ray Diffraction. III. $SmCl_3$, $EuCl_3$, and series behavior.* J. Chem. Phys., 1980. **73**: p. 442-450.

61. E.N. Rizkalla and G.R. Choppin, *Hydration and Hydrolysis of Lanthanides.* Handbook on the Physics and Chemistry of Rare-Earths, ed. K.A. Gschneider Jr. and L. Eyring. Vol. 15. 1991, New York, NY: Elsevier Science Publishers B.V.

62. E.N. Rizkalla and G.R. Choppin, *Lanthanides and Actinides Hydration and Hydrolysis.* Handbook on the Physics and Chemistry of Rare-Earths, ed. K.A. Gschneider Jr., et al. Vol. 18. 1994, New York, Ny: Elsevier Science, B.V.

63. N. Kaltsoyannis, *Relativistic Effects in Inorganic and Organometallic Chemistry.* J. Chem. Soc. Dalton Trans., 1996: p. 1-11.

64. W.D. Horrocks_Jr. and D.R. Sudnick, *Lanthanide Ion Luminescence Probes of the Structure of Biological Macromolecules.* J. Am. Chem. Soc., 1981. **14**: p. 384-392.

65. S.R. Hughes, *Lanthanides as Probes of Metal-Binding Sites in Human Brain Calbindin D_{28K}*, in *Biology*. 1999, Concordia University: Montreal, QC. p. 58.

66. D.G. Karraker, J. Chem. Educ., 1970. **47**: p. 424-430.

67. J.-C.G. Bünzli and C. Piguet, *Lanthanide-Containing Molecular and Supramolecular Polymetallic Functional Assemblies.* Chem. Rev., 2002. **102**: p. 1897-1928.

68. G. Cormier, *Molecular Dynamics Simulation and Crystal-Field Theory: Predicting the Optical Spectra and Structure of Rare-Earth Doped Inorganic Glasses*, in *Department of Chemistry and Biochemistry*. 1993, Concordia University: Montreal, QC. p. 213.

69. S.I. Weissman, *Intramolecular Energy Transfer: The Fluorescence of Complexes in Europium.* J. Chem. Phys., 1942. **10**: p. 214-217.

70. J.-C.G. Bünzli, N. Andre, M. Elhabiri, G. Muller, and C. Piguet, *Trivalent Lanthanide Ions: Versatile Coordination Centers with Unique Spectroscopic and Magnetic Properties.* J. Alloys and Compd., 2000. **303-304**: p. 66-74.

71. D. Parker, *Luminescent Lanthanide Sensors for pH, pO_2 and Selected Ions.* Coord. Chem. Rev., 2000. **205**: p. 109-130.

72. H. Tsukube and S. Shinoda, *Lanthanide Complexes in Molecular Recognition and Chirality Sensing of Biological Substrates.* Chem. Rev., 2002. **102**: p. 2389-2403.

73. G.F. de_Sá, O.L. Malta, C. de_Mello_Donegá, A.M. Simas, R.L. Longo, P.A. Santa-Cruz, and E.F. da_Silva_Jr., *Spectroscopic Properties and Design of Highly Luminescent Lanthanide Coordination Complexes.* Coord. Chem. Rev., 2000. **196**: p. 165-195.

74. J.L. Sessler, W.C. Dow, D. O'Connor, A. Harriman, G. Hemmi, T.D. Mody, R.A. Miller, F. Qing, S. Springs, K. Woodburn, and S.W. Young, *Biomedical Applications of Lanthanide(III) Texaphyrins Lutetium(III) Texaphyrins as Potential Photodynamic Therapy Photosensitizers.* J. Alloys Comp., 1997. **249**: p. 146-152.

75. P.R. Selvin, *Principles and Biophysical Applications of Lanthanide-Based Probes.* Annu. Rev. Biophys. Biomol. Struct., 2002. **31**: p. 275-302.

76. K. Matsumoto, K. Majima, T. Fukui, S. Sueda, and J. Yuan, *Fluorescent Lanthanoid Labels for Time-Resolved Fluorimetry in Biological Trace Analysis.* RIKEN Review, 2001. **35**: p. 105-106.

77. J. Nurmi, T. Wikman, M. Karp, and T. Lövgren, *High-Performance Real-Time Quantitative RT-PCR Using Lanthanide Probes and a Dual-Temperature Hybridization Assay.* Anal. Chem., 2002. **74**: p. 3525-3532.

78. J.A. Ocana, M. Callejon, and F.J. Barragan, *Application of Terbium-Sensitized Luminescence for the Determination of Grepafloxacin in Human Urine and Serum.* J. Phar. Sci., 2001. **90**: p. 1553-1557.

79. R. Naccache, F. Vetrone, J.C. Boyer, J.A. Capobianco, A. Speghini, and M. Bettinelli, *Visible Upconversion Emission of Pr^{3+} Doped Gadolinium Gallium Garnet (GGG) Nanocrystals.* J. Nanosci. Nanotechno., 2004. **4**: p. 1025-1031.

80. F. Vetrone, J.C. Boyer, J.A. Capobianco, A. Speghini, and M. Bettinelli, *Significance of Yb^{3+} Concentration on the Upconversion Mechanisms in Codoped Y_2O_3:Er^{3+}, Yb^{3+} Nanocrystals.* J. Appl. Phys., 2004. **96**: p. 661-667.

81. R. Naccache, F. Vetrone, J.C. Boyer, J.A. Capobianco, A. Speghini, M. Bettinelli, and G.C. Righini, *Upconversion Luminescence of a Calcium Sodium Aluminosilicate Glass Doped with Erbium.* Mater. Lett., 2004. **58**: p. 2207-2212.

82. J.C. Boyer, F. Vetrone, J.A. Capobianco, A. Speghini, and M. Bettinelli, *Yb^{3+} Ion As a Sensitizer for the Upconversion Luminescence in Nanocrystalline $Gd_3Ga_5O_{12}$:Ho^{3+}.* Chem. Phys. Lett., 2004. **390**: p. 403-407.

83. J.C. Boyer, F. Vetrone, J.A. Capobianco, A. Speghini, M. Zambelli, and M. Bettinelli, *Investigation of the Upconversion Processes in Nanocrystalline $Gd_3Ga_5O_{12}$:Ho^{3+}.* J. Lumin., 2004. **106**: p. 263-268.

84. F. Vetrone, J.C. Boyer, and J.A. Capobianco, *Yttrium Oxide Nanocrystals: Luminescent Properties and Applications*, in *The Encyclopedia of Nanoscience and Nanotechnology*, H.S. Nalwa, Editor. 2004, American Scientific Publishers: Stevenson Ranch, CA. p. 725-765.

85. F. Vetrone, J.-C. Boyer, and J.A. Capobianco, *Luminescence, Optical Spectroscopy, and Applications of Rare Earth Doped Y_2O_3 Nanocrystals*, in *The Handbook of Luminescence, Display Materials and Devices*, H.S. Nalwa and L.S. Rohwer, Editors. 2003, American Scientific Publishers: Los Angeles, CA. p. 141-186.

86. A.D. Sherry, *MR Imaging and Spectroscopy Applications of Lanthanide Complexes with Macrocyclic Phosphonate and Phosphonate Ester Ligands.* J. Alloys and Compd., 1997. **249**: p. 153-157.

87. R.G. Shulman and J. Wyluda, *Effects of Gadolinium Upon the H_2O Nuclear Resonance.* J. Chem. Phys., 1959. **30**: p. 335-336.

88. S. Aime, M. Botta, M. Fasano, and E. Terreno, *Lanthanide(III) chelates for NMR biomedical applications.* Chem. Soc. Rev., 1998. **27**: p. 19-29.

89. R.B. Lauffer, *Paramagnetic Metal Complexes as Water Proton Relaxation Agents for NMR Imaging: Theory and Design.* Chem. Rev., 1987. **87**: p. 901-927.

90. I.I. Stewart and G. Horlick, *Electrospray Mass Spectra of Lanthanides.* Anal. Chem., 1994. **66**: p. 3983-3993.

91. S.R. Hughes, J.A. Capobianco, and G.H. Peslherbe, *Are Trivalent Europium-Water Clusters Stable Species? A Theoretical Study of the Deprotonation of* $Eu^{3+}(H_2O)_n$ *Clusters.* to be submitted.

92. M. Bush, R.J. Saykally, and E.R. Williams, *Formation of hydrated triply charged metal ions from aqueous solutions using nanodrop mass spectrometry.* Int. J. Mass Spectrom., 2006. **253**: p. 256-262.

93. K.B. Snow and T.F. Thomas, *Mass spectrum, ionization potential, and appearance potential for fragment ions of sulfuric acid vapor.* Int. J. Mass Spectrom. Ion Processes, 1990. **96**: p. 49-68.

94. M. Gochel-Dupuis, J. Delwiche, M.-J. Hubin-Franskin, and J.E. Collin, *High-resolution HeI photoelectron spectrum of acetonitrile.* Chem. Phys. Lett., 1992. **193**: p. 41-48.

95. R.D. Bowen and A. Maccoll, *Low energy, low temperature mass spectra. 2 - low-energy, low-temperature mass spectra of some small saturated alcohols and ethers.* Org. Mass. Spectrom, 1984. **19**: p. 379-384.

96. G. Mouvier and R. Hernandez, *Ionisation and appearance potentials of alkylketones.* Org. Mass. Spectrom, 1975. **10**: p. 958-969.

97. S.R. Hughes, J.A. Capobianco, and G.H. Peslherbe, *A Theoretical Study of the Hydration of Trivalent Lanthanide Ions Across the Series.* to be submitted.

98. T. Asada and K. Nishimoto, *Monte Carlo Simulations of* $M^+Cl^-(H_2O)_n$ *(M = Li, Na) Clusters and the Dissolving Mechanism of Ion Pairs in Water.* Chem. Phys. Lett., 1995. **232**: p. 518-523.

99. M. Baaden, F. Berny, C. Madic, and G. Wipff, M^{3+} *Lanthanide Cation Solvation by Acetonitrile: The Role of Cation Size, Counterions, and Polarization Effects Investigated by Molecular Dynamics and Quantum Mechanical Simulations.* J. Phys. Chem. A, 2000. **104**: p. 7659-7671.

100. C.W. Bauschlicher, S.R. Langhoff, H. Partridge, J.E. Rice, and A. Komornicki, *A Theoretical Study of* $Na(H_2O)_n^+$ *(n=1-4).* J. Chem. Phys., 1991. **95**(7): p. 5142-5148.

101. C.W. Bauschlicher, M. Sodupe, and H. Partridge, *A Theoretical Study of the Positive and Dipositive Ions of* $M(NH_3)_n$ *and* $M(H_2O)_n$ *for M=Mg, Ca, or Sr.* J. Chem. Phys., 1992. **96**(6): p. 4453-4463.

102. A. Bakker, K. Hermanson, J. Lindgren, M.M. Probst, and P.A. Bopp, *Interaction of Aluminum(III) with Water. An Ab Initio Study.* Int. J. Quantum Chem., 1999. **75**: p. 659-669.

103. M. Beyer, E.R. Williams, and V.E. Bondybey, *Unimolecular Reactions of Dihydrated Alkaline Earth Metal Dications $M^{2+}(H_2O)_2$, M = Be, Mg, Ca, Sr, and Ba: Salt-Bridge mechanism in the Proton-Transfer Reaction $M^{2+}(H_2O)_2$ -> $MOH^+ + H_3O^+$.* J. Am. Chem. Soc., 1999. **121**: p. 1565-1573.

104. C.W. Bock and J.P. Glusker, *Organization of Water around a Beryllium Cation.* Inorg. Chem., 1993. **32**: p. 1242-1250.

105. C.W. Bock, A. Kaufman, and J.P. Glusker, *Coordination of Water to Magnesium Cations.* Inorg. Chem., 1994. **33**: p. 419-427.

106. U. Cosentino, G. Moro, D. Pitea, L. Calabi, and A. Maiocchi, *Ab initio Effective Core Potential Calculations on Lanthanide Complexes: Basis Sets and Electron Correlation Effects in the Study of $[Gd\text{-}(H_2O)_9]^{3+}$.* J. Mol. Struc., 1997. **392**: p. 75-85.

107. U. Cosentino, A. Villa, D. Pitea, G. Moro, and V. Barone, *Extension of Computational Chemistry to the Study of Lanthanide (III) Ions in Aqueous Solution: Implementation and Validation of a Continuum Solvent Approach.* J. Phys. Chem. B, 2000. **104**: p. 8001-8007.

108. A.-L. Derepas, J.-M. Soudan, V. V. Brenner, J.-P. Dognon, and P. Millie, *Can We Understand the Different Coordinations and Structures of Closed-Shell Metal Cation-Water Clusters?* J. Comput. Chem., 2002. **23**: p. 1013-1030.

109. E.D. Glendening, *Natural Energy Decomposition Analysis: Explicit Evaluation of Electrostatic and Polarization Effects with Application to Aqueous Clusters of Alkali Metal Cations and Neutrals.* J. Am. Chem. Soc., 1996. **118**: p. 2473-2482.

110. E.D. Glendening and D. Feller, *Cation-Water Interactions: The $M^+(H_2O)_n$ Clusters for Alkali Metals, M = Li, Na, K, Rb and Cs.* J. Phys. Chem., 1995. **99**: p. 3060-3067.

111. E.D. Glendening and D. Feller, *Dication-Water Interactions: $M^{2+}(H_2O)_n$ Clusters for Alkaline Earth Metals M = Mg, Ca, Sr, Ba, and Ra.* J. Phys. Chem., 1996. **100**: p. 4790-4797.

112. E.D. Glendening and P.A. Petillo, *Structure and Energetics of Gd(III) Interactions in Water and Ammonia.* J. Phys. Chem. B, 2001. **105**: p. 1489-1493.

113. K. Hashimoto and K. Morokuma, *Ab Initio Molecular Orbital Study of $Na(H_2O)_n$ (n = 1-6) Clusters and Their Ions. Comparison of Electronic Structure of the "Surface" and "Interior" Complexes.* J. Am. Chem. Soc., 1994. **116**: p. 11436-11443.

114. K. Hashimoto, N. Yoda, and S. Iwata, *Theoretical study of hydrated Be^{2+} ions.* Chem. Phys., 1987. **116**: p. 193-202.

115. K. Hashimoto, N. Yoda, Y. Osamura, and S. Iwata, *Molecular Orbital Study on the Mechanism of Oxidation of a Beryllium Atom in Acidic Solution.* J. Am. Chem. Soc., 1990. **112**(7189-7196).

116. S. Hengrasmee and M.M. Probst, *A Study of Hydrated Rare Earth Ions.* Z. Naturforsch., 1991. **46a**: p. 117-121.

117. S.R. Hughes, J.A. Capobianco, and G.H. Peslherbe, *On the Nature of Bonding Interactions in Small Metal-Ion Water Clusters.* to be submitted.

118. S.R. Hughes, T.-N.V. Nguyen, J.A. Capobianco, and G.H. Peslherbe, *A Theoretical Study of Trivalent Lanthanide Ion Microsolvation in Water Clusters from First Principles.* Int. J. Mass Spectrom., 2005. **241**: p. 283-294.

119. M.S. Islam, R.A. Pethrick, and D. Pugh, *Ab Initio Study of Potassium Ion Clusters of Methanol and Acetonitrile and a Systematic Comparison with Hydrated Clusters.* J. Phys. Chem. A, 1998. **102**: p. 2201-2208.

120. B. Kallies and R. Meier, *Electronic Structure of 3d[$M(H_2O)_6$]$^{3+}$ Ions from ScIII to FeIII: A Quantum Mechanical Study Based on DFT Computations and Natural Bond Orbital Analyses.* Inorg. Chem., 2001. **40**: p. 3101-3112.

121. A. Kaufman-Katz, J.P. Glusker, S.A. Beebe, and C.W. Bock, *Calcium Ion Coordination: a Comparison with that of Beryllium, Magnesium and Zinc.* J. Am. Chem. Soc., 1996. **118**: p. 5752-5763.

122. M. Kaupp and P.v.R. Schleyer, *Do Low-Coordinated Group 1-3 Cations $M^{n+}L_m$ (M^{n+}=K^+, Rb^+, Cs^+, Ca^{2+}, Sr^{2+}, Ba^{2+}, Sc^{3+}, Y^{3+}, La^{3+}; L=NH_3, H_2O, HF; m=1-3) with a Formal Noble-Gas Electron Configuration Favor Regular or "Abnormal" Shapes?* J. Phys. Chem., 1992. **96**: p. 7316-7323.

123. D.M. Koch and G.H. Peslherbe, *On the Transition from Surface to Interior Solvation in Iodide–Water Clusters.* Chem. Phys. Lett., 2002. **359**: p. 381-389.

124. G.D. Markham, J.P. Glusker, C.L. Bock, M. Trachtman, and C.W. Bock, *Hydration Energies of Divalent Beryllium and Magnesium Ions: an Ab Initio Molecular Orbital Study.* J. Phys. Chem., 1996. **100**: p. 3488-3497.

125. T.-N.V. Nguyen and G.H. Peslherbe, *Microsolvation of Alkali and Halide Ions in Acetonitrile Clusters.* J. Phys. Chem. A., 2003. **107**: p. 1540-1550.

126. M. Pavlov, P.E.M. Siegbahn, and M. Sandstrom, *Hydration of Beryllium, Magnesium, Calcium, and Zinc Ions Using Density Functional Theory.* J. Phys. Chem. A, 1998. **102**: p. 219-228.

127. G.H. Peslherbe, B.M. Ladanyi, and J.T. Hynes, *Cluster Ion Thermodynamic Properties: The Liquid Drop Model Revisited.* J. Phys. Chem. A, 1999. **103**: p. 2561.

128. G.H. Peslherbe, B.M. Ladanyi, and J.T. Hynes, *Free Energetics of NaI Contact and Solvent-Seperated Ion Pairs in Water Clusters.* J. Phys. Chem. A, 2000. **104**: p. 4533-4548.

129. G.H. Peslherbe, B.M. Ladanyi, and J.T. Hynes, *Structure of NaI Ion Pairs in Water Clusters.* Chem. Phys., 2000. **258**(2-3): p. 201-224.

130. T.-N.V. Nguyen, S.R. Hughes, and G.H. Peslherbe, *Microsolvation of the Sodium Iodide Ion Pair in Acetonitrile Clusters: a Theoretical Study.* to be submitted.

131. W.W. Rudolph, R. Mason, and C.C. Pye, *Aluminium(III) Hyrdation in Aqueous Solution. A Raman Spectroscopic Investigation and an Ab Initio Molecular Orbital Study of Aluminium(III) Water Clusters.* Phys. Chem. Chem. Phys., 2000. **2**: p. 5030-5040.

132. E. Wasserman, J.R. Rustad, and S.S. Xantheas, *Interaction Potential of Al^{3+} in Water From First Principles.* J. Chem. Phys., 1997. **106**(23): p. 9769-9780.

133. A. Selinger and A.W.J. Castleman, *Evidence for the Encagement of Alkali Metal Ions Through the Formation of Gas-Phase Clathrates: Cs^{+} in Water Clusters.* J. Phys. Chem., 1991. **95**: p. 8442-8444.

134. D.F. Coker, R.E. Miller, and R.O. Watts, *The infrared predissociation spectra of water clusters.* J. Chem. Phys., 1985. **82**: p. 3554-3562.

135. C.K. Jørgenson, *Electric Polarizability, Innocent Ligands and Spectroscopic Oxidation States.* Struct. Bond., 1966. **1**: p. 234-249.

136. C.K. Jørgenson, *Relations Between Softness, Covalent Bonding, Ionicity and Electric Polarizability.* Struct. Bond., 1967. **3**: p. 106-115.

137. F. Weinhold, *Natural Bond Orbital Methods*, in *Encyclopedia of Computational Chemistry.* 1998, John Wiley: New York, NY. p. 1792-1811.

138. A. Savin, R. Nesper, S. Wengert, and T.F. Fassler, *ELF: the Electron Localization Function.* Angew. Chem. Int. Ed., 1997. **36**: p. 1808-1832.

139. A.D. Becke and K.E. Edgecombe, *A Simple Measure of Electron Localization in Atomic and Molecular Systems.* J. Chem. Phys., 1990. **92**(9): p. 5397-5403.

140. R.F.W. Bader, *Atoms in Molecules - A Quantum Theory.* 1990, New York: Oxford Press.

141. R.F.W. Bader, *A Bond Path: A Universal Indicator of Bonded Interactions.* J. Phys. Chem. A, 1998. **102**: p. 7314-7323.

142. C. Gourlaouen, J.-P. Piquemal, and O. Parisel, *$[Pb(H_2O)]^{2+}$ and $[Pb(OH)]^{+}$: Four-component density functional theory calculations, correlated scalar relativistic constrained-space orbital variation energy decompositions, and topological analysis.* J. Chem. Phys., 2006. **124**: p. 174311-174311-174313.

143. C. Gourlaouen, J.-P. Piquemal, T. Saue, and O. Parisel, *Revisiting the Geometry of $nd^{10}(n+1)s^0$ $[M(H_2O)]^{p+}$ Complexes Using Four-Component Relativisitic DFT Calculations and Scalar Relativistic Correlated CSOV Energy Decompositions (M^{p+} = Cu^+, Zn^{2+}, Ag^+, Cd^{2+}, Au^+, Hg^{2+}).* J. Comput. Chem., 2005. **27**: p. 142-156.

144. A.E. Reed and F. Weinhold, *Natural Bond Orbital Analysis of Near-Hartree-Fock Water Dimer.* J. Chem. Phys., 1983. **78**(6): p. 4066-4073.

145. A.E. Reed, R.B. Weinstock, and F. Weinhold, *Natural Population Analysis.* J. Chem. Phys., 1985. **83**(2): p. 735-746.

146. E.D. Glendening and F. Weinhold, *Natural Resonance Theory Part II: Bond Order and Valency.* J. Comput. Chem., 1998. **19**: p. 610-627.

147. E.D. Glendening and F. Weinhold, *Natural Resonance Theory Part I.* J. Comput. Chem., 1998. **19**: p. 593-609.

148. M.J. Frisch, G.W. Trucks, H.B. Schlegel, G.E. Scuseria, M.A. Robb, J.R. Cheeseman, V.G. Zakrzewski, J.A.M. Jr., R.E. Stratmann, J.C. Burant, S. Dapprich, J.M. Millam, A.D. Daniels, K.N. Kudin, M.C. Strain, O. Farkas, J. Tomasi, V. Barone, M. Cossi, R. Cammi, B. Mennucci, C. Pomelli, C. Adamo, S. Clifford, J. Ochterski, G.A. Petersson, P.Y. Ayala, Q. Cui, K. Morokuma, P. Salvador, J.J. Dannenberg, D.K. Malick, A.D. Rabuck, K. Raghavachari, J.B. Foresman, J. Cioslowski, J.V. Ortiz, A.G. Baboul, B.B. Stefanov, G. Liu, A. Liashenko, P. Piskorz, I. Komaromi, R. Gomperts, R.L. Martin, D.J. Fox, T. Keith, M.A. Al-Laham, C.Y. Peng, A. Nanayakkara, M. Challacombe, P.M.W. Gill, B. Johnson, W. Chen, M.W. Wong, J.L. Andres, C. Gonzalez, M. Head-Gordon, E.S. Replogle, and J.A. Pople, *Gaussian 98*. 2001, Gaussian, Inc: Pittsburgh, PA.

149. A.D. Becke, *Density-functional thermochemistry. III. The role of exact exchange.* J. Chem. Phys., 1993. **98**(5648-5652).

150. I.N. Levine, *Quantum Chemistry*. 5 ed. 1991, Englewood Cliffs, NJ: Prentice Hall Inc.

151. W.J. Hehre, L. Radom, P.v.R. Schleyer, and J.A. Pople, *Ab Initio Molecular Orbital Theory*. 1985, New York: John Wiley and Sons.

152. M.J. Frisch, J.A. Pople, and J.S. Binkley, *Self-Consistent Molecular Orbital Methods 25. Supplementary Functions for Gaussian Basis Sets.* J. Chem. Phys., 1984. **80**: p. 3265.

153. M. Dolg, H. Stoll, and H. Preuss, *Energy-adjusted Ab Initio Pseudopotentials for the Rare Earth Elements.* J. Chem. Phys., 1989. **90**: p. 1730-1734.

154. D. Andrae, U. Haeussermann, M. Dolg, H. Stoll, and H. Preuss, *Energy-adjusted pseudopotentials for the rare earth elements.* Theor. Chim. Acta, 1990. **75**: p. 173-194.

155. S.F. Boys and F. Bernardi, *The calculation of small molecular interactions by the differences of separate total energies. Some procedures with reduced errors.* Mol. Phys., 1970. **19**: p. 553-559.

156. G.H. Grant and W.G. Richards, *Computational Chemistry.* 1 ed. 1995, New York, NY: Oxford University Press.

157. B.H. Besler, K.M.J. Merz, and P.A. Kollman, *Atomic Charges Derived from Semiempirical Methods.* J. Comput. Chem., 1990. **11**: p. 431-439.

158. F.W. Biegler-Konig, R.F.W. Bader, and T.-H. Tang, *Calculation of the Average Properties of Atoms in Molecules. II.* J. Comput. Chem., 1982. **3**(3): p. 317-328.

159. F. Biegler-Konig, J. Schonbohm, and D. Bayles, *AIM2000 - A Program to Analyse and Visualize Atoms in Molecules.* J. Comput. Chem., 2001. **22**: p. 545-559.

160. F. Biegler-Konig and J. Schonbohm, *An Update to the AIM2000 - Program for Atoms in Molecules.* J. Comput. Chem., 2002. **23**: p. 1489-1494.

161. F. Weinhold, *NBO 4.M Program.* 1996, University of Wisconsin/Theoretical Chemistry Instititute: Madison, Wisconsin.

162. S. Noury, X. Krokidis, F. Fuster, and B. B. Silvi, *Computational Tools for the Electron Localization Function Topological Analysis.* Comput. Chem., 1999. **23**: p. 597-604.

163. E. Pepke, J. Murray, J. Lyons, and Y. Hwu, *SciAn is a free visualization software designed for high-performance graphic workstations. It is available online at the CCL website (http://www.ccl.net/cca/software/AIX/SciAn/index.shtml).*

164. D.F. Shriver, P.W. Atkins, and C.H. Langford, *Inorganic Chemistry.* 1 ed. 1990, New York, NY: W.H. Freeman and Company.

165. A.J. Stone, *The Theory of Intermolecular Forces.* 1 ed. 1997, New York, NY: Oxford University Press.

166. M. Kaupp, P.v.R. Schleyer, H. Stoll, and H. Preuss, *Pseudopotential approaches to Ca, Sr and Ba hydrides. Why are some alkaline earth MX_2 compounds bent?* J. Chem. Phys., 1991. **94**: p. 1360-1366.

167. M. Kaupp, P.v.R. Schleyer, H. Stoll, and H. Preuss, *The question of bending of the alkaline earth dihalides MX_2 (M = beryllium, magnesium, calcium, strontium, barium; X = fluorine, chlorine, bromine, iodine). An ab initio pseudopotential study.* J. Am. Chem. Soc., 1991. **113**: p. 6012-6020.

168. R.J. Gillespie, S. Noury, J. Pilmé, and B. Silvi, *An Electron Localization Function Study of the Geometry of d^0 Molecules of the Period 4 Metals Ca to Mn.* Inorg. Chem., 2004. **43**: p. 3248-3256.

169. Q.K. Timerghazin, T.-N. Nguyen, and G.H. Peslherbe, *Asymmetric solvation revisited: The importance of hydrogen bonding in iodide-acetonitrile clusters.* J. Chem. Phys., 2002. **116**: p. 6867-6870.

170. L. Rincón and R. Almeida, *On the Topology of the Electron Charge Density at the Bond Critical Point of the Electron-Pair Bond.* J. Phys. Chem. A, 1998. **102**: p. 9244-9254.

171. Y. Okuno, *A Cluster Model Study of Contact Ion Pair Formation of t-BuCl in Aqueous Solution: Calculational Evidence for Nucleophilic Solvent Assistance in S_N1 Reaction.* J. Phys. Chem. A, 1999. **103**: p. 190-196.

172. W. Meier, P. Bopp, M.M. Probst, E. Spohr, and J.-I. Lin, *Molecular Dynamics Studies of Lanthanum Chloride Solutions.* J. Phys. Chem., 1990. **94**: p. 4672-4682.

173. F.M. Floris and A. Tani, *A Study of Aqueous Solutions of Lanthanide Ions by Molecular Dynamics Simulation with ab initio Effective Pair Potentials.* J. Chem. Phys., 2001. **115**: p. 4750-4765.

174. H.J. Seifert and S. Funke, *Solution Enthalpies of Hydrates $LnCl_3.xH_2O$ (Ln=Ce-Lu).* Thermochim. Acta, 1998. **320**: p. 1-7.

175. Y. Marcus, *Complexes With Water*. Gmelin Handbuch der Anorganischen Chemie, ed. E.S.-R. T. Moeller. Vol. D3. 1980, New York, NY: Springer-Verlag.

176. V. Haase, H.K. Kugler, M. Lehl-Thalinger, and U. Trobisch-RauBendorf, *Verhlaten der Ionen in Losung*. Gmelin Handbuch der Anorganischen Chemie, ed. H.K. Kugler, H. Baergmann, and V. Haase. Vol. B7. 1979, New York, NY: Springer-Verlag.

177. L. Helm, F. Foglia, T. Kowall, and A.E. Merbach, *Structure and Dynamics of Lanthanide Ions and Lanthanide Complexes in Solution.* J. Phys.: Condens. Matter, 1994. **6**: p. A137-A140.

178. S. Galera, J.M. Lluch, A. Oliva, J. Bertrán, F. Foglia, L. Helm, and A.M. Merbach, *Monte Carlo Simulations of the Tripositive Lanthanide Ions in Aqueous Solution.* New. J. Chem., 1993. **17**: p. 773-779.

179. C. Cossy and A.E. Merbach, *Recent Developments in Solvation and Dynamics of the Lanthanide (III) Ions.* Pure Appl. Chem., 1988. **60**: p. 1785-1796.

180. T. Kowall, F. Foglia, L. Helm, and A.E. Merbach, *Molecular Dynamics Simulation Study of Lanthanide Ions Ln^{3+} in Aqueous Solution Including Water Polarization. Change in Coordination Number from 9 to 8 Along the Series.* J. Am. Chem. Soc., 1995. **117**: p. 3790-3799.

181. T. Kowall, F. Foglia, L. Helm, and A.E. Merbach, *Molecular Dynamics Simulation Study of Lanthanide Ions Ln^{3+} in Aqueous Solution. Analysis of the Structure of the First Hydration Shell and of the Origin of Symmetry Fluctuations.* J. Phys. Chem., 1995. **99**: p. 13078-13087.

182. J.A. Pople, M. Head-Gordon, and K. Raghavachari, *Quadratic Configuration Interaction. A General Technique for Determining Electron Correlation Energies.* J. Chem. Phys., 1987. **87**: p. 5968-5975.

183. M. Dolg, H. Stoll, A. Savin, and H. Preuss, *Energy-adjusted Pseudopotentials for the Rare Earth Elements.* Theor. Chim. Acta, 1989. **75**: p. 173-194.

184. Q.K. Timerghazin and G.H. Peslherbe, *Halide Ions in a Methyl Pocket: Competition Between Hydrogen Bonding and Ion-Dipole Interactions in Acetonitrile-Halide Complexes.* Submitted for publication.

185. L.X. Dang and T.M. Chang, *Molecular dynamics study of water clusters, liquid, and liquid–vapor interface of water with many-body potentials.* J. Chem. Phys., 1997. **106**: p. 8149.

186. L. Perera and F.G. Amar, *Charge localization in negative ion dynamics: Effect on caging of Br in Ar_n and $(CO_2)_n$ clusters.* J. Chem. Phys., 1989. **90**: p. 7354-7368.

187. W.H. Press, *Numerical Recipes, The Art of Scientific Computing.* 1992, Cambridge: Cambridge University Press.

188. W.S. Benedict, N. Gailar, and E.K. Plyler, *Rotation-Vibration Spectra of Deuterated Water Vapor.* J. Chem. Phys., 1956. **24**: p. 1139-1165.

189. D.R. Lide, *CRC Handbook of Chemistry and Physics*. 77 ed. 1996, Boca Raton, FL: CRC.

190. N. Metropolis, A.W. Rosenbluth, M.N. Rosenbluth, A.H. Teller, and E. Teller, *Simulations of Liquids and Solids*. 1987, New York: North-Holland.

191. P. Atkins, ed. *Physical Chemistry.* 6th ed., ed. W.H.F.a. Co. 1997, Freeman: New York.

192. A.K. Rappé and W.A.G. III, *Charge Equilibration for Molecular Dynamics Simulation.* J. Phys. Chem., 1991. **95**: p. 3358-3363.

193. R. Janes and E. Moore, *Metal-Ligand Bonding.* 2004, Cambridge, UK: Royal Society of Chemistry.

194. L.C. Thompson, *Complexes*, in *Handbook on the Physics and Chemistry of Rare-Earths*, J. K.A. Gschneider and L. Eyring, Editors. 1979, North-Holland: New York, NY.

195. L. Tilkens, K. Randall, J. Sun, M.T. Berry, P.S. May, and T. Yamase, *Spectroscopic Evidence for Equilibrium Between Eight- and Nine-Coordinate $Eu^{3+}(aq)$ Species in 0.1 M $EuCl_3(aq)$.* J. Phys. Chem. A, 2004. **108**: p. 6624-6628.

196. A.H. Narten and R.L. Hahn, *Direct Determination of Ionic Solvation from Neutron Diffraction.* Science, 1982. **217**: p. 1249-1250.

197. M.L. Steele and D.L. Wertz, *Solvent Effects on the Coordination of Nd^{3+} in Concentrated $NdCl_3$ Solutions.* Inorg. Chem., 1977. **16**: p. 1225-1228.

198. L. Helm and A.E. Merbach, *Water Exchange on Metal Ions: Experiments and Simulations.* Coord. Chem. Rev., 1999. **187**: p. 151-181.

199. S. Chaussedent and A. Monteil, *Molecular Dynamics Simulation of Trivalent Europium in Aqueous Solution: A Study on the Hydration Shell Structure.* J. Chem. Phys., 1996. **105**: p. 6532-6537.

200. S. Chaussedent, A. Monteil, M. Ferrari, and L.D. Longo, *Molecular Dynamics Simulations of study of Eu^{3+} in an aqueous solution: luminescence spectrum from simulated environments.* Phil. Mag. B, 1998. **77**: p. 681-688.

201. F.C.J.M. van_Veggel and D.N. Reinhoudt, *New, accurate Lennard-Jones parameters for trivalent lanthanide ions, tested on [18]Crown-6.* Chem. Eur. J., 1999. **5**: p. 90-95.

202. M. Dolg, H. Stoll, and H. Preuss, *A Combination of Quasirelativistic Pseudopotential and Ligand Field Calculations for Lanthanoid Compounds.* Theor. Chim. Acta, 1993. **85**: p. 441-449.

203. Preliminary calculations with regards to the relative stabilities of $Ln^{3+}(H_2O)$ and $Ln^{2+}(OH)$ clusters suggests that the latter appears more stable by ~40 kcal/mol. This may explain in part why trivalent lanthanide water clusters have not been successfully detected under conventional spray conditions.

204. C.K. Jørgenson, *Theoretical Chemistry of Rare Earths*. Handbook on the Physics and Chemistry of Rare-Earths, ed. K.A. Gschneider and L. Eyring. Vol. 1. 1979, New York, NY: North-Holland.

205. Previous calculations of the dipole moment of water in $Gd^{3+}(H_2O)$ using the Natural Bond Orbital (NBO) method have suggested that the dipole moment of the complexed water molecule may in fact be closer to 5.7 D [112]. This value is in excellent agreement with the predictions of our model potentials (~6.0 D).

206. K. Mickskei, D.H. Powell, L. Helm, E. Brücher, and A.E. Merbach, *Water Exchange on the Light Lanthanide Aqua Ions $[Pr(H_2O)_9]^{3+}$ and $[Nd(H_2O)_9]^{3+}$: a Variable Temperature and Magnetic Field ^{17}O NMR Study.* Magn. Reson. Chem., 1993. **31**: p. 1011-1020.

207. D.H. Powell and A.E. Merbach, *Water Exchange on the Light Lanthanide Aqua Ions $[Pr(H_2O)_9]^{3+}$ and $[Nd(H_2O)_9]^{3+}$: a Variable Temperature and Magnetic Field ^{17}O NMR Study.* Magn. Reson. Chem., 1994. **32**: p. 739-745.

208. P. Lindqvist-Reis, K. Lamble, S. Pattanaik, I. Persson, and M. Sandström, *Hydration of Yttrium(III) Ion in Aqueous Solution. An X-Ray Diffraction and XAFS Structural Study.* J. Phys. Chem. B, 2000. **104**: p. 402-408.

209. P. Vitorge and M. Masella, *A Theoretical Study of $[Be,(H_2O)_n]^{2+}$, $[BeOH,(H_2O)_{n-1}]^{+}$ and $[Be(OH)_2,(H_2O)_{n-2}]$ Aggregates (n = 1-6). Incidence of the First Hydration Shells on the Hydrolysis Reactions of Be^{2+} and $BeOH^{+}$ Systems.* Chem. Phys. Lett., 2000. **332**: p. 367-374.

210. J.P. Perdew and A. Zunger, *Self-interaction correction to density-functional approximations for many-electron systems.* Phys. Rev. B, 1981. **23**: p. 5048-5079.

211. P.M.W. Gill, *A New Gradient-Corrected Exchange Functional.* Mol. Phys., 1996. **89**: p. 433-445.

212. D. Feller, E.D. Glendening, D.E. Woon, and M.W. Feyereisen, *An Extended Basis Set ab initio Study of Alkali Metal Cation-Water Clusters.* J. Chem. Phys., 1995(3526-3542).

213. H.A. Jann, Proc. R. Soc. Lond., 1938. **A164**: p. 117-131.

214. H.A. Jann and E. Teller, Proc. R. Soc. Lond., 1937. **A161**: p. 220-225.

215. J.-C.G. Bünzli and A. Milicic-Tang, *FT-IR and Fluorometric Investigation of Rare-Earth and Metal Ion Solvation Part 16. Solid State and Solution Study of Acetonitrile-Coordinated Lanthanide Solvates $[Ln(CH_3CN)_9](AlCl_4)_3$].* Inorg. Chim. Acta, 1996. **252**: p. 221-228.

216. H.-S. Kim, *Solvent effect on La^{3+} to Nd^{3+} ion mutation: a Monte Carlo simulation study.* Chem. Phys. Lett., 2000. **330**: p. 570-576.

217. H.-S. Kim, *Solvent Effect on Relative Gibbs Free Energy and Structural Property of Eu^{3+} to Yb^{3+} Ion Mutation: A Monte Carlo Simulation Study.* Bull. Korean Chem. Soc., 2001. **22**: p. 877-882.

218. H.S. Kim, *A Monte Carlo simulation study of solvent effect on Eu^{3+} to Nd^{3+} ion mutation.* Chem. Phys., 2001. **269**: p. 295-302.

219. M.J. Frisch, G.W. Trucks, H.B. Schlegel, G.E. Scuseria, M.A. Robb, J.R. Cheeseman, J.A. Montgomery_Jr., T. Vreven, K.N. Kudin, J.C. Burant, J.M. Millam, S.S. Iyengar, J. Tomasi, V. Barone, B. Mennucci, M. Cossi, G. Scalmani, N. Rega, G.A. Petersson, H. Nakatsuji, M. Hada, M. Ehara, K. Toyota, R. Fukuda, J. Hasegawa, M. Ishida, T. Nakajima, Y. Honda, O. Kitao, H. Nakai, M. Klene, X. Li, J.E. Knox, H.P. Hratchian, J.B. Cross, V. Bakken, C. Adamo, J. Jaramillo, R. Gomperts, R.E. Stratmann, O. Yazyev, A.J. Austin, R. Cammi, C. Pomelli, J.W. Ochterski, P.Y. Ayala, K. Morokuma, G.A. Voth, P. Salvador, J.J. Dannenberg, V.G. Zakrzewski, S. Dapprich, A.D. Daniels, M.C. Strain, O. Farkas, D.K. Malick, A.D. Rabuck, K. Raghavachari, J.B. Foresman, J.V. Ortiz, Q. Cui, A.G. Baboul, S. Clifford, J. Cioslowski, B.B. Stefanov, G. Liu, A. Liashenko, P. Piskorz, I. Komaromi, R.L. Martin, D.J. Fox, T. Keith, M.A. Al-Laham, C.Y. Peng, A. Nanayakkara, M. Challacombe, P.M.W. Gill, B. Johnson, W. Chen, M.W. Wong, C. Gonzalez, and J.A. Pople, *Gaussian 03*. 2004, Gaussian, Inc: Wallingford, CT.

220. P.A. Steiner and W. Gordy, *Precision measurement of dipole moments and other spectral constants of normal and deuterated methyl fluoride and methyl cyanide.* J. Mol. Spectrosc., 1966. **21**: p. 291-301.

221. E.M. Cabaleiro-Lago and M.A. Rios, *Ab Initio Study of $M(CH_3CN)_n$ Clusters ($M = Li^+, Na^+, Mg^{2+}$) in Gas Phase.* Chem. Phys., 2000. **254**: p. 11-23.

222. K.M.S. Saxena and S. Fraga, *Electric Dipole Polarizabilities of Lanthanide and Actinides.* J. Chem. Phys., 1972. **57**: p. 1800-1801.

223. W.E. Putnam, D.M. McEachern_Jr., and J.E. Kilpatrick, *Entropy and Related Thermodynamic Properties of Acetonitrile (Methyl Cyanide).* J. Chem. Phys., 1965. **42**: p. 749-755.

224. H.B. Schlegel, S.S. Iyengar, X. Li, J.M. Millam, G.A. Voth, G.E. Scuseria, and M.J. Frisch, *Ab initio Molecular Dynamics: Propagating the Density Matrix with Gaussian Orbitals: III. Comparison with Born-Oppenheimer Dynamics.* J. Chem. Phys., 2002. **117**: p. 8694-8704.

225. H.B. Schlegel, J.M. Millam, S.S. Iyengar, G.A. Voth, A.D. Daniels, G.E. Scuseria, and M.J. Frisch, *Ab initio Molecular Dynamics: Propagating the Density Matrix with Gaussian Orbitals.* J. Chem. Phys., 2001. **114**: p. 9758-9763.

226. Q. Cui, M. Elstner, E. Kaxiras, T. Frauenheim, and M. Karplus, *A QM/MM Implementation of the Self-Consistent Charge Density Functional Tight Binding (SCC-DFTB) Method.* J. Phys. Chem. B, 2001. **105**: p. 569-585.

227. M. Haugk, J. Elsner, T. Heine, T. Frauenheim, and G. Seifert, *A Parallel Code for a Self-Consistent Charge Density Functional Based Tight Binding Method: Total Energy Calculations for Extended Systems.* Comput. Mater. Sci., 1999. **13**: p. 239-251.

228. S. Chaussedent, *Étude par Simulation Numérique de la Structure et de la Dynamique d'un Ion Luminescent en Solution dans l'Eau. Calcul des Proprietés Spectroscopiques*, in *Department of Physics*. 1997, Université d'Angers: Angers. p. 181.

229. R.P. Leavitt, C.A. Morrison, and D.E. Wortman, *Rare-Earth Ion-Host Crystal Field Interactions 3. Three-Parameter Theory of Crystal Fields.* 1975, Harry Diamond Laboratories.

230. P.B. Petersen and R.J. Saykally, *Evidence for an Enhanced Hydronium Concentration at the Liquid Water Surface.* J. Phys. Chem. B, 2005. **109**: p. 7976-7980.

231. P.B. Petersen, R.J. Saykally, M. Mucha, and P. Jungwirth, *Enhanced Concentration of Polarizable Anions at the Liquid Water Surface: SHG Spectroscopy and MD Simulations of Sodium Thiocyanide.* J. Phys. Chem. B, 2005. **109**: p. 10915-10921.

232. J.W. Ponder, *TINKER - Software tools for molecular design.* 2004, Washington University School of Medicine: St. Louis, Missouri.